FATIGUE PERFORMANCE EVALUATION OF WESTRACK ASPHALT MIXTURES USING VISCOELASTIC CONTINUUM DAMAGE APPROACH

Final Report
(Report No. FHWA/NC/2002-004)

To North Carolina Department of Transportation
(Research Project No. HWY-0678)

Submitted by

Y. Richard Kim, Ph.D., P.E.
Campus Box 7908
Department of Civil Engineering
North Carolina State University
Raleigh, NC 27695-7908
Ph: 919-515-7758
Fax: 919-515-7908
E-mail: kim@eos.ncsu.edu

Jo Sias Daniel, Ph.D.
Former Graduate Student

Haifang Wen, Ph.D.
Former Graduate Student

April 2002

Technical Report Documentation Page

1. Report No. **FHWA/NC/2002-004**	2. Government Accession No.	3. Recipient's Catalog No.
4. Title and Subtitle Fatigue Performance Evaluation of WesTrack Asphalt Mixtures Using Viscoelastic Continuum Damage Approach		5. Report Date April 2002
		6. Performing Organization Code
7. Author(s) Y. Richard Kim, Jo S. Daniel, and Haifang Wen		8. Performing Organization Report No.
9. Performing Organization Name and Address North Carolina State University Department of Civil Engineering Campus Box 7908 Raleigh, NC 27695-7908		10. Work Unit No. (TRAIS)
		11. Contract or Grant No.
12. Sponsoring Agency Name and Address U.S. Department of Transportation Federal Highway Administration 400 7th Street, SW Washington, DC 20590-0001		13. Type of Report and Period Covered Final Report July 1998 – December 2000
		14. Sponsoring Agency Code HWY-0678
15. Supplementary Notes		

16. Abstract

The primary objective of this project is to develop laboratory test methods and a fundamentally sound fatigue model that accurately predict or rank the fatigue performance of asphalt mixtures in the field. For the validation of the model, eight WesTrack mixtures with varying gradations, asphalt contents, and air void contents were used. Both direct tension and indirect tension tests were conducted.

This report presents the findings from direct tension and indirect tension tests. From the direct tension testing, a methodology was developed by which the material response under any uniaxial tensile testing condition (type of loading and temperature) can be predicted from the material response obtained from a single testing condition. The methodology makes use of a uniaxial constitutive model for asphalt concrete that is based upon the elastic-viscoelastic correspondence principle and work potential theory, a continuum damage theory based on thermodynamics of irreversible process. Uniaxial tensile testing is performed under controlled crosshead mode for both cyclic and constant rate to failure tests. Various strain amplitudes, frequencies, and rates are applied at several test temperatures. A single characteristic curve can be found that describes the reduction in material integrity as damage grows in the specimen regardless of the applied loading conditions (cyclic versus monotonic, amplitude/rate, frequency). The characteristic curve at any temperature can be found by utilizing the time-temperature superposition principle and the concept of reduced time. Eight WesTrack mixtures are tested and the methodology is used to successfully predict the fatigue damage at different testing conditions from a single condition. A test and analysis procedure for the fatigue characterization of asphalt mixtures based on this methodology is proposed and potential applications are discussed.

In this report, also presented are the viscoelastic characterization of asphalt concrete in indirect tensile testing and the development of a simple performance test for fatigue cracking. The analytical solutions to calculate creep compliance and center strain from displacements measured on the specimen surface were developed based upon the theory of viscoelasticity. These developments were verified by 3-D finite element viscoelastic analysis and tests. A simple performance test was developed based on these solutions and work potential theory. To evaluate its validity, the indirect tensile tests were performed on WesTrack asphalt mixtures varying aggregate gradations, asphalt contents, and air void contents. Fracture energy obtained from indirect tensile strength testing and creep testing was highly correlated with field performance of these mixtures at WesTrack. A combination of indirect tensile creep and strength testing was proposed as a simple performance test for fatigue cracking.

17. Key Words Fatigue, Cracking, WesTrack, Viscoelastic, Performance Test, Asphalt Concrete, Continuum Damage	18. Distribution Statement		
19. Security Classif. (of this report) Unclassified	20. Security Classif. (of this page) Unclassified	21. No. of Pages 231	22. Price

Form DOT F 1700.7 (8-72) **Reproduction of completed page authorized**

ABSTRACT

The primary objective of this project is to develop laboratory test methods and a fundamentally sound fatigue model that accurately predict or rank the fatigue performance of asphalt mixtures in the field. For the validation of the model, eight WesTrack mixtures with varying gradations, asphalt contents, and air void contents were used. Both direct tension and indirect tension tests were conducted.

This report presents the findings from direct tension and indirect tension tests. From the direct tension testing, a methodology was developed by which the material response under any uniaxial tensile testing condition (type of loading and temperature) can be predicted from the material response obtained from a single testing condition. The methodology makes use of a uniaxial constitutive model for asphalt concrete that is based upon the elastic-viscoelastic correspondence principle and work potential theory, a continuum damage theory based on thermodynamics of irreversible process. Uniaxial tensile testing is performed under controlled crosshead mode for both cyclic and constant rate to failure tests. Various strain amplitudes, frequencies, and rates are applied at several test temperatures. A single characteristic curve can be found that describes the reduction in material integrity as damage grows in the specimen regardless of the applied loading conditions (cyclic versus monotonic, amplitude/rate, frequency). The characteristic curve at any temperature can be found by utilizing the time-temperature superposition principle and the concept of reduced time. Eight WesTrack mixtures are tested and the methodology is used to successfully predict the fatigue damage at different testing conditions from a single condition. A test and analysis procedure for the fatigue characterization of asphalt mixtures based on this methodology is proposed and potential applications are discussed.

In this report, also presented are the viscoelastic characterization of asphalt concrete in indirect tensile testing and the development of a simple performance test for fatigue cracking. The analytical solutions to calculate creep compliance and center strain from displacements measured on the specimen surface were developed based upon the theory of viscoelasticity. These developments were verified by 3-D finite element viscoelastic analysis and tests. A simple performance test was developed based on these solutions and work potential theory. To evaluate its validity, the indirect tensile tests were performed on WesTrack asphalt mixtures varying aggregate gradations, asphalt contents, and air void contents. Fracture energy obtained from indirect tensile strength testing and creep testing was highly correlated with field performance of these mixtures at WesTrack. A combination of indirect tensile creep and strength testing was proposed as a simple performance test for fatigue cracking.

DISCLAIMER

ACKNOWLEDGMENTS

The authors would like to acknowledge the support of the North Carolina Department of Transportation and the Federal Highway Administration. Also, special thanks go to Dr. Sirous Alavi at Nichols Consulting Company and Mr. John D'Angello at Federal Highway Administration for their help in collecting WesTrack materials and cores.

TABLE OF CONTENTS

LIST OF TABLES

LIST OF FIGURES

1. INTRODUCTION

Fatigue cracking is one of the most influential distresses that govern the service life of asphalt concrete pavements. Fatigue cracks are due to repeated traffic loading and/or temperature cycling over extended periods that induce combinations of tensile and shear stresses in asphalt concrete layers. These stresses initiate microcracks and cause them to propagate, densify, and coalesce to form macrocracks. For many years, significant research efforts have focused on developing reliable fatigue prediction models. These models usually relate the *initial* response (such as tensile strain or dissipated energy) of asphalt mixture to the fatigue life. As a result, they cannot accurately account for complex damage evolution under realistic loading conditions (e.g., multi-level loading, changing rest periods, varying loading rates, etc.) that occur throughout the service life of pavement systems. These models are simple to use because the only response of the mixture that needs to be measured is at the initial stage of fatigue testing. However, with the advanced automatic control/data acquisition systems available today, this advantage of simplicity is not substantial.

Development of a fundamentally sound fatigue model serves two important purposes. For pavement engineers, this model can provide accurate information on fatigue performance of asphalt concrete under realistic loading conditions, leading to better assessment of fatigue life of a new pavement or the remaining life of an existing pavement. For materials engineers, the fatigue model founded on basic principles in mechanics provides relationships between material properties (chemical or mechanical) and model parameters, which can be used for selection or design of more fatigue-resistant binders or mixtures.

Since the fatigue of asphalt concrete is the result of microcrack initiation and propagation processes governed by the local state of stress and strain, a reliable fatigue performance prediction model must be based on a constitutive model that describes the stress-strain behavior of the material under realistic loading and environmental conditions. It is well known that the deformation behavior of asphalt concrete is dependent upon time variables (e.g., rate of loading, durations of loading and rest, and aging), temperature, and stress state (including stress magnitude and path). Effects of these variables can be incorporated into the constitutive model using fundamental principles that have been successfully applied to other viscoelastic particulate composites.

In the previous FHWA project (DTFH 61-92-C-00170), some advancements were made in the fatigue performance prediction modeling of asphalt concrete (Kim et al. 1997). A uniaxial viscoelastic continuum damage model was developed by applying the elastic-viscoelastic correspondence principle to separate out the effect of viscoelasticity and then employing internal state variables based on work potential theory to account for damage evolution under loading and microdamage healing during rest periods. Through the verification study, it was found that the constitutive model has the ability to predict the hysteretic behavior of the material under both monotonic and cyclic loading up to failure, varying loading rates, random rest durations, multiple stress/strain levels, and different modes of loading (controlled-stress versus controlled-strain).

This research is divided into two major tasks. The first task utilizes the direct tension test method and applies the viscoelastic continuum damage model developed from the previous FHWA project to the investigation of the fatigue performance of various mixtures in the WesTrack test pavement project. The continuum damage model is extended to include the effect of temperature and used to investigate the effect of moisture on the fatigue performance of asphalt mixtures. The second task focuses on the development of a simple performance test method. Both the direct tension and indirect tension tests are performed on various WesTrack mixtures, and the results are evaluated against the known field performance of these mixtures. For the indirect tension test, theory of viscoelasticity is applied to develop solutions for material properties (e.g., creep compliance and Poisson's ratio) and the tensile strain at the center of the specimen.

In Section 2, primary objectives of this research are presented along with an executive summary of the findings from this research. Theoretical backgrounds behind the theories used in this research are presented in Section 3. Sections 4 and 5 describe the test methods, materials, and specimen fabrication methods used in this research. Section 6 presents the research effort in developing a damage characteristic curve using the direct tension test that accounts for the effects of loading rate and frequency, strain amplitude, and temperature. In Section 7, theory of viscoelasticity is applied to the indirect tension test to develop analytical solutions for creep compliance, Poisson's ratio, and center strain. The development of a simple performance test and its validation efforts are presented in Section 8. Finally, conclusions and recommendations for the future research are made in Section 9.

2. OBJECTIVES AND SUMMARY

2.1 Objectives

The principal objectives of the research were:

(1) to investigate the causes for early fatigue failure of WesTrack pavements using the viscoelastic continuum damage model,
(2) to evaluate the effects of mix variables (e.g., asphalt content, air voids content, aggregate gradation) and testing conditions (e.g., temperature and moisture) on fatigue performance of asphalt concrete using the viscoelastic continuum damage fatigue model,
(3) to verify or calibrate the fatigue performance prediction by the viscoelastic continuum damage fatigue model using actual performance data from the experimental pavement sections, and
(4) to evaluate the viscoelastic continuum damage fatigue models with different levels of simplification under varying mix and testing conditions to develop a simple test method for fatigue cracking.

2.2 Summary

The primary purpose of this research is to develop laboratory test and analysis methods that accurately predict or rank the fatigue performance of mixtures in the field. The mixtures evaluated in this study contain a single aggregate and asphalt source, but with different gradations, asphalt contents and air void contents. Eight mixtures are evaluated in this study: a low, optimum, and high asphalt content at 8% air voids, and an optimum asphalt content at 4% air voids for two different gradations. The field performance of these mixtures is known from the testing performed at the WesTrack load track test facility located near Reno, Nevada. Additionally, pavement cores are obtained from the load track for various mixtures and tested in the laboratory.

Laboratory testing is performed in both direct tension and indirect tension (IDT) on laboratory mixed, laboratory compacted specimens. IDT testing is also performed on pavement cores obtained from the test track. The IDT testing is performed on 100 mm diameter, 38 mm thick specimens and consists of a creep compliance test followed by constant crosshead rate loading to failure at 20^{o}C. Horizontal and vertical strains are measured over a 50 mm gage length in the center of the specimen on both faces. Analytical solutions to calculate the creep compliance and center strain from the surface displacement measurements are developed based on the theory of linear viscoelasticity. Verification is performed using 3-D finite element viscoelastic analysis and testing.

A simple performance test for fatigue cracking is developed by applying Schapery's work potential theory to testing of IDT specimens. The simple performance test is expected to provide reliable information on the performance of the asphalt concrete mixture from a laboratory mixed-laboratory compacted (LMLC) specimen obtained from the Superpave volumetric mix design process. The fracture energy, the area under the stress-strain curve up to peak stress from the indirect tensile strength test, was found to be a good indicator for field performance. The ranking of the mixtures with respect to this parameter agree with the ranking of the mixtures in the field with respect to the percentage of fatigue cracking at known ESAL applications. This indicates that the indirect tensile strength test is a strong candidate for a simple performance test for fatigue cracking.

Validation of the proposed simple performance test for fatigue cracking is accomplished by testing actual pavement cores. The field mixed-field compacted (FMFC) specimens obtained from the test pavement more accurately represent the in-place pavement material than the LMLC specimens. Field cores were obtained from ten different sections and represented a wide range of fatigue performance in the field. Again, fracture energy was found to be a good indicator of fatigue performance in the field and was able to distinguish between the performance of mixtures with different gradations, asphalt contents, and air void contents. A modified logit model was used to represent the relationship between fracture energy and fatigue cracking and is shown in Figure 2.1. A high correlation with fatigue cracking was also found using strain energy and damage energy.

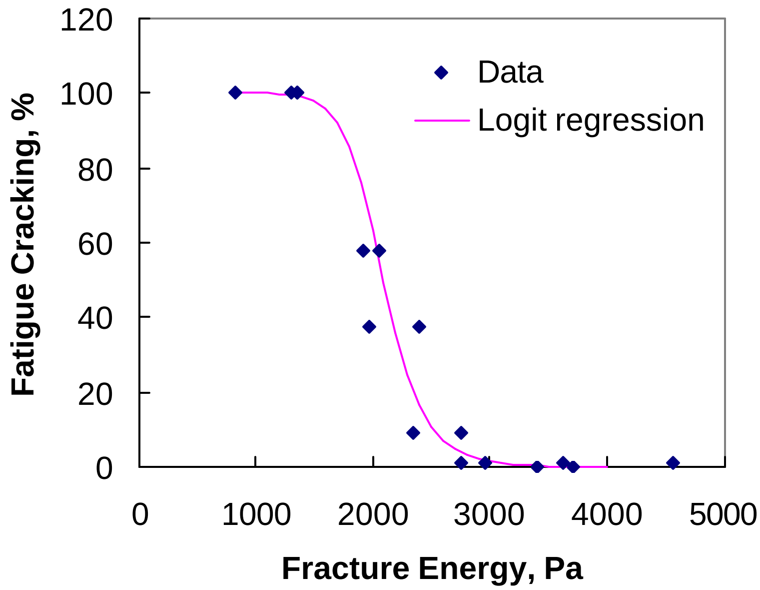

Figure 2.1 Relationship between Field Performance and Fracture Energy

The direct tension testing is performed on 150 mm high, 75 mm diameter specimens. Strains are measured over a 100 mm gage length in the middle of the specimen using four LVDTs spaced 90^o apart around the circumference of the specimen. The testing performed in uniaxial tension includes frequency sweep at 5^o and 20^oC followed by either constant cyclic loading at 1 or 10 Hz to failure or constant crosshead rate loading to failure. Both types of failure tests are performed at different amplitudes or rates and at the two different temperatures.

The work potential theory approach used in the IDT simple performance test development is also applied to direct tension testing. Using the work potential and various other parameters a reliable indicator for fatigue cracking in the field could not be found with direct tension testing. The difference in compaction direction versus testing direction in the IDT and direct tension methods is the likely cause.

A prediction methodology based on a uniaxial constitutive model is developed from the direct tension testing. The uniaxial model is based upon the theory of viscoelasticity, the elastic-viscoelastic correspondence principle, and work potential theory to describe the damage growth in the specimen. Using the constitutive model, a characteristic curve is developed that describes the reduction in the material integrity as a function of the damage growth in the specimen. It was found that a single characteristic curve is developed from cyclic testing at any frequency or amplitude and constant crosshead rate testing at any rate for a particular temperature. In other words, the individual characteristic curves found from testing at 1 Hz and10 Hz at different strain amplitudes, and constant crosshead rate tests at different rates all overlap when plotted together, as shown in Figures 2.2 and 2.3. The power of this lies in the fact that the material response under ANY loading history can be predicted using the characteristic curve developed from a single test.

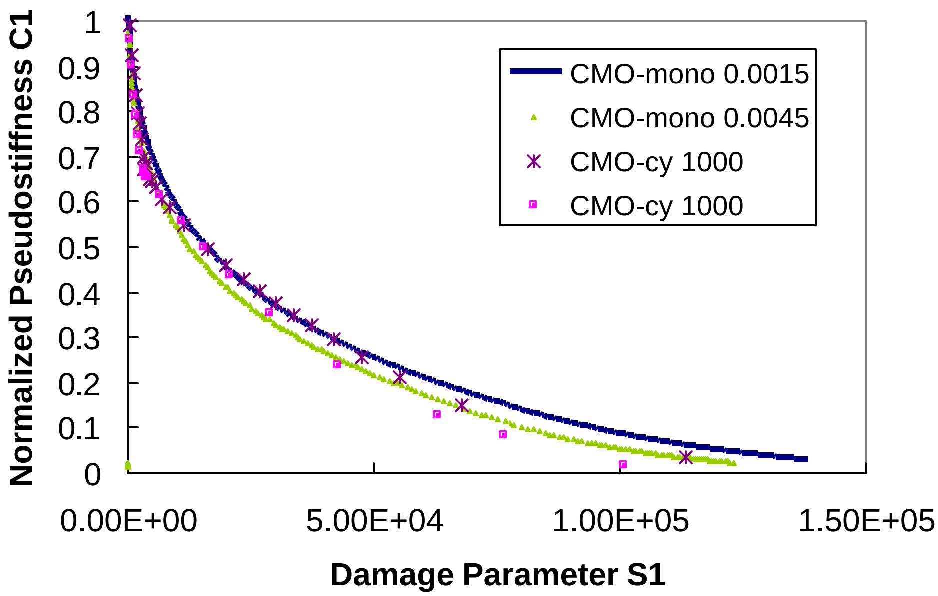

Figure 2.2 Characteristic C_1 versus S_1 Curve for Cyclic and Monotonic Testing on CMO Mixture at 20^{o}C (Cyclic Testing at 1000 Crosshead Microstrain Amplitude, Monotonic Testing at Two Crosshead Strain Rates)

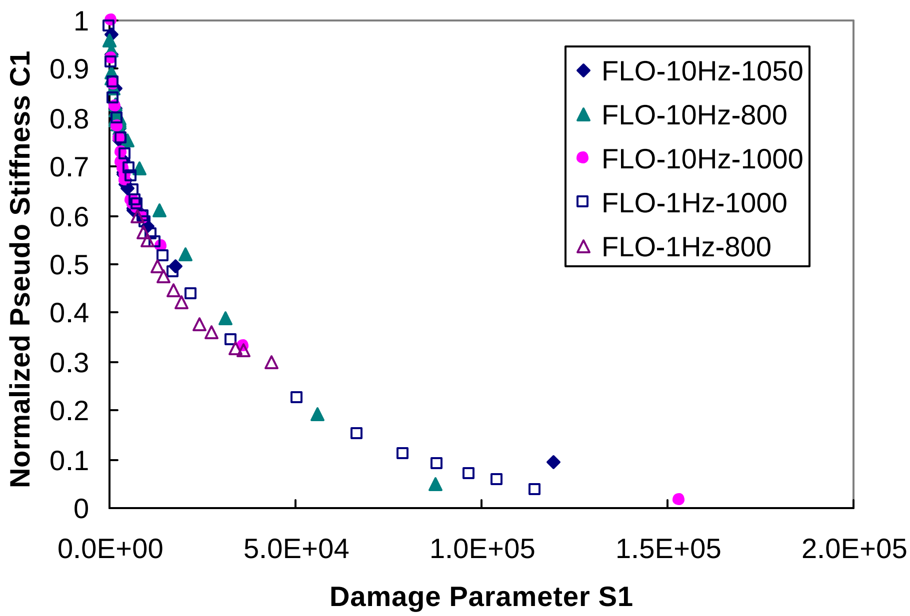

Figure 2.3 Characteristic C_1 versus S_1 Curve for 10 Hz and 1 Hz Cyclic Testing at 20°C on FLO Mixture at Several Strain Amplitudes (Crosshead Microstrain Values Range between 800 and 1050)

Additionally, the time-temperature superposition principle and the concept of reduced time are used to shift the characteristic curve to different temperatures, as shown in Figure 2.4. Thus, if the time-temperature shift factors are known as a function of temperature, the material response under any strain history and at any temperature can be predicted from the characteristic curve developed from a handful of tests. Prediction errors of peak stress from the monotonic test or number of cycles to failure from the cyclic fatigue tests were typically 10-15%, with a maximum error around 30%. For comparison, sample-to-sample variability in replicate cyclic fatigue tests was found to be up to 80%.

Based on the prediction methodology, a fatigue test and analysis procedure is proposed that takes advantage of the single characteristic curve incorporating the effect of loading history (path, rate, and amplitude) and temperature. The proposed procedure requires a week of testing time and will provide predicted information that would take up to several months to obtain through a full testing program. This fatigue and analysis procedure greatly reduces the required testing time in addition to the material cost and timesavings associated with sample fabrication. The procedure can be applied to a wide range of testing and design scenarios incorporating various levels of complexity depending upon the particular application and agency preferences.

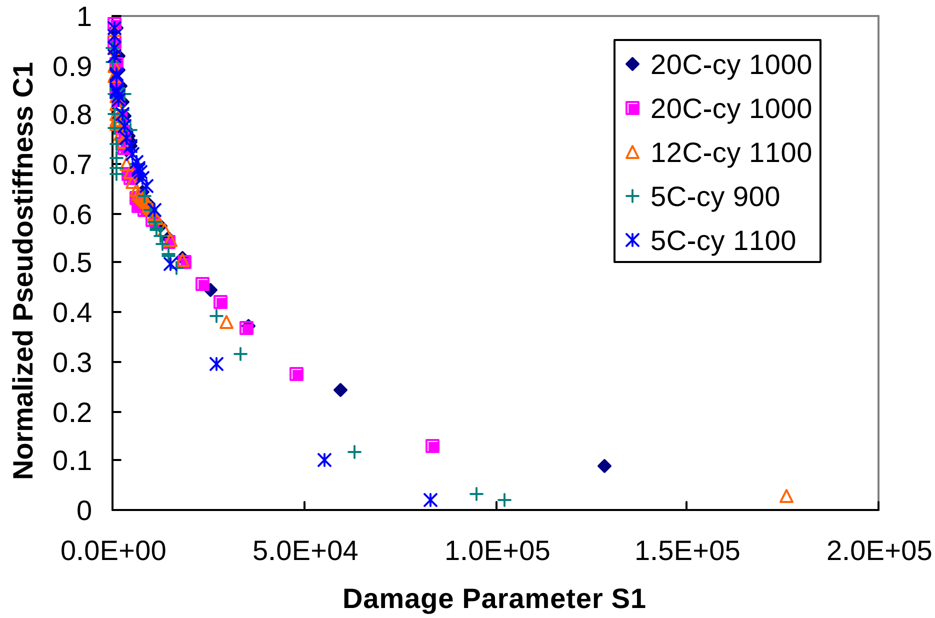

Figure 2.4 Cyclic Characteristic C_1 versus S_1 Curves Shifted to Reference Temperature of 20^oC for CML Mixture

3. THEORETICAL BACKGROUND

3.1 Uniaxial Testing

The evolution of the research presented herein began with the work of Kim and Little (1990). Kim and Little successfully applied Schapery's (1981) nonlinear viscoelastic constitutive theory for composite materials with distributed damage to sand asphalt concrete under cyclic loading. In this model, a viscoelastic problem is transformed to an elastic case by replacing physical strains by pseudo strains based on the extended elastic-viscoelastic correspondence principle (Schapery 1984). A damage parameter based on a microcrack growth law and pseudo strain values are used to describe the effect of growing damage on the deformation behavior of the material.

Schapery (1990) developed work potential theory for elastic materials with growing damage based on the thermodynamics of irreversible processes. The theory uses an internal state variable formulation to describe the structural changes with damage growth and was also extended to viscoelastic media. This theory was successfully applied to asphalt concrete under monotonic loading (Park et al. 1996) and cyclic loading (Lee 1996, Kim et al. 1997, Lee and Kim 1998a). It is the work by Lee that forms the foundation for the current research.

This section presents the basic theories that are applied in this research, starting with the theory of viscoelasticity, followed by the elastic-viscoelastic correspondence principle and time-temperature superposition. Finally, the work potential theory and the constitutive model developed by Lee (1996) are presented.

3.1.1 Theory of Viscoelasticity

Viscoelastic materials such as asphalt concrete exhibit time or rate dependence, meaning that the material response is not only a function of the current input, but the entire input history. The response of a linear viscoelastic body to any input history is described using a convolution integral. For a system to be considered linear, the conditions of homogeneity and superposition must be satisfied:

Homogeneity: $$R\{AI\} = A\,R\{I\} \tag{3.1}$$

Superposition: $$R\{I_1+I_2\} = R\{I_1\} + R\{I_2\} \tag{3.2}$$

where I, I_1, I_2 = input histories,
R = response, and
A = arbitrary constant.

The brackets { } indicate that the response is a function of the input history. The homogeneity, or proportionality condition essentially states that if the input is doubled, the response doubles as well. The superposition condition states that the response to the sum of two inputs is equivalent to the sum of the responses from the individual inputs.

For linear viscoelastic materials, the response-input relationship is expressed through the hereditary integral:

$$R = \int_{-\infty}^{t} R_H(t,t)\frac{dI}{dt}dt \tag{3.3}$$

where R_H is the unit response function. With a known unit response function, the response to any input history can be calculated. The lower limit of the integration can be reduced to 0^- (zero minus, just before time zero) if the input starts at time t=0 and both the input and response are equal to zero at t<0. The value of 0^- is used instead of 0 to allow for the possibility of a discontinuous change in the input at t=0. For notational simplicity, 0 is used as the lower limit in all successive equations and should be interpreted as 0^- unless specified otherwise. Equation (3.3) is applicable to an aging system in which the response measurement at any time is a function of both the time of loading and the time of fabrication. The unit response function, R_H, is then a three dimensional surface.

Commonly, the assumption of a non-aging system is made, and Equation (3.3) reduces to:

$$R = \int_{0}^{t} R_H(t-t)\frac{dI}{dt}dt \tag{3.4}$$

This simplifies the unit response function to a two-dimensional curve. For the uniaxial loading considered in this research, the non-aging, linear viscoelastic stress-strain relationships are:

$$s = \int_{0}^{t} E(t-t)\frac{de}{dt}dt \tag{3.5}$$

$$e = \int_{0}^{t} D(t-t)\frac{ds}{dt}dt \tag{3.6}$$

where E(t) is the relaxation modulus and D(t) is the creep compliance, both unit response functions.

3.1.2 Correspondence Principle

Schapery (1984) proposed the extended elastic-viscoelastic correspondence principle, which is applicable to both linear and nonlinear viscoelastic materials. He suggested that constitutive equations for certain viscoelastic media are identical to those for the elastic cases, but stresses and strains are not necessarily physical quantities in the viscoelastic body. Instead, they are *pseudo* variables in the form of convolution integrals. According to Schapery, the uniaxial pseudo strain (ε^R) is defined as:

$$e^{R} = \frac{1}{E_{R}} \int_{0}^{t} E(t - t) \frac{de}{dt} dt \tag{3.7}$$

where ε = uniaxial strain;
E_R = reference modulus that is an arbitrary constant;
$E(t)$ = uniaxial relaxation modulus;
t = elapsed time from specimen fabrication and the time of interest; and
τ = time when loading began.

Using the definition of pseudo strain in Equation (3.7), Equation (3.5) can be rewritten as:

$$s = E_{R} e^{R} \tag{3.8}$$

A correspondence can be found between Equation (3.8) and a linear elastic stress-strain relationship (Hooke's Law). The power of pseudo strain can be seen in Figure 3.1. Figure 3.1(a) shows the stress-strain behavior for controlled-stress cyclic loading within the material's linear viscoelastic range (such as for a complex modulus test). Because the material is being tested in its linear viscoelastic range, no damage is induced and the hysteretic behavior and accumulating strain are due to viscoelasticity only. Figure 3.1(b) shows the same stress data plotted against the calculated pseudo strains. All of the cycles collapse to a single line with a slope of 1.0 (E_R=1.0). The use of pseudo strain essentially accounts for the viscoelasticity of the material and allows for the separate characterization of damage within the specimen.

3.1.3 Uniaxial Constitutive Model Using Work Potential Theory

The constitutive model that is used as the basis of this research was developed by Kim and Lee (Lee 1996, Kim et al. 1997, Lee and Kim 1998a). The model uses the elastic-viscoelastic correspondence principle to eliminate the time dependence of the material. Work potential theory (Schapery 1990) is then used to model both the damage growth and healing in the material. The term damage is defined as all structural changes except linear viscoelasticity that result in the reduction of stiffness or strength as the material undergoes loading. Microdamage healing includes everything except linear viscoelastic relaxation that contribute to the recovery of stiffness or strength during rest periods and can include such things as fracture healing, steric hardening, and nonlinear viscoelastic relaxation.

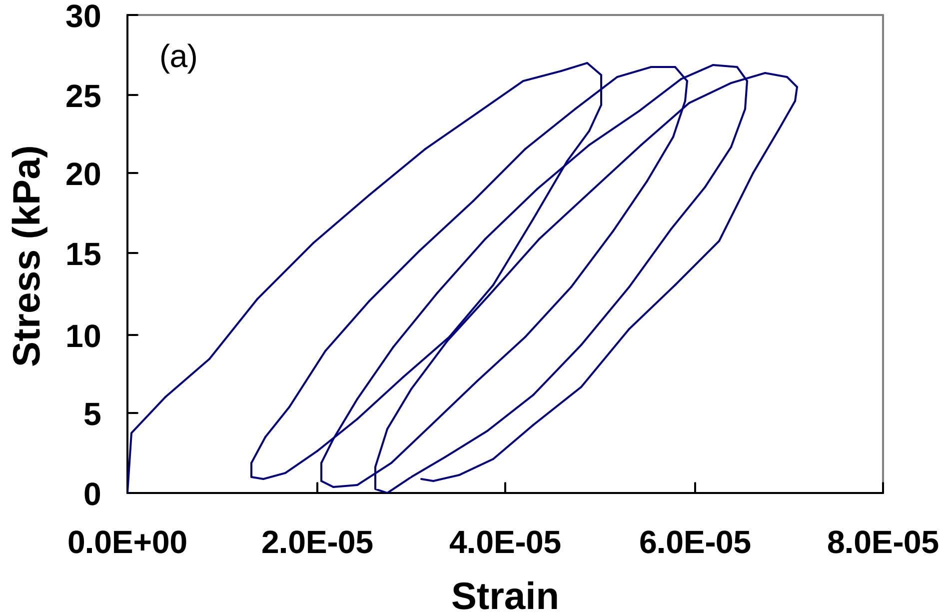

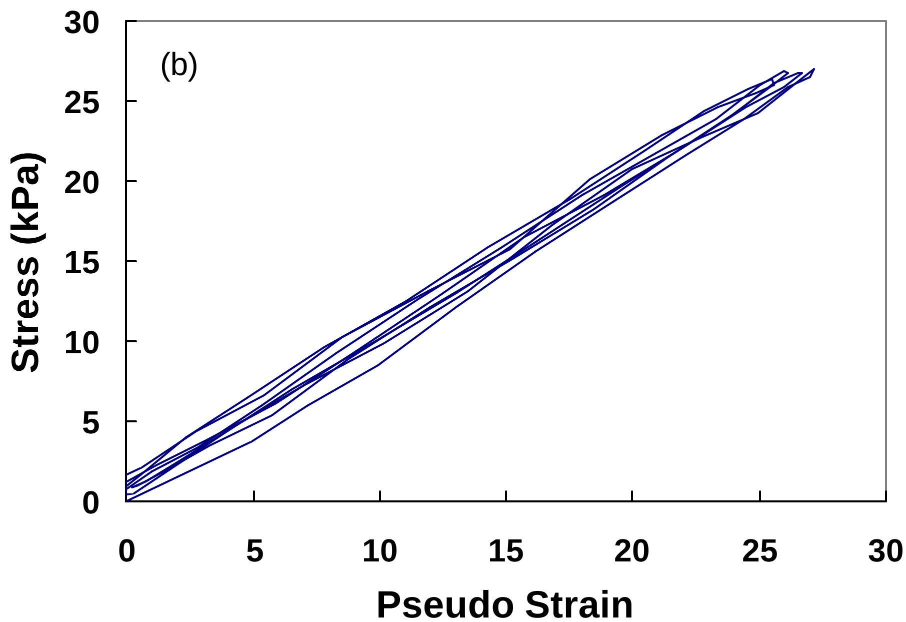

Figure 3.1 (a) Stress–Strain Behavior for Mixture under LVE Cyclic Loading; (b) Stress-Pseudo Strain Behavior for Same Data

Schapery (1990) developed a theory using the method of thermodynamics of irreversible processes to describe the mechanical behavior of elastic composite materials with growing damage. The following three fundamental elements comprise the work potential theory:

1. Strain energy density function

$$W = W(\varepsilon_{ij}, S_m) \tag{3.9}$$

2. Stress-strain relationship

$$\sigma_{ij} = \frac{\partial W}{\partial \varepsilon_{ij}} \tag{3.10}$$

3. Damage evolution law

$$-\frac{\partial W}{\partial S_m} = \frac{\partial W_s}{\partial S_m} \tag{3.11}$$

where σ_{ij} and ε_{ij} are stress and strain tensors, respectively. S_m are internal state variables and $W_s=W_s(S_m)$ is the dissipated energy due to structural changes. Using Schapery's elastic-viscoelastic correspondence principle (CP) and rate-type damage evolution law (Schapery 1984 and 1990, Park et al. 1996), the physical strains, ε_{ij}, are replaced with pseudo strains, ε_{ij}^R, to include the effect of viscoelasticity. The use of pseudo strain as defined in Equation (3.7) accounts for all the hereditary effects of the material through the convolution integral. Thus, the strain energy density function $W=W(\varepsilon_{ij}, S_m)$ transforms to the pseudo strain energy density function:

$$W^R = W^R(\varepsilon_{ij}^R, S_m) \tag{3.12}$$

Schapery's CP cannot be used to transform the elastic damage evolution law to use with viscoelastic materials because both the available force for growth of S_m and the resistance against the growth of S_m in the damage evolution law are rate-dependent for most viscoelastic materials (Park et al. 1996). Therefore, the following form similar to power-law crack growth laws is used to describe the damage evolution in a viscoelastic material:

$$\dot{S}_m = \left(-\frac{\partial W^R}{\partial S_m}\right)^{\alpha_m} \tag{3.13}$$

where $\dot{S}_m$ is the damage evolution rate, W^R is the pseudo strain energy density function, and α_m are material constants.

Using Schapery's work potential theory and CP, Lee and Kim (1998b) developed a mode of loading independent constitutive model that describes the fatigue and microdamage healing of asphalt concrete under cyclic loading. Lee and Kim (1998b) used uniaxial tensile cyclic loading tests with various loading amplitudes to study the mechanical behavior of asphalt concrete. They were able to account for the hysteretic behavior due to both loading-unloading and repetitive loading in the linear viscoelastic range using pseudo strains. In damage-inducing testing, they observed that the slope of the stress – pseudo strain loop decreases as loading continues in both controlled stress and controlled strain testing. The change in the slope of the loop represents the reduction in the stiffness of the material as damage accumulates. To represent the change in slope, Lee and Kim (1998b) used the secant pseudo stiffness, S^R, defined as:

$$S^R = \frac{s_m}{e_m^R} \tag{3.14}$$

where e_m^R is the peak pseudo strain in each stress-pseudo strain cycle, and σ_m is the stress corresponding to e_m^R. In modeling, Lee (1996) found it necessary to normalize the pseudo stiffness by the initial pseudo stiffness, I, to account for sample to sample variation. The normalized pseudo stiffness, C, is then:

$$C = \frac{S^R}{I} \tag{3.15}$$

It is useful to present the uniaxial constitutive equations for linear elastic and linear viscoelastic materials with and without damage to show how the more complex models evolve from simpler ones:

Elastic Body without Damage:	$\sigma = E_R\varepsilon$	(3.16)
Elastic Body with Damage:	$\sigma = C(S_m)\varepsilon$	(3.17)
Viscoelastic Body without Damage:	$\sigma = E_R\varepsilon^R$	(3.18)
Viscoelastic Body with Damage:	$\sigma = C(S_m)\varepsilon^R$	(3.19)

where E_R is a constant and $C(S_m)$ is a function of internal state variables (ISVs) S_m that represent the changing stiffness of the material due to microstructure changes such as accumulating damage or healing. In Equation (3.16), E_R is Young's modulus. A correspondence is seen between the elastic and viscoelastic constitutive equations; that is, the viscoelastic equations take the same form as the elastic ones with pseudo strain replacing physical strain.

Based on experimental data of asphalt concrete under continuous, uniaxial cyclic loading in tension, Kim et al. (1997) proposed a constitutive model that describes the mechanical behavior of the material under these conditions:

$$s = I\left(e_e^R\right)[F + G] \tag{3.20}$$

where I = initial pseudo stiffness,

ϵ_e^R = effective pseudo strain,

F = damage function, and

G = hysteresis function.

The effective pseudo strain accounts for the accumulating pseudo strain in a controlled stress mode. A mode factor is also applied to the damage function, F, to allow a single expression for both modes of loading. The parameter I is used to account for sample-to-sample variability in the asphalt specimens. The damage function, F, represents the change in slope of the stress-pseudo strain loop as damage accumulates in the specimen. The hysteresis function G describes the difference in the loading and unloading paths. More details of this model can be found in Lee and Kim (1997) and Lee (1996).

To determine the fatigue life from Equation (3.19), Kim et al. (1997) found that the hysteresis function, G, need not be considered and that stress and pseudo strain values at peak loads only are sufficient. For a controlled-strain testing mode, the constitutive equations then become:

$$W_m^R = \frac{I}{2} C_1(S_1)\left(\epsilon_m^R\right)^2 \qquad (3.21)$$

$$\sigma_m = I C_1(S_1)\epsilon_m^R \qquad (3.22)$$

The function C_1 represents S^R, as can be seen from Equations (3.15) and (3.22). The evolution law becomes:

$$\dot{S}_m = \left(-\frac{\partial W_m^R}{\partial S_m}\right)^{\alpha_m} \qquad (3.23)$$

To characterize the function C_1 in Equation (3.22), the damage evolution law and experimental data are used. With the measured stresses and calculated pseudo strains, C_1 values can be determined through Equation (3.15). To find the dependence of C_1 on S_1, the values of S_1 must be obtained through Equation (3.23). The current form of Equation (3.23) is not suitable for finding S_1 because it requires prior knowledge of the $C_1(S_1)$ function through Equation (3.21). Lee (1996) uses the chain rule in Equation (3.24) to eliminate S_1 from the right hand side of the evolution equation and obtain an explicit expression for S_1 in Equation (3.25):

$$\frac{dC}{dS} = \frac{dC}{dt}\frac{dt}{dS} \qquad (3.24)$$

$$S_1 = \int_0^t \left[\frac{I}{2} \frac{dC_1}{dt} \left(e_m^R\right)^2 \right]^{\frac{a}{(1+a)}} dt \tag{3.25}$$

Both the function C_1 and e_m^R are dependent upon time t, and thus a numerical approximation can be used with the measured data to obtain S_1 as a function of time:

$$S_1(t) \cong \sum_{i=1}^{N} \left[\frac{I}{2} \left(e_{mi}^R\right)^2 \left(C_{i-1} - C_i\right) \right]^{\frac{a}{(1+a)}} \left(t_i - t_{i-1}\right)^{\frac{1}{(1+a)}} \tag{3.26}$$

Lee and Kim (1998a, 1998b) found an appropriate expression for the parameter α:

$$a = \left(1 + 1/m\right) \tag{3.27}$$

where m is the slope of the log E(t)-log (t) relationship. This relationship is validated by cross-plotting the measured C_1 values against the S_1 values obtained from Equation (3.26) and observing that two different strain level data fall on the same curve. The relationship between C_1 and S_1 can then be found by performing a regression on the data. Lee (1996) found that the function follows the form:

$$C_1(S_1) = C_{10} - C_{11}(S_1)^{C_{12}} \tag{3.28}$$

The regression coefficient C_{10} is close to 1.0, as would be expected at a negligible damage level (S_1 goes to zero) because the material is in the linear viscoelastic range of behavior and there exists a one-to-one relationship between stress and pseudo strain (i.e., S^R=1). To account for the mode-of-loading differences, Lee (1996) uses the following normalized damage parameter, S_{1n}, to achieve a single functional form that describes both loading conditions:

$$S_{1n} = \frac{S_1}{S_{1f}} \tag{3.29}$$

where S_{1f} is the value of the damage parameter at failure. Lee (1996) defines failure as a 50% reduction in initial pseudo stiffness, or C_1=0.5. Using this model, Lee (1996) was able to successfully predict the damage growth of asphalt concrete under monotonic loading at various strain rates and cyclic loading under both controlled-stress and controlled-strain modes.

3.2 Elastic Solutions for Indirect Tension Test

Indirect tension testing is done by applying a compressive force to a cylindrical specimen along two diametrically opposite, arc-shaped loading strips, as shown in Figure 3.2. Unlike the uniaxial test, the stress and strain distributions in the indirect tensile specimen are complicated. Generally, the mechanical characterization of material in an indirect tensile test is based upon the elastic solutions derived by Hondros (1959) in which an approximation of the plane stress problem is assumed to simplify the analysis.

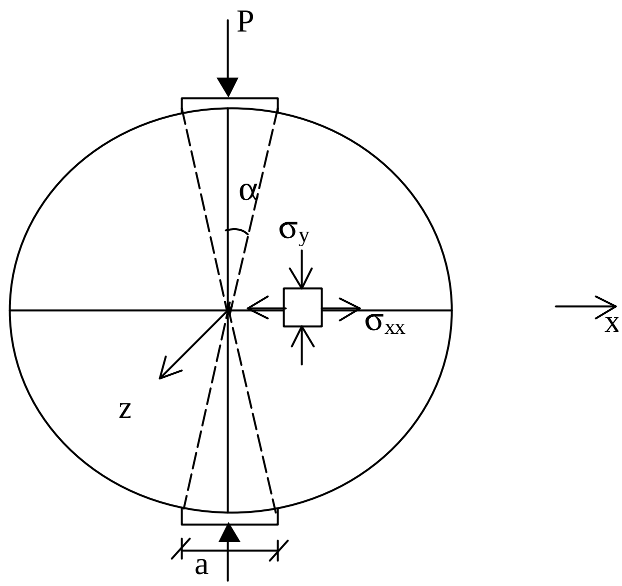

Figure 3.2 Schematic of Indirect Tension Test

In Hondros' analysis, the stresses along the horizontal diameter are:

$$\sigma_x(x) = \frac{2P}{\pi a d}\left[\frac{(1-x^2/R^2)\sin 2\alpha}{1+2x^2/R^2\cos 2\alpha + x^4/R^4} - \tan^{-1}\left(\frac{1-x^2/R^2}{1+x^2/R^2}\tan\alpha\right)\right]$$
$$= \frac{2P}{\pi a d}\left[f(x) - g(x)\right] \tag{3.30}$$

$$\sigma_y(x) = -\frac{2P}{\pi a d}\left[\frac{(1-x^2/R^2)\sin 2\alpha}{1+2x^2/R^2\cos 2\alpha + x^4/R^4} + \tan^{-1}\left(\frac{1-x^2/R^2}{1+x^2/R^2}\tan\alpha\right)\right]$$
$$= -\frac{2P}{\pi a d}\left[f(x) + g(x)\right] \tag{3.31}$$

The stresses along the vertical diameter are:

$$\sigma_x = \frac{2P}{\pi a d}\left[\frac{(1-y^2/R^2)\sin 2\alpha}{1-2y^2/R^2\cos 2\alpha + y^4/R^4} - \arctan\left(\frac{1+y^2/R^2}{1-y^2/R^2}\tan\alpha\right)\right]$$
$$= \frac{2P}{\pi a d}\left[m(y) - n(y)\right] \tag{3.32}$$

$$\sigma_y = -\frac{2P}{\pi a d}\left[\frac{(1-y^2/R^2)\sin 2\alpha}{1-2y^2/R^2\cos 2\alpha + y^4/R^4} + \arctan\left(\frac{1+y^2/R^2}{1-y^2/R^2}\tan\alpha\right)\right]$$

$$= -\frac{2P}{\pi a d}\left[m(y) + n(y)\right] \tag{3.33}$$

where P = applied load,
a = loading strip width,
d = thickness of specimen,
R = specimen radius, and
α = radial angle.

Figure 3.3 shows the stress distribution along the horizontal and vertical axes. Noteworthy is that the stresses are independent of Poisson's ratio, indicating that normalized stress distribution is only a function of specimen geometry and is material-independent.

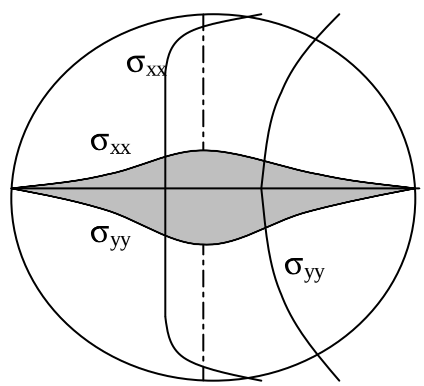

Figure 3.3 Stress Distribution along Horizontal and Vertical Diameters

In this study, an attempt was made to develop three-dimensional solutions for the indirect tensile test. The solution to a two-dimensional problem may be used to construct the solution to a certain three-dimensional problem in the case of vanishing stresses, σ_z, τ_{xz}, and τ_{yz}, the first being the normal stress, the other two being the shear stresses in the xy plane (Wijk 1978).

Suppose that the potential function of the two-dimensional problem is $\varphi(x, y)$, then the normal stresses are $\sigma_x(x, y)$ and $\sigma_y(x, y)$ in the following (Wijk 1978):

$$\sigma_x = \frac{\partial^2 \varphi(x, y)}{\partial y^2} \tag{3.34}$$

$$\sigma_y = \frac{\partial^2 \varphi(x,y)}{\partial x^2} \tag{3.35}$$

Three-dimensional solutions may be obtained for the indirect tensile test with the following observations:

$$\sigma_z(x, y, z) = \tau_{zx}(x, y, z) = \tau_{zy}(x, y, z) = 0 \tag{3.36}$$

Based on this observation, Wijk derived the following equations for stresses:

$$\sigma_x(x, y, z) = \sigma_x(x, y) + \frac{\partial^2 \Delta\varphi(x, y, z)}{\partial y^2} \tag{3.37}$$

$$\sigma_y(x, y, z) = \sigma_y(x, y) + \frac{\partial^2 \Delta\varphi(x, y, z)}{\partial x^2} \tag{3.38}$$

$$\Delta\varphi(x, y, z) = -\frac{z^2}{2(1/\nu + 1)}\left\{\frac{\partial^2}{\partial x^2} + \frac{\partial^2}{\partial y^2}\right\}\varphi(x, y) \tag{3.39}$$

where ν is Poisson's ratio.

Input Equation (3.39) into Equations (3.37) and (3.38), and obtain:

$$\sigma_x(x, y, z) = \sigma_x(x, y) - \frac{z^2}{2(1/\nu + 1)}\left\{\frac{\partial^2}{\partial x^2 \partial y^2} + \frac{\partial^2}{\partial y^4}\right\}\varphi(x, y) \tag{3.40}$$

$$\sigma_y(x, y, z) = \sigma_y(x, y) - \frac{z^2}{2(1/\nu + 1)}\left\{\frac{\partial^2}{\partial x^4} + \frac{\partial^2}{\partial x^2 \partial y^2}\right\}\varphi(x, y) \tag{3.41}$$

In order to use these stress solutions to obtain solutions for displacements, it is recongnized that at both sides of an indirect tensile test specimen, stress σ_z is completely vanished. Therefore, the stress-strain relationship in a three-dimensional problem is the same as that in the following two-dimensional problem:

$$\varepsilon_x = (\sigma_x - \nu\sigma_y)/E \tag{3.42}$$

$$\varepsilon_y = (\sigma_y - \nu\sigma_x)/E \tag{3.43}$$

where E is Young's modulus.

The three-dimensional stresses, σ_x and σ_y from Equations (3.40) and (3.41), are input into Equations (3.42) and (3.43), thus obtaining the following general expressions of three-dimensional strain distribution:

$$e_x = \Big\langle\; s_x(x,y) - \frac{z^2}{2(1/n+1)}\left\{\frac{\partial^2}{\partial x^2 \partial y^2} + \frac{\partial^2}{\partial y^4}\right\} j\,(x,y) -$$
$$n[s_y(x,y) - \frac{z^2}{2(1/n+1)}\left\{\frac{\partial^2}{\partial x^4} + \frac{\partial^2}{\partial x^2 \partial y^2}\right\} j\,(x,y)]\;\Big\rangle / E \tag{3.44}$$

$$e_y = \Big\langle\; s_y(x,y) - \frac{z^2}{2(1/n+1)}\left\{\frac{\partial^2}{\partial x^4} + \frac{\partial^2}{\partial x^2 \partial y^2}\right\} j\,(x,y) -$$
$$n[s_x(x,y) - \frac{z^2}{2(1/n+1)}\left\{\frac{\partial^2}{\partial x^2 \partial y^2} + \frac{\partial^2}{\partial y^4}\right\} j\,(x,y)]\;\Big\rangle / E \tag{3.45}$$

The horizontal and vertical displacements under a certain loading may be obtained by integrating the function of strain along the gauge length. The linear three-dimensional solutions for the vertical and horizontal displacements across a 50.8 mm (2 inches) gauge length on a 100.8 mm (4 inches) diameter specimen are written as follows:

$$U = \frac{P(0.23 + n + 0.78n^2 + 80.6n^2 d^2)}{Ed(1+n)} \tag{3.46}$$

$$V = \frac{P(0.3 + 1.38n + 0.78n^2 + 222n^2 d^2)}{Ed(1+n)} \tag{3.47}$$

where U, V = horizontal and vertical displacements, respectively,
P = load,
ν = Poisson’s ratio,
d = thickness of specimen, and
E = Young’s modulus.

For a specimen of 152.4 mm (6 inches) diameter, the vertical and horizontal displacements across a 50.8 mm (2 inches) gauge length are:

$$U = \frac{P(0.18 + 0.773n + 0.588n^2 + 30.81n^2 d^2)}{Ed(1+n)} \tag{3.48}$$

$$V = \frac{P(0.21 + 0.89n + 0.68n^2 + 48.5n^2 d^2)}{Ed(1+n)} \tag{3.49}$$

4. TEST METHODS

There are several types of testing performed in this research. They can be classified as either damage-inducing tests, or non-damage-inducing tests. The non-damage-inducing tests are performed within the linear viscoelastic range of the material to measure the linear viscoelastic properties. Damage-inducing tests measure the fracture and healing properties of the material.

4.1 Linear Viscoelastic Tests

The frequency sweep and creep compliance tests are performed in this research to obtain the linear viscoelastic material properties of the various mixtures. From these tests, other viscoelastic material properties such as relaxation modulus can be predicted. The procedures used for predicting relaxation modulus from creep compliance and frequency sweep data are detailed in the following section.

4.1.1 Frequency Sweep Test

The frequency sweep test consists of a haversine loading applied to the specimen, as shown in Figure 4.1. The load amplitude is adjusted based on the material stiffness, temperature, and frequency to keep the strain response within the linear viscoelastic range. To do this, a microstrain level of 50-75 is targeted. The loading is applied until steady-state is achieved, at which point several cycles of data are collected. After each frequency, a five-minute rest period is allowed for specimen recovery before the next loading block is applied. The frequencies are applied from the fastest to the slowest.

From the frequency sweep test, the complex modulus, E*, the dynamic modulus, |E*|, and the phase angle, ϕ, can be determined. The complex modulus is composed of the storage and loss moduli in the following manner:

$$E^{*} = E' + iE'' \tag{4.1}$$

where E' = storage modulus,
E" = loss modulus, and
$i = (-1)^{1/2}$.

The dynamic modulus is the amplitude of the complex modulus and is defined as follows:

$$\left|E^{*}\right| = \sqrt{(E')^{2} + (E'')^{2}} \tag{4.2}$$

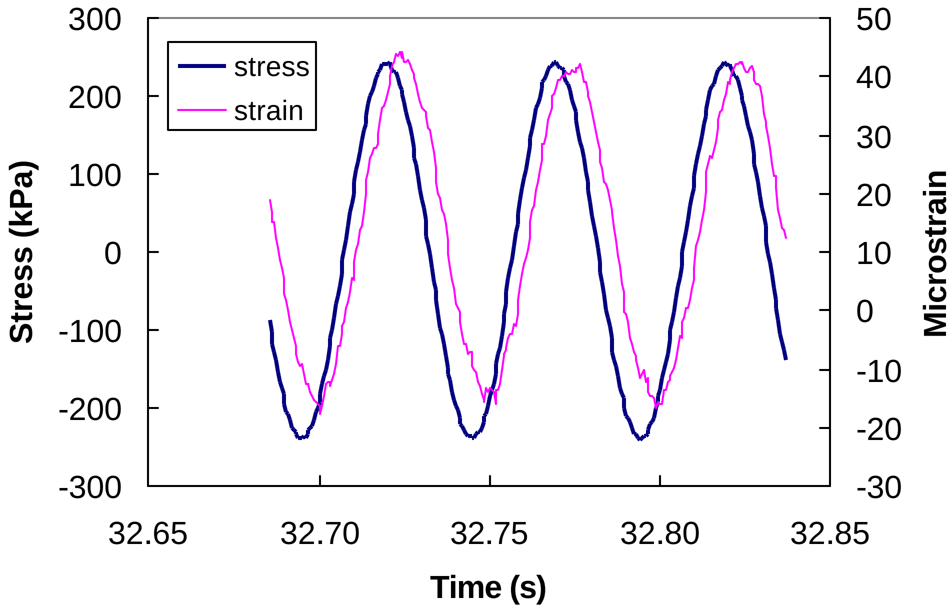

Figure 4.1 Frequency Sweep Test

The values of the storage and loss moduli are related to the dynamic modulus and phase angle as follows:

$$E' = |E^*| \cos \phi \quad \text{and} \tag{4.3}$$

$$E'' = |E^*| \sin \phi \tag{4.4}$$

Figure 4.2 shows the graphical relationship between all of these parameters. As the material becomes more viscous, the phase angle increases and the loss component of the complex modulus increases. Conversely, a decreasing phase angle indicates more elastic behavior and a larger contribution from the storage modulus.

The dynamic modulus at each frequency is calculated by dividing the steady state stress amplitude (σ_{amp}) by the strain amplitude (εamp) as follows:

$$|E^*| = \frac{\sigma_{amp}}{\varepsilon_{amp}} \tag{4.5}$$

The phase angle, ϕ, is related to the time lag, Δt, between the stress input and strain response and the frequency of testing:

$$\phi = 2\pi f \Delta t \tag{4.6}$$

where f is the loading frequency. As the testing temperature decreases or the rate (frequency) increases the dynamic modulus will increase and the phase angle will decrease due to the time dependence or viscoelasticity of the material.

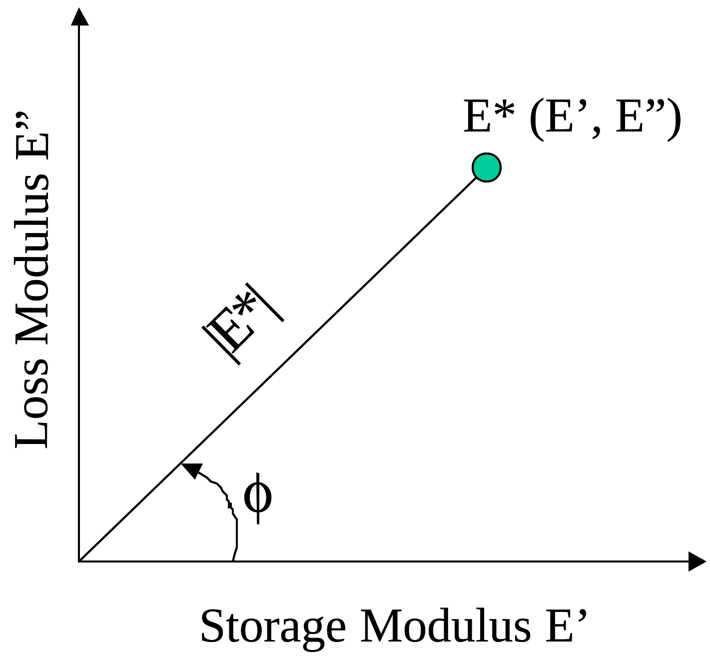

Figure 4.2 Complex Modulus Schematic Diagram

4.1.2 Creep Compliance Test

The creep compliance test applies a constant load for a period of time and measures the strain response, as shown in Figure 4.3. The uniaxial creep compliance is calculated using the quasi-elastic method to approximate the linear viscoelastic convolution integral (Kim et al. 1995):

$$D(t) = \frac{e(t)}{s\ (t)} \tag{4.7}$$

The method of calculating the creep compliance for the indirect tension test is discussed in a subsequent section. The appropriate load level for creep compliance testing is determined by testing a specimen with increasing load levels, each of which is followed by a low magnitude reference load to determine the linear viscoelastic range. Figure 4.4 shows a typical creep compliance curve.

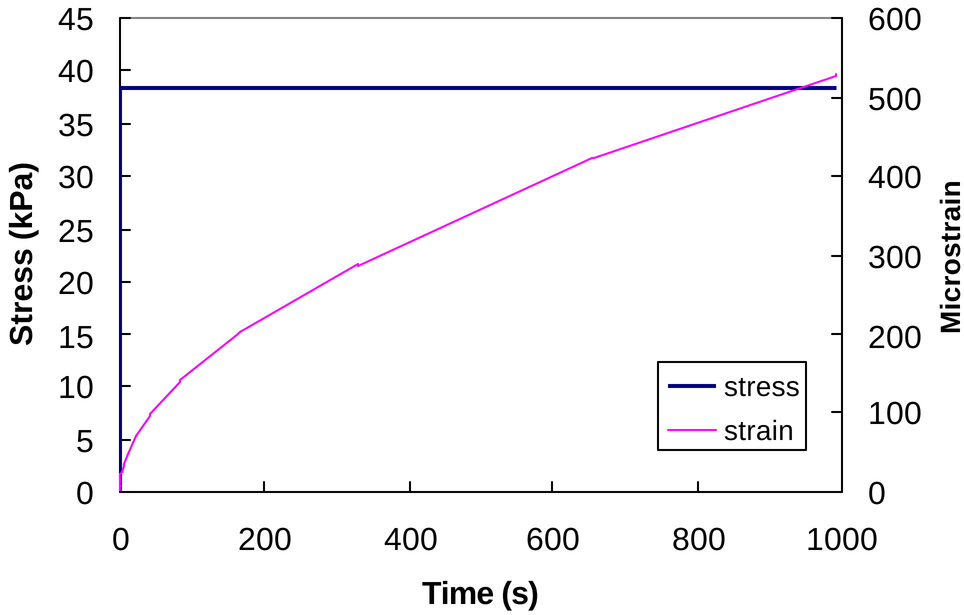

Figure 4.3 Creep Test

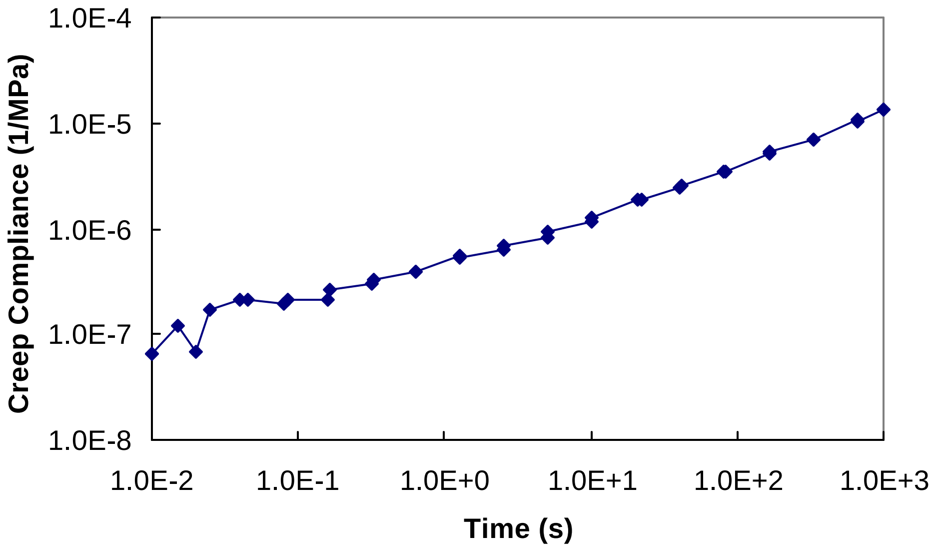

Figure 4.4 Typical Creep Compliance Curve

4.1.3 Relationships among Viscoelastic Material Properties

The viscoelastic material properties that are of interest are the creep compliance, relaxation modulus, and complex modulus (from which dynamic modulus and phase angle are determined). The creep compliance and complex modulus can be easily obtained from an appropriate test as described in the previous section. The relaxation modulus is more difficult to measure reliably from testing due to equipment constraints. However, the relaxation modulus is essential for the calculation of pseudo strain in Equation (3.7). Through the theory of linear viscoelasticity, all of these material properties are related and can be predicted from a measured property. Typically, either the creep compliance or frequency sweep test is performed and the remaining properties, particularly the relaxation modulus, are predicted from the measured property. In this research, relaxation modulus is predicted from both complex modulus and creep compliance. The details on the prediction procedures are presented in Appendix A.

4.2 Damage Inducing Tests

The damage inducing tests are performed to describe the behavior of the different mixtures under growing damage. This section describes the different types of tests that were performed in the uniaxial and indirect tension modes.

4.2.1 Uniaxial Continuous Cyclic Test to Failure

This test consists of a constant crosshead strain amplitude haversine loading applied continuously to the specimen in the tensile direction until failure occurs. Frequencies of 1 Hz and 10 Hz are used for the fatigue testing in this research. The amplitude is chosen to achieve failure of the specimen in a desired number of cycles based on the fact that the higher the amplitude, the faster the specimen will fail. Figures 4.5 and 4.6 show the stress-strain cycles for the strains measured using the ram displacements and on-specimen or plate-to-plate LVDT displacements, respectively. The ram stress-strain curves show constant strain amplitude and decreasing stress amplitude (more horizontal loops) and decreasing mean stress (loops moving downward) as loading continues. The LVDT stress-strain curves show the same stress response; however, the strain amplitude and mean strain are both increasing. The difference between the ram LVDT measurements and the on-specimen LVDT measurements is due to machine compliance; that is, the specimen is not experiencing a true controlled-strain or controlled-stress mode of loading, but rather a mixed mode of loading. A detailed study of the machine compliance and instrumentation issues is presented in Appendix B.

The stiffness (load amplitude divided by applicable strain amplitude) decreases as fatigue loading continues, following an s-shaped curve shown in Figure 4.7. The phase angle increases as damage accumulates in the specimen until failure occurs, and then decreases as the stress and strain become more in-phase as there is decreasing resistance from the specimen, which can be seen in Figure 4.8. Both Figures 4.7 and 4.8 show the stiffness and phase angles calculated from the plate-to-plate and on-specimen LVDTs. The values measured from the two different gage lengths are similar and follow the same trend. This is important because if failure occurs outside of the on-specimen LVDT gage length, analysis can still be performed using the plate-to-plate deformation measurements.

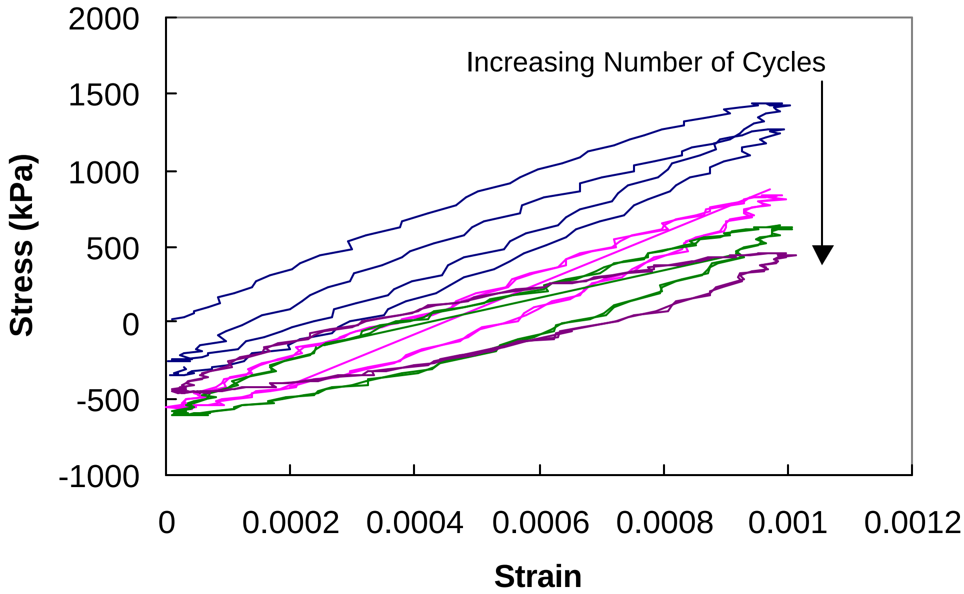

Figure 4.5 Stress-Strain Loops in Cyclic Test Measured Using Ram Displacements

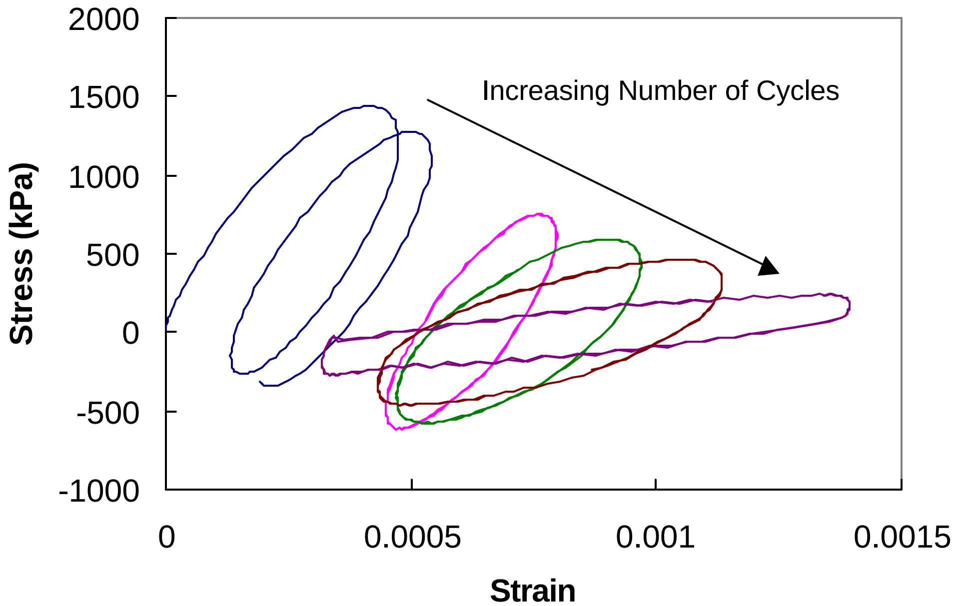

Figure 4.6 Stress-Strain Loops in Cyclic Test Measured Using LVDT Displacements

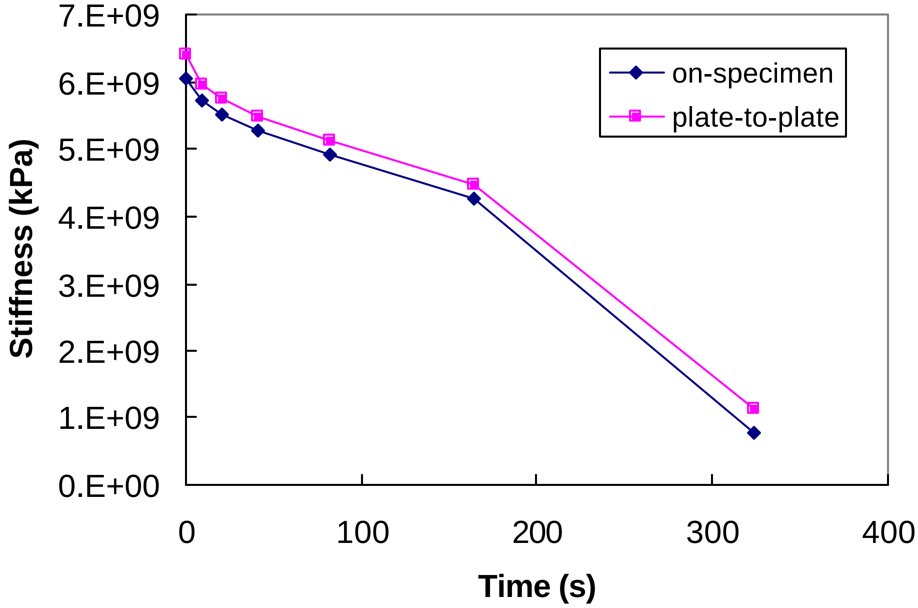

Figure 4.7 Stiffness Reduction over Time from On-Specimen and Plate-to-Plate LVDT Measurements

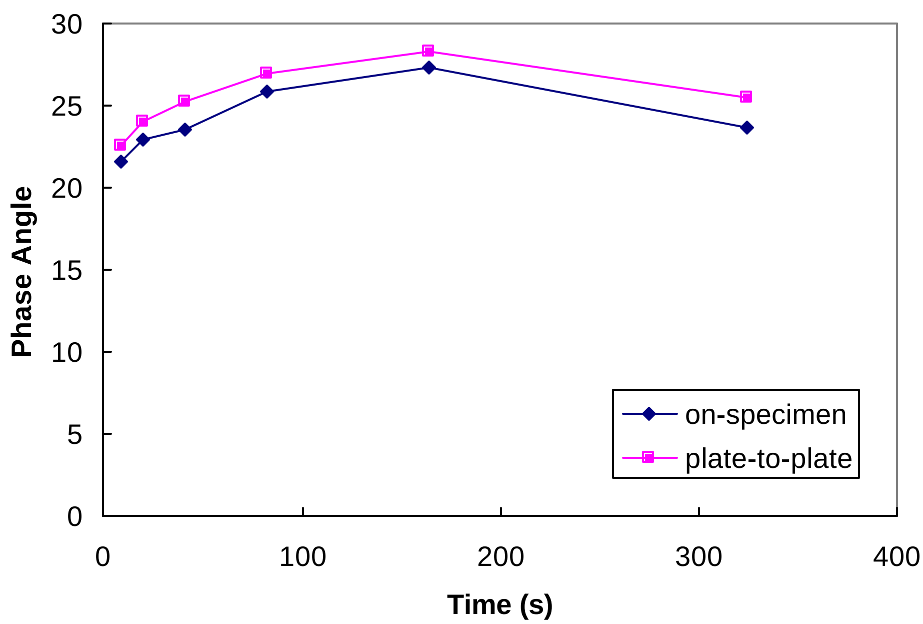

Figure 4.8 Phase Angle as a Function of Time from On-Specimen and Plate-to-Plate LVDT Measurements

4.2.2 Uniaxial Cyclic Healing Test

In this test, a constant crosshead-strain amplitude at 10 Hz is applied to the specimen in loading blocks. Between each loading block a rest period of varying duration is applied to allow the specimen to recover and for microcrack healing to take place. A typical test history is shown in Table 4.1.

Table 4.1 Typical Cyclic Healing Test History

Segment	Number of Cycles In Loading Group	Rest Period (s)
1	500	
2		20
3	500	
4		40
5	500	
6		80
7	500	
8		360
9	500	
10		1280
11	500	
12		1280
13	500	
14		360
15	500	
16		80
17	500	
18		40
19	500	
20		20
21	Cont. to failure	

The same rest period durations and sequence are used for each test, and the number of cycles in each loading block is determined from the continuous cyclic testing at the same strain amplitude. The goal is to measure the healing at different levels of damage, but to apply the entire sequence of loading blocks and rest periods before the specimen fails.

During each loading block, the stiffness of the material decreases until loading stops. During the rest period, the stiffness increases due to both linear viscoelastic recovery and healing of microcracks as proven by Lee and Kim (1998b). After the rest period, the healed material is damaged at a faster rate until it rejoins the damage curve of the virgin material; the effect of the rest period is to increase the eventual number of cycles to failure. From this test, the healing potential and the cyclic fatigue behavior of the healed material is determined.

4.2.3 Uniaxial Constant Crosshead Rate Test

In the constant crosshead rate test, a specimen is pulled apart using a constant crosshead strain rate, as shown in Figure 4.9. A typical stress response curve is shown as well as the on-specimen and plate-to-plate LVDT strain measurements. Due to the machine compliance, the on-specimen and plate-to-plate LVDT measurements follow a power curve up until failure. After failure, the plate-to-plate measurements become linear with a rate close to that of the ram; the increase of on-specimen strain becomes linear as well, but with a higher rate, due to the difference in gage length from which strains are calculated. The ram and plate-to-plate deformations are divided by the same gage length, whereas the on-specimen deformations are divided by a smaller gage length. For the same deformation measurement, which is the case after failure, the on-specimen strain will be larger. From this test the pre- and post-peak behavior can be evaluated. It is also postulated that the cyclic fatigue behavior can be predicted from these data, as has been done successfully by Schapery (1982) for solid rocket propellant. In this report, the monotonic test refers to the constant crosshead rate test.

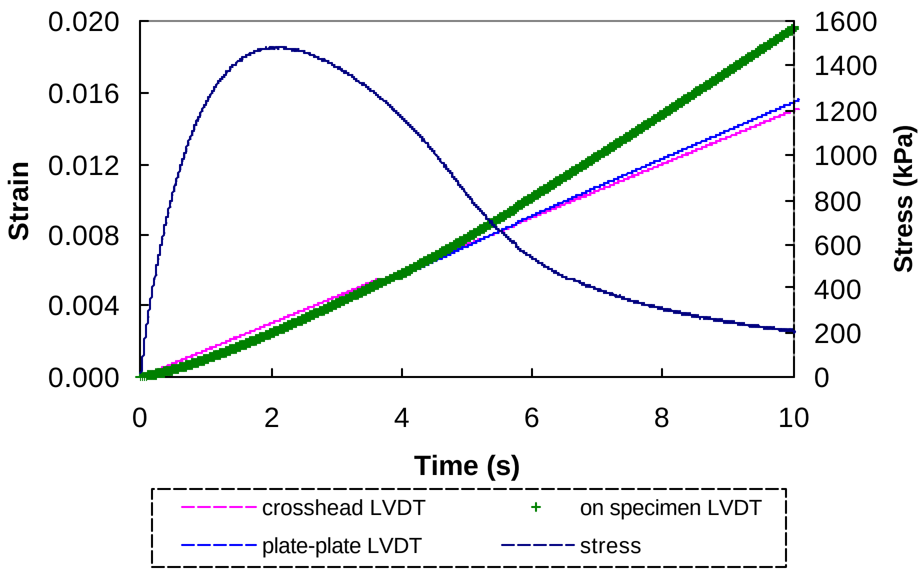

Figure 4.9 Stress and Strain Measurements for Constant Crosshead Rate Test

4.2.4 Indirect Tensile Strength Test

The tensile strength test is designed to apply a load to the specimen at a constant crosshead rate, similar to the uniaxial monotonic test. Figure 4.10 shows a schematic of a tensile strength test. Ideally, it is desirable to have a constant-strain-rate input. Since the strain is calculated using the measured displacement across the 2 inch gauge length, it is difficult to conduct such a test. Instead, a constant-crosshead-rate monotonic test was performed, controlling the movement of crosshead at 2 inches/minute. The maximum level of crosshead movement was selected so that the resulting load level reached its peak value and was decreasing. However, the test should be finished or be stopped before the specimen is split completely to prevent damage to LVDTs mounted on the specimen surface. Tensile strength, total energy (TE), strain energy (SE), and damage energy (DE) may be obtained from the test results. The definitions of total energy, strain energy, and damage energy are shown in Figure 4.11.

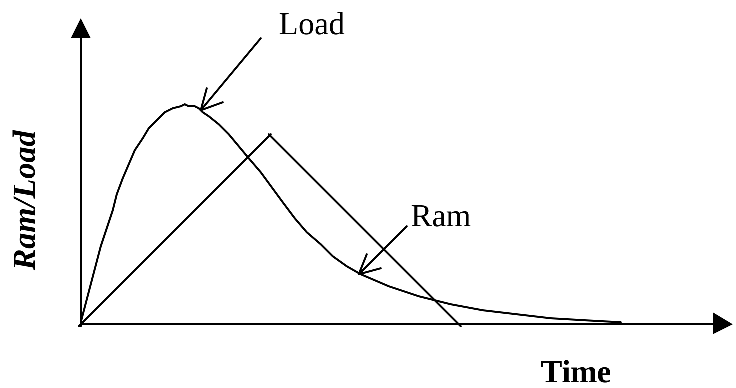

Figure 4.10 Schematic of Tensile Strength Test

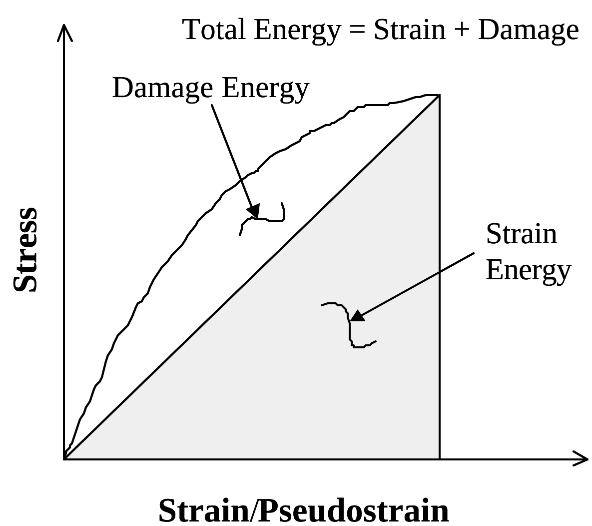

Figure 4.11 Definition of Energies

4.2.5 Moisture Sensitivity

The effect of moisture on the uniaxial fatigue performance of several mixtures was evaluated following the ASTM 4867 standard test method with a few exceptions. The optional freeze cycle was eliminated and cylindrical specimens at various air void content levels were tested. The specimens were vacuum saturated and then placed in a 60^{o}C water bath for 24 hours. The specimens were then brought back to room temperature and the surfaces were dried to allow the testing plates to be glued and cured prior to fatigue testing. Only continuous fatigue testing was performed on the moisture-exposed specimens; that is, the effect of moisture on healing was not investigated in this project.

4.3 Testing Program

The testing program for this research followed a particular sequence to minimize damage to the specimens and ensure the most consistent measured data. When testing is performed at different temperatures, the progression is from the lowest temperature to the highest. In this way, if any damage of the specimen is unintentionally induced in the specimen at the higher temperatures, the material properties at the lower temperatures are still valid. It is much easier to induce damage in asphalt concrete at higher temperatures because of the decreasing strength of the material. With the same concept in mind, testing is performed at faster rates first, then at the slower rates. The frequency sweep test runs from the highest to the lowest frequency and is followed by a creep test, if applicable. Once the linear viscoelastic testing is completed, the desired damage inducing test is performed. Adequate time is allowed between temperatures for the specimen to fully achieve equilibrium. A specimen with an embedded thermocouple was used to find the average time to equilibrium to and from various temperatures. Following each application of loading for the LVE material property measurements, an adequate rest period is applied to allow the specimen to recover completely. Five minute rest periods are applied between subsequent frequency sweep loading blocks, and a two hour recovery period follows the 1000 second creep test.

Due to limitations in computer memory, and the need for a reasonably fast data acquisition rate to capture the necessary information, only snapshots of data can be acquired during the frequency sweep and cyclic damage tests. For the frequency sweep tests, at least 10 cycles of data at a rate of 100 points per cycle are collected after steady state is achieved for that particular loading frequency. In the continuous cyclic fatigue tests, one second snapshots of data at a rate of 100 points per cycle (1000 points per second for the 10 Hz loading frequency) are collected on a logarithmic scale up to a time increment of 2 to 10 minutes, depending upon the projected failure time of the specimen. If specimens are expected to fail in a shorter amount of time, the time between successive snapshots is reduced in an attempt to acquire data close to the actual failure point and to adequately describe the changing material behavior as damage grows in the specimen. For the fatigue and healing tests, several snapshots of data are collected during the first loading block. From that point forward, data are collected at the beginning and end of each loading block to capture the transitions between the rest periods and loading. This can be a delicate operation, particularly if the timing between the control and data acquisition computers is not perfectly synchronized.

5. MATERIALS AND SPECIMEN FABRICATION

The asphalt concrete mixtures tested in this study are either WesTrack mixtures or a North Carolina mix. The North Carolina mixture is used in the developmental stage of performance prediction test protocol where specific characteristics of WesTrack mixtures did not need to be tested. This substitution was necessary to save the limited amount of WesTrack mixtures available in this research for final performance testing. The WesTrack mixtures are used to develop a simple performance test for fatigue in indirect tension and a simplified fatigue test and analysis procedure for uniaxial tension testing. This section describes the materials and the specimen fabrication procedures for all of the testing conducted in this study. Arizona SPS-9 mixtures were not studied because, based on numerous contacts with ADOT pavement engineers, the research team was not confident in obtaining the actual construction materials in a timely manner.

5.1 North Carolina Mixture

The North Carolina SPS-9 mixture, which meets the Superpave specification for 12.5 mm mix design, was used in this research. The aggregate blend consists of 95.5%, by mass, granite aggregates obtained from three stockpiles in Lemon Springs, NC, 3.5% natural sand (Rambeaut sand), and 1% bag house fines. The aggregate gradation falls below the restricted zone as shown in Figure 5.1.

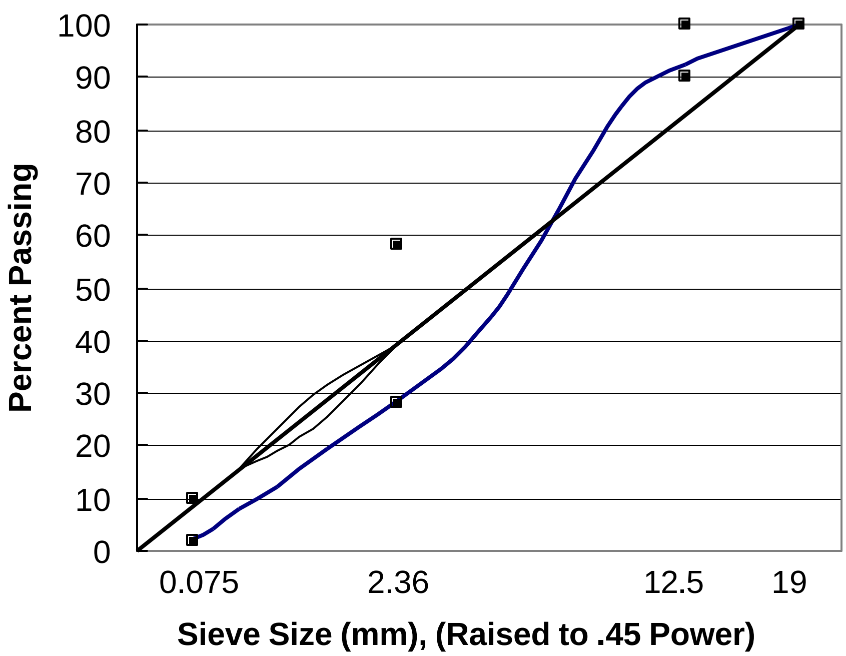

Figure 5.1 Aggregate Gradation of North Carolina Mix

Aggregates were mixed with 5.2% unmodified asphalt PG 70-22 obtained from the Citgo Asphalt Company in Paulsboro, New Jersey. The theoretical maximum specific gravity of the North Carolina mixture is 2.481. Specimens 150 mm in diameter and 115 mm in height were compacted to approximately four percent air void at a temperature of 153°C using the IPC Superpave Gyratory Compactor.

5.2 WesTrack Mixtures

WesTrack is a pavement test facility located about 30 miles southeast of Reno, Nevada (WesTrack Team 2000a, 2000b). The test track consists of two tangent sections connected by spiral curves, with all 26 of the pavement test sections constructed on the tangents. The tangent sections are 10.4 m in width, with two 3.7 m width lanes and a 1.2 m asphalt shoulder outside the test lane. Each test section is 70 m in length, with the first 25 m used for a transition zone, 40 m for performance monitoring and 5 m for destructive sampling. The test sections were loaded using autonomous (driverless) vehicles with four triple trailer combinations. The vehicles operated up to 22 hours a day during the loading period to achieve the desired 10 million ESALs. A schematic of the test track is shown in Figure 5.2.

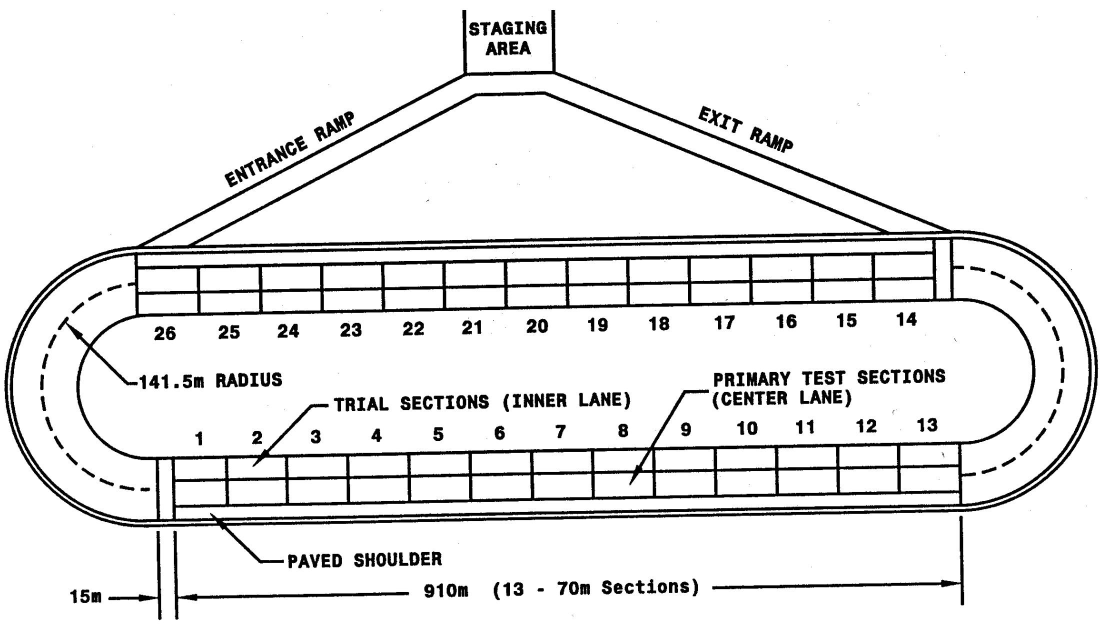

Figure 5.2 Schematic of WesTrack Test Facility (from WesTrack Report)

The 26 sections of the test track use the same type of aggregate, a local crushed andesite from Dayton, Nevada and a natural (Wadsworth) sand. The binder is a PG 64-22 obtained from a west coast refinery and is a blend of US crudes. Three different gradations (coarse, fine, and fine plus) are used for the different test sections with varying air void and asphalt contents to evaluate the sensitivity of the mix performance to these changes. The asphalt contents used are low, optimum, and high and are expressed by the total weight of mixture. The optimum asphalt content is that obtained from Superpave volumetric design. The low asphalt content is optimum minus 0.7% and the high is optimum plus 0.7%. The air void contents are 4%, 8%, and 12% (low, medium, and high). The different asphalt and air void contents were chosen to be statistically different from one another and to ensure different performance. Table 5.1 summarizes the different sections. Note that the impractical combinations such as the low asphalt/low air void content and high asphalt/high air void content were not constructed. The numbers in the table indicate the section number on the track (Figure 5.2) where that mixture was placed.

Table 5.1 WesTrack Pavement Sections (from WesTrack Team 2000a)

Design Air Void Content	*Aggregate Gradation*								
	Fine			Fine Plus			Coarse		
	Design Asphalt Contents (%)								
(%)	Low	Opt.	High	Low	Opt.	High	Low	Opt.	High
Low	N/A	4	18	N/A	12	9/12	N/A	23	25
Medium	2	1/15	14	22	11/19	13	8	5/24	7
High	3/16	17	N/A	10	20	N/A	26	6	N/A

5.3 Specimen Fabrication

In this project, the coarse and fine gradations were chosen for evaluation. The two 19 mm gradations are shown in Figure 5.3. The coarse gradation falls below the Superpave restricted zone and the fine gradation falls above the zone. Four cells from each gradation are evaluated as shown by the shaded cells in Table 5.1. The high (12%) air void content was not chosen due to the inability to fabricate these specimens in the laboratory using the Superpave Gyratory Compactor. The specimen identifications used in this project are based on the gradation (F or C), air void content (L, M, or H), and asphalt content (L or O) and are shown in Table 5.2 with the corresponding WesTrack identifications. These abbreviations will be used from this point forward to identify the different mixtures.

Both the design and as-constructed gradations were available for the research team. A detailed study based on laboratory sieve analysis of different aggregate gradations showed that the materials sampled from the construction process were coarser than those used for the original mix design. Therefore, different stockpile materials were assembled to meet the as-constructed gradations. The results from this gradation evaluation study are documented in Appendix C. The aggregate and asphalt cement are mixed at 150^{o}C and then aged for four hours at 135^{o}C (short term oven aging) before being compacted at 140^{o}C.

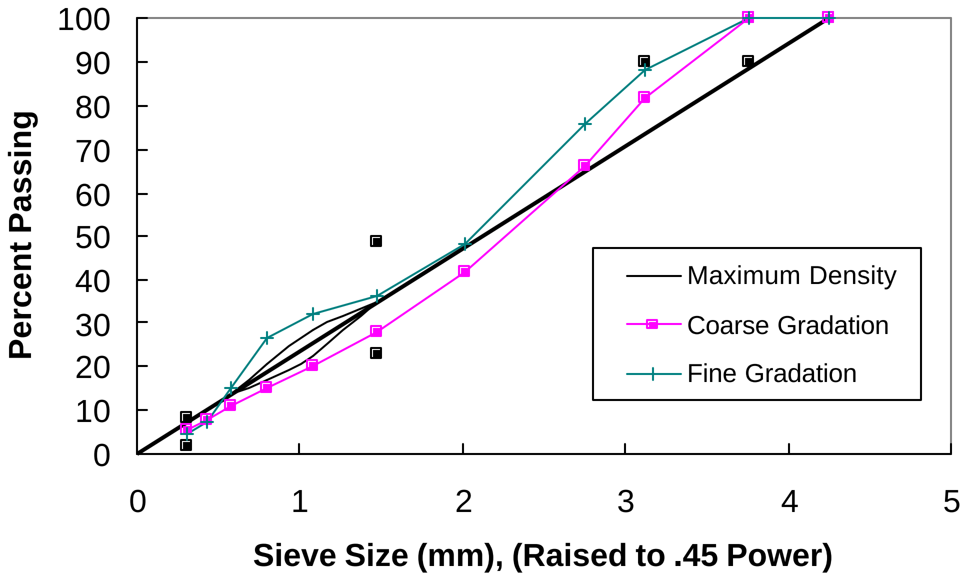

Figure 5.3 WesTrack Coarse and Fine Gradations

Table 5.2 Mixture Identifications

Gradation	% Air Void	% Asphalt	Project ID	WesTrack ID
Coarse	Low	Optimum	CLO	ML
	Medium	Low	CML	LM
		Optimum	CMO	MM
		High	CMH	HM
Fine	Low	Optimum	FLO	ML
	Medium	Low	FML	LM
		Optimum	FMO	MM
		High	FMH	HM

5.3.1 Uniaxial Test Specimens

As a result of the specimen geometry study by Chehab et al. (2000), 150 mm high, 75 mm diameter cylindrical specimens were chosen for uniaxial testing in this project. The specimens are cored and cut from a 150 mm diameter gyratory compacted specimen. Figure 5.4 shows a compacted gyratory specimen and the test specimen that is cut and cored from the center of the plug. The height of the gyratory plug depends upon the desired air voids within the final test specimen. The compaction heights for 7200 g of mixture are shown in Table 5.3.

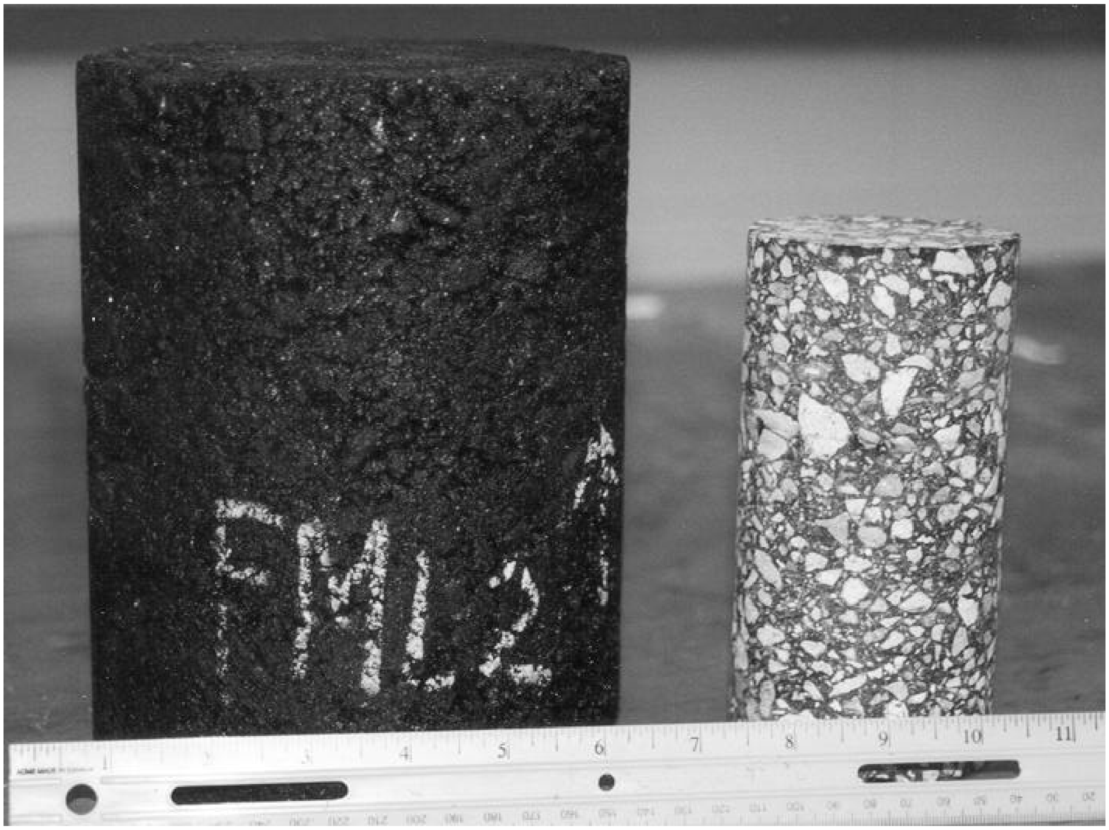

Figure 5.4 Whole and Cut Gyratory Specimens

Table 5.3 Mixture Compaction Information

Mixture	Gmm	IDT Compaction Height (mm)	Uniaxial Compaction Height (mm)	Uniaxial Avg # Gyrations to Compaction
FLO	2.388	116.0	187.4	10.9
FML	2.424	119.4	197.8	2.8
FMO	2.388	121.8	197.8	2.6
FMH	2.387	119.2	197.8	1.7
CLO	2.386	115.3	185.7	33.7
CML	2.409	121.7	197.0	19.5
CMO	2.386	121.6	197.0	11.4
CMH	2.363	121.0	197.0	10.5

Table 5.3 also shows the average number of gyrations required to reach the desired compaction height for each of the mixtures. The low air void mixtures require more gyrations and as the asphalt content decreases with the 8% air void mixtures more gyrations are needed because of the stiffer mixture. The fine gradation mixtures are more easily compacted, with the 8% air void specimens only requiring a couple of gyrations to reach the desired height. The gyratory compactor does not apply partial gyrations, so in many cases the specimens were over compacted with the application of a whole number of gyrations. This results in a larger variability in measured air voids and a higher percentage of those specimens could not be used for testing. The variability in air voids for each mixture are shown in Table 5.4.

In the case of FMH mixture, 8% air voids could not be achieved. The low number of gyrations also causes concern about the aggregate orientation within the specimens and the possible specimen-to-specimen variability. A fewer number of gyrations will result in less consistent aggregate orientation and perhaps greater anisotropy with respect to air void distribution in the specimen. The cutting and coring process produces a specimen with the least air void distribution both vertically and radially, according to the study by Chehab et al. (2000). Once specimens are fabricated, they are stored in sealed bags to minimize further aging before testing. Also, the compaction direction is marked and the specimens are stored and tested in the same orientation as they were compacted.

Table 5.4 Air Void Measurements for axial Uniaxial Compacted Specimens

Mixture	**Target**	**Average**	**Standard Deviation**
FLO	4.0	3.9	0.42
FML	8.0	8.2	0.51
FMO	8.0	7.8	0.71
FMH	8.0	5.3	0.36
CLO	4.0	4.1	0.56
CML	8.0	7.8	0.29
CMO	8.0	8.2	0.42
CMH	8.0	7.9	0.50

5.3.2 Laboratory Fabricated Indirect Tension Specimens

Specimens 100 mm in diameter and 38 mm thick were chosen for indirect tension testing as a result of the specimen geometry study conducted by Chehab et al. (2000). Two specimens are cored and cut from the center of a 150 mm diameter, approximately 115 mm tall gyratory plug. The actual compaction heights to achieve the desired specimen air void content using 4400 g of the mixture are shown in Table 5.3.

5.3.3 Indirect Tension Specimens from Field Cores

Field cores were sampled from the WesTrack pavements. Figure 5.5 illustrates the basic approach used to obtain test specimens for indirect tension testing from a field core. Specimens were sliced from the middle of each of the two lifts to obtain a relatively uniform section unaffected by layer interfaces.

It was noted that traffic direction was marked on the field cores. Thus, arrow heads were drawn at the end of the line on the top side of the specimen to indicate the direction of load application for the indirect tensile test. The arrows thereby indicate that the tensile stresses induced in the indirect tensile test are coincidental to the longitudinal tensile stresses that cause fatigue cracking in the field.

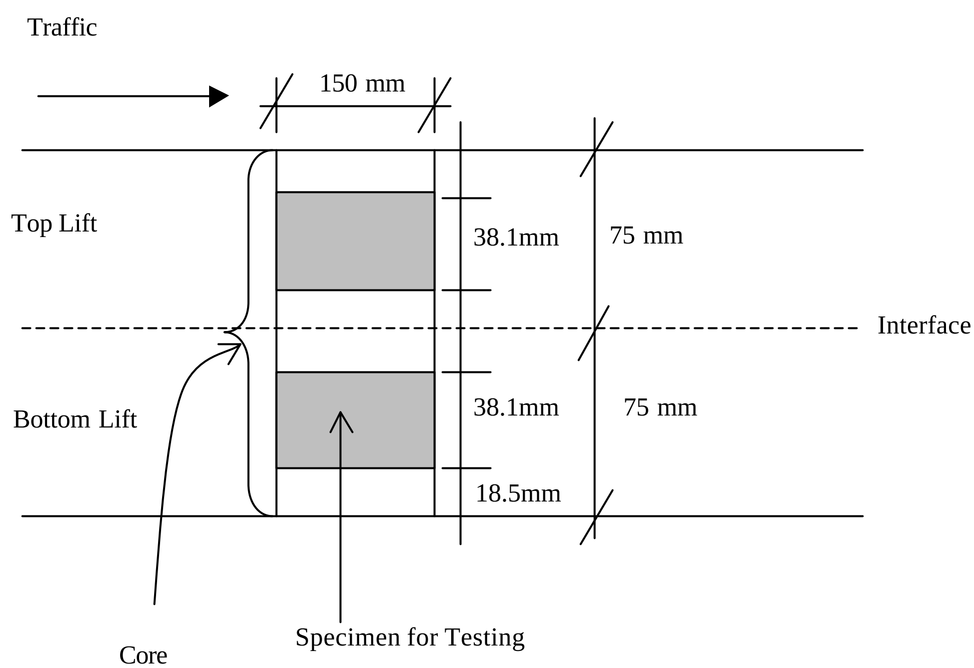

Figure 5.5 Locations of Specimens Cored from Field Core

Air void measurements of the field cores were performed using both the SSD method and the CoreLok measurement device. The values obtained from the two methods are reported in Table 5.5. The “r” following the mixture ID indicates that the core was taken from the replacement section constructed after the failure of the original section.

5.4 Uniaxial Test Configuration

Prior to testing, steel end plates are glued to the specimen using Devcon Plastic Steel epoxy. A gluing jig is used to minimize any eccentricities due to unparallel specimen ends and is shown in Figure 5.6. Four loose core type LVDTs (099X-SBs) are mounted to the specimen surface at 90^o radial intervals using a 100 mm gage length.

Table 5.5 Comparison of Air Void Measurement Using SSD and Corelok

Mixture ID		Bulk Specific Gravity		Air Void (%)	
		SSD	CoreLok	SSD	CoreLok
FMO	Top	2.286	2.292	6.1	5.8
	Bottom	2.268	2.272	5.8	5.7
FML	Top	2.267	2.271	6.9	6.8
	Bottom	2.244	2.243	6.8	6.9
FHL	Top	2.190	2.192	11.6	11.6
	Bottom	2.230	2.226	8.4	8.5
FLO	Top	2.319	2.322	4.2	4.1
	Bottom	2.317	2.32	3.9	3.9
CLO	Top	2.33	2.33	3.6	3.7
	Bottom	2.300	2.308	3.9	3.6
CHOr	Top	2.153	2.114	10.9	12.5
	Bottom	2.126	2.093	13.0	14.4
CMOr	Top	2.300	2.297	5.8	5.9
	Bottom	2.277	2.273	7.1	7.3
CHLr	Top	1.999	2.099	18.5	14.4
	Bottom	2.022	2.124	17.6	13.5

Additionally, two spring-loaded (D5-200AG) LVDTs are mounted 180^o apart to measure the plate-to-plate deformations. The ram and LVDT deformations and load cell measurements are collected using a National Instruments data acquisition board and Labview software. The specimen setup is shown in Figure 5.7.

Testing is performed using a closed-loop servo-hydraulic testing system manufactured by MTS. A 8.9 kN (2000 lb) or 89 kN (20,000 lb) load cell is used depending upon the anticipated testing loads. The temperature is controlled with an environmental chamber that uses liquid nitrogen for cooling and a feedback system that maintains the temperature during testing.

During preliminary testing, a phase lag in the LVDT measurements from electronic and dynamic effects was discovered and must be subtracted from any measured values to get the true material response. The phase lag is a function of the testing frequency, LVDT type, LVDT mount type, and gage length. The phase angle adjustments as a function of frequency for the testing setup used in this project for the XSB and D5 LVDTs are described by Equations (5.1) and (5.2), respectively.

$$XSB\,adj = 0.0008 f^2 + 0.6835 f + 1.8603 \tag{5.1}$$

$$D5\,adj = -0.0036 f^2 + 0.2853 f + 0.3397 \tag{5.2}$$

A detailed description of the procedure used to determine the phase angle adjustment can be found in Appendix B.

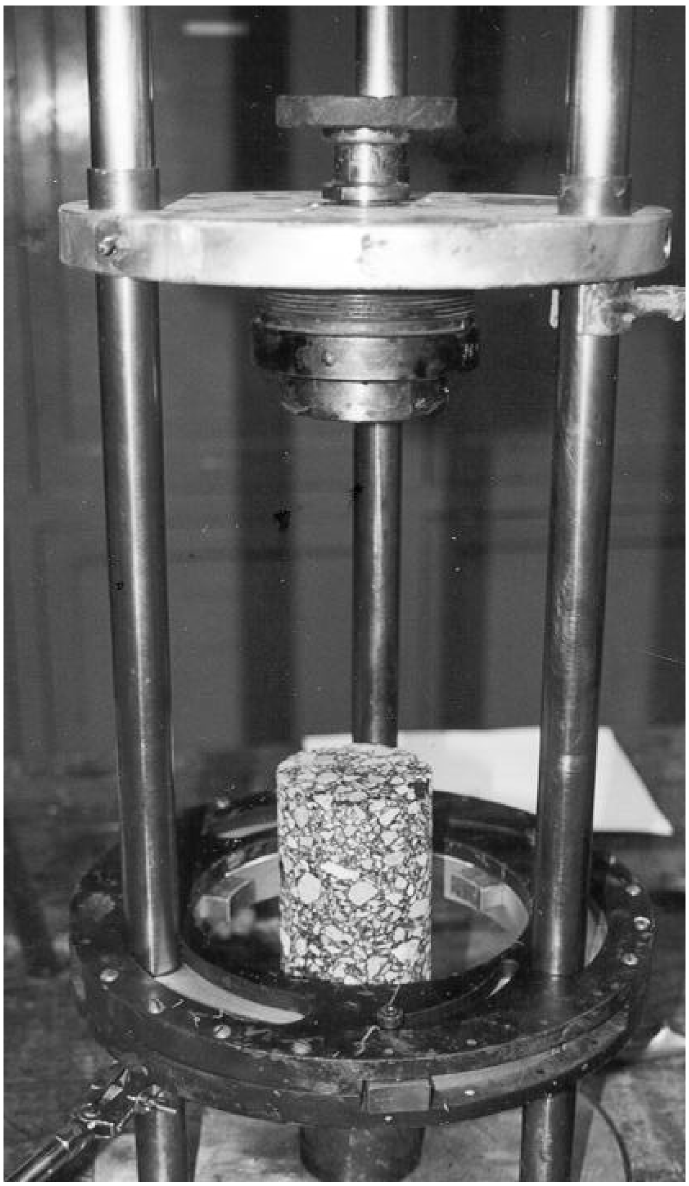

Figure 5.6 Gluing Jig

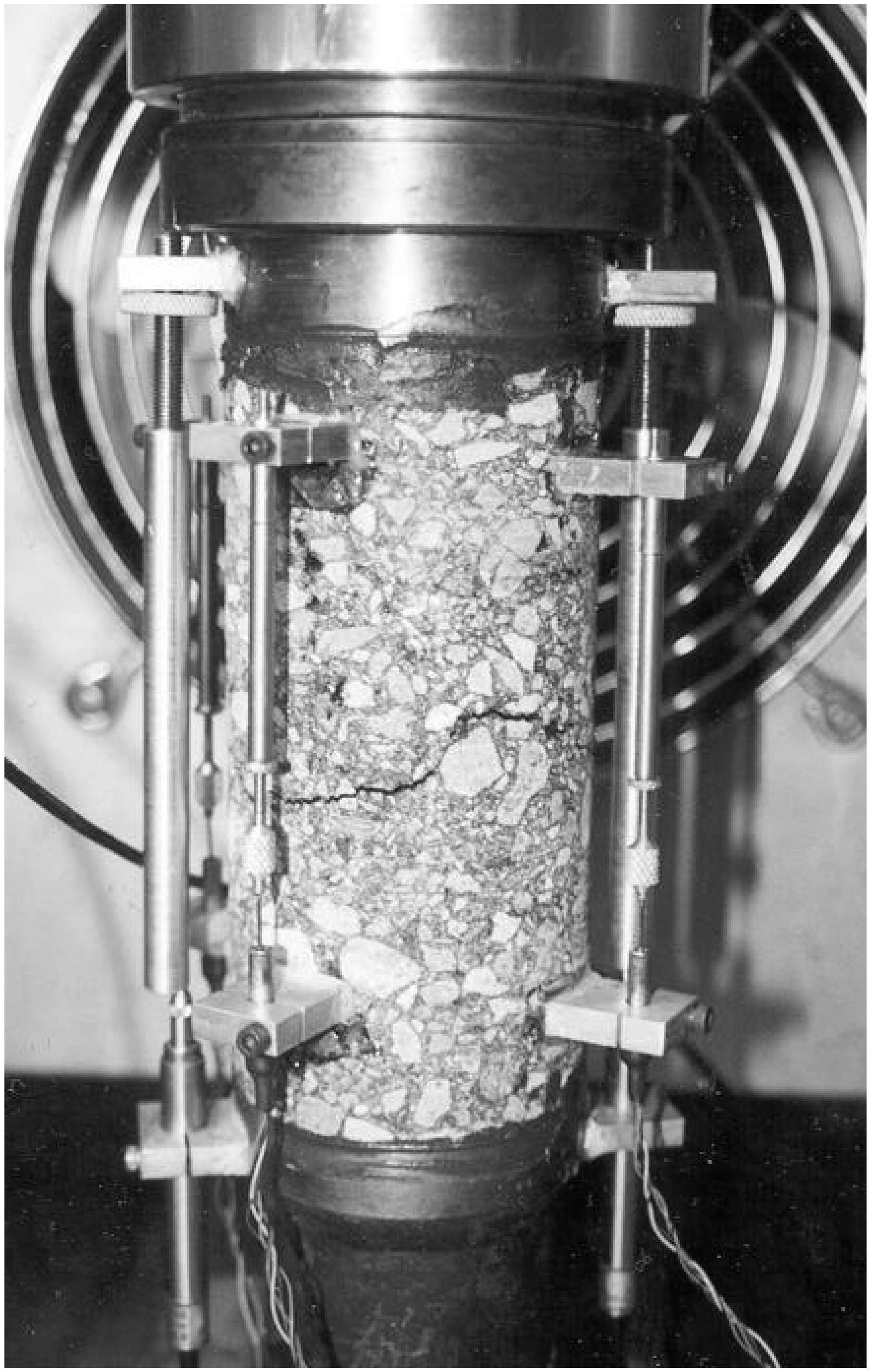

Figure 5.7 Specimen Test Setup

The viscoelastic material properties for the eight WesTrack mixtures are measured from the frequency sweep test. All eight mixtures are tested at 20°C. Eight frequencies (20, 10, 5, 2, 1, 0.5, 0.2, and 0.1 Hz) are used for these mixtures, with a data acquisition rate of 100 points per cycle. Frequency sweep tests at 0°C or 5°C using six frequencies (20, 10, 3, 1, 0.3, and 0.1 Hz) were performed on some of the mixtures. Master curves are then generated using the time-temperature superposition principle. The relaxation modulus is predicted from the dynamic modulus and phase angle master curves through linear viscoelastic theory as described in Appendix A.

5.5 Indirect Tension Test Configuration

AASHTO TP9-96 provides the standard test method for indirect tensile test. One of the major differences between the AASHTO TP9-96 setup and the setup used in this study is that AASHTO TP9-96 uses a loading frame with four columns whereas this study uses the SHRP Load Guide Device (LGD) with two columns. According to the NCHRP 1-28 study (Barksdale et al. 1997), this device allows less rocking and less friction along the columns than other types of loading apparatus,. Another difference is the gauge length used to mount the LVDTs for measurement of deformations. AASHTO TP9-96 uses the gauge length set at 25.4 mm (one inch), whereas the gauge length used in this study is 50.8 mm (2 inches). The advantage of using the larger gauge length is that it minimizes the effect of large aggregates located in between the two gauge points and stress concentration in the vicinity of loading strips. At the end of this section, the gauge length study conducted using the Digital Image Correlation technique is presented. The plan-view of the apparatus that holds the LVDTs is presented in Figure 5.8.

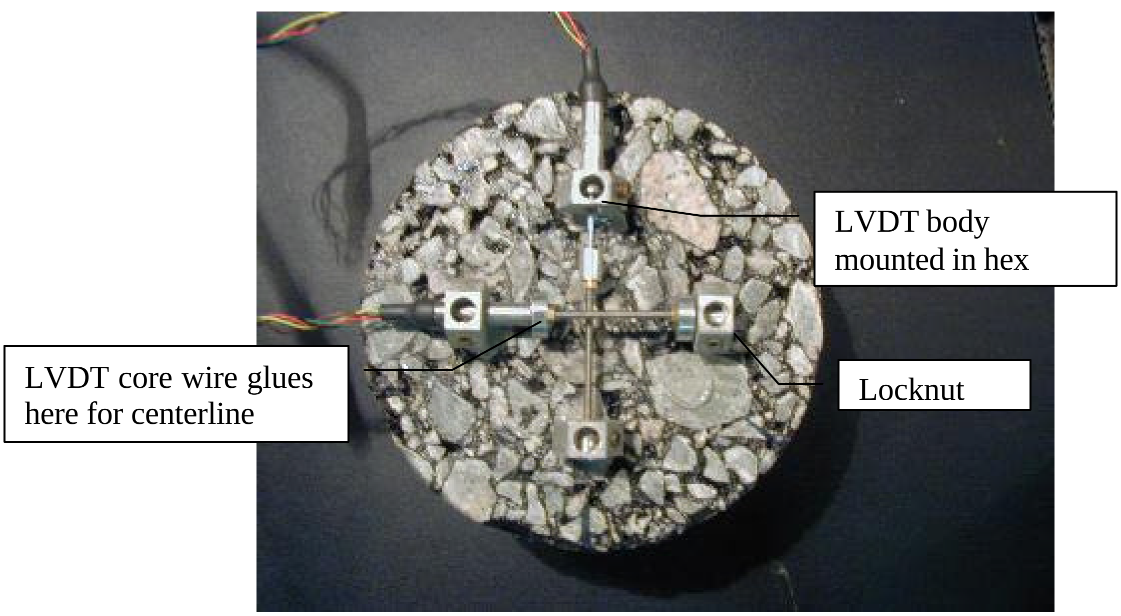

Figure 5.8 Plan View of LVDTs Glued to a Specimen

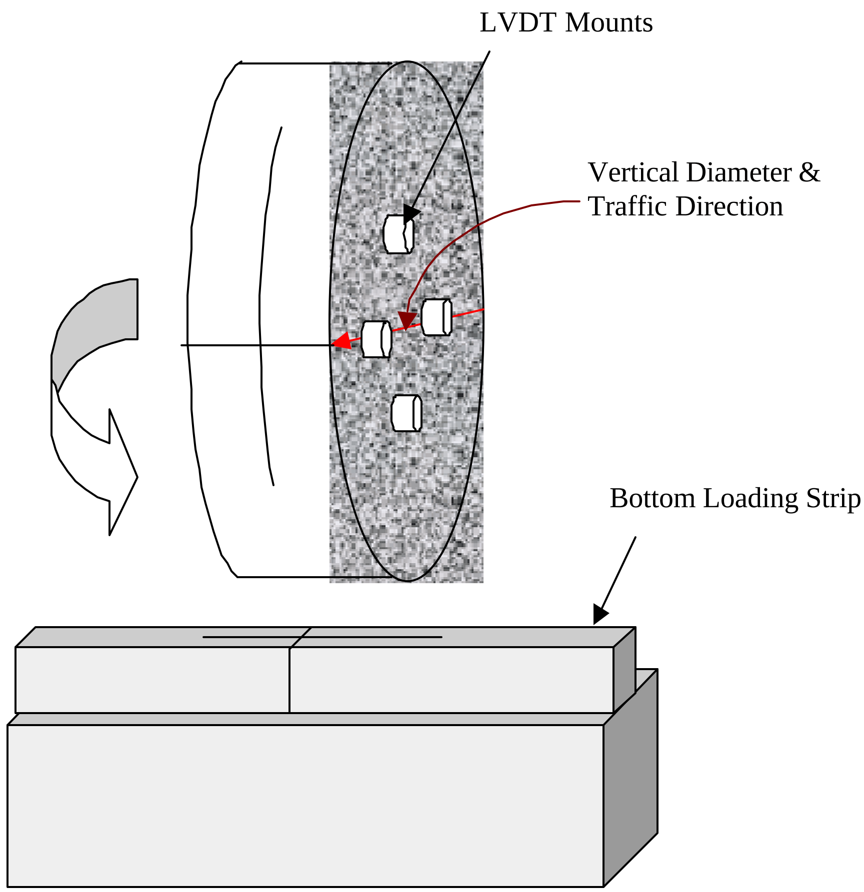

Figure 5.9 Positioning Specimen on Loading Strip

All the indirect tension tests were performed using the MTS servo-hydraulic closed-loop testing machine. An environmental chamber was used to control the temperature of the specimens. Prior to testing, the specimen was placed into the chamber at the testing temperature for at least two hours for conditioning. Displacements were measured by XSB LVDTs and loads were measured by the MTS load cell. Test data were collected by the National Instrument LabView data acquisition board.

In an attempt to validate the applicability of the theory of viscoelasticity to the indirect tensile testing, mode, creep, and cyclic loading tests were conducted on the North Carolina mixes. Creep tests at several different temperatures were performed to obtain the thermorheological properties. To minimize the sample-to-sample variation, a series of tests was performed on each individual specimen. Since the same specimen underwent various combinations of tests and temperatures, a relatively low stress/strain level was applied to the specimen to ensure negligible damage during the entire testing period. The loading level was reduced when testing was performed at higher temperatures. To check the extent of damage that the specimen received during a series of tests, additional creep tests were conducted at 20°C at the end of all the tests as a rheological fingerprint. All other tests were conducted at 20°C. For WesTrack specimens, a creep test was conducted first, followed by an indirect tensile strength test after a 30-minute rest period.

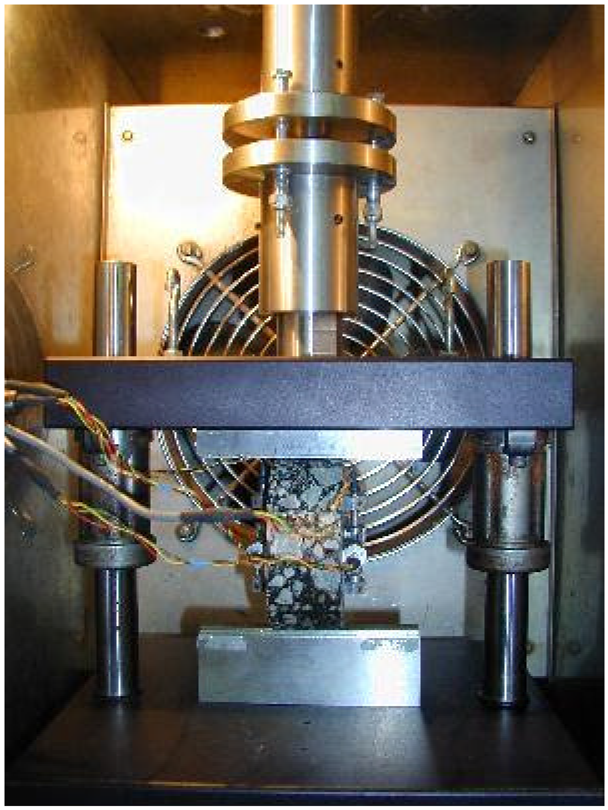

Figure 5.10 Test Configuration of Indirect Tensile Test

GAUGE LENGTH STUDY USING DIC

The Digital Image Correlation (DIC) method is a noncontact, full-field displacement/strain analysis method that compares images of deformed specimens with that of an initial, undeformed specimen. The basic setup of the DIC technique requires a digital camera, a lighting system, a frame grabber, a PC, and software for post-analysis. The camera is positioned perpendicular to a specimen having a black and white pattern.

One of the major advantages of DIC over a conventional LVDT or strain gauge system is that it is a full-field displacement measurement technique that allows postprocessing of images. It allows users to adjust gauge lengths and positions after the test is run. This aspect of DIC is useful when displacements/strains vary within the area of interest, such as the middle area in the IDT specimen. Instead of mounting multiple sensors, one may use DIC as a single sensor and obtain information from various areas and gauge lengths through postprocessing. In addition, DIC can determine the load-induced deformation separately from the rigid body translation (also known as rocking in the IDT testing and caused by the improper setting of the specimen and/or loading fixture) owing to its ability to measure full-field displacements. These abilities permit users to obtain correct measurements from a test that would have been discarded otherwise.

It is this full-field measurement ability of DIC that makes this technique uniquely suitable for the determination of a proper gauge length for the IDT specimen. Figure 5.11 shows the vertical displacement fields determined by DIC in the 100 mm diameter IDT specimen at two different loading stages (pre-peak and post-peak) during the constant-crosshead-rate strength test. The square block in the middle of the specimen represents the volume of the specimen covered by a 50 mm gauge length. All the vertical and horizontal displacement and strain fields were evaluated using DIC, and it was the vertical displacement that showed the effect of stress concentration under the loading strips most clearly. It can be seen from this figure that the effect of loading strips reaches slightly over into the area covered by the 50 mm gauge length. The same type of investigation of the images from three replicates suggests that there is a minimal effect from the loading strip on the displacement fields in the middle 50 mm gauge length.

Another important consideration in the selection of gauge length is that of the requirements for the traditionally known representative volume element (RVE). In material testing and modeling, it is important to measure responses from the RVE so that the resulting model can represent the material being tested. The RVE is defined as the volume of a material in which material properties are constant throughout and responses under a mechanical load are independent of aggregate size and specimen boundary conditions. It is commonly accepted that the minimum ratio of maximum aggregate size to gauge length is 1:3 to 1:4. Assuming the minimum ratio of 1:3, Superpave 19 mm gradation requires a 57 mm gauge length to satisfy the RVE requirement. For a 38 mm gradation, a 114 mm gauge length is required. Considering the RVE requirement, and that most of the gradations used in pavement construction have the largest aggregate size at or below 19 mm, a 50 mm gauge length seems to be more appropriate than the 25 mm gauge length recommended by AASHTO TP9-96.

It needs to be noted that the conclusions from Figure 5.11 are based on a 100 mm diameter specimen. Of course, when a larger diameter specimen is used, such as 150 mm diameter specimens compacted by the Superpave Gyratory Compactor, the 50 mm gauge length becomes even more conservative.

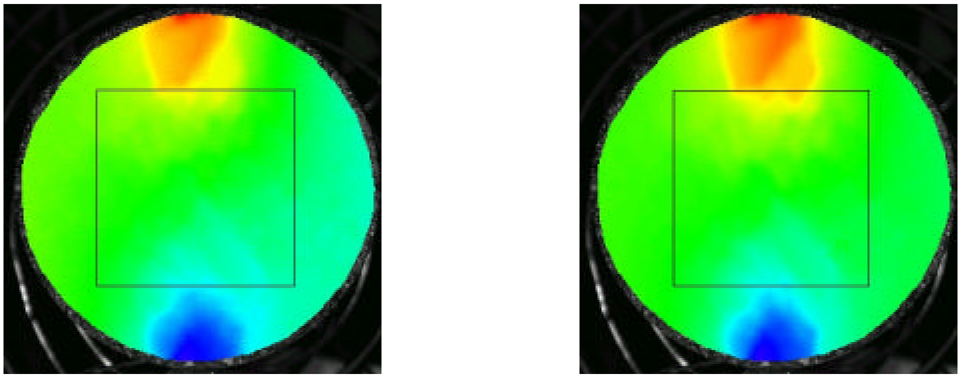

Figure 5.11 Vertical Displacement DIC Images at Two Different Loading Stages (Pre-peak and Post-peak) in IDT Strength Test

6. UNIAXIAL TESTING

6.1 Viscoelastic Material Properties

6.1.1 Dynamic Modulus and Phase Angle

The dynamic modulus and phase angle values for specimen FMO12 are shown in Figures 6.1 and 6.2 for both the 20°C and 5°C testing. The values calculated from the on-specimen and plate-to-plate LVDTs are shown. There is very little difference in the measured properties from the two different gage lengths, indicating that either may be used for analysis. Using 20°C as the reference temperature, the 5°C data is shifted to the right to form a master curve, as shown in Figure 6.3. The individual specimen dynamic modulus master curves are plotted together for the CLO mixture in Figure 6.4. Also shown is a line representing the average material response determined from fitting the data from all of the specimens; a solid line represents the normal specimens and a dashed line represents the moisture exposed specimens, if applicable. The dynamic modulus master curves for the other seven mixtures can be found in the Appendix D. The corresponding mean square error (mse) is calculated using the following equation as a measure of the specimen-to-specimen variability:

$$mse = \sqrt{\frac{1}{n-1}\sum\left(y-\hat{y}\right)^2} \qquad (6.1)$$

where n = number of observations,
y = measured value, and
$\hat{y}$ = predicted value.

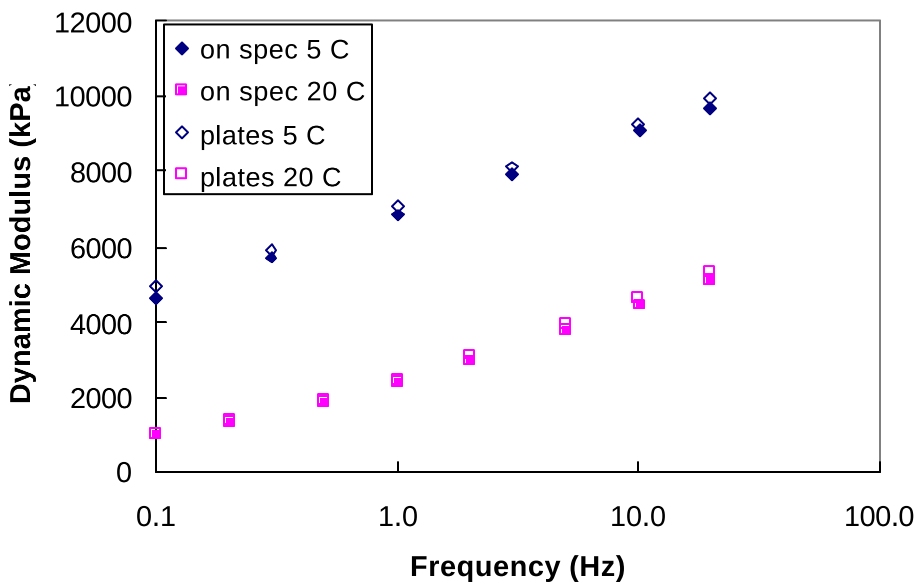

Figure 6.1 Dynamic Modulus Values for Specimen FMO12 at 20°C and 5°C

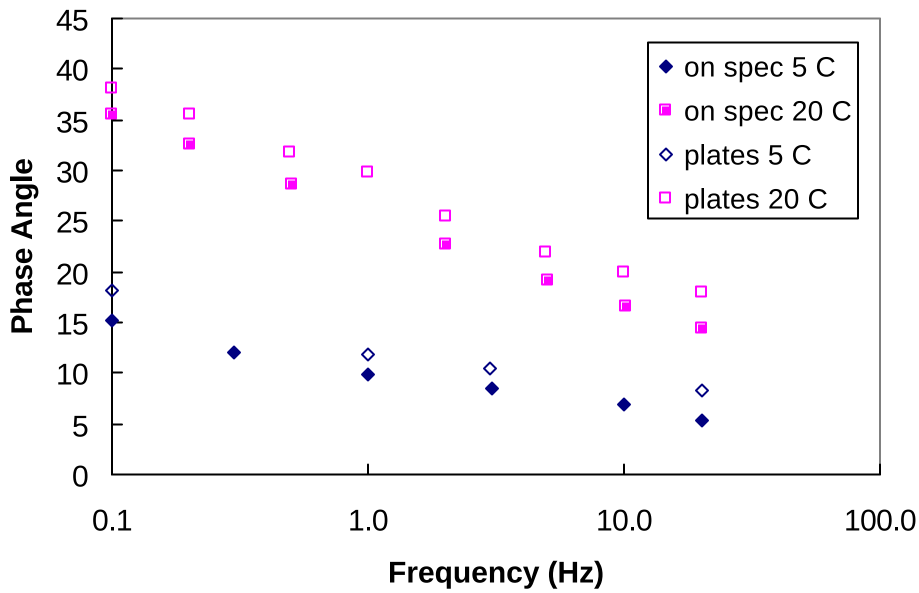

Figure 6.2 Phase Angle Values for Specimen FMO12 at 20°C and 5°C

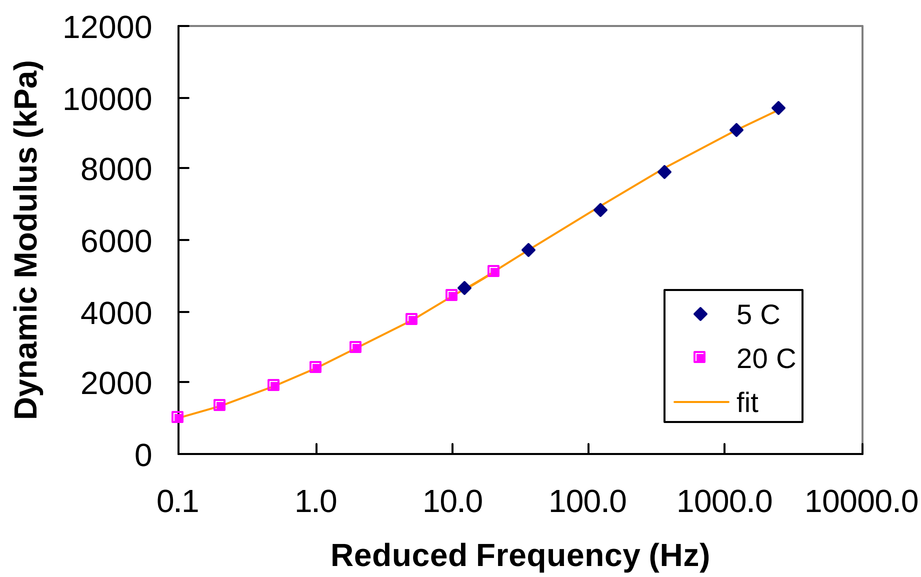

Figure 6.3 Dynamic Modulus Master Curve for Specimen FMO12 at Reference Temperature of 20°C

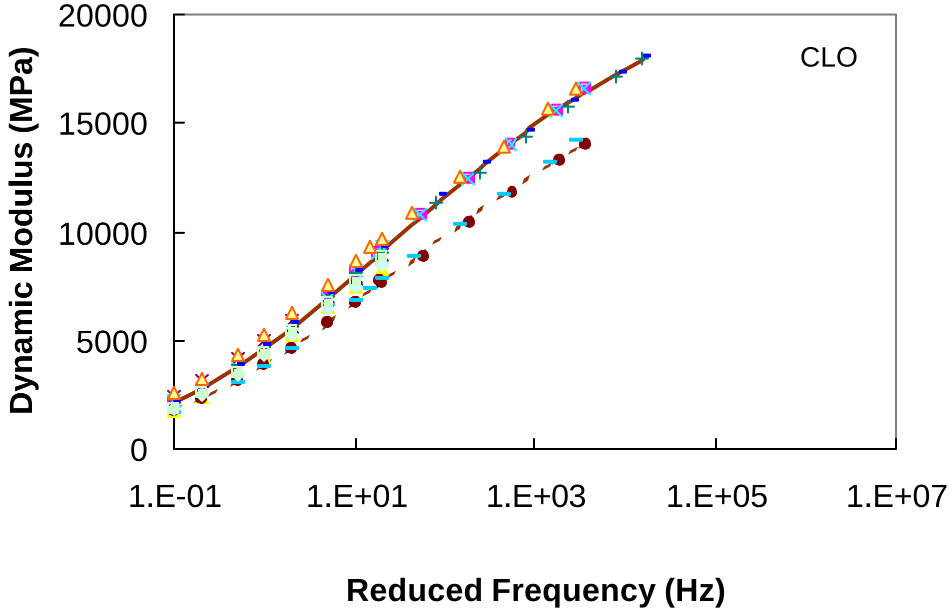

Figure 6.4 Dynamic Modulus Master Curves for CLO Mixture

Table 6.1 summarizes the dynamic modulus and phase angle mse values for each mixture. In general, the fine mixtures have greater variablilty in the dynamic modulus measurements than the coarse mixtures, with the exception of CML. This likely stems from the specimen fabrication process and the difference in compactiblity of the two gradations. As shown in Section 5.3.1, the fine gradation required fewer gyrations to reach compaction height, and there is likely a less consistent aggregate orientation and air void distribution, which results in a higher sample-to-sample variability in testing, as shown by the dynamic modulus measurements. The mse's for the phase angle measurements show no trend with respect to the gradation.

Table 6.1 Dynamic Modulus and Phase Angle Mean Square Error Values

Mixtures Tested Dry

Mixture	**FLO**	**FML**	**FMO**	**FMH**	**CLO**	**CML**	**CMO**	**CMH**
|E*| mse (MPa)	593	624	275	805	305	661	396	352
Phase mse (deg)	2.02	1.24	1.44	2.51	1.71	2.11	2.15	2.77

Mixtures Subject to Moisture

Mixture	**mFLO**	**mFMO**	**mCLO**	**mCMO**
|E*| mse (MPa)	117	241	137	1172
Phase mse (deg)	1.55	1.45	1.78	1.58

Figures 6.5 and 6.6 show the dynamic modulus master curves for the coarse and fine mixtures, respectively. The modulus values for the coarse mixtures show the expected trends with respect to air void and asphalt contents. The 4% air void mixture (CLO) has a higher modulus than the 8% air void mixture (CMO). Within the 8% air void content mixtures, increasing asphalt content results in lower dynamic modulus values. The resilient modulus values reported by Epps et al. (1999) show the same trend with respect to air void and asphalt contents. The fine mixtures follow the same trends with the exception of FMH, which has a higher dynamic modulus than both FML and FMO mixtures. This difference is due to the lower air void content in the FMH mixtures. The FMH mixtures could only be fabricated with 5.5% air voids while both the FML and FMO mixtures contain 8% air voids.

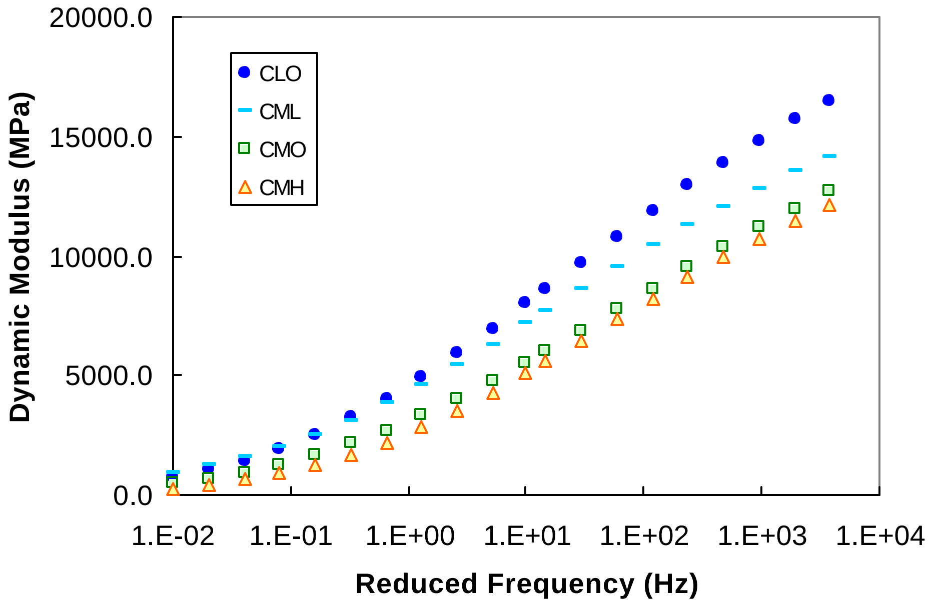

Figure 6.5 Dynamic Modulus Master Curves for Coarse Mixtures

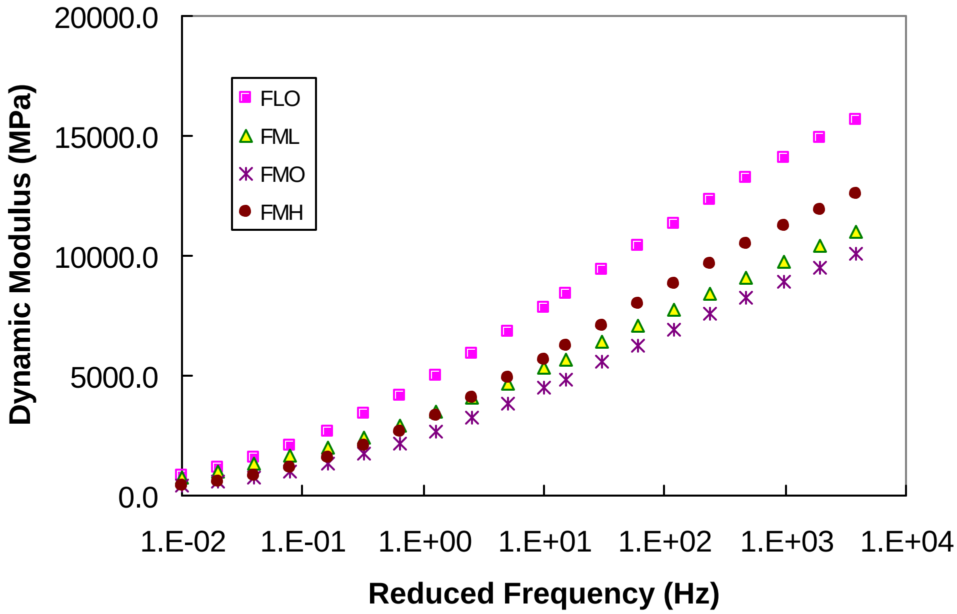

Figure 6.6 Dynamic Modulus Master Curves for Fine Mixtures

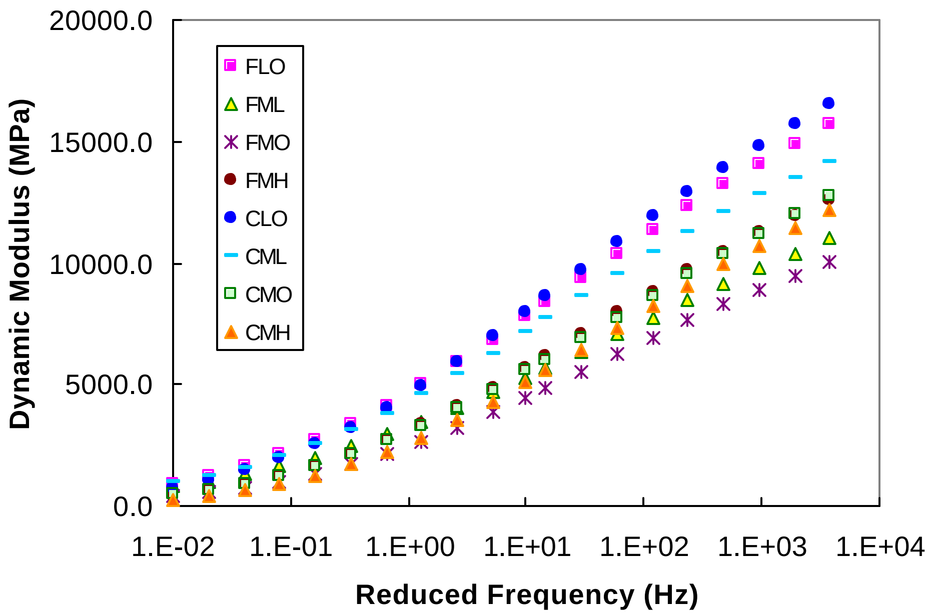

Figure 6.7 Dynamic Modulus Master Curves for All Mixtures

Figure 6.7 shows the response of each of the mixtures and allows for comparison of the coarse and fine gradations. In three cases, the coarse mixture is stiffer than the corresponding fine mixture (i.e., CMO versus FMO). The CMH and FMH mixtures cannot be compared due to the air void differences. However, one can observe that the FMH mixture would also have a lower dynamic modulus than the CMH mixture if it fell below the FMO mixture, as would be expected at 8% air voids. The phase angle master curves for all of the mixtures are shown in Figure 6.8. The trends with respect to air void and asphalt contents are not as clear, but in general, the coarse mixtures have higher phase angles than the fine mixtures.

The effect of moisture on the dynamic modulus and phase angle are shown in Figures 6.9 and 6.10. The specimens exposed to moisture have a lower dynamic modulus and slightly higher phase angle. The decrease in modulus is greater with the CLO and FLO mixtures (4% air void) than with the CMO and FMO (8% air void) mixtures. This is the opposite trend of what would be expected; in the field the moisture will have greater contact area and will migrate further into the specimen resulting in more stripping at higher air void contents. However, the vacuum saturation process used in the laboratory is likely to have damaged the 4% air void specimens.

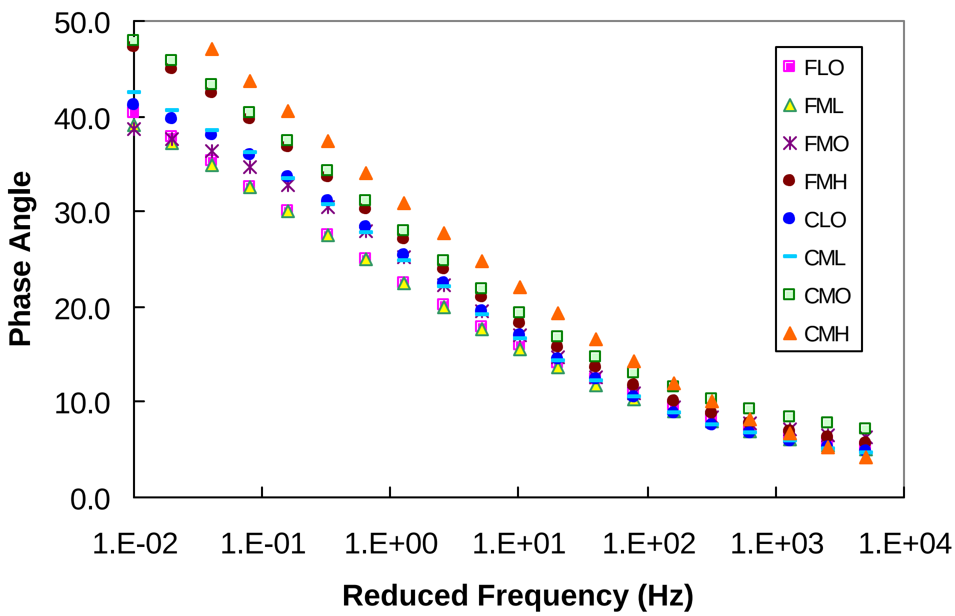

Figure 6.8 Phase Angle Master Curves for All Mixtures

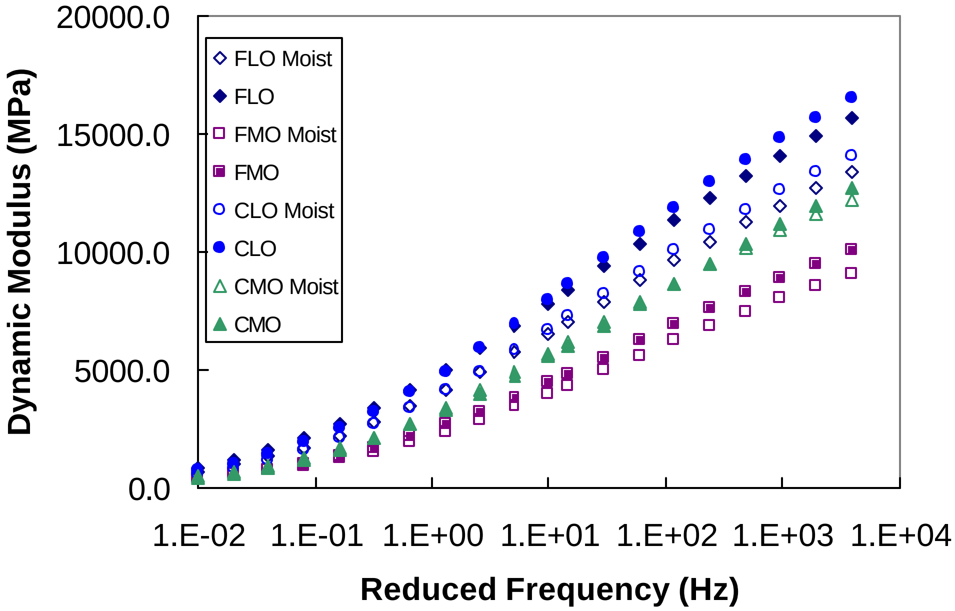

Figure 6.9 Effect of Moisture on Dynamic Modulus

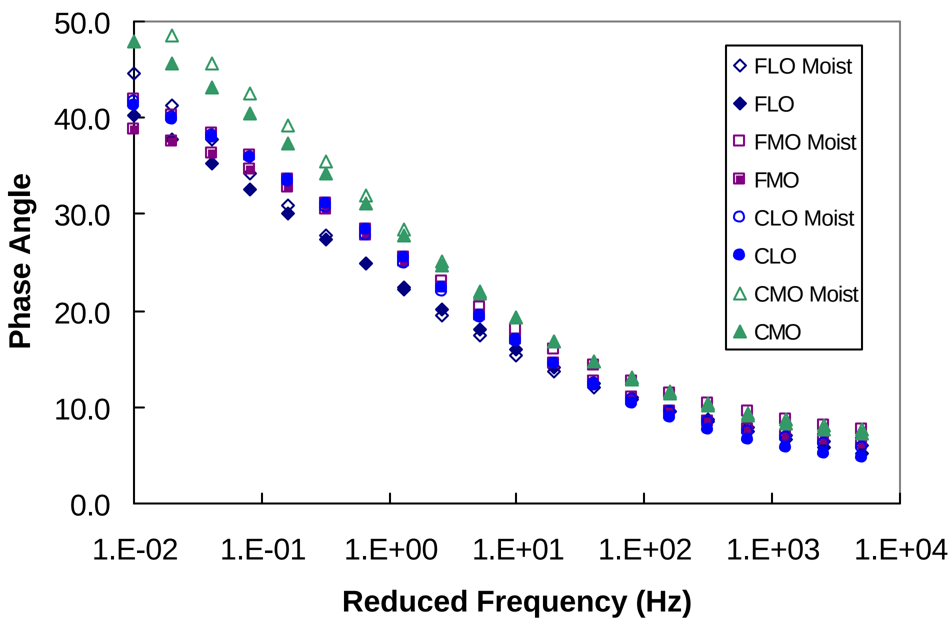

Figure 6.10 Effect of Moisture on Phase Angle

6.1.2 Relaxation Modulus

The relaxation modulus for each mixture is predicted from the dynamic modulus and phase angle master curves using the relationships presented in Appendix A. In cases where a master curve was not available for a specimen (testing only performed at 20^{o}C), the average relaxation modulus for that mixture was used in the analysis. The average relaxation modulus curves for all eight mixtures are shown in Figure 6.11.

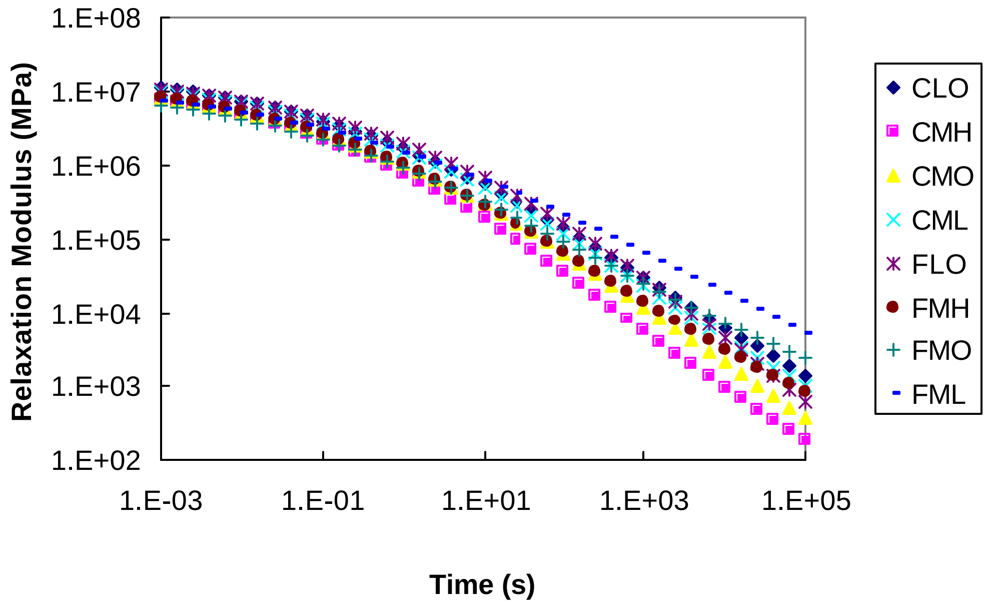

Figure 6.11 Relaxation Modulus Curves for All Mixtures

6.2 Calculation of Pseudo Strains

Pseudo strain is an important parameter in Schapery's correspondence principle and therefore any analysis applying the CP to viscoelastic materials. The pseudo strain at any time, t, is a function of both the relaxation modulus and the strain history from zero to time t as follows:

$$e^R = \frac{1}{E_R}\int_o^t E(t-t)\frac{de}{dt}dt \tag{6.2}$$

Due to the impracticality of collecting the entire strain history for many tests, the approach taken is to find the analytical forms of the relaxation modulus and strain history as a function of time.

Taking advantage of the fact that the definition of pseudo strain in Equation (6.2) is linear, meaning it satisfies the criteria of homogeneity and superposition, a superposition technique is used to calculate the pseudo strain under different loading histories.

6.2.1 Constant Crosshead-Rate Monotonic Loading

In a constant crosshead rate test shown in Figure 6.12, the on-specimen LVDT strains follow a power function up to a point (t_1) and then follow a constant slope until the test is terminated. The strain history, and thus the pseudo strain calculation, must be broken up into the following two different time ranges because of the changing functional form of the strain:

$$e_1 = a * t^b \quad when \;\; 0 < t < t_1 \tag{6.3}$$

$$e_2 = ct + d \quad when \;\; t > t_1 \tag{6.4}$$

where a, b, c, and d are regression coefficients.

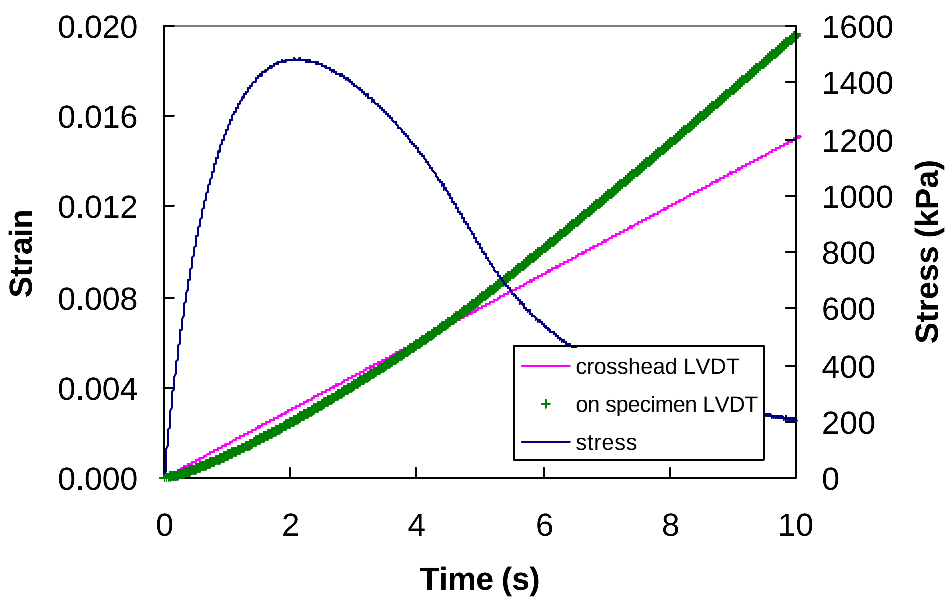

Figure 6.12 Constant Crosshead Rate Test

From Equations (6.2), (6.3), and (6.4), the pseudo strain at any time $t>t_1$ is calculated using:

$$e^R = \int_0^{t_1} E(t-t)\frac{de_1}{dt}dt + \int_{t_1}^{t} E(t-t)\frac{de_2}{dt}dt \tag{6.5}$$

$$e^{R} = \int_{0}^{t_1} E(t-t)\left[bat^{b-1}\right]dt + \left\{ c\left[E_{\infty} t + \sum_{i=1}^{N} E_i r_i \left(1 - e^{-\frac{t}{r_i}} \right) \right] \right\} \tag{6.6}$$

A closed form solution for the second integral is found using the Prony series representation of the relaxation modulus. However, the first integral must be evaluated numerically. Due to some potential difficulties in numerical integration, an alternative approach is proposed by recognizing the fact that the entire strain history can be approximated by a series of linear segments. This so-called piece-wise linear approach results in the following closed form solution for the pseudo strain at any time, t:

$$e^{R} = \int_{0}^{t_1} E(t-t)c_1 dt + \int_{t_1}^{t_2} E(t-t)c_2 dt + \Lambda + \int_{t_n}^{t} E(t-t)c_n dt \tag{6.7}$$

Using the prony series representation of the relaxation modulus, and setting u=(t-τ), Equation (6.7) becomes:

$$e^{R} = c_1 \left[E(u)\right]_{t-t_1}^{t} + c_2 \left[E(u)\right]_{t-t_2}^{t-t_1} + \Lambda + c_n \left[E(u)\right]_{t-t_n}^{0} \tag{6.8}$$

where $E(u) = E_{\infty} u + \sum_{i=1}^{N} E_i r_i \left(1 - e^{-\frac{u}{r_i}} \right)$ (6.9)

6.2.2 Controlled-Crosshead Amplitude Cyclic Loading

In the controlled crosshead cyclic testing, the on-specimen and plate-to-plate LVDTs exhibit permanent strain accumulation in addition to the cyclic strain as shown in Figure 6.13. It is difficult to fit a single function to describe both the permanent and cyclic portions of the strain, so the method of superposition is used. First, the permanent strain is fit and then subtracted from the total strain to leave the cyclic portion. The cyclic strain is then fit independently, and the two pseudo strains are calculated and added back together to get the total pseudo strain. The permanent strain can be described as:

$$\varepsilon = a + bt^{n} + ct + dt^{2} + et^{3} \tag{6.10}$$

For a more accurate representation over the whole test, up to three different time ranges are fit, and the regressed coefficients are only used in the appropriate time range for pseudo strain calculation. The first range fit is from time zero through the first half of the first cycle, which for 10 Hz loading is 0.05s. This allows for an accurate calculation of pseudo strain in the first loading path. The second range is typically from time zero up to 20-30 seconds, which gives an accurate fit of the initial accumulation of the permanent strain. Finally, the range from time zero to the end of the test is fit to describe the asymptotic and any tertiary permanent strain that occurs near failure, shown in Figure 6.14.

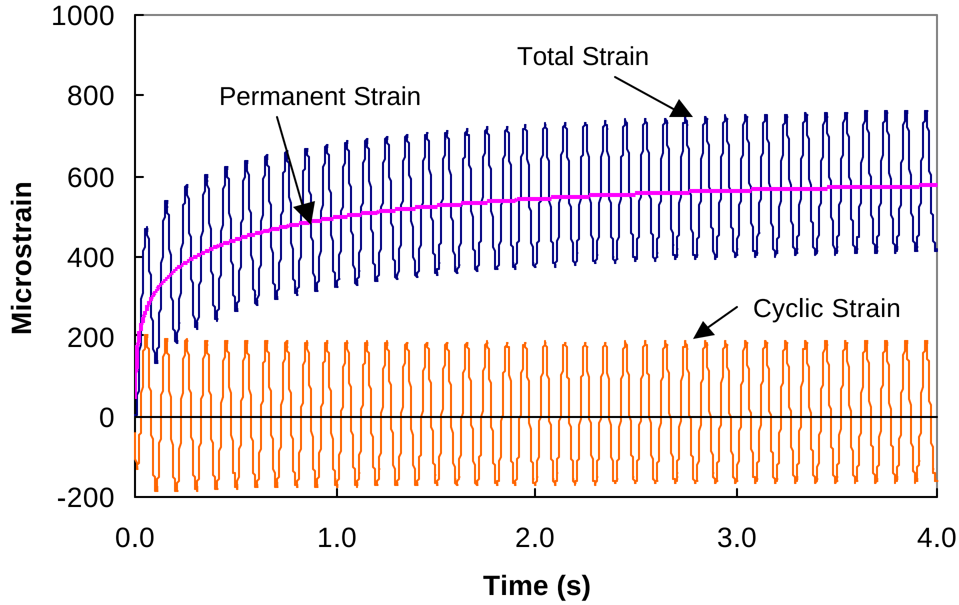

Figure 6.13 Total, Permanent, and Cyclic Strains

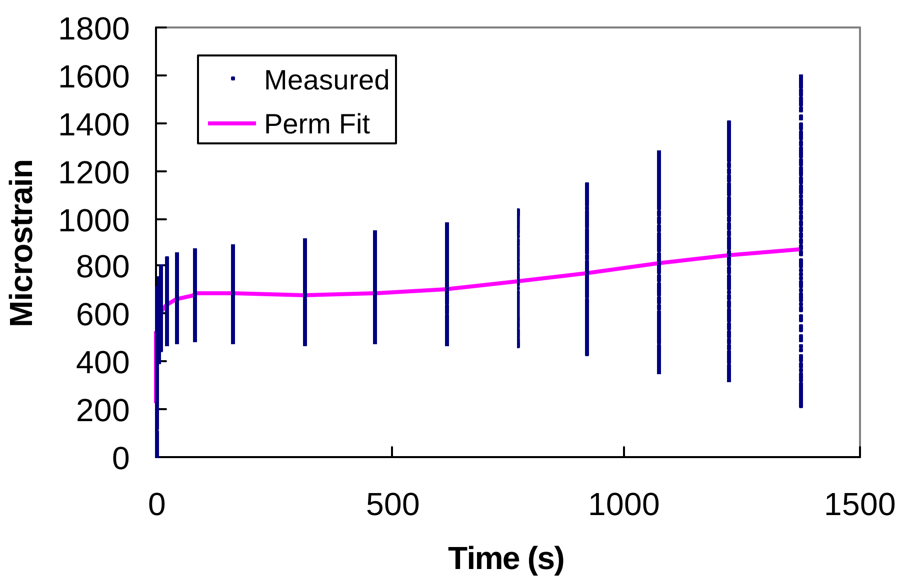

Figure 6.14 Entire Strain History for Cyclic Fatigue Test

For the second and third time ranges, the permanent strain is subtracted from the total strain to get the extracted cyclic strain, as shown in Figure 6.13. The cyclic strain for each group is then fit using the following equation:

$$\varepsilon = a_\varepsilon + b_\varepsilon \cos(\omega t + \theta_\varepsilon) \tag{6.11}$$

If the permanent strain is fit well, the coefficent "a" in Equation (6.11) will be a small number. The frequency, ω, is found by first fitting the stress data using:

$$\sigma = a_\sigma + b_\sigma \cos(\omega t + \theta_\sigma) \tag{6.12}$$

The phase angle is determined using:

$$\phi = \theta_\varepsilon - \theta_\sigma \tag{6.13}$$

and the stiffness for each group of cycles can be found by dividing the stress amplitude, b_σ, by the strain amplitude, b_ε.

The cyclic and permanent pseudo strains are calculated independently. Assuming steady state harmonic response, the cyclic pseudo strain is:

$$\varepsilon^R = b_\varepsilon |E^*| \cos(\omega t + \theta + \phi) \tag{6.14}$$

The coefficients from each group of cycles are used for this calculation.

A closed-form solution is difficult to obtain for the permanent strain, so the piece-wise linear approach described in the previous section is used. Additionally, the permanent pseudo strain calculation must be split into three integrals because of the three sets of coefficients used in fitting:

$$e^R = \frac{1}{E_R}\left[\int_0^{t_1} E(t-t)\frac{de_1}{dt}dt + \int_{t_1}^{t_2} E(t-t)\frac{de_2}{dt}dt + \int_{t_2}^{t} E(t-t)\frac{de_3}{dt}dt\right] \tag{6.15}$$

The first integral incorporates the first loading path. This ensures that the initial pseudo strain value is zero and that the first cycle of pseudo strain is calculated more accurately than if only one set of coefficients were used. The second integral uses the second set of fit coefficients and runs from time t_1 to t_2, the end of the second fit. The third integral is from time t_2 to the end of the test. It is important to remember that the t in the $E(t-\tau)$ term is the current time, so as an example, the value of pseudo strain at a time between t_1 and t_2 has a contribution from both the first and second integrals.

The calculation of the cyclic portion of the pseudo strain makes use of the steady-state assumption. For this assumption to be valid, the strain response must have remained constant (steady) for a long enough period of time such that the effect of any changing strain at early times has diminished. Also, the strain must have a single dominant frequency. To investigate whether a dominant frequency exists, a Fast Fourier Transform was performed on several data sets. A typical frequency spectrum is displayed in Figure 6.15 and shows that a strong dominant frequency of 10 Hz exists and there is little contribution from other frequencies in the strain history. The cyclic pseudo strain is also

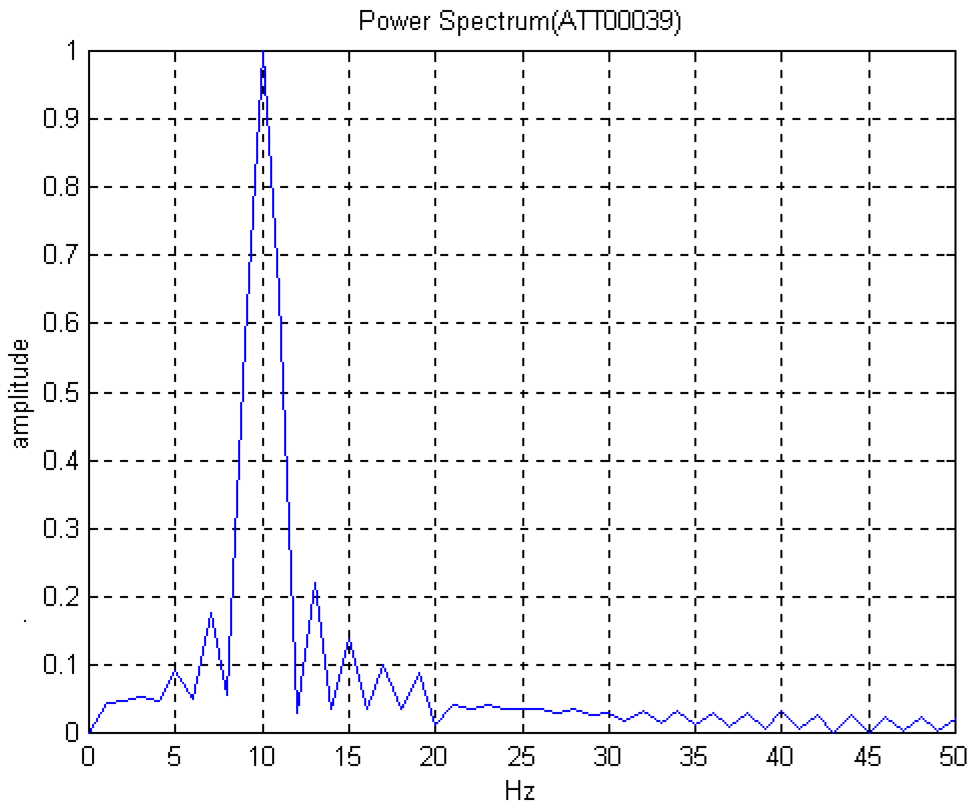

Figure 6.15 Power Spectrum from FFT Analysis of Cyclic Strain Data

calculated using the piece-wise linear approach and compared with that calculated using the steady state assumption in Figure 6.16. The piece-wise linear approach was performed for 20, 30, 40, and 50 segments per cycle. The resulting pseudo strains were the same regardless of the number of segments used in the analysis. For the two specimens analyzed in this manner, the steady state assumption underpredicts the pseudo strain by about 10%. This amount of error in the cyclic portion of the pseudo strain calculation does not result in a significant difference in the material functions C_1 and S_1, as shown in Figure 6.17. Therefore, to avoid the long computational time (several hours compared to several minutes) associated with the piece-wise linear calculation of the cyclic pseudo strain, the steady state assumption is used for this research.

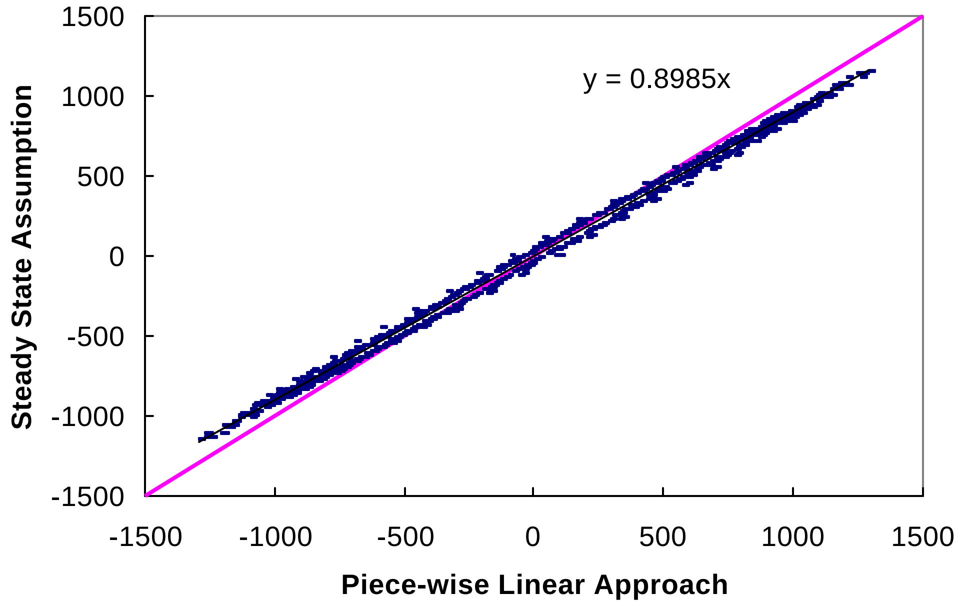

Figure 6.16 Comparison of Cyclic Pseudo strains Calculated Using Piece-Wise Linear Approach and Steady State Assumption

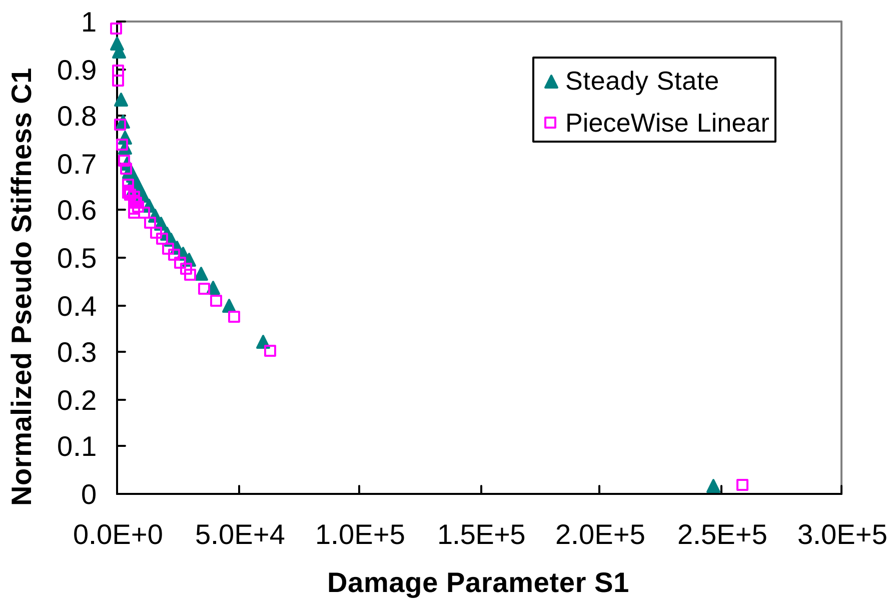

Figure 6.17 Difference in C_1-S_1 Curve Using Piece Wise Linear Approach and Steady State Assumption

6.3 Determination of Material Functions C_1 and S_1

Once the pseudo strain has been calculated for the entire time range of data, the pseudo stiffness can be determined. The pseudo stiffness is defined as the slope of a line drawn from the origin to a particular stress-pseudo strain coordinate and is illustrated in Figure 6.18. Pseudo stiffness is calculated by dividing stress by pseudo strain:

$$S^R = \frac{s}{e^R} \tag{6.16}$$

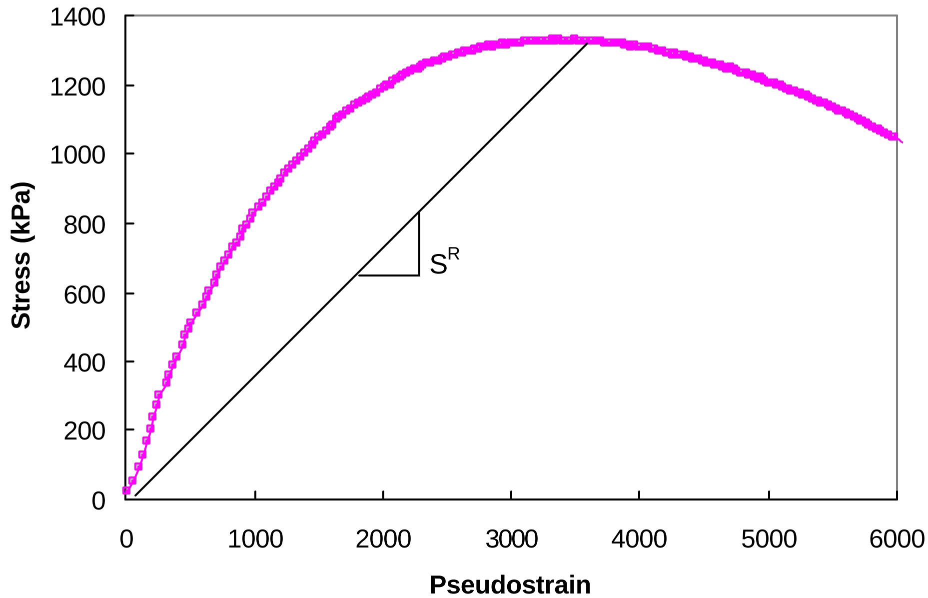

Figure 6.18 Definition of Pseudo stiffness

For the constant crosshead-rate testing, this definition is used for the entire loading history. In the case of cyclic testing, this definition is used for the first loading path. Each cycle thereafter, only the pseudo stiffness at peak pseudo strain is calculated:

$$S^R = \frac{s_{\max}}{e^R_{\max}} \tag{6.17}$$

where $\sigma_{\max}$ is the stress corresponding to the maximum pseudo strain in each cycle. Figure 6.19 shows the stress-pseudo strain curves of the initial portion of first loading path for two monotonic tests and two cyclic tests for the CLO mixture. The two monotonic tests were performed at different rates and the two cyclic tests at different strain amplitudes. A line of equality is also shown in the figure. As can be observed from this figure, all four of the tests follow the line of equality initially for some time before deviating. This reflects the initial portion of loading where the material response is still in the linear viscoelastic range. Going back to the definition of pseudo strain in Equation (3.7), if the material response is in the LVE range and a reference modulus (E_R) of 1.0 is used, the calculated pseudo strain should be equal to the stress, which is what is observed in Figure 6.19. As loading continues, damage is induced and the stress-pseudo strain curve deviates from the line of equality. The point at which the deviation occurs depends upon the loading rate applied; that is, at slower loading rates, the damage occurs at a lower stress level due to the rate dependent nature of the material. This was also experimentally observed by Lee (1996). It is important to note that the cyclic data shown is from the first loading path only, and thus some damage is induced even during the first cycle of loading, which is typical in controlled-displacement testing.

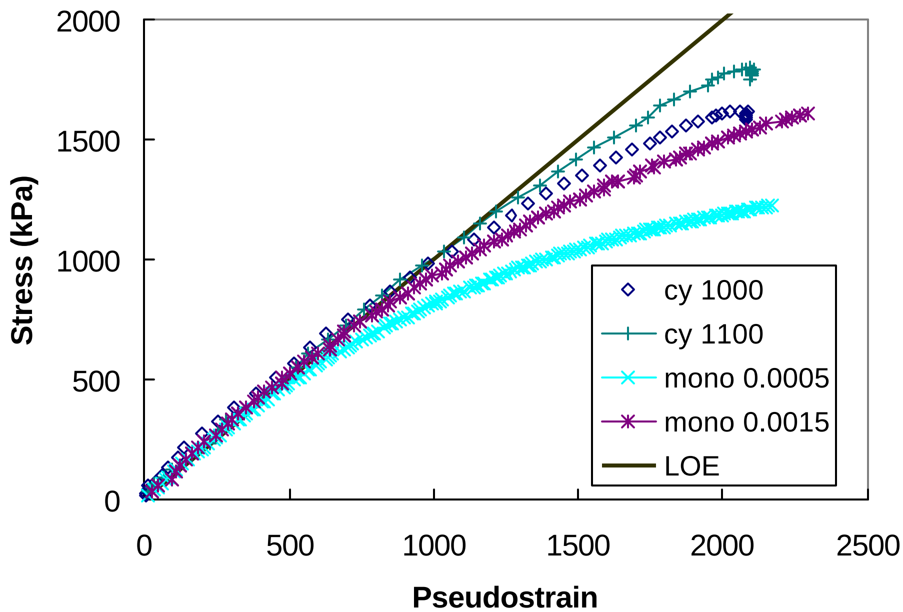

Figure 6.19 Initial Stress-Pseudo strain Curves for Cyclic and Monotonic Tests on CLO Mixture

A more careful observation of the initial loading shown in Figure 6.19 will reveal that the slope of the stress-pseudo strain curves do not follow the line of equality exactly. In fact, the actual slope can range between 0.95 and 1.05 due to sample-to-sample variability. To account for this inherent variability, Lee (1996) uses the following normalized form of pseudo stiffness, C_1, for the material characterization:

$$C_1 = \frac{S^R}{I} \tag{6.18}$$

where I is the initial slope of the stress-pseudo strain curve. Due to variability in the stress measurements, I is determined by performing a linear regression on the stress-pseudo strain data up to the point of deviation from the LOE, which in the case of the CLO mixture shown in Figure 6.19, is up to a pseudo strain value of about 500. Any specimen with an I value falling outside the 0.95-1.05 range should be reanalyzed for errors in the relaxation modulus or pseudo strain calculation.

Once the C_1 values are known, the values for the damage parameter, S_1, can be calculated using (recall that α=1+1/m, where m is the slope of the linear portion of the relaxation modulus on a log-log scale):

$$S_1(t) = \sum_{i=1}^{N}\left[\frac{I}{2}\left(e^R\right)^2\left(C_{i-1} - C_i\right)\right]^{\frac{a}{1+a}}\left(t_i - t_{i-1}\right)^{\frac{1}{1+a}} \tag{6.19}$$

For the monotonic testing, this equation can be used for the entire loading history because the damage grows continuously throughout the test. In the case of cyclic loading, damage can only accumulate during the tensile loading portion of each cycle. Hence, only the time associated with the tensile loading portion (approximately a quarter of the whole cycle time) should be included in the calculation of S_1. This observation reduces Equation (6.19) to:

$$S_1(t) = \sum_{i=1}^{N}\left[\frac{I}{2}\left(e^R\right)^2\left(C_{i-1} - C_i\right)\right]^{\frac{a}{1+a}}\left(\frac{t_i - t_{i-1}}{4}\right)^{\frac{1}{1+a}} \tag{6.20}$$

Also recall for cyclic loading that only the peak pseudo strain values are calculated, hence the calculated C_1 and S_1 values are associated with the peak pseudo strain only. This is because the hysteresis within each cycle is not needed to describe the damage accumulation over time, as reported by Lee et al. (2000). However, because damage does accumulate during the first loading path in cyclic tests, the material functions C_1 and S_1 must be calculated at various points along the initial loading path up to the peak ε^R value.

6.4 Characteristic Curve

Figures 6.20 and 6.21 show how the normalized pseudo stiffness, C_1, changes with time for cyclic tests at 10 Hz performed at various strain amplitudes for the FLO and CLO mixtures, respectively. There is a distinct difference in each curve due to the different applied strain amplitude. The higher the strain amplitude, the quicker the pseudo stiffness decreases as loading continues. Figures 6.22 and 6.23 show the accumulation of damage (S_1) for the same specimens shown in Figures 6.20 and 6.21. As can be seen in both mixtures, damage accumulates faster during the tests with greater strain amplitudes.

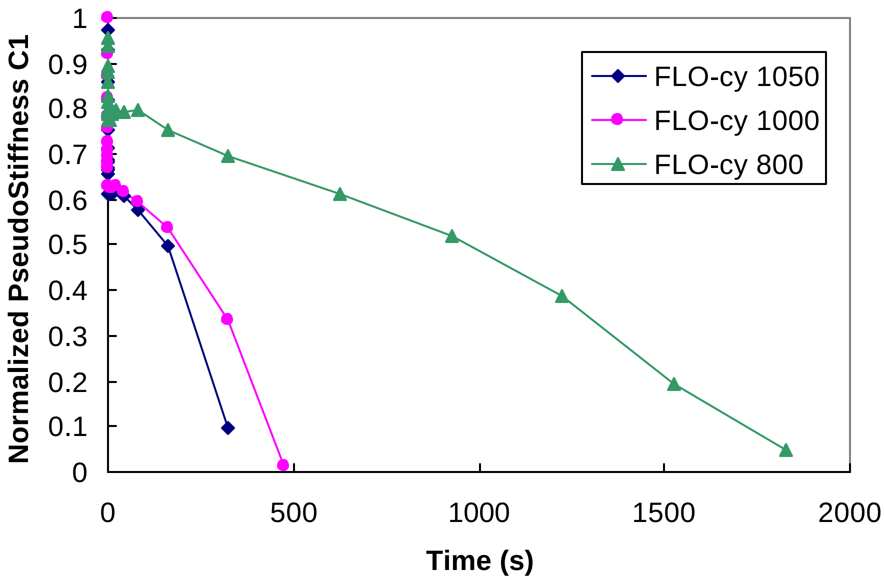

Figure 6.20 Normalized Pseudo stiffness as a Function of Time for FLO Mixture Tested at 10 Hz and Three Cyclic Strain Amplitudes

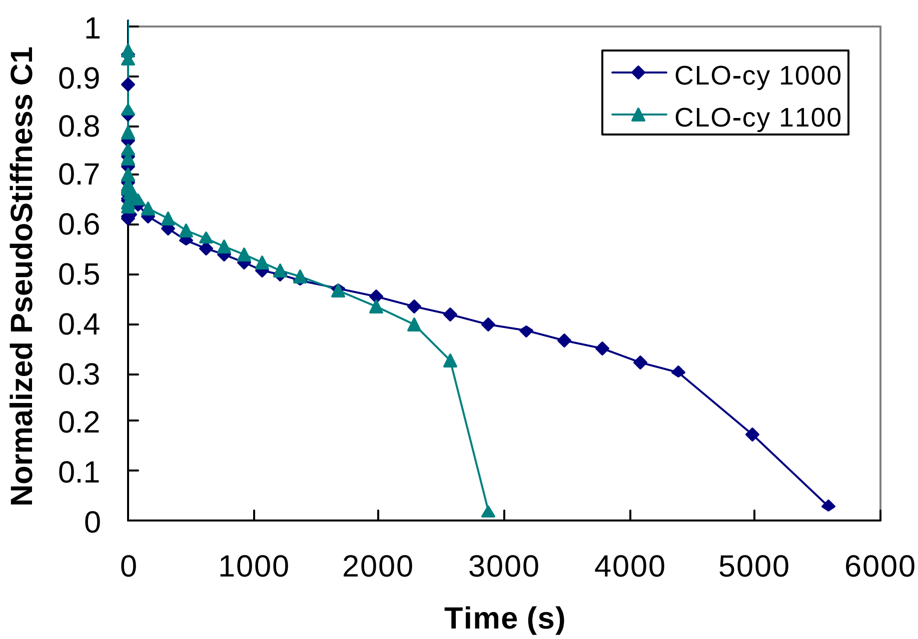

Figure 6.21 Normalized Pseudo stiffness as a Function of Time for CLO MixtureTested at Two 10 Hz Cyclic Strain Amplitudes

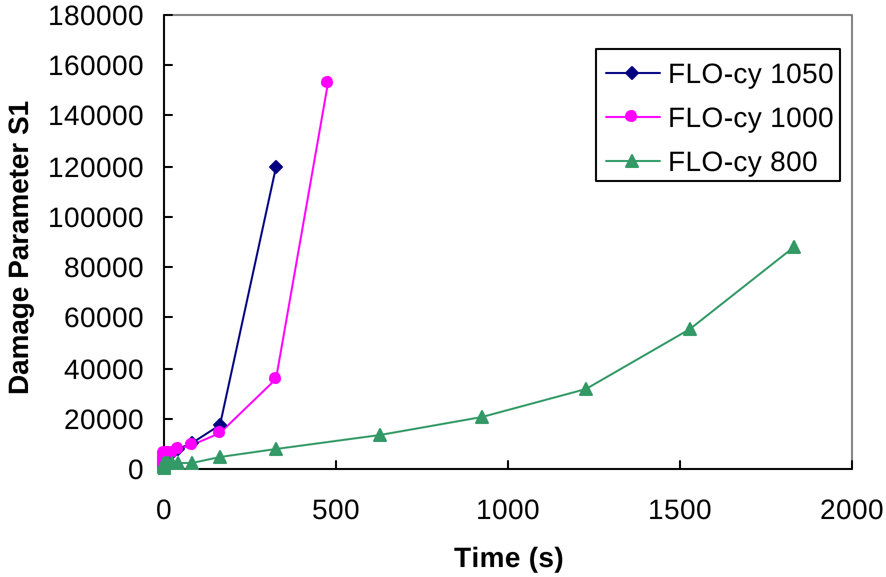

Figure 6.22 Damage Parameter as a Function of Time for FLO Mixture Tested at Three 10Hz Cyclic Strain Amplitudes

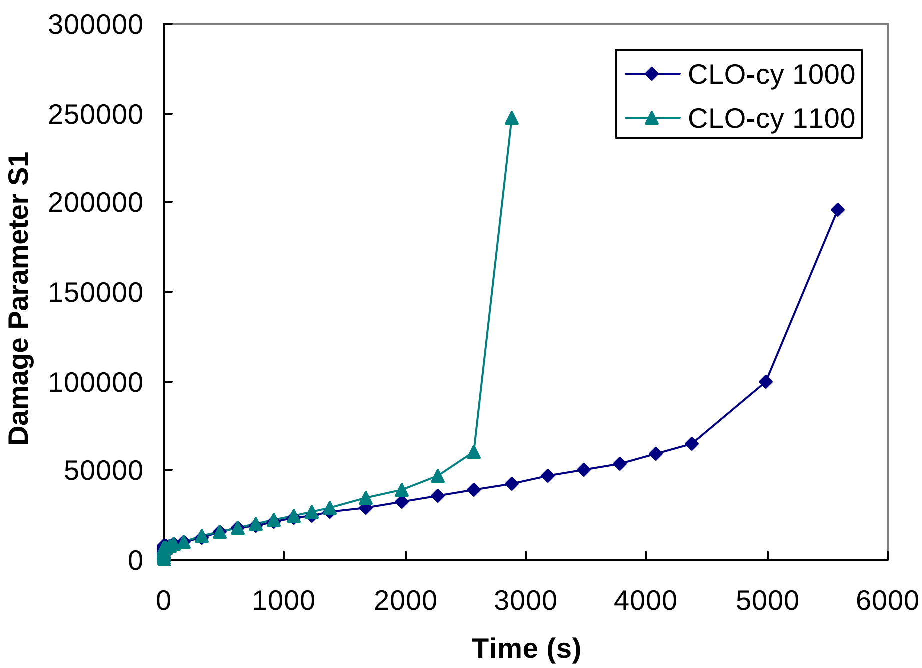

Figure 6.23 Damage Parameter as a Function of Time for CLO Mixture Tested at Two 10 Hz Cyclic Strain Amplitudes

The true power of the constitutive model developed by Lee and Kim (1998b) is demonstrated by cross-plotting the C_1 and S_1 values, as shown in Figures 6.24 and 6.25 for the same two mixtures. Now, the different strain amplitude data collapse to a single characteristic curve that describes the changing material integrity (C_1) as damage (S_1) accumulates in the specimen. This characteristic curve is developed for all of the mixtures tested in this study and the individual C_1 versus S_1 curves can be found in Appendix D.

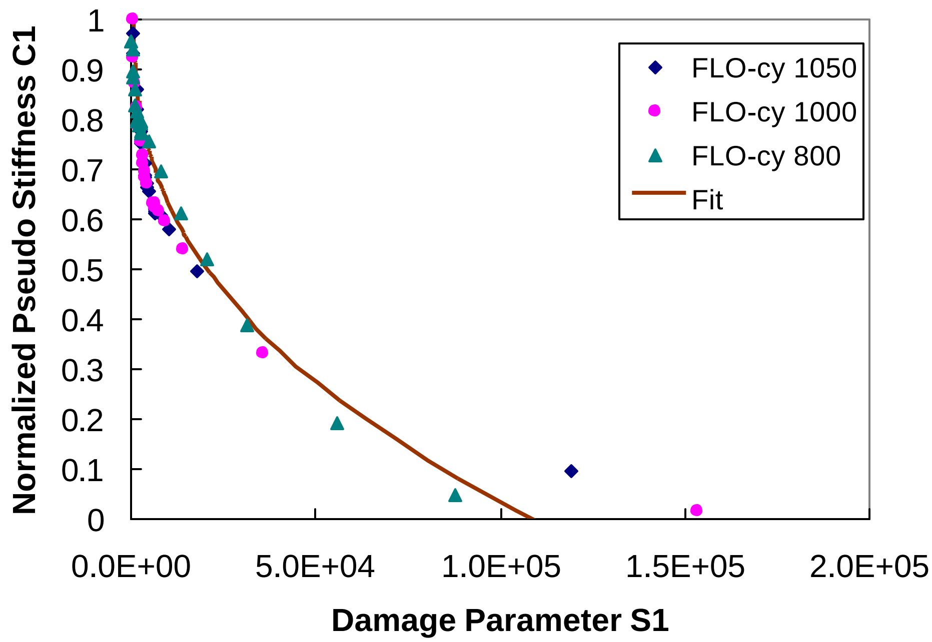

Figure 6.24 Characteristic C_1 versus S_1 Curve for FLO Mixture Tested at Three 10 Hz Cyclic Strain Amplitudes

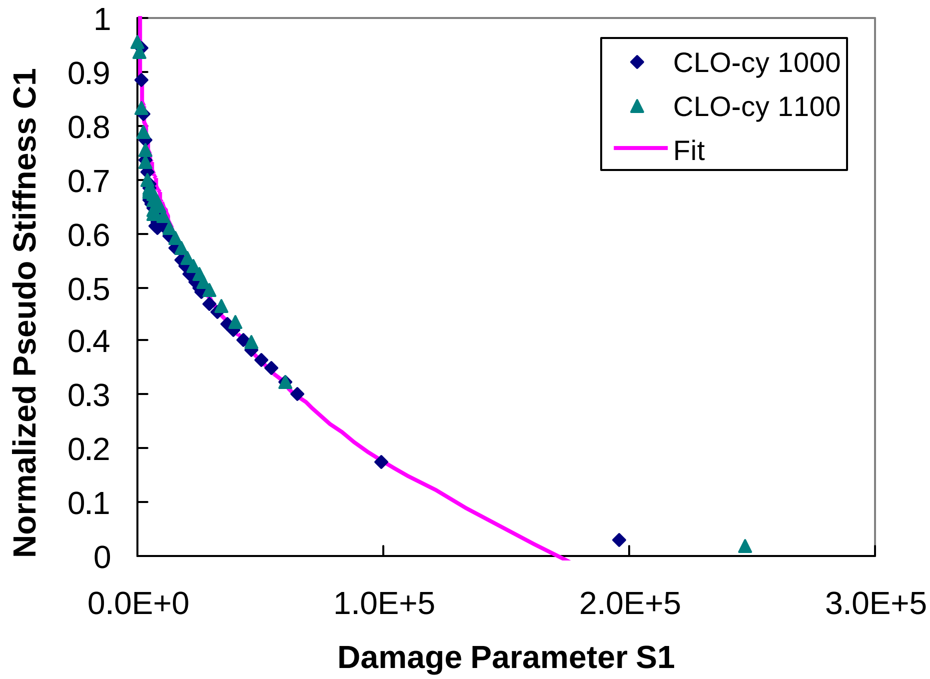

Figure 6.25 Characteristic C_1 versus S_1 Curve for CLO Mixture Tested at Two 10 Hz Cyclic Strain Amplitudes

A characteristic curve can also be developed for cyclic testing at different frequencies, constant crosshead-rate testing, and testing at different temperatures. Figure 6.26 shows the characteristic curve for cyclic testing at two strain amplitudes and 1 Hz for the FLO mixture. The monotonic curves for testing at two different strain rates at both 20°C and 5°C for the CMO mixture are shown in Figure 6.27. Finally, the characteristic curves from cyclic testing at different strain amplitudes at 10 Hz on the CML mixture at 20, 12, and 5°C are shown in Figure 6.28. In all cases, different strain amplitudes or rates collapse to form a single curve when C_1 and S_1 values are cross-plotted.

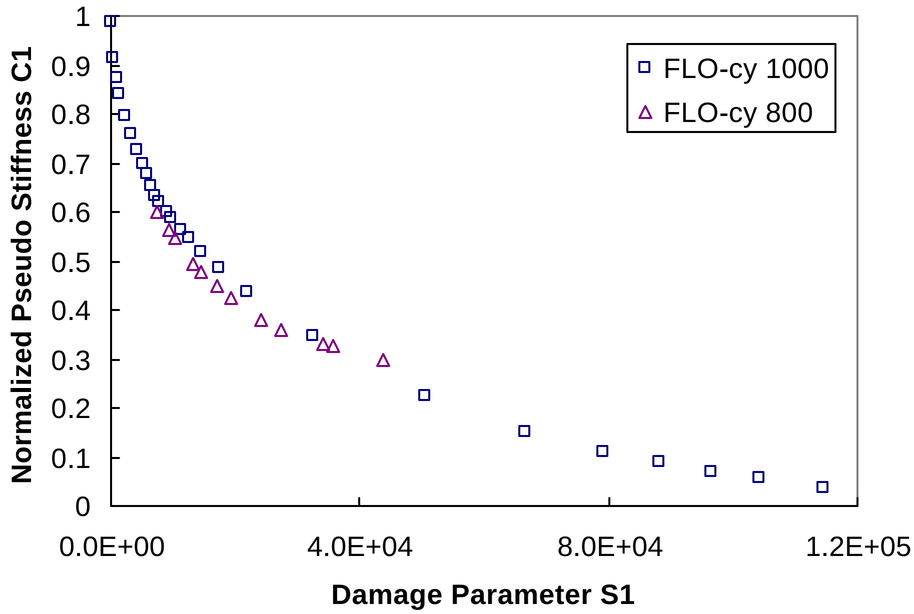

Figure 6.26 Characteristic C_1 versus S_1 Curve for 1 Hz Cyclic Testing on FLO Mixture at Two Strain Amplitudes

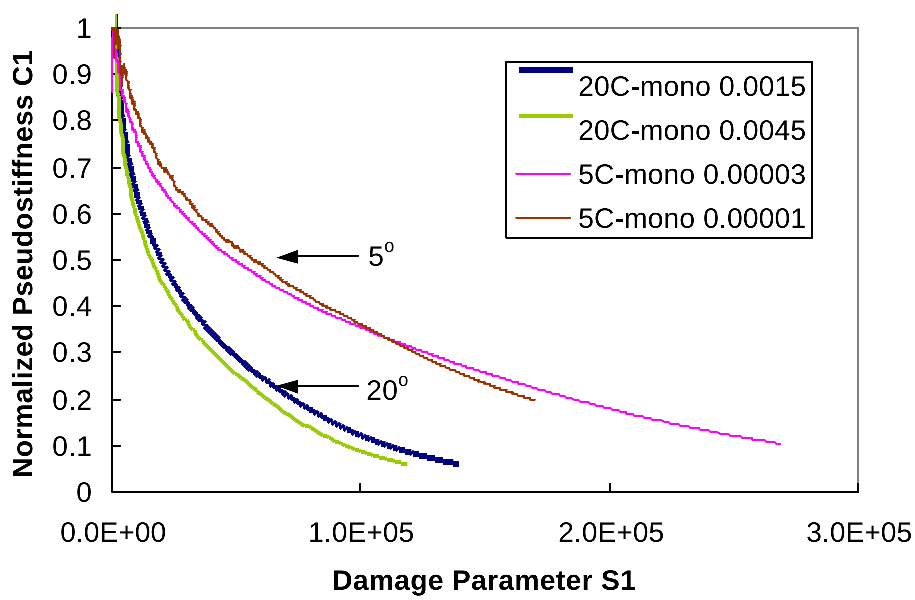

Figure 6.27 Characteristic C_1 versus S_1 Curves for Monotonic Testing at Two Rates and Temperatures on CMO Mixture

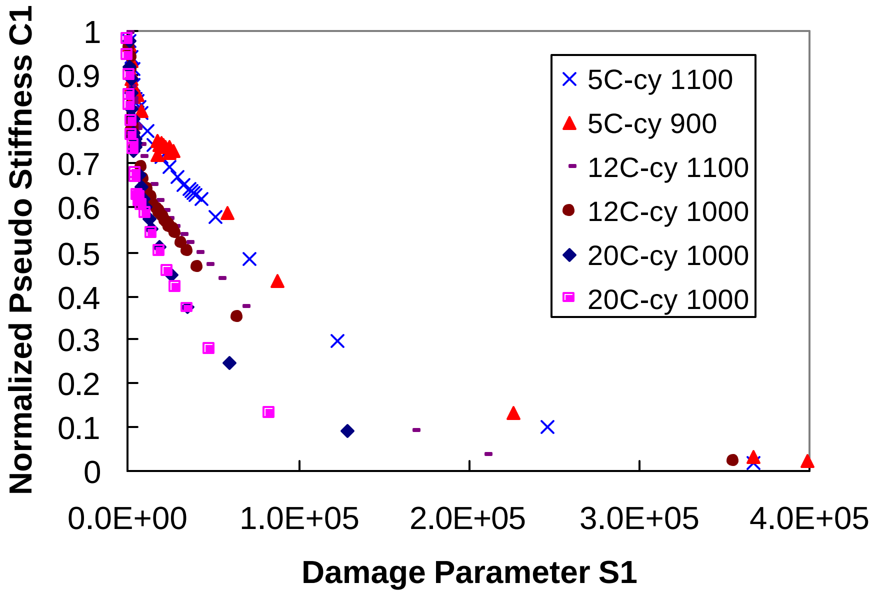

Figure 6.28 Characteristic C_1 versus S_1 Curves for Cyclic Testing at Two Strain Amplitudes and Three Temperatures on CML Mixture

Table 6.2 C_1-S_1 Coefficients for All Mixtures

Mixture [a]	C_{11}	C_{12}
FLO	0.00976	0.400
mFLO	0.00455	0.483
FML	0.00405	0.493
FMO	0.00560	0.463
mFMO	0.00265	0.552
FMH	0.00863	0.414
CLO	0.00830	0.402
mCLO	0.00618	0.435
CML	0.00672	0.438
CMO	0.01080	0.396
mCMO	0.01390	0.367
CMH	0.00714	0.429

[a] An ‘m’ preceeding the mixture name refers to the moisture exposed specimens

The functional form of $C_1(S_1)$ is:

$$C_1(S_1) = 1 - C_{11}(S_1)^{C_{12}} \tag{6.21}$$

where C_{11} and C_{12} are coefficients. The values of these coefficients are determined by fitting the functional form to the experimental data from several tests, as shown for the mixtures in Figures 6.24 and 6.25. The coefficients for each mixture are shown in Table 6.2. The data and actual fits for each mixture can be found in Appendix D.

The characteristic curves for the fine and coarse mixtures are shown in Figures 6.29 and 6.30, respectively. In both mixtures, the effect of air void content is very evident; the 4% air void specimens show a much slower degradation than the 8% air void specimens. This indicates that the damage grows faster in the specimens with higher air void content, as is expected. Neither gradation shows much of a difference with respect to asphalt content; the characteristic curves for the three asphalt contents are basically the same. The FMH mixture shows a different curve because of the difference in air void content (5.5% versus 8% for the FMO and FML mixtures). Figure 6.31 illustrates the difference between the two gradations. For both air void levels, the characteristic curve for the coarse mixture falls above that for the corresponding fine mixture, indicating that the coarse mixture is more resistant to continuous fatigue damage in direct tension. However, the field performance on the track showed that the fine mixtures performed better than the coarse mixtures.

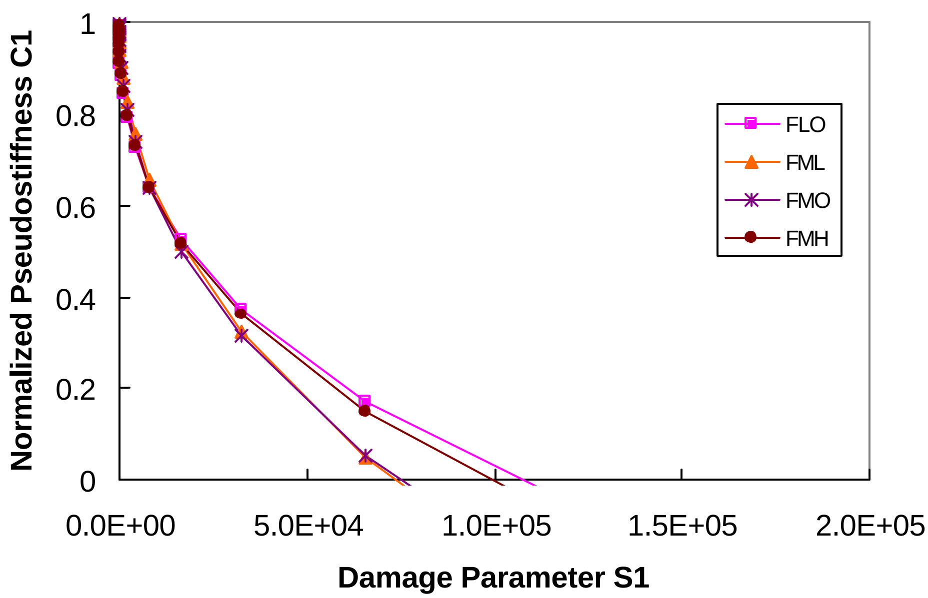

Figure 6.29 Characteristic C_1 versus S_1 Curves for Fine Mixtures

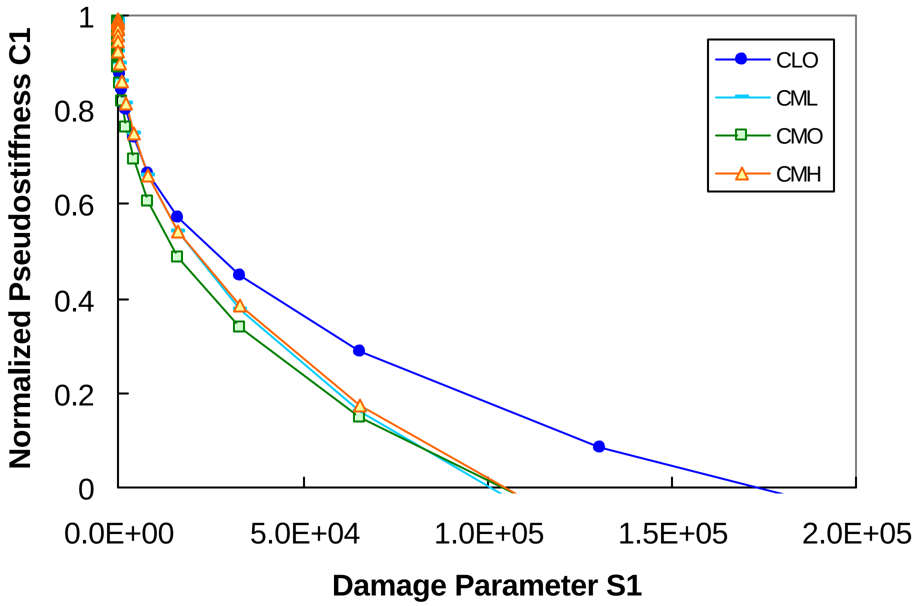

Figure 6.30 Characteristic C_1 versus S_1 Curves for Coarse Mixtures

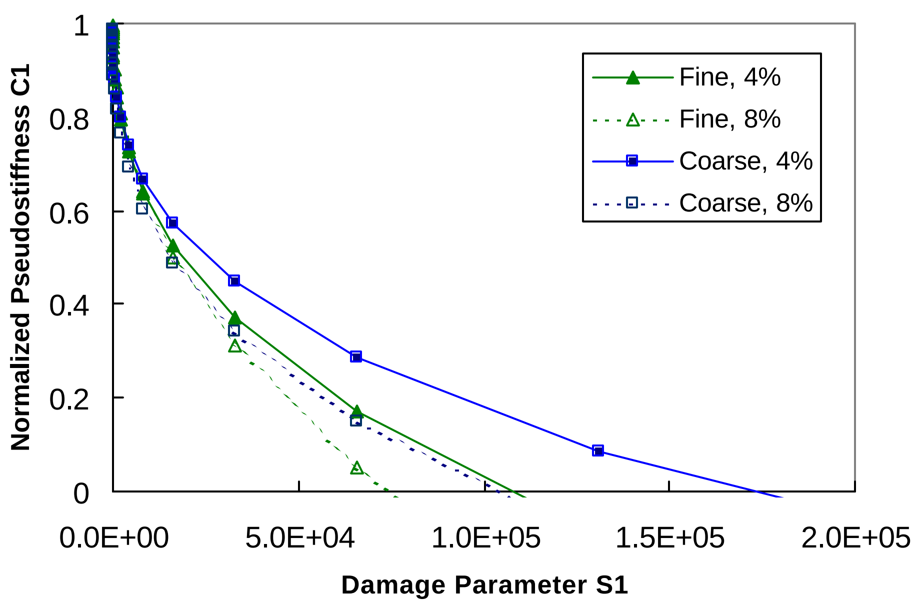

Figure 6.31 Comparison of Characteristic C_1 versus S_1 Curves for Coarse and Fine Gradations

6.5 Definition of Failure

In both the monotonic and cyclic testing it is important to define the point at which failure occurs for performance comparisons. In the previous testing by Lee (1996), failure was defined as a 50% reduction in initial pseudo stiffness, which corresponds to C_1=0.5. Initial testing in this research showed that C_1=0.5 was an unnecessarily conservative value based upon visual observations during the testing; hence, a new failure criterion was investigated.

To determine the failure criterion, an examination of the stiffness, C_1, LVDT strain amplitude, and phase angle over the duration of cyclic loading was made. Figures 6.32 and 6.33 show the four parameters as a function of time for specimen CLO7; the trends are similar for all of the specimens. Both the stiffness (stress amplitude divided by strain amplitude) and C_1 have an S-shaped decrease over time with a sharp drop-off around failure. The LVDT strain amplitude increases steadily until a sharp increase occurs around failure. Directly observing these three parameters, one can identify the range of time in which failure occurs, but it is difficult to quantify the change in slope that would indicate failure for computer programming or automation purposes. The phase angle, on the other hand, increases up to failure, after which point it decreases. The change in the sign of the slope (from positive to negative) makes the phase angle an ideal indicator of failure; that is, when the slope of the phase angle versus time curve changes from positive to negative, failure has occurred.

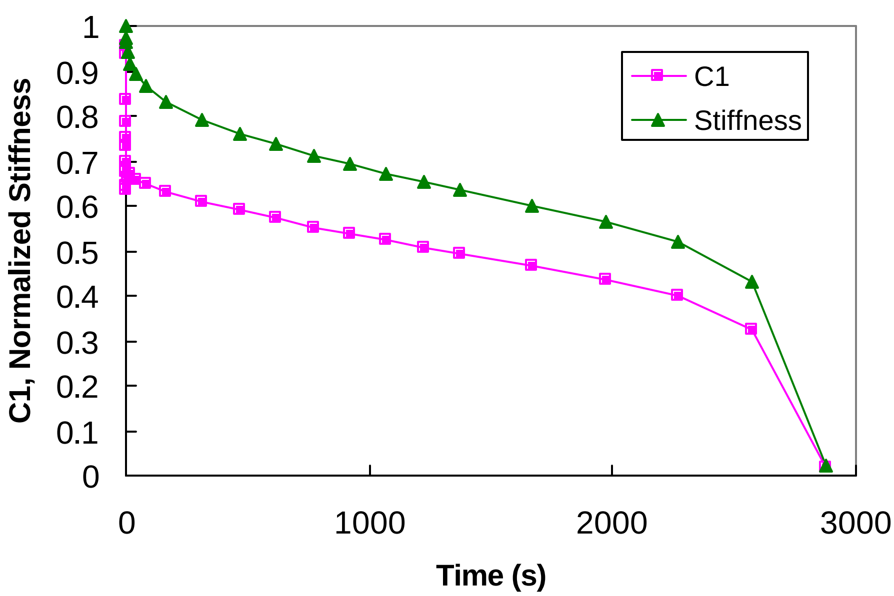

Figure 6.32 Normalized Stiffness and C_1 as a Function of Time for Specimen CLO7

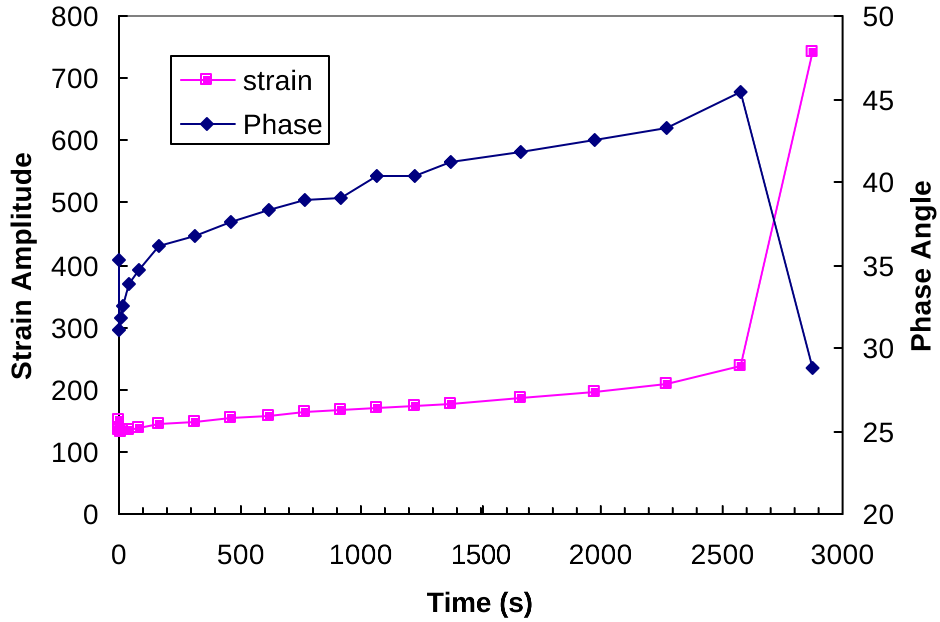

Figure 6.33 Phase Angle and On-Specimen LVDT Microstrain Amplitude as a Function of Time for Specimen CLO7

There is some difficulty in applying this methodology to the testing in this research because only snapshots of data were collected during the course of a fatigue test. Although an exact failure point cannot be reasonably determined from the acquired data, a range of time (and hence a range of C_1 values) within which failure occurred can be found. For CLO7, failure could have occurred anywhere between 2,300 and 2,700 seconds, which corresponds to a C_1 range of 0.4-0.18. A study of all available specimens showed that the average range over which failure could have occurred was between C_1 values of 0.42 and 0.15, with the midpoint of this range being 0.29.

A reasonable failure criterion must be applicable to both cyclic and monotonic testing. Failure of a specimen tested in monotonic loading can be defined at the time when localization of the microcracks occurs. Using the strain data from both the on-specimen and plate-to-plate LVDT measurements, localization can be identified as the point at which the two stress-strain curves separate, as shown in Figure 6.34. Up until the point of localization, the whole specimen is deforming such that the strains measured over the two different gage lengths are equal. Once the microcracks coalesce to form a macrocrack, the deformation is localized to a particular area and therefore the two different gage lengths produce different strain measurements (i.e., the same deformation is divided by two different gage lengths). Upon examining the available monotonic data, the average C_1 value at which localization takes place is 0.31.

Based on the study of failure for both the monotonic and cyclic testing, a failure criteria of C_1=0.3 was chosen for use in the remainder of this study.

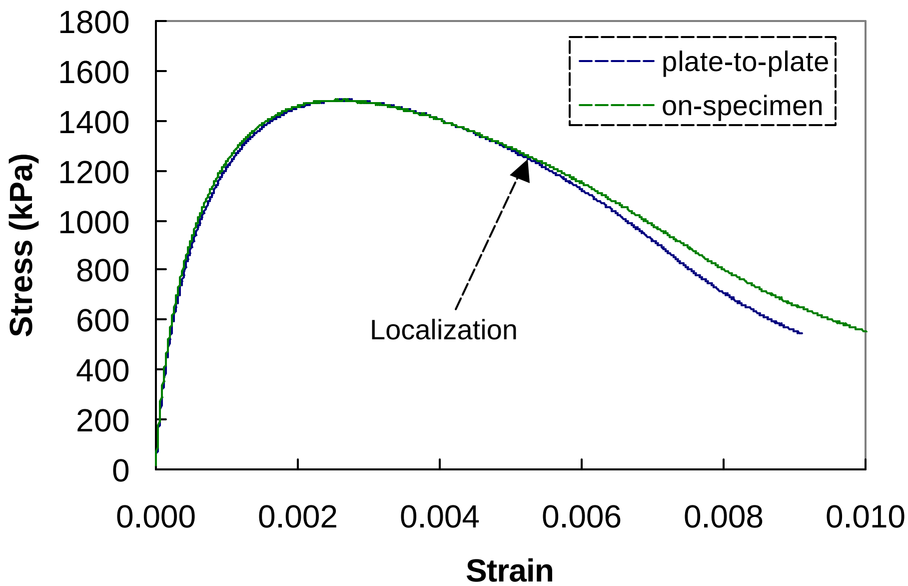

Figure 6.34 Point of Localization in a Constant Crosshead Rate Test

6.6 Effect of Moisture on Fatigue Behavior

The specimens subject to moisture show lower dynamic modulus values. The dynamic modulus of the 4% air void content specimens show a greater decrease than the 8% air void specimens. This could be a result of damage induced in the low air void specimens during the vacuum saturation process. The 4% air void specimens have a more discontinuous pore structure than the 8% air void specimens and hence the forced saturation may induce damage in the 4% specimens and not have as much effect on the 8% air void specimens. The effect of moisture on the fatigue life, or characteristic curve for the four mixtures is shown in Figure 6.35. The specimens subject to moisture are less fatigue resistant that those tested dry, with the exception of the CMO mixture, which shows similar performance. The CMO mixture showed the least amount of reduction in dynamic modulus as well.

To quantify the effect of moisture, the values of the damage parameter at failure, S_{1f}, are compared in Table 6.3. The ratio of the moist to dry S_{1f} value is calculated and shown in the table along with the available tensile strength ratios (TSR) reported in the WesTrack database (2000). The tensile strength ratios were performed on laboratory mixed and compacted specimens and are only available for the FMO and CMO mixtures.

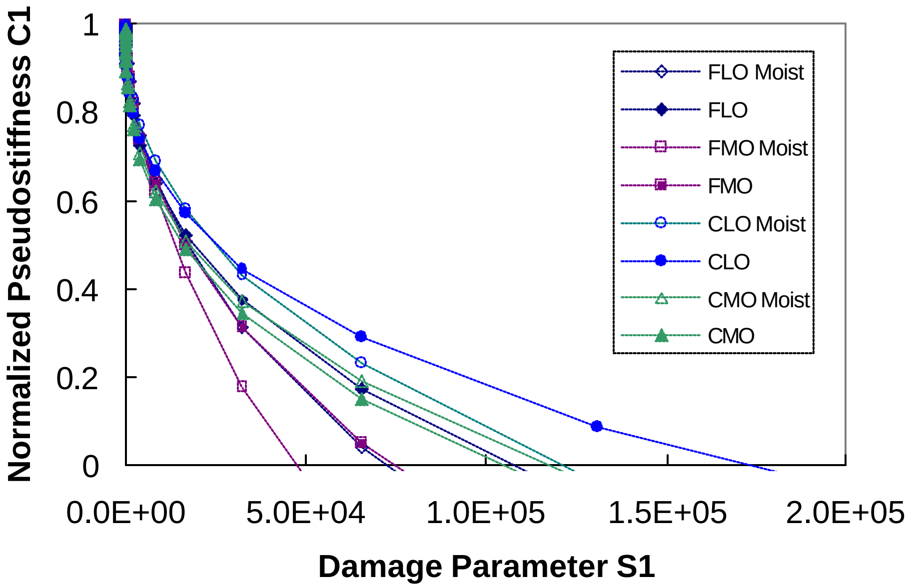

Figure 6.35 Effect of Moisture on Characteristic C_1 versus S_1 Curves

Table 6.3 Comparison of S_{1f} Values from Moist and Dry Specimens

Mixture	Moist S_{1f}	Dry S_{1f}	S_{1f} Ratio	TSR
FLO	34,062	42,955	0.79	N/A
FMO	24,413	34,009	0.72	0.81
CLO	52,699	62,655	0.84	N/A
CMO	43,631	38,405	1.13	0.89

The coarse mixture has higher ratios for both the S_{1f} comparison and the TSR. The CMO mixture has a ratio greater than 1.0 for the S_{1f} comparison, indicating that the moisture exposure did not affect the fatigue behavior, which is what was visually observed from the characteristic curve and from the dynamic modulus values.

6.7 Effect of Healing on Fatigue Behavior

The effect of rest periods is to extend the fatigue life of the asphalt concrete; this phenomenon has been measured in the laboratory (Sias 1996, Lee 1996) as well as in the field (Y. Kim 1997, Kim and Kim 1997, Katzke 1997). Time, material, and resource limitations prevented an in-depth study of the healing properties of the WesTrack mixtures. However, a comparison of the fatigue life with and without rest periods at particular strain amplitudes was performed and is shown in Table 6.4.

Immediately noticeable is the number of healing tests that failed before the continuous test at the same strain amplitude. The likely reason for this is the large sample-to-sample variability that existed due to the specimen fabrication and compaction procedure. This is very evident when looking at the differences in the fatigue lives of the few replicate continuous tests that were performed. There were not any replicate tests performed for the fine mixture; however, the dynamic modulus data showed that the fine mixture appears to have more variability than the coarse mixture.

Keeping the inherent variability in mind, some general trends can still be observed from the available data. Overall, the 4% air void mixtures have larger increase in the fatigue life than those with 8% air voids and the mixtures with higher asphalt content also show a greater increase in fatigue life. It also appears that the fine mixture shows greater increases in N_f than the coarse mixture.

Table 6.4 Summary of Fatigue Lives with and without Rest Periods

Mixture	**Ram Amplitude (microstrain)**	**N_f without Rest Periods** [a]	**N_f with Rest Periods**	**% increase in N_f** [b]
FLO	1,000	3,400	1,150	-
FLO	800	13,700	71,200	419
FML	600	35,800	21,000	-
FMO	960	2,460	5,200	111
FMO	860	11,000	600	-
FMH	800	23,200	15,000	-
FMH	1,000	2,450	7,200	194
CLO	1,100	26,000	16,200	-
CLO	1,000	44,000	63,200	44
CML	1,000	5,520 10,300	9,700	76 -
CMO	1,000	8,400 13,400	9,200	9.5 -
CMH	1,000	8,350 9,600	19,200	130 100

[a] More than one value in this column indicates replicate tests.
[b] A dash indicates that the healing test has a lower N_f than the continuous test.

6.8 Prediction Methodology

In Section 6.4, the characteristic curves for various frequency cyclic testing, monotonic testing, and testing at different temperatures were found. A methodology is presented in this section by which the material response from a particular test condition (type of loading and temperature) can be used to predict the material response at any other desired condition. The obvious advantage to the existence of such a methodology is that the materials and time required for a broad range of testing results is greatly reduced. The basis of this methodology is in the characteristic curve. First, the effect of different frequencies in cyclic testing will be examined followed by the addition of constant crosshead rate testing and finally the effect of temperature will be included.

6.8.1 Cyclic Testing at Different Frequencies

The ability of any prediction scheme to account for different loading frequencies is important because loading frequency is associated with traffic speed on the pavement in the field. A method that can account for frequency will enable predictions of any imaginable traffic speed condition; from high speed interstates to slow moving loads along secondary roads or toll areas along highways.

Recall from Section 6.4 that testing was performed on the FLO mixture at frequencies of 10 Hz and 1 Hz. Figure 6.36 shows the characteristic curves for two specimens tested at 10 Hz and two specimens tested at 1 Hz. All four of the curves overlap, indicating that a single C_1 versus S_1 relationship can describe the cyclic fatigue behavior of a particular mixture at any frequency and any strain amplitude.

6.8.2 Cyclic and Constant Crosshead Rate Testing

It is not difficult to extend the overlap of different cyclic frequencies to monotonic testing. A constant crosshead rate test can be thought of as a slow cyclic test where failure happens to occur during the first loading path. Therefore, the characteristic curve from a monotonic test should overlap that from a cyclic test. Figures 6.37-6.39 show that this is indeed the case for the CLO, CMO, and CML mixtures. An overlap between the two test methods is shown for two different temperatures for the CML mixture.

Knowing that a single characteristic curve exists at a particular temperature for any direct tension loading history, the material response at a desired test condition can be predicted from the response of a known condition. Due to the limited number of actual tests performed for each mixture, a traditional statistical analysis is not possible. However, the errors between the measured and predicted values for the existing tests can give a feel for the variablilty associated with this prediction methodology.

The procedure for predicting the response is most straightforward in cases where the strain history is known. This applies for controlled-strain testing or if the prediction is being done from a test in which the strain history was measured, as is the case for this research. From the strain history and relaxation modulus, the pseudo strains can be calculated for the entire history. With the pseudo strain and functional form of the charactreristic curve in the following, the stress response can be predicted:

$$s\,(t) = C_1(S_1)e^R(t) \tag{6.22}$$

$$C_1(S_1) = 1 - C_{11}(S_1)^{C_{12}} \tag{6.23}$$

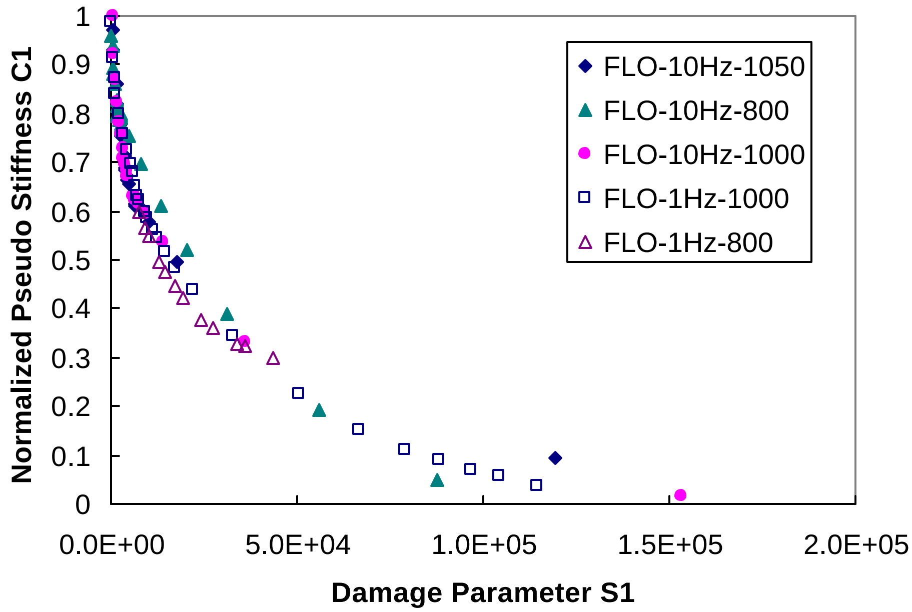

Figure 6.36 Characteristic C_1 versus S_1 Curve for 10 Hz and 1 Hz Cyclic Testing at 20°C on FLO Mixture at Several Strain Amplitudes

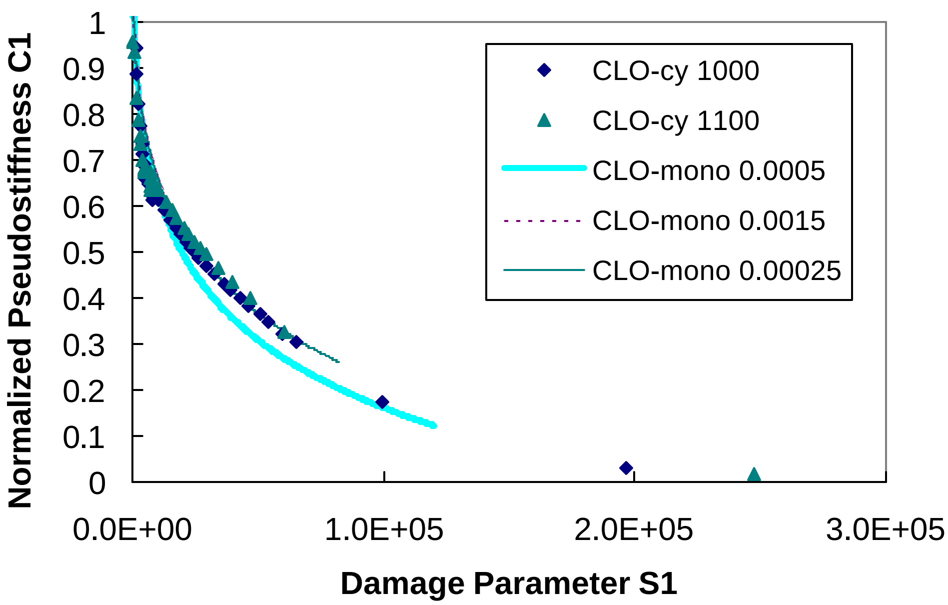

Figure 6.37 Characteristic C_1 versus S_1 Curve for Cyclic and Monotonic Testing on CLO Mixture at 20°C

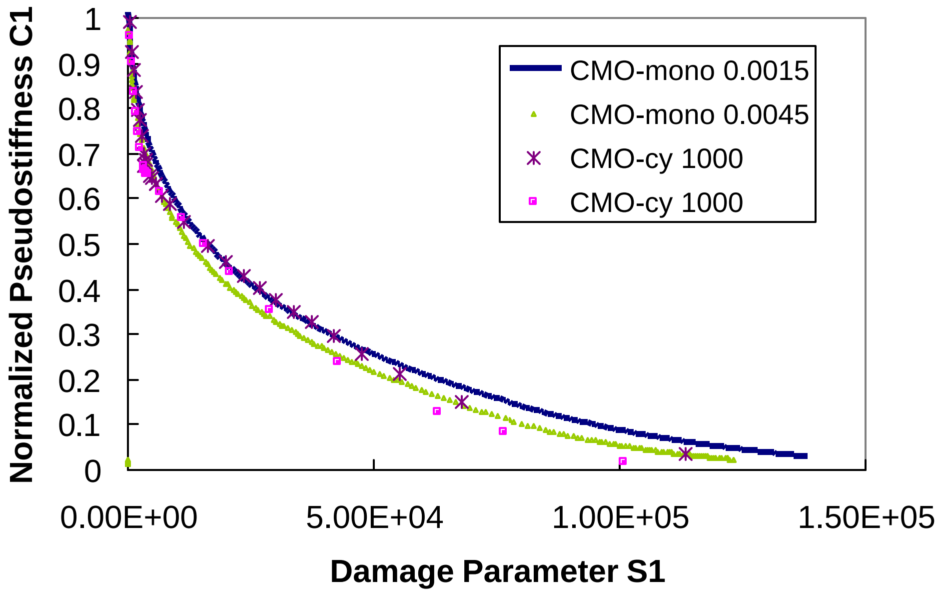

Figure 6.38 Characteristic C_1 versus S_1 Curve for Cyclic and Monotonic Testing on CMO Mixture at 20°C

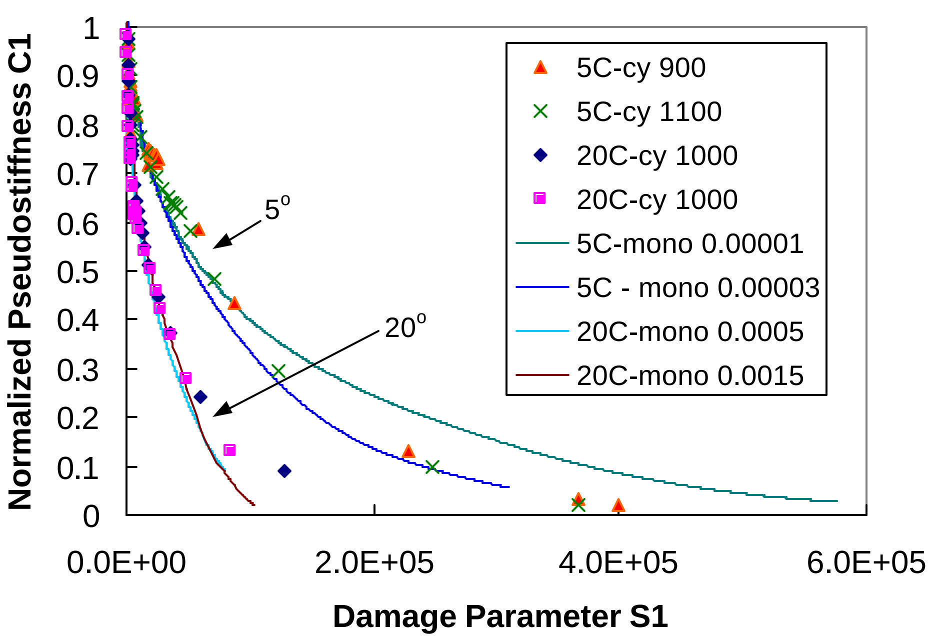

Figure 6.39 Characteristic C_1 versus S_1 Curves for Cyclic and Monotonic Testing on CML Mixture at Two Temperatures

As can be seen, the value of the damage parameter at each time during the test must be known to predict the stress. To calculate the damage parameter, the normalized pseudo stiffness is needed, which in turn requires the value of stress. Therefore, the stress to be predicted appears in both sides of Equation (6.22). In this research, an error minimization technique is used to calculate the predicted stress because of the difficulty associated with separating stress from the damage parameter. A series of stress values are assumed and the value right hand side of Equation (6.22) is calculated for each of these values and the value that gives the smallest error between the right and left hand sides is the final predicted value. The exact value can be found if the stress increment between successive guesses is small enough although computational time can become an issue and an appropriate balance between the two must be achieved for a particular application.

To evaluate the accuracy of the predictions with respect to measured data, it is helpful to choose a single parameter from which the percent error can be calculated. For the constant crosshead rate tests, the peak stress is chosen and the number of cycles to failure is used for the cyclic testing. Several types of predictions are made: using the C_1-S_1 curve from all available data (includes both monotonic and cyclic), using the curve from a single test, and using the curve from just one type of testing (cyclic or monotonic). Prediction from the overall curve is made for each specimen and the other predictions are made in some cases to show the worst-case scenario for the existing data. Tables 6.5 and 6.6 summarize the measured and predicted values for the peak stresses and number of cycles to failure, respectively from the overall C versus S curve. The percent errors calculated with respect to the measured values are shown in these tables as well. These tables also show the predictions from a single C versus S curve for the CMO and CLO mixtures to demonstrate the possible (or worst case for these mixtures) errors.

The errors between the measured and predicted peak stress values are less than 20%, with the exception of one of the CML test specimens (CML11). Figures 6.40 and 6.41 show the measured and predicted stresses for two monotonic tests. These figures show the best and worst cases for the mixtures tested and all other predictions are shown in Appendix D. No replicate monotonic tests at the same rate exist for any of the mixtures, so the prediction error cannot be compared with expected sample-to-sample variability. For the cyclic tests, errors are less than 10% between predicted and measured values. Figures 6.42 and 6.43 show the measured and predicted peak stress values for two specimens. With the CMO, CML, and CMH mixtures, replicate tests were performed at the same strain amplitude; the two CMO mixture specimens failed in 8,400 and 13,400 cycles, the two CML specimens failed in 5,520 and 10,300 cycles and the two CMH specimens failed in 8,350 and 9,600 cycles. The sample-to-sample variability for these two mixtures (based on the two replicate tests) is anywhere between 10% and 80% depending upon which test is used as the reference value. In the case of the cyclic testing, the existing data show that the sample-to-sample variability can be greater than the errors associated with the predictions using the characteristic curve from a single specimen, tested either in cyclic or monotonic mode.

Table 6.5 Measured and Predicted Peak Stress Values for Monotonic Tests

Specimen	Peak Stress (kPa)	Peak Stress from overall C-S curve (% error)	Peak Stress from designated curve (% error)
CMO8	1,675	1,714 (2.3%)	1,584[a] (-5.4%)
CMO3	1,482	1,328 (-10.4%)	1,228[a] (-17.1%)
CLO10	1,331	1,565 (17.5%)	1,539[b] (15.6%)
CLO14	1,264	1,351 (5.8%)	1,340[b] (5.0%)
CML10	1,783	1,777 (-0.3%)	-
CML9	1,253	1,380 (10.0%)	-
CML11	1,676	2,222 (32%)	-
CML12	1,684	1,552 (-7.8%)	-

[a] Predicted from cyclic CMO4 curve
[b] Predicted from overall cyclic curve

Table 6.6 Measured and Predicted Number of Cycles to Failure for Cyclic Tests

Specimen	N_f	N_f from overall C-S curve (% error)	N_f from designated curve (% error)
CMO4	8,400	8,650 (3.0%)	9,000[a] (7.1%)
CMO5	13,400	12,300 (-8.2%)	13,200[a] (-1.5%)
CLO6	44,000	42,000 (-4.5%)	25,820[b] (-0.7%)
CLO7	26,000	25,800 (-0.8%)	42,500[b] (-3.4%)
CML1	5,520	5,000 (-9.4%)	-
CML5	10,300	9,900 (-3.9%)	-
CML7	164,000	163,500 (-0.3%)	-
CML8	20,600	21,400 (3.9%)	-

[a] Predicted from CMO3 monotonic test
[b] Predicted from all cyclic tests

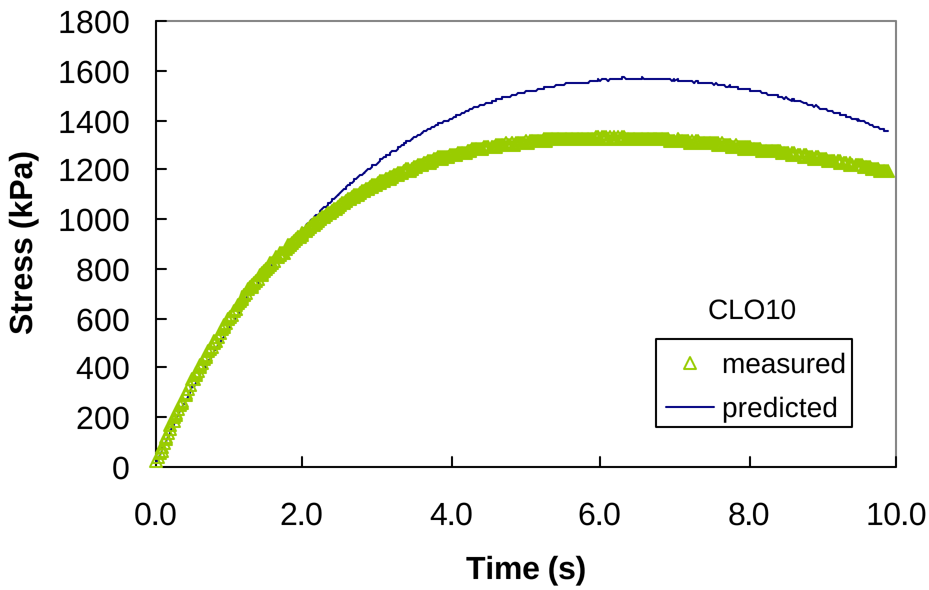

Figure 6.40 Measured and Predicted Stress Values for CLO10 Monotonic Test

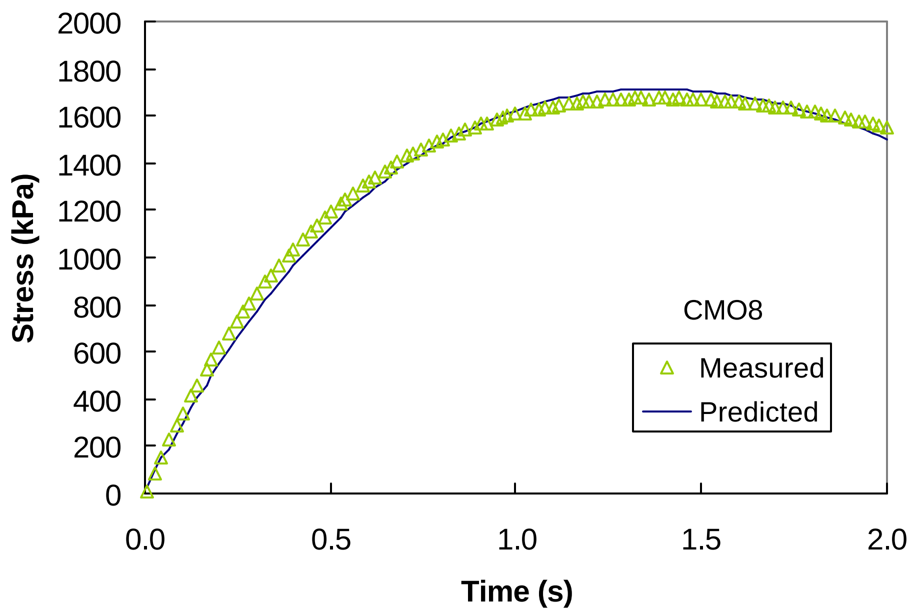

Figure 6.41 Measured and Predicted Stress Values for CMO8 Monotonic Test

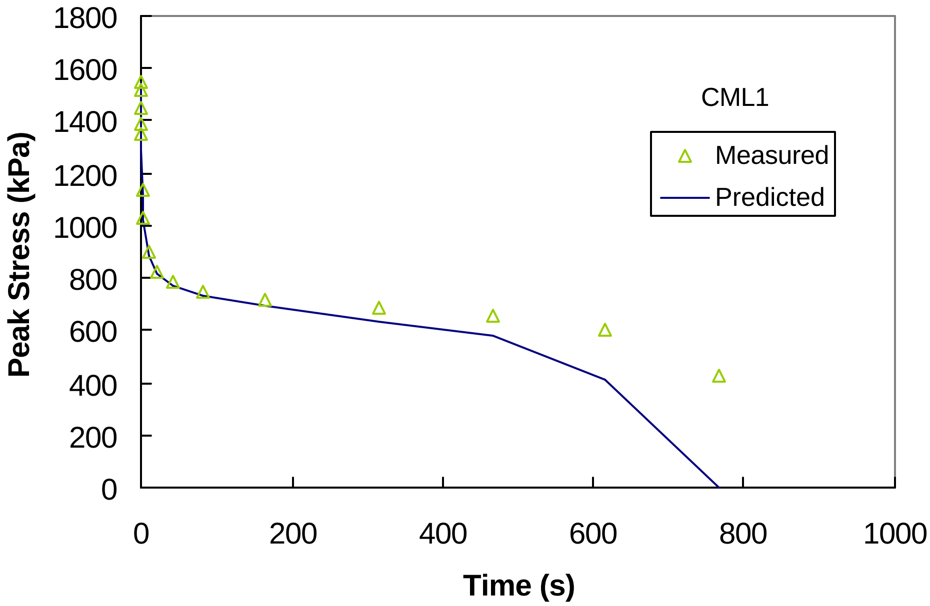

Figure 6.42 Measured and Predicted Stress Values for CML1 Cyclic Test

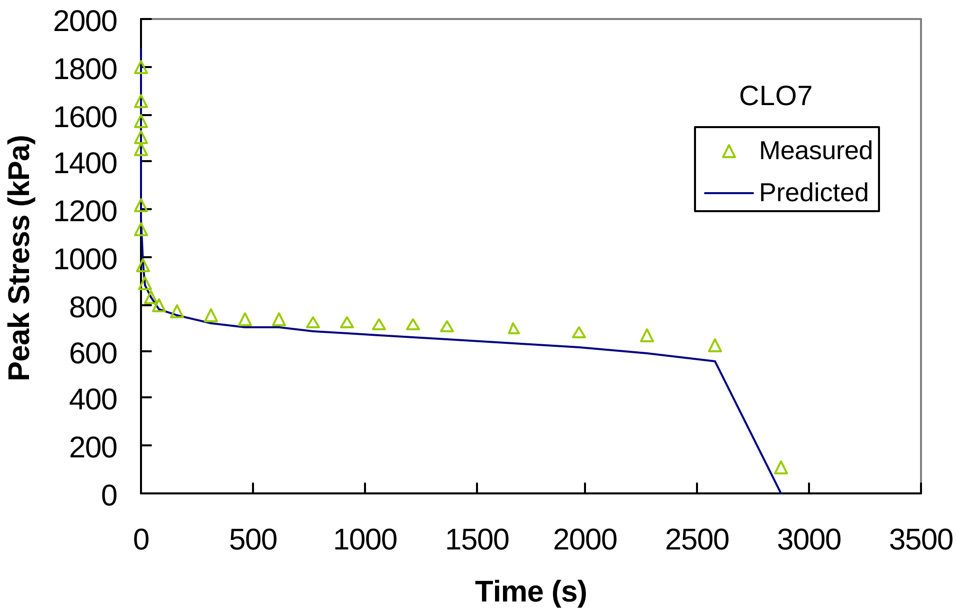

Figure 6.43 Measured and Predicted Stress Values for CLO7 Cyclic Test

6.8.3 Incorporating the Effect of Temperature

Recent research (Kim et al., 2001) has shown that the time-temperature superposition not only holds for undamaged material (linear viscoelastic range), but for damaged material as well. If the characteristic curve is a true material function, the curve at any temperature can be found using the time-temperature superposition principle. In this section, the concept of reduced time is used to investigate whether or not predictions can be made from one temperature to another.

To make use of the time-temperature superposition principle, time, t, is replaced by reduced time, ξ, in the pseudo strain and damage parameter calculations:

$$e^{R} = \int_{0}^{x} E(x - x') \frac{de}{dx'} dx' \tag{6.24}$$

$$S_1 = \sum_{i=1}^{N} \left[\frac{I}{2} \left(e^{R}\right)^2 \left(C_{i-1} - C_i\right) \right]^{\frac{a}{(1+a)}} \left(x_i - x_{i-1}\right)^{\frac{1}{(1+a)}} \qquad \text{for monotonic} \tag{6.25}$$

$$S_1 = \sum_{i=1}^{N} \left[\frac{I}{2} \left(e^{R}\right)^2 \left(C_{i-1} - C_i\right) \right]^{\frac{a}{(1+a)}} \left(\frac{x_i - x_{i-1}}{4}\right)^{\frac{1}{(1+a)}} \qquad \text{for cyclic} \tag{6.26}$$

Once this analysis is done, the C_1-S_1 curves shifted to a particular temperature can be compared with those measured at the same temperature. Figure 6.44 shows the two CML specimens tested at 20^{o}C and the test data shifted from both 12^{o}C and 5^{o}C. When reduced time is used, all of the data collapse to form a single characteristic curve. Using the same prediction procedure as before, the percent error in the number of cycles to failure predicted from the lower temperatures is shown in Table 6.7. The peak stress values measured at 20^{o}C and predicted from 5^{o}C are shown for specimen CML1 in Figure 6.45. The predictions are within 30%, which is less than the 10-80% sample-to-sample variability reported earlier.

Prediction of higher temperature behavior from a lower temperature (as for the data above) only requires a portion of the measured data because the reduced time range is shorter than the measured time range. Interpolation is done to calculate the pseudo strains at the reduced times that fall between measured values. However, calculating the pseudo strains and damage parameter values using the reduced time can be problematic when low temperature behavior is predicted from high temperature behavior. In this case, the reduced time scale is larger than the measured time scale and the measured data must be extrapolated.

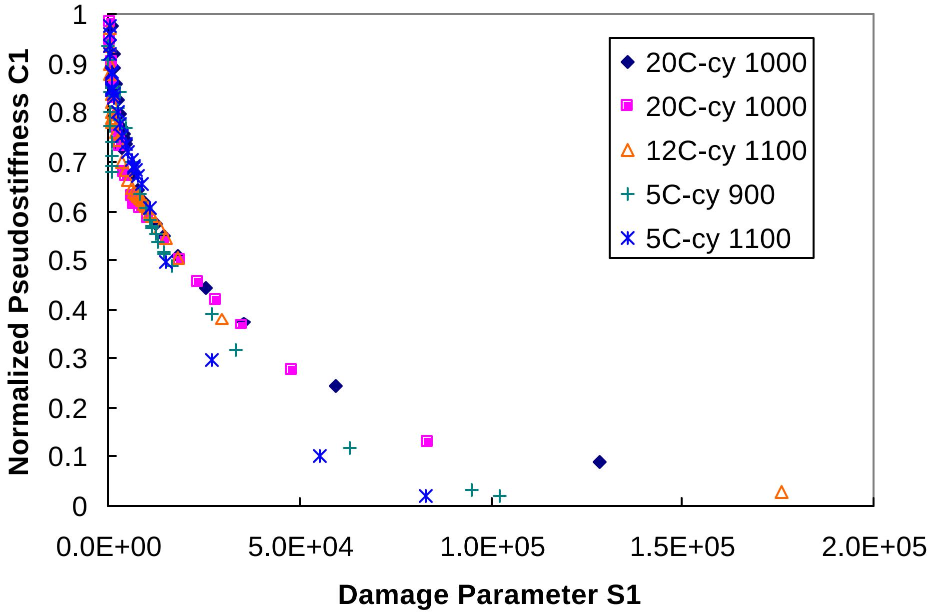

Figure 6.44 Cyclic Characteristic C_1 versus S_1 Curves Shifted to Reference Temperature of 20^{o}C for CML Mixture

Table 6.7 Measured and Predicted Number of Cycles to Failure for Various Temperatures

Specimen	**Test Temp (^{o}C)**	**Measured N_f**	**Predicted from 5^{o}C (% error)**	**Predicted from 12^{o}C (% error)**	**Predicted from 20^{o}C (% error)**
CML1	20	5,520	4,500 (-18.0%)	6,200 (12.0%)	-
CML5	20	10,300	9,000 (-12.6%)	11,200 (8.7%)	-
CML13	12	10,500	13,500 (28.6%)	-	11,000 (4.8%)
CML14	12	37,400	37,000 (-1.1%)	-	37,500 (0.3%)
CML7	5	162,000	-	164,000 (1.2%)	168,000 (3.7%)
CML8	5	20,000	-	24,200 (21.0%)	22,200 (11%)

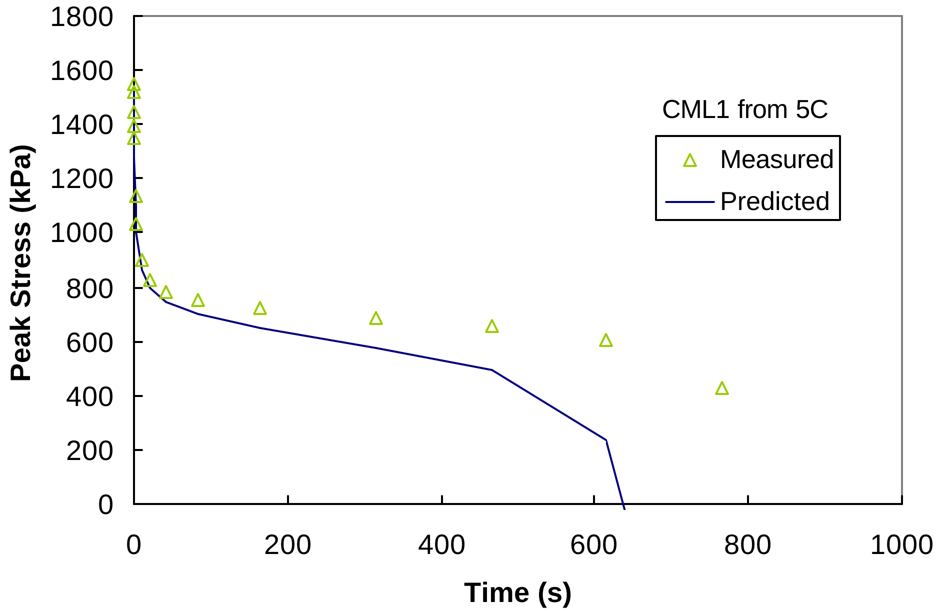

Figure 6.45 Measured and Predicted Stress Values from 5°C for CML1 Cyclic Test

To avoid the use of extrapolated data, an approximate method can be applied that takes advantage of the fact that the pseudo strain values calculated using reduced time are essentially the same at different temperatures. Figure 6.46 shows the pseudo strains for several specimens calculated using the measured data at the original test temperature plotted against the pseudo strains calculated using reduced time when shifting to 20°C.

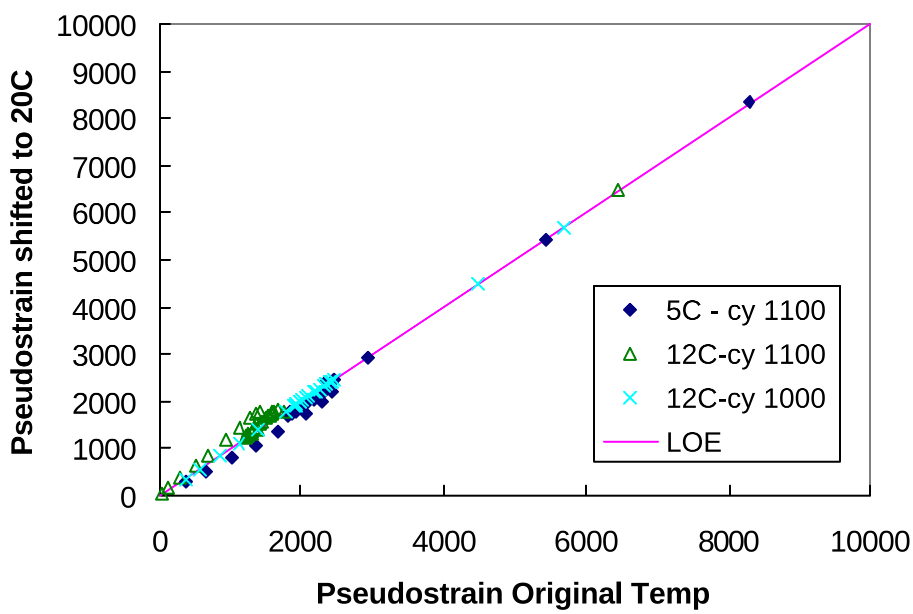

Figure 6.46 Pseudo strains Calculated at 20°C and at Original Test Temperature

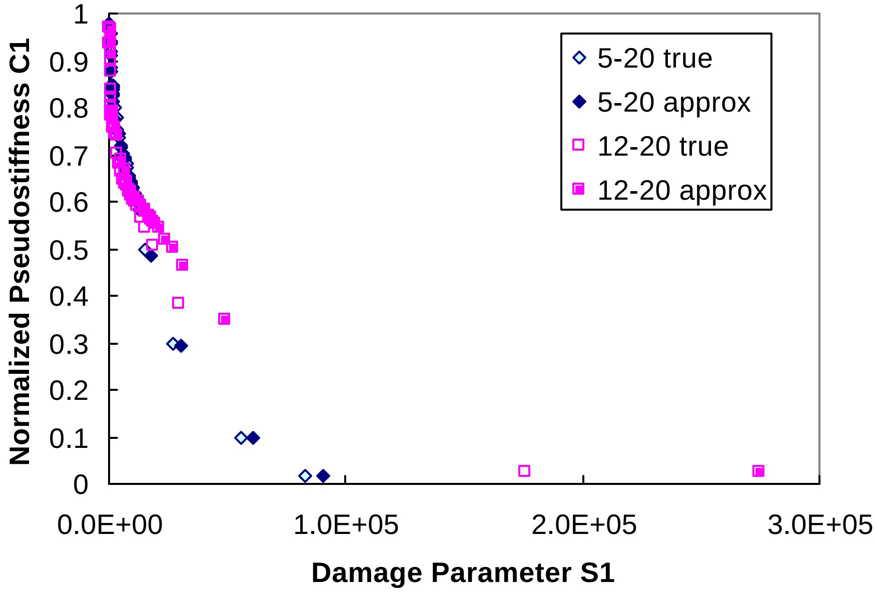

Figure 6.47 Effect of Pseudo Strain Approximation on Characteristic C_1 versus S_1 Curve

All of the data points fall very close to the line of equality. Taking advantage of the nearly identical pseudo strain values, the C_1-S_1 curves for different temperatures can be determined by simply using the reduced time and the original pseudo strain values to calculate the damage parameter in Equation (6.26). The resulting C_1-S_1 curves from the calculated and approximated pseudo strains are shown in Figure 6.47. The magnitude of difference is about the same as that between data shifted from various temperatures.

Table 6.8 shows the difference in the measured and predicted peak stress values for the CMO monotonic tests predicted from other temperatures. The approximate method described above is used. In all of the predictions, the coefficients from the overall data (including cyclic and monotonic) at each temperature are used instead of individual test data. Predictions at 12°C are not included because monotonic testing was not performed at this temperature. The errors are of the same magnitude as those seen for predictions from cyclic data in Table 6.7.

6.9 Proposed Test Procedure for Fatigue Characterization

This section introduces a proposed test procedure for the fatigue characterization of asphalt mixtures based upon the methodology discussed in the previous section. The test procedure provides a concise explanation of the steps that need to be taken for the methodology to be applied to testing of any mixture. Following the description of the proposed test procedure, potential applications and scenarios for its use are discussed.

Table 6.8 Measured and Predicted Peak Stress Values for Various Temperatures

Specimen	Test Temperature (^oC)	Measured Peak Stress (kPa)	Predicted from other test temperature (% error)
CMO3	20	1,482	1,328 (-10.4%)
CMO8	20	1,675	1,469 (-12.3%)
CMO9	5	1,732	2,190 (26%)
CMO14	5	1,301	1,451 (11.5%)

6.9.1 Proposed Test Procedure

Flowcharts for the proposed testing procedure and associated analysis are shown in Figures 6.48 and 6.49, respectively. The following discussion explains the steps in the proposed testing and analysis procedure.

The proposed test procedure begins with the characterization of the linear viscoelastic properties of the desired mixture. The accurate characterization of relaxation modulus in particular is very important for the calculation of pseudo strains. Due to experimental difficulties in measuring the relaxation modulus directly, the proposed linear viscoelastic test method is the frequency sweep test, from which the relaxation modulus can be predicted. The advantage of using the frequency sweep test over the creep test is twofold: first, the frequency sweep test performed with a mean stress of zero prevents the accumulation of permanent strain in the specimen (McGraw 2000), and second, the testing time required for the frequency sweep test is significantly less than that for the creep test. The creep test requires a long recovery time due to the static loading whereas the recovery period after a frequency sweep test is short because of the fast loading rates applied.

It is highly recommended that the strain measurements be made on the specimen itself; either using contact sensors mounted on the specimen surface or non-contact techniques. The advantage of on-specimen strain measurements is that the true material response is measured, which does not include any effects of machine compliance, or if the appropriate gage length is used, end effects, in the specimen itself.

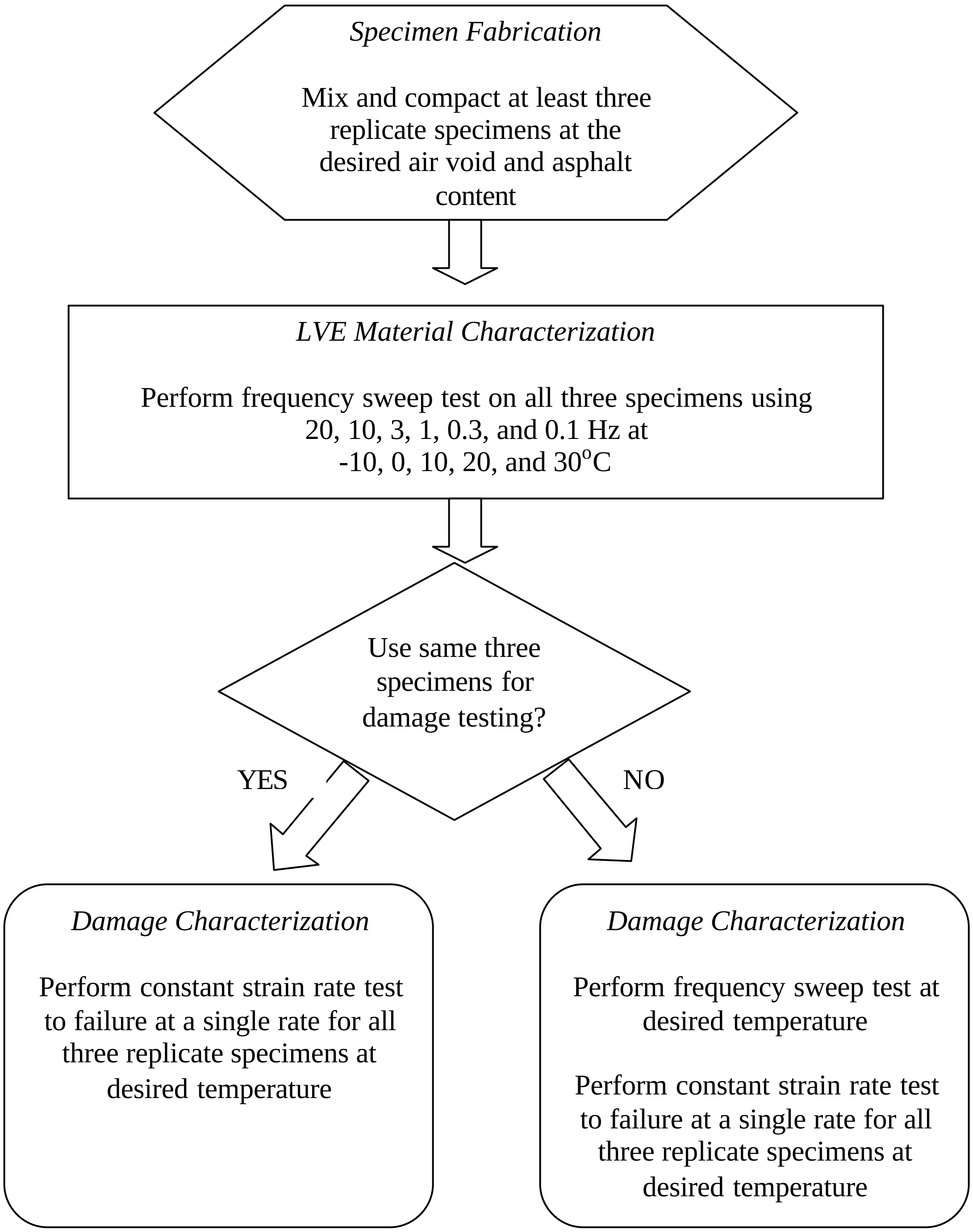

Figure 6.48 Flowchart for Proposed Test Procedure

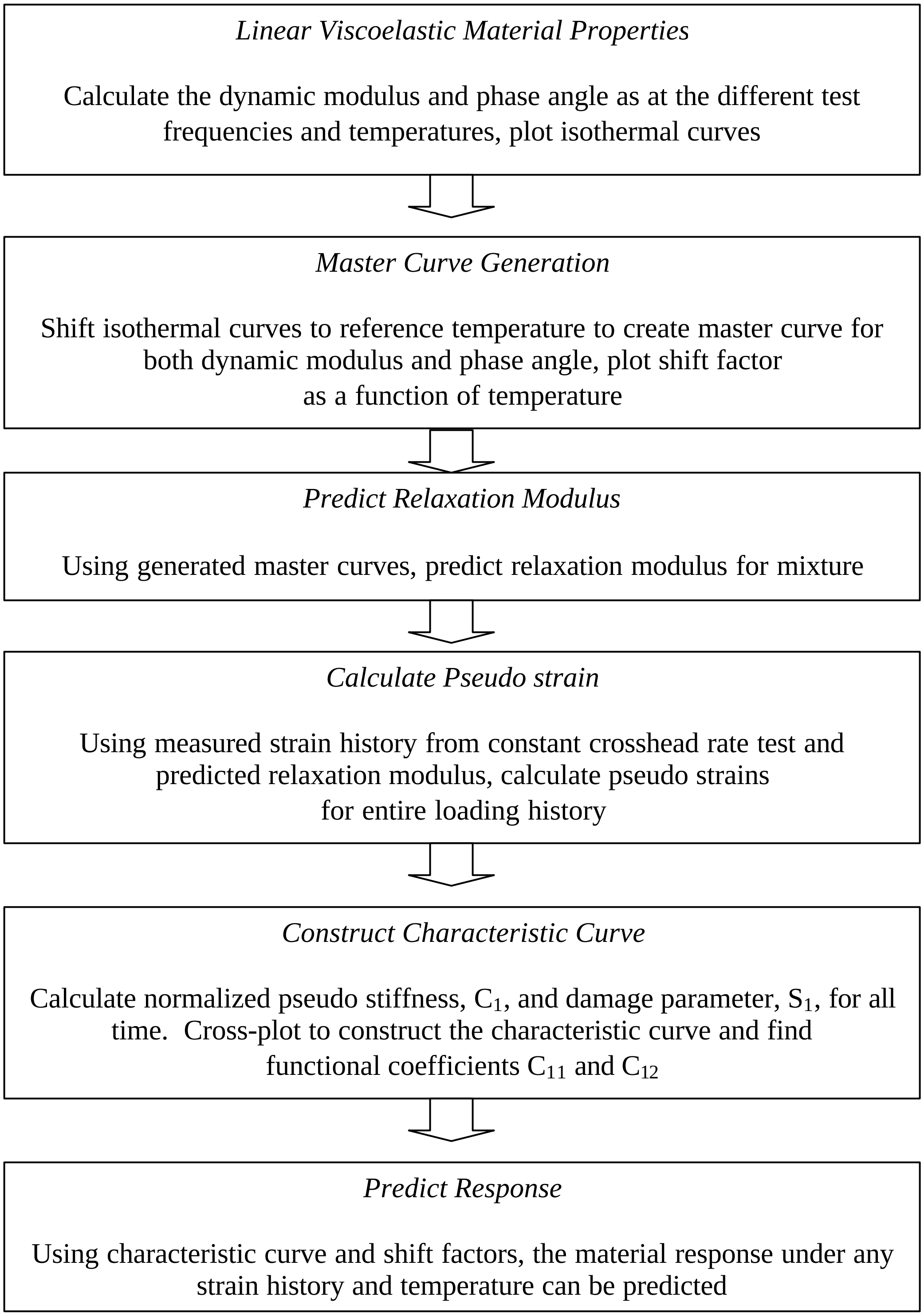

Figure 6.49 Flowchart for Proposed Test Procedure Analysis

The suggested temperatures and frequencies for the testing have been shown to provide a good representation of a wide range of behavior for various asphalt mixtures. However, the actual temperatures and frequencies can be adjusted based on agency experience and the actual properties of the mixture being tested. Microstrain levels of 50-70 should be targeted at each frequency-temperature combination to ensure that the linear viscoelastic response is measured and that damage is not induced in the specimens. If an agency prefers, the damage tests can be performed on separate specimens than those on which the LVE testing is conducted. However, it is recommended that a frequency sweep test on the separate specimen be performed at the damage test temperature for comparison with the overall mixture master curve. More temperatures and frequencies may be tested; the requirement is only that the testing cover an appropriate range of material behavior for the application. It is also important to ensure the desired reference temperature is included in the temperatures used to create the master curves. The testing should be performed from the lowest temperature to the highest and at each temperature the frequencies should be applied from the highest to the lowest.

Using the time-temperature superposition principle, the isothermal dyanamic modulus and phase angle curves can be shifted to the reference temperature to form a single master curve as a function of reduced frequency. From this procedure, the shift factor for each temperature is determined. The shift factor is essential for predicting the damage characteristics of the material at various temperatures. Once the dynamic modulus and phase angle master curves are fit to a functional form, the relaxation modulus can be predicted.

The strain rate for the constant crosshead rates should be chosen such that brittle fracture does not occur in the specimen. The faster the loading is applied, the more likely brittle fracture is to occur, and as the mixture becomes stiffer, brittle fracture will occur at slower rates. To use the methodology developed in this research, the experiment must be able to measure the damage as it grows in the asphalt specimen up to and beyond failure. This is not possible with a brittle fracture. The first time a particular mixture is tested, the appropriate strain rate must be determined through a trial and error process.

The pseudo strain as a function of time can be calculated knowing the strain history from the monotonic test and the relaxation modulus predicted from the frequency sweep testing. Using the initial portion of the stress-pseudo strain curve, the I value can be determined for each specimen and the normalized pseudo stiffness, C_1, and damage parameter, S_1, can be calculated for the entire loading history. Cross-plotting these two parameters creates the characteristic curve that describes how damage evolves in that mixture. Using the time-temperature shift factors obtained from the frequency sweep master curve construction, the characteristic curve can be shifted to any desired temperature. The range of temperatures for which this procedure is to be applied must be within the reasonable range of temperatures at which fatigue cracking is expected to occur. At higher temperatures, rutting will be the main pavement distress instead of fatigue cracking and the prediction of the fatigue performance would not be useful. The functional form of the characteristic curve at any reasonable temperature can then be used to predict the material behavior under any known strain history.

The test procedure proposes that at least three replicate specimens be tested using the same experimental values (frequencies, temperatures, strain rate) to allow for the measurement of sample-to-sample variability. Depending upon the application, testing at other strain rates and temperatures, or cyclic testing may be performed on other sets of specimens for verification purposes.

6.9.2 Applications

This test procedure can be applied to many different design scenarios. For an overall project design, the proposed procedure can be used to evaluate the fatigue performance of different asphalt-aggregate combinations within a pavement system. The analysis can incorporate any number of levels of complexity. A simple analysis can be performed at a single temperature, load level and pavement cross-section, or multiple load levels on different cross sections can be evaluated through seasonal changes. The available time for project design and the required level of prediction accuracy will determine the complexity of the analysis performed.

Once an asphalt and aggregate source has been identified for a particular application, this test procedure can be used for analysis of various gradations and asphalt contents with respect to fatigue behavior. This is basically how the procedure is applied to the WesTrack mixtures in this project. The differences in the fatigue life under a known strain history with two different aggregate gradations and various asphalt and air void contents were determined using a variation of this test procedure.

This procedure can also be used in thickness design by examining the effect of the thicknesses and properties of the various pavement layers on the fatigue life of the asphalt concrete can be determined. This information can be used to perform a cost anlaysis allowing the most cost-efficient pavement system to be designed. Seasonal variations can also be taken into account in this procedure.

The test and analysis procedure described herein can be very advantageous for any application in which the fatigue behavior under a variety of testing and environmental conditions needs to be determined. Application of the proposed procedure can greatly reduce the amount of testing that must be performed and the corresponding time and materials required. This can be applied to both practical situations that agencies deal with on a daily basis, or any potential research that requires such information.

7. DETERMINATION OF VISCOELASTIC PROPERTIES FROM IDT TEST

Elastic solutions for the indirect tensile test have been reviewed in Section 3.2. In order to convert these elastic solutions into viscoelastic solutions, the elastic-viscoelastic correspondence principle is employed in this study.

Creep compliance is one of the essential mechanical properties in the study of hysteretic behavior of asphalt concrete. The relaxation modulus also can be predicted from creep compliance through the theory of viscoelasticity. AASHTO TP9-96 provides the method to determine creep compliance from indirect tensile testing. However, the method is not applicable to the displacement measurement across the 50.8 mm gauge length that is used in this study. Moreover, the method is based on the approximation of elastic analysis. In this study, the theory of viscoleasticity was used to develop a method for determination of creep compliance from deformations measured from a 50.8 mm gauge length.

In indirect tension testing, a microcrack is initiated at the center of the specimen and propagates towards the loading strips along the vertical diameter due to the tensile stress. Therefore, the response of the material at the center of the testing specimen is of interest. Since the stress and strain distribution in the indirect tension specimen is non-uniform, the strain at the center of the specimen is not equal to the average strain obtained by dividing measured displacement by gauge length. Therefore, the relationship between center strain and measured displacement was derived based on the theory of viscoelasticity.

Several approaches were combined to verify the relationships derived. First, three-dimensional viscoelastic finite element analysis was used to check the theoretical derivations. Secondly, considering the relatively simple expression of stress and strain in the uniaxial direct tension specimen, creep compliance obtained from an indirect tension test was compared to that from a direct tension test. To eliminate the effects of sample variation on the comparison, both the direct tension test and the indirect tension test were conducted on specimens taken from one Superpave Gyratory compacted sample. Thirdly, pseudo strain was determined to check the applicability of the theory of viscoelasticity to asphalt concrete in the indirect tension testing mode. On the other hand, pseudo strain could be used to verify the theoretical developments. To calculate pseudo strain, the relaxation modulus needs to be predicted from creep compliance. The interrelationship between creep compliance and the relaxation modulus presented in Appendix A was used to convert creep compliance into a relaxation modulus.

As previously described, different specimen geometries were used in this study. The effects of specimen geometry on the characterization of asphalt concrete were studied using the finite element analysis and experiment.

7.1 Development of Creep Compliance Calculation Method for Indirect Tension Specimen

As discussed in Section 3, two-dimensional and three-dimensional solutions are available for the analysis of an indirect tension specimen. The three-dimensional solution theoretically provides more accurate results. However, it is cumbersome to operate the complicated equations. It was documented (Zhang 2000) that plane stress conditions are approximated fairly closely for a relatively thin (around 25.4 mm) specimen. Since the thickness of specimen used in this study was 38.1 mm, a creep compliance calculation method was developed based on Hondros' two-dimensional elastic solution of stresses.

In Hondros' analysis, the stresses along the horizontal diameter are expressed as follows:

$$\sigma_x(x) = \frac{2P}{\pi a d}\left[\frac{(1-x^2/R^2)\sin 2\alpha}{1+2x^2/R^2\cos 2\alpha + x^4/R^4} - \tan^{-1}\left(\frac{1-x^2/R^2}{1+x^2/R^2}\tan\alpha\right)\right] = \frac{2P}{\pi a d}\left[f(x)-g(x)\right] \tag{7.1}$$

$$\sigma_y(x) = -\frac{2P}{\pi a d}\left[\frac{(1-x^2/R^2)\sin 2\alpha}{1+2x^2/R^2\cos 2\alpha + x^4/R^4} + \tan^{-1}\left(\frac{1-x^2/R^2}{1+x^2/R^2}\tan\alpha\right)\right] = -\frac{2P}{\pi a d}\left[f(x)+g(x)\right] \tag{7.2}$$

where P = applied load,
a = loading strip width,
d = thickness of specimen,
R = specimen radius, and
α = radial angle.

Because of the small specimen thickness, 38.1 mm, plane stress condition is assumed in the specimen. That is,

$$\varepsilon_x(x) = \frac{1}{E}(\sigma_x - \nu\sigma_y) \tag{7.3}$$

where E is Young's modulus and ν is Poisson's ratio.

Due to the viscoelastic nature of asphalt concrete, strain is also time-dependent. The elastic-viscoelastic correspondence principle was used to obtain the viscoelastic solutions from the elastic solutions. The elastic-viscoelastic correspondence principle states that the viscoelastic equations are identical to the elastic equations in the Laplace transformed domain with the substitution of the Carson transformed modulus for the elastic modulus. In this study, Poisson's ratio is assumed to be constant. Thus, the transformed form of the stress-strain relationship is:

$$\bar{\varepsilon}(x,s) = \frac{1}{\tilde{E}}(\bar{\sigma}_x - \nu\bar{\sigma}_y) \tag{7.4}$$

where $\bar{e}$, $\bar{s}_x$, and $\bar{s}_y$ are Laplace transformed strain and stresses while $\tilde{E}$ is the Carson transformed modulus. According to the theory of viscoelasticity, the relationship between the relaxation modulus and creep compliance is:

$$\tilde{E} \times \tilde{D} = 1 \tag{7.5}$$

where $\tilde{D}$ is the Carson transformed creep compliance. Substitute $\tilde{E}$ with $\tilde{D}$, and Equation (7.4) becomes:

$$\bar{e}(x,s) = \tilde{D}(\bar{s}_x - n\bar{s}_y) \tag{7.6}$$

Equations (7.1), (7.2), and (7.6) yield:

$$\bar{e}(x,s) = \tilde{D}\frac{2\bar{P}}{pad}\left[(1+n)f(x) + (n-1)g(x)\right] \tag{7.7}$$

where P = $P_0H(t)$ for a creep test and
H(t) = 0, when t<0; 1, when t>0.

Performing the inverse Laplace transform on both sides of Equation (7.7) yields:

$$e(x,t) = \frac{(1+n)f(x) + (n-1)g(x)}{pad}\int_0^t D(t-t)\frac{dP}{dt}dt \tag{7.8}$$

For the creep test, Equation (7.8) becomes:

$$e(x,t) = 2P_0D(t)\frac{(1+n)f(x) + (n-1)g(x)}{pad} \tag{7.9}$$

The horizontal deformation of specimen U is obtained by integrating strain over the gauge length:

$$U(t) = \int_{-l}^{l} e(x,t)dx \tag{7.10}$$

where l is half of the gauge length. Equations (7.9) and (7.10) yield:

$$U(t) = \frac{2P_0D(t)}{pad}\left[(1+n)\int_{-l}^{l} f(x)dx + (n-1)\int_{-l}^{l} g(x)dx)\right] \tag{7.11}$$

After rearranging, creep compliance, D(t), is represented as:

$$D(t) = \frac{U(t)}{2P_0 A} \tag{7.12}$$

where $A = \dfrac{(1+n)\int_{-l}^{l} f(x)dx + (n-1)\int_{-l}^{l} g(x)dx}{pad}$

According to Hondros' solution, the stresses along the vertical diameter are:

$$s_x = \frac{2P}{pad}\left[\frac{(1-y^2/R^2)\sin 2a}{1-2y^2/R^2\cos 2a + y^4/R^4} - \arctan\left(\frac{1+y^2/R^2}{1-y^2/R^2}\tan a\right)\right] = \frac{2P}{pad}\left[m(y) - n(y)\right] \tag{7.13}$$

$$s_y = -\frac{2P}{pad}\left[\frac{(1-y^2/R^2)\sin 2a}{1-2y^2/R^2\cos 2a + y^4/R^4} + \arctan\left(\frac{1+y^2/R^2}{1-y^2/R^2}\tan a\right)\right] = -\frac{2P}{pad}\left[m(y) + n(y)\right] \tag{7.14}$$

Similar to the procedure above, creep compliance is represented, in terms of vertical deformation, V(t), as:

$$D(t) = \frac{V(t)}{2P_0 B} \tag{7.15}$$

where $B = \dfrac{(n-1)\int_{-l}^{l} n(y)dy - (1+n)\int_{-l}^{l} m(y)dy}{pad}$

Equating Equations (7.12) and (7.15) yields:

$$n = -\frac{a_1 U(t) + b_1 V(t)}{a_2 U(t) + b_2 V(t)} \tag{7.16}$$

$$D(t) = -\frac{d}{P}\left[cU(t) + eV(t)\right] \tag{7.17}$$

where a_1, a_2, b_1, b_2, c, and e are coefficients related to specimen diameter and gauge length for displacement measurements. Values of these coefficients from different diameters and gauge lengths are shown in Table 7.1.

It is noteworthy that Equation (7.17) is independent of Poisson's ratio and hence is material-independent. This is attributed to a two-dimensional plane stress assumption. Poisson's ratio could not be removed from Equation (7.17) if the viscoelastic solution was based upon a three-dimensional elastic solution, as shown in Equations (3.15) and (3.16).

Table 7.1 Coefficients Used to Calculate Poisson's Ratio and Creep Compliance

Specimen Diameter (mm)	Gauge Length (mm)	a_1	a_2	b_1	b_2	c	e
100	27.4	3.385	1.081	1	3.122	0.7874	2.2783
	50.8	4.580	1.316	1	3.341	0.4032	1.024
150	27.4	3.172	1.039	1	3.060	1.199	3.533
	50.8	3.673	1.154	1	3.192	0.611	1.685
	76.2	4.559	1.330	1	3.311	0.415	1.034

7.2 Determination of Center Point Strain from Horizontal Deformation Measurement

Given that the maximum tensile strain along the horizontal diameter occurs at the center point of the specimen and that the fatigue plane is along the vertical diameter, the measured displacement across the gauge length must be converted into the center point strain, instead of the average strain, in order to study the stress-strain relationship of the element where crack is initiated.

Based on Equation (7.9) and the theory of viscoelasticity, along the horizontal diameter of the indirect tension specimen, the center point strain, $e_{x=0}$, in a creep test is represented as follows:

$$e_{x=0}(t) = D(t)\frac{2P_0}{pad}[(1+n)f(x=0)+(n-1)g(x=0)] \tag{7.18}$$

Equations (7.11) and (7.18) yield:

$$e_{x=0} = U\frac{a+bn}{c+dn} = UA \tag{7.19}$$

where a, b, c, and d are coefficients related to specimen diameter and gauge length used. Table 7.2 shows the values of these coefficients for specimens with different diameters and gauge lengths.

It is seen from Equation (7.19) that the strain-displacement relationship is independent of stress. Therefore, Equation (7.19) is applicable to specimens subjected to any loading condition, whether constant-strain-rate loading or controlled-stress cyclic loading, etc. It is found that the strain-displacement relationship in Equation (7.19) is dependent on Poisson's ratio, indicating that the relationship is material-dependent. Theoretically, the strain-displacement relationship should be independent of Poisson's ratio. Again, the dependence in Equation (7.19) is ascribed to the plane stress assumption. Figure 7.1 shows the effect of changes in Poisson's ratio on the parameter A in Equation (7.19). The number before the hyphen stands for specimen diameter while the one after the hyphen stands for gauge length. Even though Poisson's ratio increases from 0.1 to 0.5, there is only a slight change of A. Therefore, it is concluded that the effect of plane stress assumption on the strain calculation is negligible.

Table 7.2 Coefficients in Equation (7.19)

Specimen Diameter (mm)	Gauge Length (mm)	a	b	c	d
100	25.4	12.4	37.7	0.291	0.908
	50.8	12.4	37.7	0.471	1.57
150	25.4	8.48	27.6	0.207	0.634
	50.8	8.48	27.6	0.373	1.18
	76.2	8.48	27.6	0.478	1.59

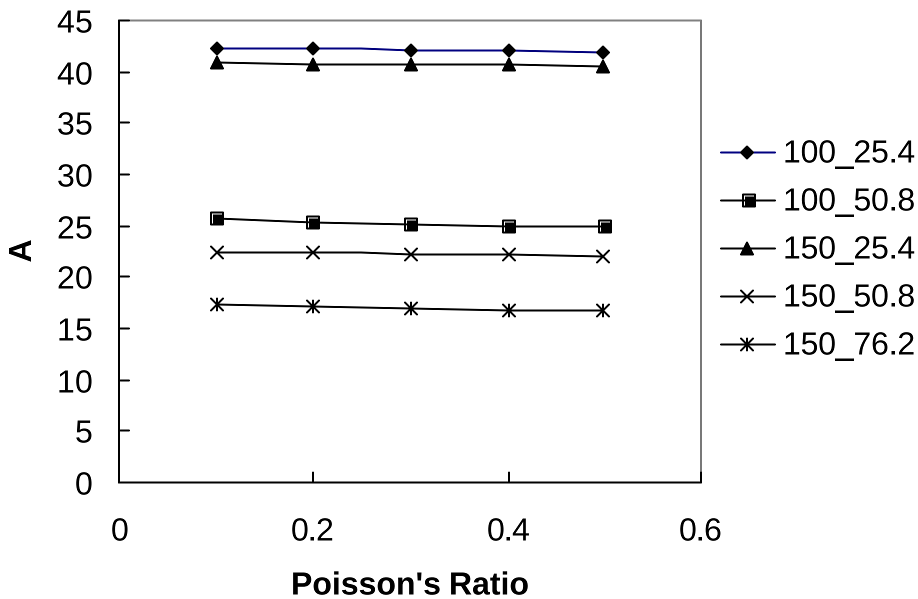

Figure 7.1 Effect of Change in Poisson's Ratio on Strain Calculation

7.3 Verification Using Three-Dimensional Viscoelastic Finite Element Analysis

7.3.1 Verification of Creep Compliance Calculation Method

Three-dimensional viscoelastic finite element analysis is used to verify the creep compliance calculation in Equation (7.17). Using ABAQUS software, the 3-D finite element model is developed to analyze an IDT specimen of 100 mm diameter and 38 mm thickness loaded by a 12.8 mm wide steel loading strip. Due to its symmetry, only a quarter of the specimen is used and meshed, as shown in Figure 7.2. A constant load was applied to the loading strip for 100 seconds. The step used to accomplish the analysis was controlled by automatic time incrementation.

Indirect tensile specimen deformations are obtained by using known values of creep compliance in the form of a Prony series and Poisson's ratio. The standard test configuration described in Chapter 4 is used. The horizontal and vertical deformations across the 50.8mm gauge length are used to calculate the creep compliance using Equation (7.17). The calculated creep compliance is compared with creep compliance predicted from the relaxation modulus. The procedure of verification is shown in the following flowchart:

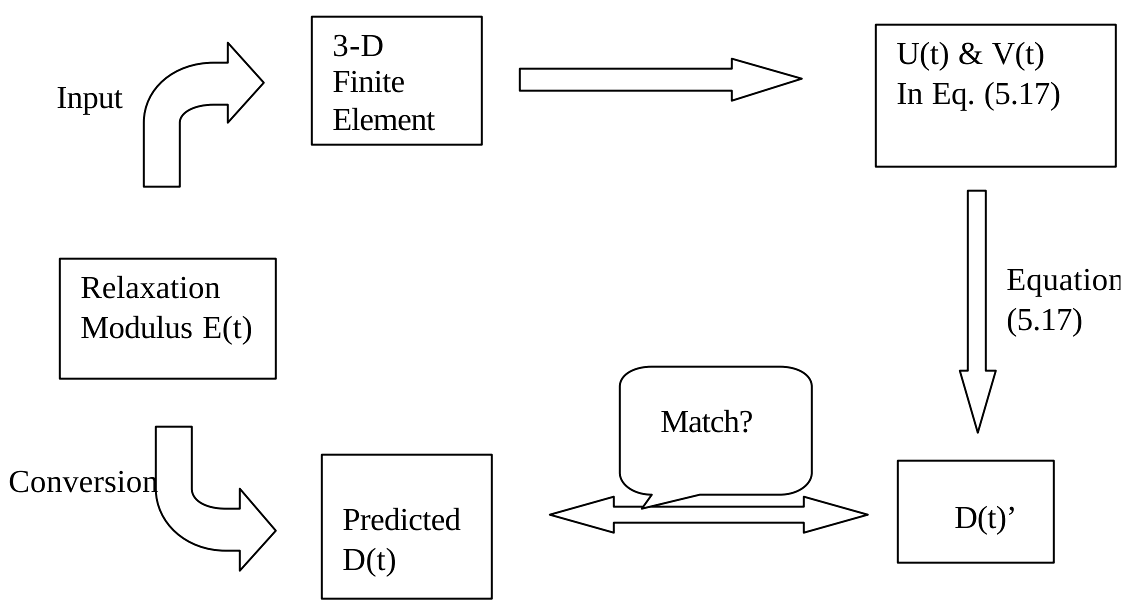

Material parameters needed for the ABAQUS viscoelastic model are the normalized shear modulus and bulk modulus in terms of a Prony series, whereas the modulus obtained from the laboratory in this study is the relaxation modulus. An analytical procedure is needed to convert the relaxation modulus into the creep compliance and the relaxation modulus into the shear and bulk moduli. The approach to convert the relaxation modulus into creep compliance is presented in Appendix A. Assuming the material is isotropic and non-aging, the relationship among the relaxation modulus, shear modulus, and bulk modulus may be represented as:

$$\tilde{K} = \frac{\tilde{E}}{3(1-2\tilde{n})} \tag{7.20}$$

$$\tilde{G} = \frac{\tilde{E}}{2(1+\tilde{n})} \tag{7.21}$$

where $\tilde{K}$ = Carson transform of the bulk relaxation modulus,
$\tilde{G}$ = Carson transform of the shear relaxation modulus,
$\tilde{E}$ = Carson transform of the relaxation modulus, and
$\tilde{n}$ = Carson transform of Poisson's ratio.

Assuming Poisson's ratio does not change with time, the Carson transform of Poisson's ratio ($\tilde{n}$) becomes a constant (ν). Therefore, the shear and bulk moduli may be estimated from the relaxation modulus in the following relationship:

$$K(t) = \frac{E(t)}{3(1-2n)} \tag{7.22}$$

$$G(t) = \frac{E(t)}{2(1+n)} \tag{7.23}$$

The relaxation modulus in the form of a Prony series is presented as:

$$E(t) = E_g + \sum_{i=1}^{11} E_i e^{-\frac{t}{r_i}} \tag{7.24}$$

where E_i and τ_i are constants and are tabulated in Table 7.3.

Creep compliance was determined from the relaxation modulus using a numerical integration method based on the creep compliance and relaxation modulus convolution integral. With viscoelastic finite element analysis, the horizontal and vertical displacements across a 50.8 mm gauge length, U(t) and V(t) in Equation (7.17), were obtained and used to calculate the creep compliance.

The analysis results are shown in Figure 7.3 in which "converted D(t)" is the creep compliance predicted from the known relaxation modulus and "Equation (7.17)" is the calculated creep compliance using the viscoelastic solution.

Figure 7.3 shows a good correspondence between creep compliances from Equation (7.17) and the predicted creep compliance, thus indicating the validity of the creep compliance calculation method developed for this test setup using a 50.8 mm gauge length.

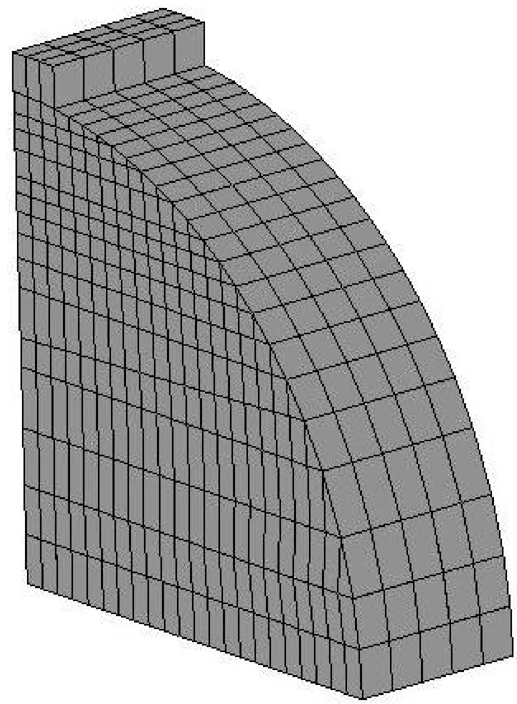

Figure 7.2 3-D Finite Element Model Mesh of Indirect Tension Specimen

Table 7.3 Coefficients in a Prony series representation E(t) (after Lee, 1996)

i	ρ_i (sec)	E_i (Gpa)
1	1E-5	2.03E+02
2	1E-4	3.77E+03
3	1E-3	3.59E+03
4	1E-2	2.52E+03
5	1E-1	1.29E+03
6	1E+00	4.09E+02
7	1E+01	1.31E+02
8	1E+02	3.40E+01
9	1E+03	1.22E+01
10	1E+04	1.61E+00
11	1E+05	1.76E+00
E_g=3.5 Gpa		

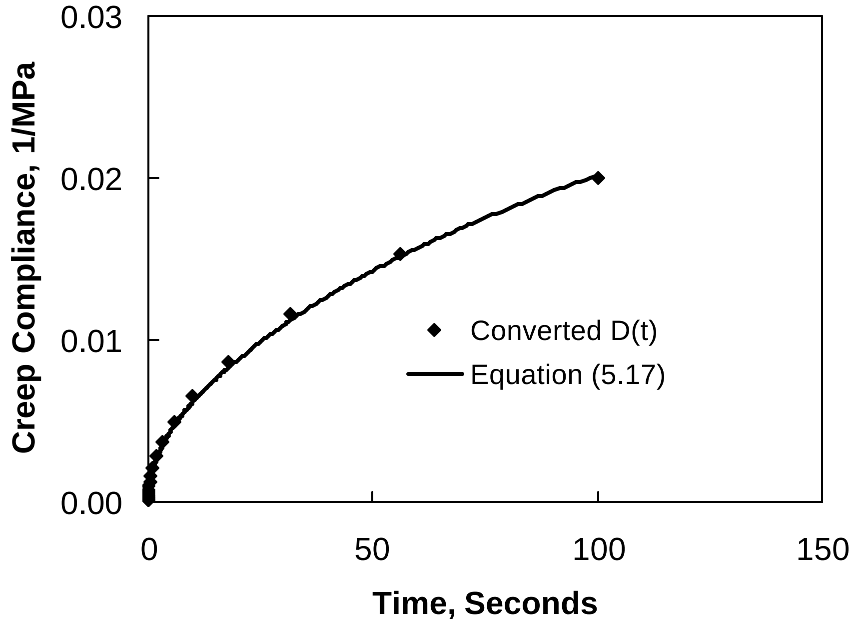

Figure 7.3 Verification of Creep Compliance Calculation

7.3.2 Verification of Calculation of Center Strain Using Finite Element Method

From the finite element analysis, the displacements across the 50.8 mm gauge length and the center point strain may be obtained directly. The center point strain may also be calculated from Equation (7.19) with the known displacement. Therefore, Equation (7.19) can be verified using the procedure shown in the following flowchart:

The elastic analysis of this finite element model was used to warrant the accuracy of finite element mesh by checking with the known elastic theoretical IDT stress/strain solution while viscoelastic analysis of uniaxial finite element model was used to check the viscoelastic material and loading input based upon theoretical viscoelastic uniaxial stress/strain solutions. The strain at the center of IDT specimen can be obtained from finite element analysis output using the nodal strain.

Figure 7.4 compares strain obtained from the finite element analysis to calculated strain using Equation (7.19). The average strain (measured deformation divided by gauge length) is also shown in Figure 7.4 for comparison. It is seen from Figure 7.4 that the calculated center strain is very close to that obtained from the finite element analysis, indicating that Equation (7.19) calculates center strain from the displacement accurately.

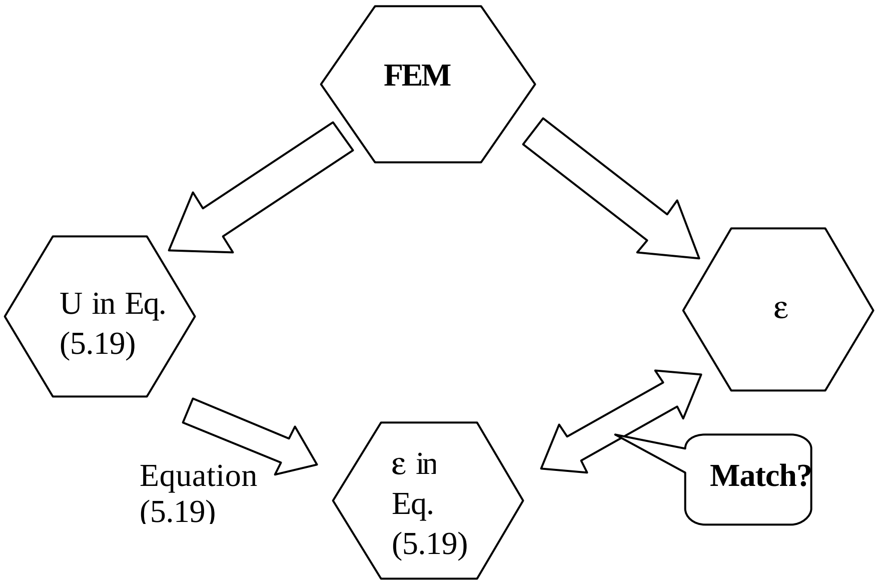

7.4 Verification Using Uniaxial Direct Tension Testing and Indirect Tension Testing

Finite element analysis indicates that the theoretical developments accurately represent the properties of materials in indirect tensile tests. Considering the relatively simple stress and strain state in a direct tension specimen, the test result from the uniaxial test may provide the reference to that of indirect tension tests. Thus, creep compliance obtained from an indirect tension creep test was compared to that obtained from a direct tension creep test.

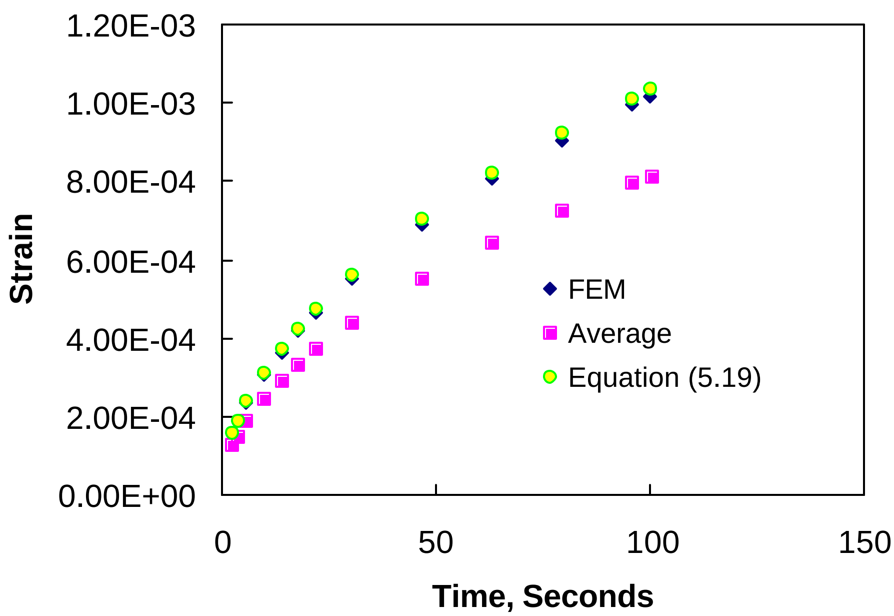

Figure 7.4 Verification of Center Strain Calculation

In a direct tension test, the stress and strain are represented as:

$$s = \frac{P(t)}{A},\ e = \frac{L(t)}{GL} \tag{7.25}$$

where P = load applied,
A = circular cross-section area,
L = measured displacement, and
GL = gauge length.

Creep compliance from a direct tension creep test is calculated, as follows:

$$D(t) = \frac{s\ (t)}{e(t)} \tag{7.26}$$

To eliminate the effects of sample variation on the comparison, both direct tension and indirect tension tests were conducted on specimens out of one Superpave Gyratory compacted sample. A direct tension creep test was first conducted on the specimen cored and cut from an SGC sample. The specimen used in the direct tension test was cut into two indirect tension specimens. Figure 7.5 illustrates the procedure to prepare the direct tension specimen and indirect tension specimens.

The comparison was based upon the assumption that the sample was homogeneous and isotropic. Therefore, it is presumed that the values of creep compliance obtained from different testing modes and from different parts of the specimen would be close to each other. Three SGC samples were fabricated using the North Carolina mix. An 80 lb load was used in the direct tension test and a 50 lb load was used in the indirect tension test. The durations of both the direct tension and indirect tension tests were 100 seconds. A 50.8 mm gauge length in the middle of the specimen was used to measure the vertical deformation. Figure 7.6 presents the comparison between the result from the direct tension test and that from the indirect tension test. A fairly large discrepancy was found. Several factors may be attributed to the discrepancy:

(1) The SGC sample could not be considered homogenous, especially due to the air void distribution. Since two indirect tension specimens were cut out of a uniaxial test specimen, the indirect tension creep test was conducted only on part of the uniaxial test specimen, a factor which may have caused the discrepancy. However, according to the findings reported in Chapter 5, the air void distribution in a direct tension specimen is relatively uniform, indicating that the composition of the IDT test specimen is similar to that of the uniaxial test specimen.

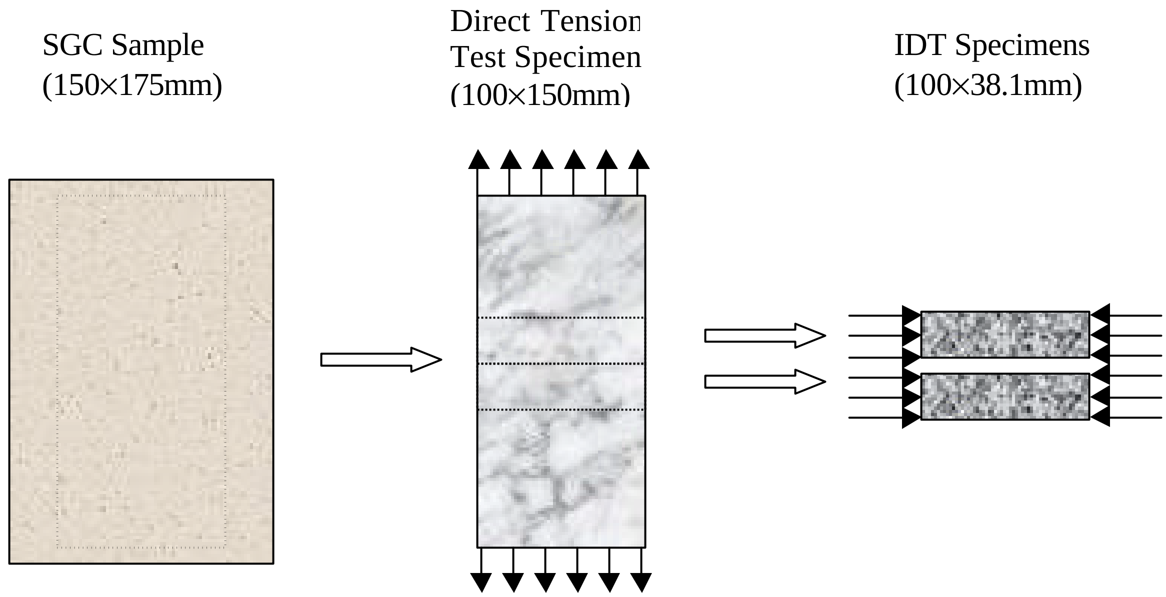

Figure 7.5 Preparation for Direct Tension Specimen and Indirect Tension Specimen

(2) The stress/strain state in the direct tension specimen is not uniform. In the uniaxial direct tension test, the specimen was glued to the end plates that constrained the ends of the specimen from deforming horizontally. This constraint causes the non-uniform stress/strain distribution in the specimen. Finite element analysis was performed to check the stress/strain distribution in the direct tension specimen. Figure 7.7 presents the results of the finite element analysis. It was observed that the strain distribution along the axis of the cylindrical specimen is not uniform. This is ascribed to the effects of the end plates. However, within the range of the 50.8 mm gauge length, the non-uniformity in the strain distribution is relatively small. Therefore, the non-uniformity of stress/strain distribution has an insignificant effect on the test result of the direct tension specimen.

(3) Asphalt concrete compacted by the Superpave Gyratory Compactor may be anisotropic. As stated in Chapter 2, the direction of tensile stress in an indirect tension test is perpendicular to that in a uniaxial direct tension test. It is highly possible that asphalt concrete specimen compacted by SGC is not an isotropic material. Therefore, it seems that the anisotropicity of asphalt concrete may cause the difference of results from the indirect tension test and the uniaxial direct tension creep test.

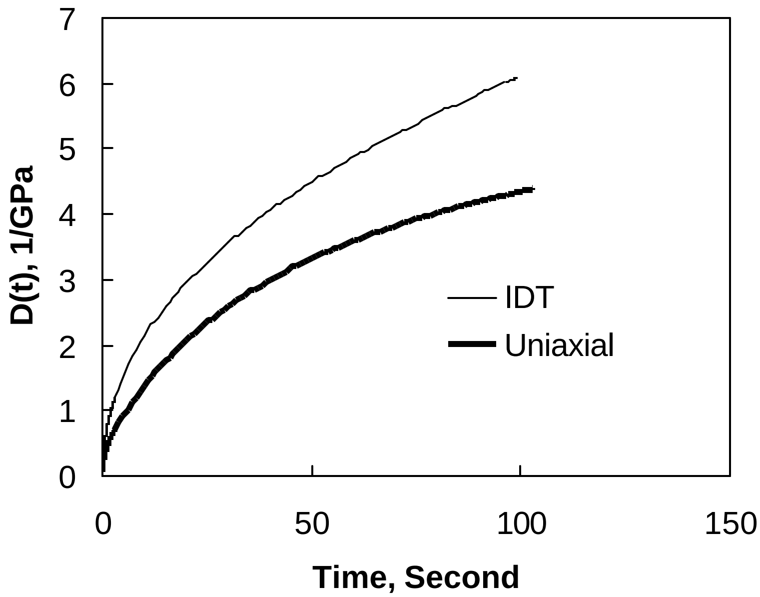

Figure 7.6 Comparison of Creep Compliance from IDT and Uniaxial Test

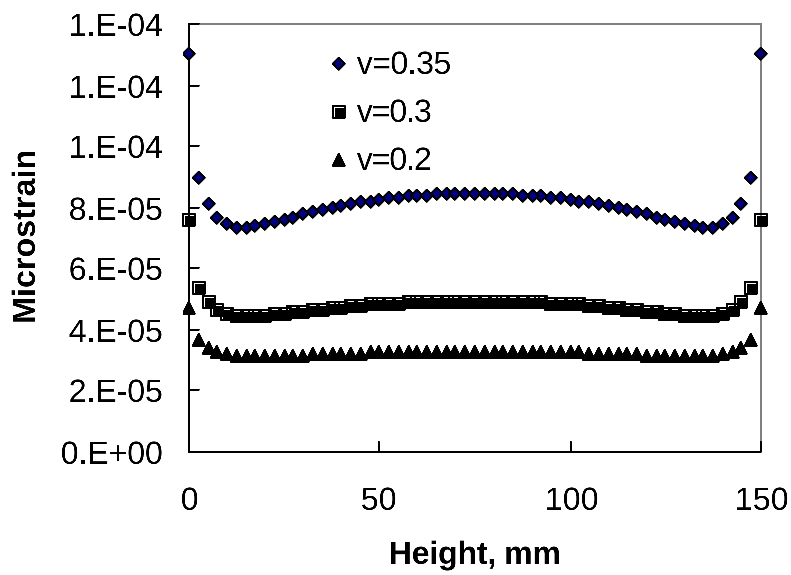

Figure 7.7 Strain Distribution along Axis of Uniaxial Direct Tension Specimen with End Plates

7.5 Application of Correspondence Principle to Indirect Tension Specimen

A series of tests was conducted to check the applicability of the correspondence principle to asphalt concrete in an indirect tension testing mode. Creep tests at different temperatures were performed to obtain a creep compliance master curve. The methods to convert creep compliance into the relaxation modulus in the indirect tension mode are described. Cyclic tests were conducted to study the hysteretic behavior of the stress-strain relationship and the applicability of the correspondence principle.

7.5.1 Creep Test

Creep Compliance Master Curve Construction

Since asphalt concrete is a thermorheologically simple material, the time and temperature dependent creep response may be represented by a single parameter, reduced time, through the time-temperature superposition principle. Creep compliance tests were performed at –10, 0, 10, 20, and 30°C to obtain thermorhelogical properties of the material. The creep compliance master curve was constructed by horizontally shifting the creep curves at various temperatures to the creep curve at a reference temperature of 20°C. The specimens were conditioned to the testing temperatures for a minimum of two hours before the test. Applied loads at different temperatures are given in Table 7.4.

Table 7.4 Creep Test Parameters

Temperature (°C)	-10	0	10	20	30
Load (lbs)	500	300	200	80	30

The creep curves at various temperatures are plotted in Figure 7.8, with a log-log scale, before shifting. The master curve was constructed and is presented in Figure 7.9. Time-temperature shift factors at different temperatures were obtained from the above shifting process, and their dependency on temperature is illustrated in Figure 7.10. The data of the master curve were firstly smoothed by representing them using the power law series (PLS), as follows:

$$D(t) = D_0 + \sum_{i=1}^{N} \frac{D_i}{(1+\frac{t_i}{t})^n} \tag{7.27}$$

where $D(t)$ = creep compliance,
t = time,
D_0 = short time (glassy) compliance,
D_i = retardation strengths, and

t_i = retardation times.

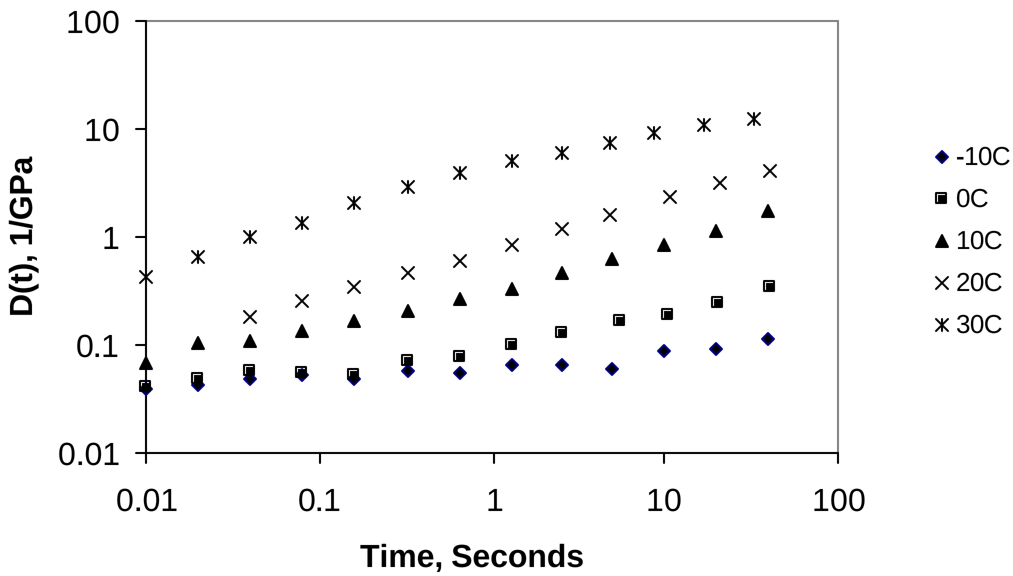

Figure 7.8 Creep Compliance Curves at Different Temperatures before Shifting

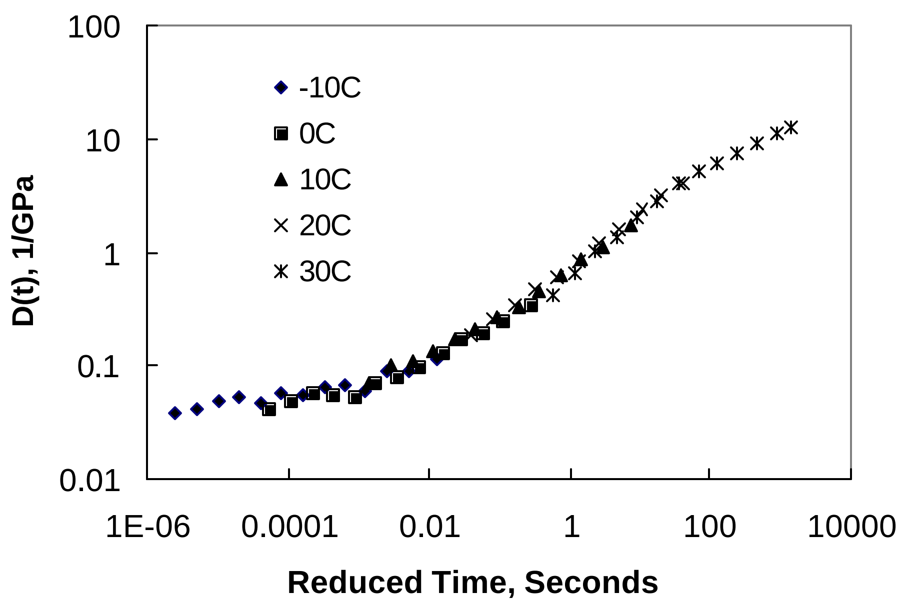

Figure 7.9 Creep Compliance Master Curve after Shifting on IDT Specimens

Here, n is the slope of the linear portion of the creep compliance master curve with a log-log scale. A one-decade interval of τ_i was used for the N=5 and N=11 series. The coefficients D_i's were found by solving a system of linear algebraic equations based on a weighted least squares fitting scheme. The reciprocal of the value of each data point was used as the weight. Figure 7.11 shows the raw data of creep compliance and PLS fitting. It seems that using an 11-term series results in a wavy fitting for largely scattered data, whereas the waviness is not found when using a 5-term series. Therefore, it was proposed to use a 5-term PLS series. A MATLAB code was written to accomplish the curve fitting.

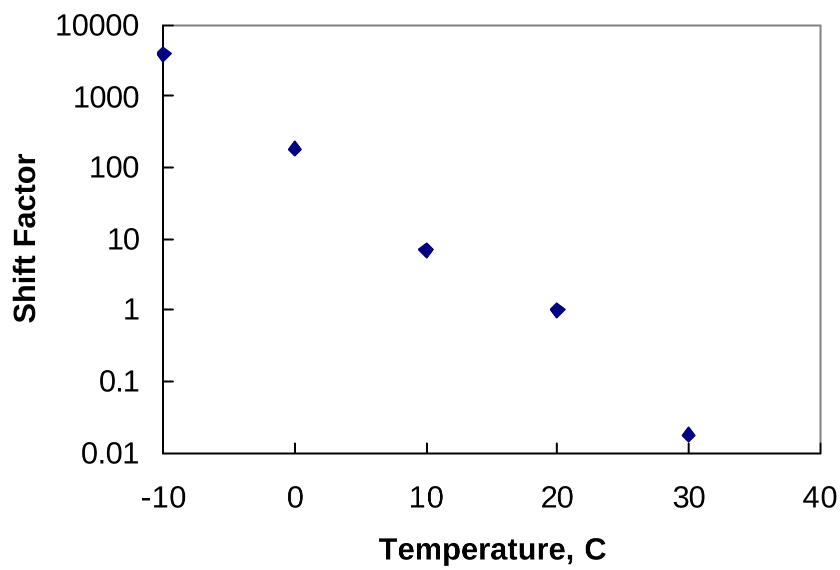

Figure 7.10 Relationship between Shift Factor and Temperature

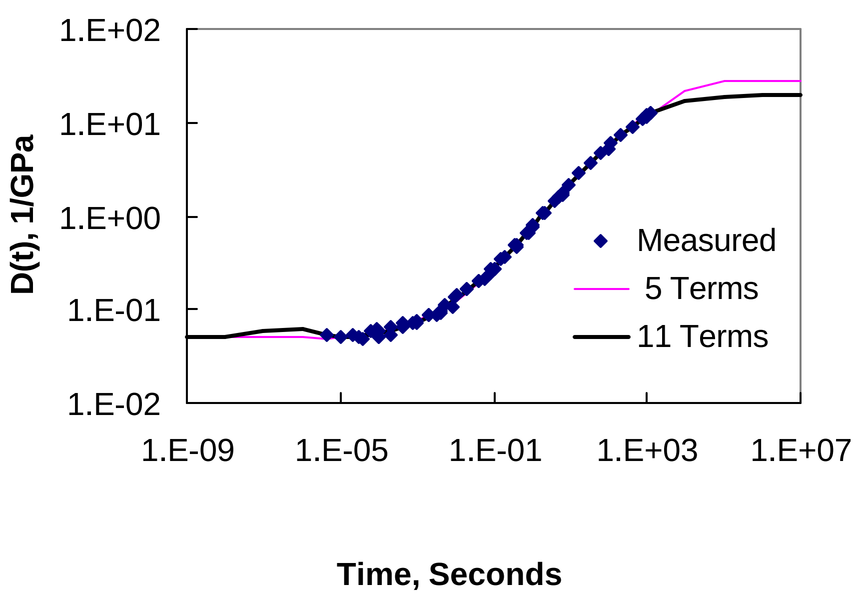

Figure 7.11 Curve Fitting of Creep modulus Compliance Using PLS

Interconversion Between Creep Compliance and Relaxation Modulus:

A power law series comprising multiple power law terms is capable of portraying a globally smooth, broadband viscoelastic behavior with minimal impact from local variance of data. However, from the viewpoint of computation, a Prony series representation is preferable to a power law series because of the computational efficiency associated with the exponential basis function of a Prony series. Therefore, the Prony series was fitted to the reconstructed data by the now-established power law series representation. The five-term power law series was used to generate data. Figure 7.12 shows the resultant Prony series fit (with N=11), as shown in Equation (7.28), as well as the parent power law series fit together with the experimental data.

$$D(t) = D_g + \sum_{i=1}^{N} D_i (1 - e^{-\frac{t}{t_i}}) \qquad (7.28)$$

The relaxation modulus and creep compliance are related by a convolution integral, as follows:

$$\int_0^t E(t-t)D(t)dt = t \text{ for t>0} \qquad (7.29)$$

where D(t) is represented by a Prony series.

Equation (7.29) was solved numerically using an appropriate numerical integration scheme. Another MATLAB code was written to obtain an approximate relaxation modulus. The converted relaxation data were fitted into a Prony series in Equation (7.30). The relaxation modulus predicted from creep compliance is graphically presented in Figure 7.12.

$$E(t) = E_{\infty} + \sum_{i=1}^{N} E_i e^{-\frac{t}{r_i}} \qquad (7.30)$$

where $E(t)$ = relaxation modulus,
t = time,
$E_{¥}$ = long time (rubbery) modulus,
E_i = relaxation strengths, and
r_i = relaxation times.

A common numerical approach normally requires that the integral be decomposed into a great number of intervals because of the spread of function over many decades of time; however, this may render inaccurate results and cause computational difficulties unless the intervals are carefully selected. Therefore, another approach was explored to convert creep compliance into the relaxation modulus, the so-called piecewise method. The PLS model was used to generate a series of data over a range that is divided into multiple intervals. The generated data within each interval were locally fitted into a pure power law (PPL) model. The relaxation modulus within one interval was predicted using the following equation:

$$E(t) = \frac{\sin(n\pi)}{n\pi D(t)} \tag{7.31}$$

where n = power value of local pure power law expression, and
D(t) = creep compliance within one interval.

The relaxation modulus data predicted were fitted into a Prony series model. In general, the approach is effective in obtaining desirable relaxation modulus representation.

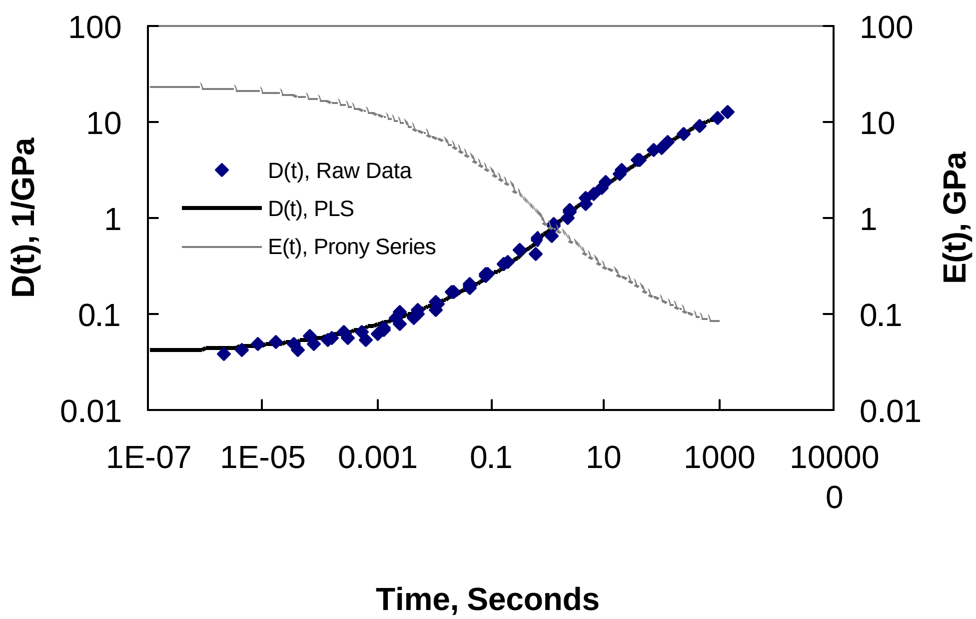

Figure 7.12 Creep Compliance and Converted Relaxation Modulus

7.5.2 Cyclic Test and Pseudo-strain Calculation

In the cyclic loading tests performed at 20°C, a loading amplitude of 50 lbs was used so as not to induce any significant damage. The horizontal displacement response under constant amplitude of cyclic loading without rest periods is represented as:

$$U_x = A + \sum_{i=1}^{10} B_i e^{-\frac{t}{\tau_i}} + C\cos(2\pi f t + \phi) \tag{7.32}$$

where A, B_i, C, and ϕ are non-linear regression constants and are shown in Table 7.5 for a particular mix. The coefficients will change for different specimens, depending on their individual response to the loading. The regression must be done for each test to represent the strain felt by the specimen.

Table 7.5 Non-linear Regression Results of Equation (7.32) Coefficients of a Particular Mix

Parameter	Value
A	-0.0133
B_1	0.0116
B_2	-0.0117
B_3	0.0002
B_4	-0.0003
B_5	-0.0004
B_6	-0.0015
B_7	-0.0126
B_8	0.0561
B_9	-0.0041
B_{10}	-0.0113
B_{11}	-0.0125
C	-0.0003
ϕ	-0.3673

The measured and regressed horizontal displacements for a particular mix are shown in Figure 7.13. The regressed displacement values are then used to calculate a center strain.

From Equation (7.3), the horizontal stress at the center point of the specimen is:

$$s = s_x - n s_y = \frac{2P}{ptd}[1-\cos(t)](1+3v) \qquad (7.33)$$

The stress in Equation (7.33), $s_x - n s_y$, which is representative of the actual stress state in the indirect tension specimen, is called biaxial stress, distinguishing it from the tensile stress, $s_x = \frac{2P}{ptd}$.

From Equation (7.19), the center point strain is obtained, as follows:

$$e_{x=0} = \left[A + \sum_{i=1}^{10} B_i e^{-\frac{t}{t_i}} + C\cos(2pft + f) \right] \frac{(a+bn)}{c+dn} \qquad (7.34)$$

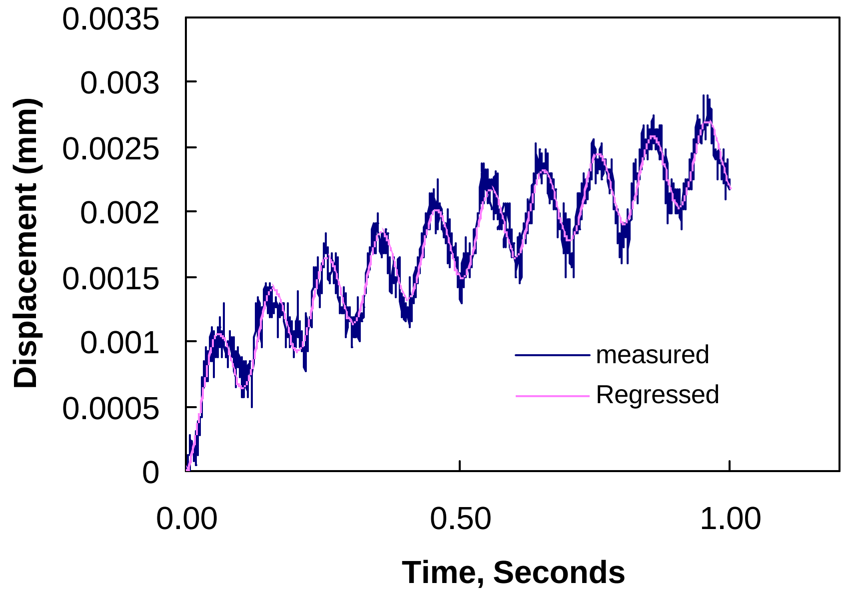

Figure 7.13 Measured and Regressed Horizontal Displacements

Pseudo strain is an essential parameter for applying Schapery's correspondence principle to the hysteretic stress-strain behavior of asphalt concrete. According to the theory of viscoelasticity, pseudo strain is represented as:

$$e^R = \frac{1}{E^R}\int_0^t E(t-t)\frac{\partial e}{\partial t}\,dt \tag{7.35}$$

where E(t) = relaxation modulus, and
E^R = reference modulus, 1.0 in this research.

The relaxation modulus is predicted from the master creep compliance curve as described previously and represented as:

$$E(t) = E_g + \sum_{i=1}^{11} E_i\,(1 - e^{-\frac{t}{t_i}}) \tag{7.36}$$

where E_g, E_i and τ_i are the constants and are shown in Table 7.6 for a particular mix. Figures 7.14 and 7.15 show the biaxial stress against time. Hysteretic stress-strain behavior is presented in Figure 7.16. As expected, the stress-strain loops shift to the right-hand side with increasing permanent strain accumulation. The area inside each stress-strain loop decreases over time as the energy dissipated from each subsequent cycle is reduced. In Figure 7.17, the same stresses are plotted against pseudo strains. Hysteretic behavior due to loading-unloading and repetitive loading has disappeared using pseudo strain. The 45° straight line in Figure 7.17 indicates that no damage was induced inside the specimen and that the theory of linear viscoelasticity is applicable to the characterization of asphalt concrete in an indirect tension testing mode. On the other hand, it demonstrates that the derivations for creep compliance and center strain are accurate and applicable to characterizing asphalt concrete. If either of the developments for creep compliance and for center strain were invalid, the correspondence principle applied to asphalt concrete would not be validated.

The correspondence principle has been theoretically and experimentally proven to be an effective tool for characterizing the fatigue behavior of asphalt concrete in a uniaxial direct tension testing mode. The validation of the applicability of the correspondence principle to asphalt concrete in an indirect tension testing mode demonstrates that the approach used to investigate asphalt concrete in a one-dimensional problem has the potential to be utilized in a two-dimensional problem.

Table 7.6 Prony Series Coefficients of Relaxation Modulus for a Particular Mix

i	E_i(Gpa)	τ_i
1	-0.7501	1E-5
2	2.1726	1E-4
3	-7.3908	1E-3
4	8.4669	1E-2
5	4.0806	1E-1
6	1.0472	1
7	0.1158	1E+1
8	0.0506	1E+2
9	0.0031	1E+3
10	0.0017	1E+4
11	-0.0002	1E+5
E_g=0.099 GPa		

.

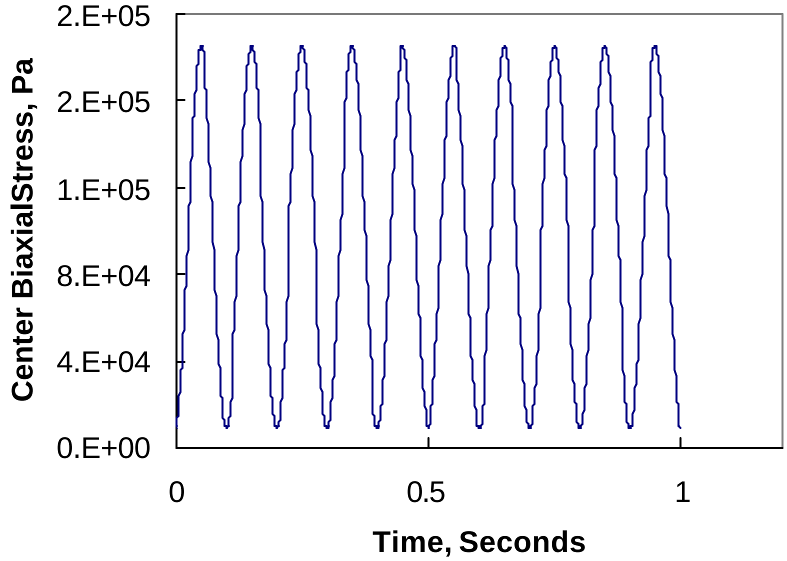

Figure 7.14 Stress vs. Time for Cyclic Tests

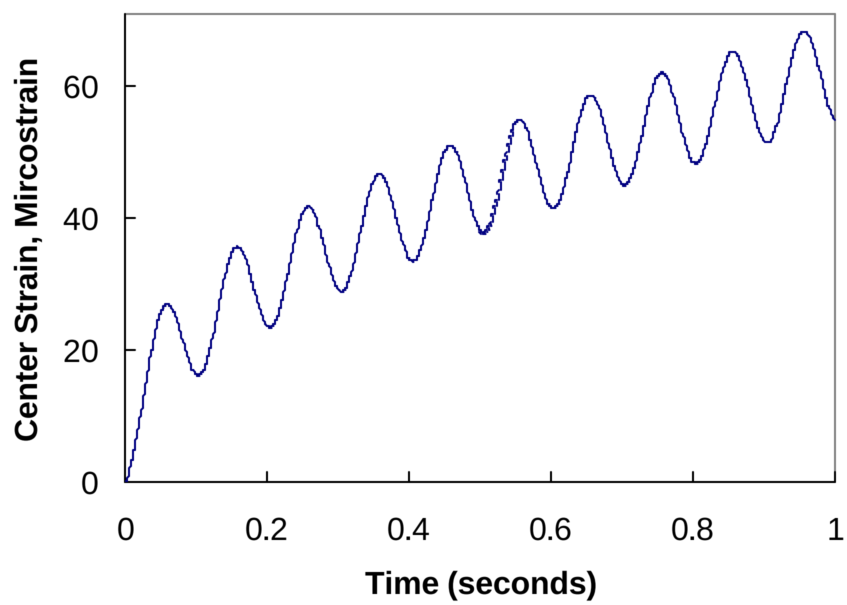

.

Figure 7.15 Smoothed Center Strain vs. Time

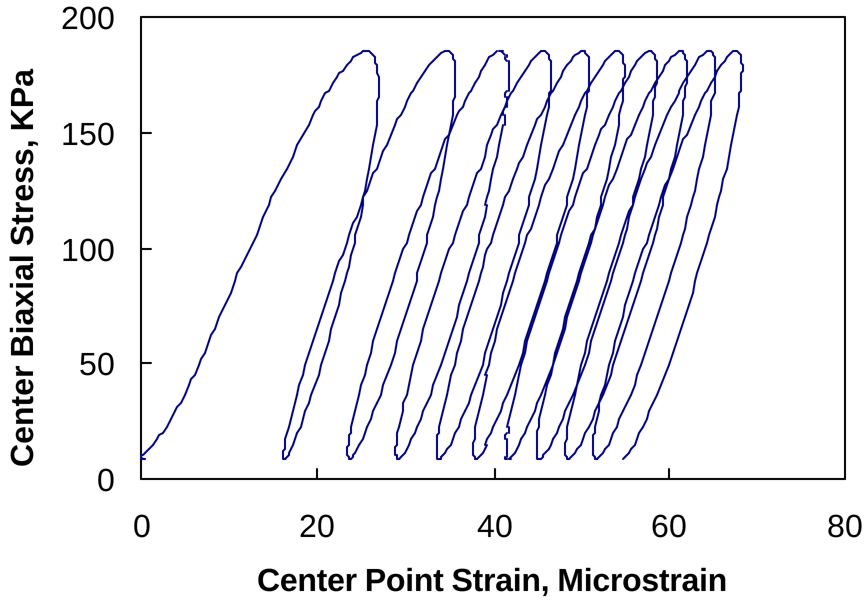

Figure 7.16 Biaxial Stress vs. Center Strain

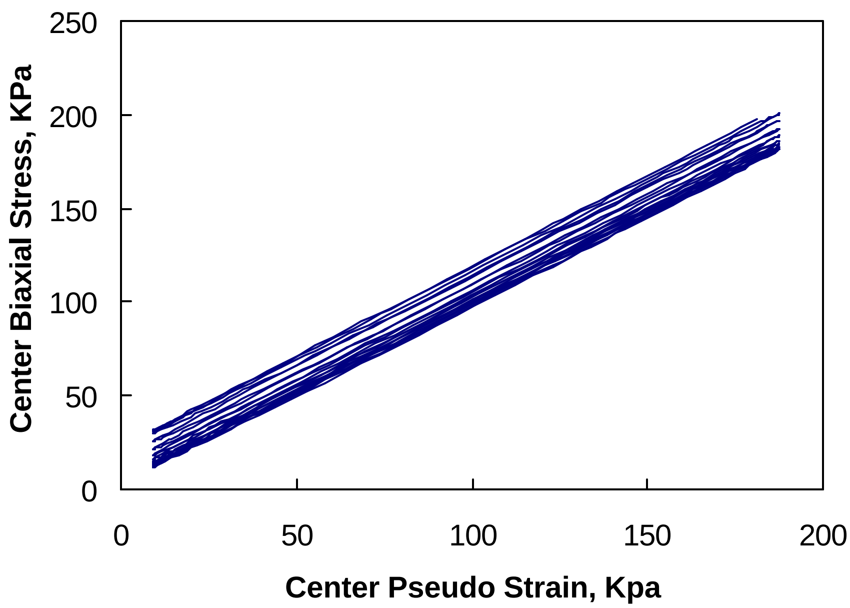

Figure 7.17 Biaxial Stress vs. Pseudo Strain

7.6 Effect of Specimen Geometry

In this study, the samples compacted by the IPC Servopac Gyratory Compactor were 150 mm in diameter by 115 mm in height. Air void contents in the samples vary along the height and diameter. The air void contents in the outer ring and at both ends of the sample are higher than that of the core of the sample. Thus, the samples were cored and cut to obtain two replicates of 100 mm diameter and 38.1 mm thickness. However, uncored specimens are preferred from the viewpoint of practical operation.

One of the disadvantages of using uncored specimens with a 150 mm diameter is that the rough lateral surface of the specimens makes it hard to position and to align them. Another critical consideration is the air void variation inside the uncored specimen; that is, the air void in the outer ring is more than 2% higher than that of the core. The air void non-uniformity inside the uncored specimen complicates the study of asphalt concrete because during testing load is directly applied to the outer ring, while the measurements are taken from the gauges in the middle of the specimen. Considering the above observations, the effects of geometry and air void variation on asphalt properties were studied using viscoelastic finite element viscoelastic analysis.

Two SGC samples, 150 mm diameter by 115 mm height, were fabricated such that the indirect tension specimens, 100 mm diameter by 38.1 mm thickness, have a 4% air void from one sample and a 6% air void from the other. Creep tests at different temperatures of 0, 13, and 20°C were conducted to obtain the creep compliance master curves of specimens with 4% and 6% air void contents, respectively. Creep compliances were converted into the relaxation modulus. Three cases were studied using finite element viscoelastic analysis, as shown in Figure 7.18.

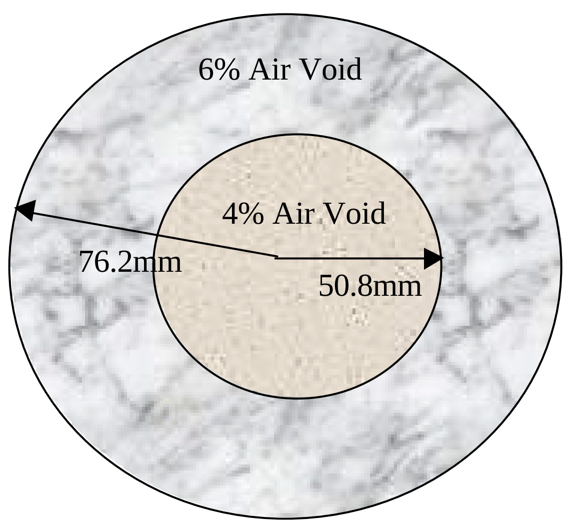

Case I: Combined Air Void Distribution and 152.4 mm Diameter

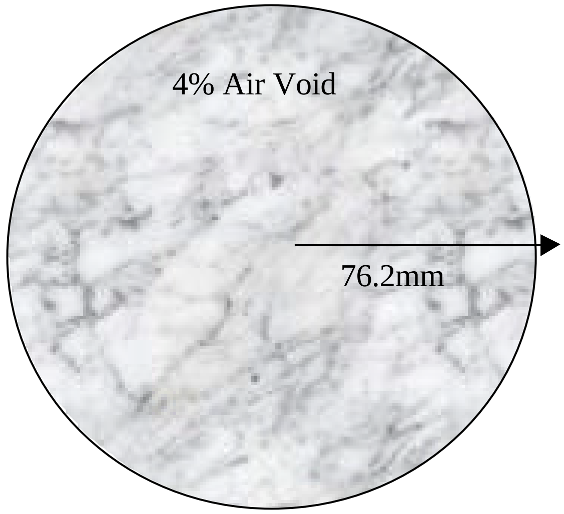

Case II: Uniform Air Void Distribution and 152.4 mm Diameter

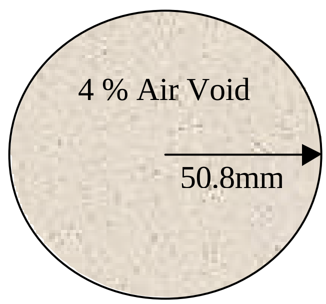

Case III: Uniform Air Void Distribution and 101.6 mm Diameter

Figure 7.18 Three Cases Studied Using Finite Element Method

The three cases studied here are representative of three kinds of specimens typically used to characterize asphalt concrete in the laboratory. These cases are described in the following:

a. Case I has a 152.4 mm diameter and non-uniform air void distribution. The air void content of the core is 4% while that of the outer ring is 6%. It simulates the laboratory- fabricated specimen cut from the SGC sample.
b. Case II has a 152.4 mm diameter and uniform air void distribution. It simulates the field cores obtained from the WesTrack sections and used in this study.

c. Case III has a 101.6 mm diameter and uniform air void distribution. It is similar to the laboratory- fabricated specimen cut and cored from the SGC sample.

The relaxation moduli measured from the 4% and 6% air void specimens were input to the finite element models of the three cases. The horizontal and vertical displacements across three gauge lengths (27.4, 50.8, and 76.2 mm) were obtained. Creep compliances were calculated according to the viscoelastic solution using Equation (7.17) and/or the ASSHTO TP9-96 method. The results are shown in Figures 7.19 through 7.21, where *LVE* is the linear viscoelastic solution, *D, AV4%* is the experimentally measured creep compliance of the specimen with 4% air voids, and *D, AV6%* is the experimentally measured creep compliance with 6% air voids.

For all three cases the linear viscoelastic solutions for a 27.4 mm, 50.8 mm, and 76.2 mm gauge lengths agree well with the properties of the material. Also, the curves are graphically indistinguishable. The TP9 method, however, underestimates the creep compliance. This finding indicates that the linear viscoelastic solutions give the actual material property of the specimen core on which the LVDTs were mounted and that the effect of the outer ring with the higher air void content on creep compliance is negligible.

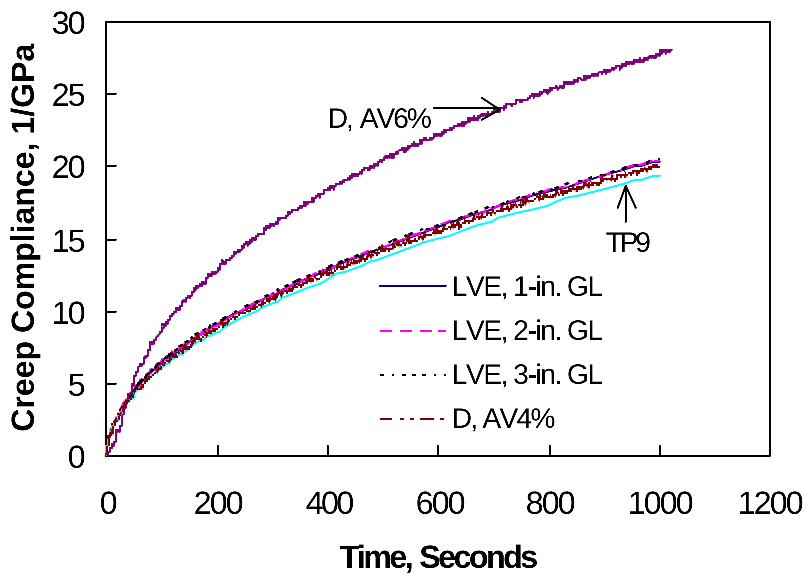

Figure 7.19 Finite Element Analysis Results for Case I

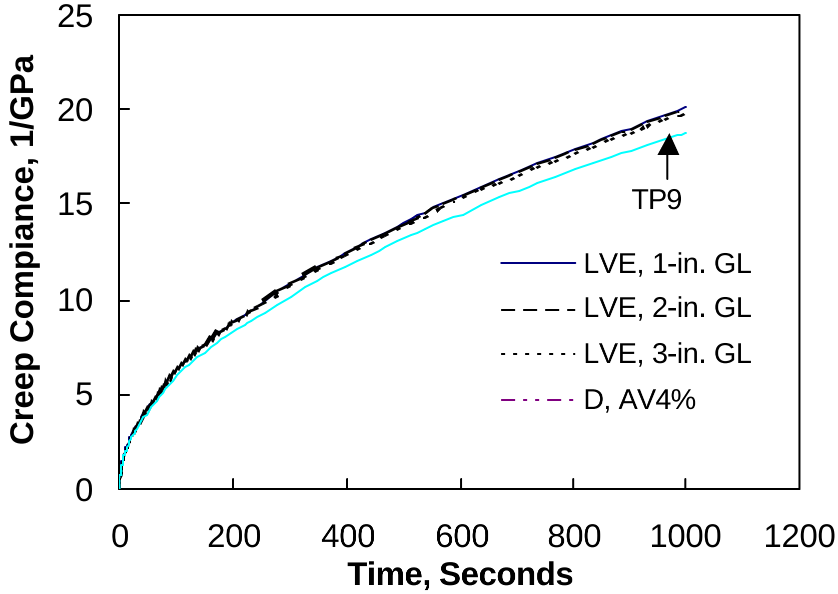

Figure 7.20 Finite Element Analysis Result for Case II

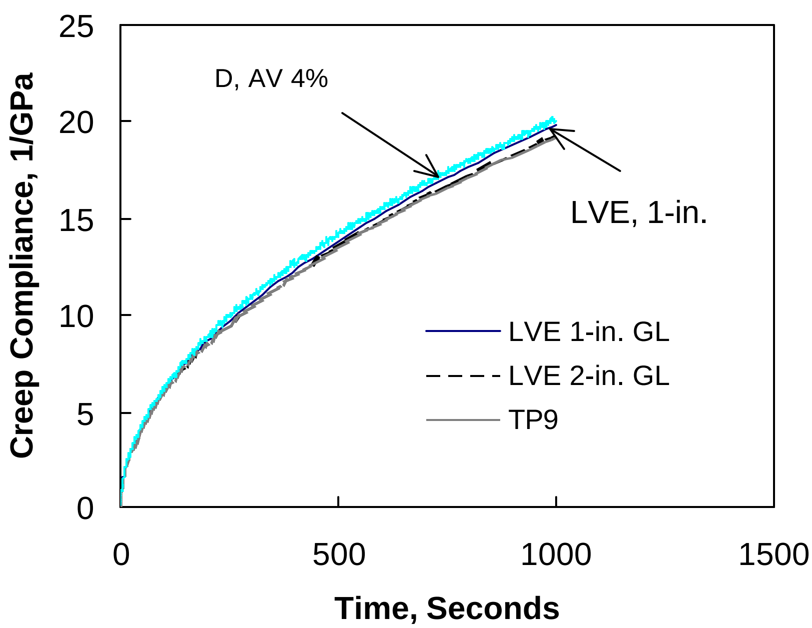

Figure 7.21 Finite Element Results for Case III

It is noteworthy that the field cores have smooth lateral surfaces while the surfaces of uncored laboratory specimens are rough. Therefore, cored specimens are preferred to avoid experimental errors and reduce variability. Moreover, the above investigation focused on the behavior of asphalt concrete within the linear viscoelastic range. The effects of a higher level of air void in the outer ring on the results of a monotonic test remain unknown. Based upon these observations, 100 mm diameter specimens cored from 150 mm SGC specimens and 150 mm diameter field cores were selected for testing in this study.

7.7 Effect of Bulging

The displacement measurement accuracy may be affected by the bulging of the indirect tension specimen. Figure 7.22 illustrates the bulging that occurred during the test. The effect of bulging on measurement is dependent on the gauge length and test temperature. The bulging effect was studied for specimens with different diameters and gauge lengths at temperatures of 0, 13, and 20°C using the finite element analysis. These results are shown in Figures 7.23 and 7.24. It appears that for the horizontal measurement, the error due to bulging increases with the decrease of gauge length, and the opposite is true for vertical measurement. Temperature has a minor effect on the errors for both the horizontal and vertical measurements. It was found that the maximum error due to bulging for either vertical or horizontal measurements is less than 5 percent. For the 50 mm gauge length and 20°C test temperature to be recommended later in this report, the error was 2.4% for the horizontal measurement and 2.5% for the vertical measurement. Thus, the bulging effect in this study was disregarded.

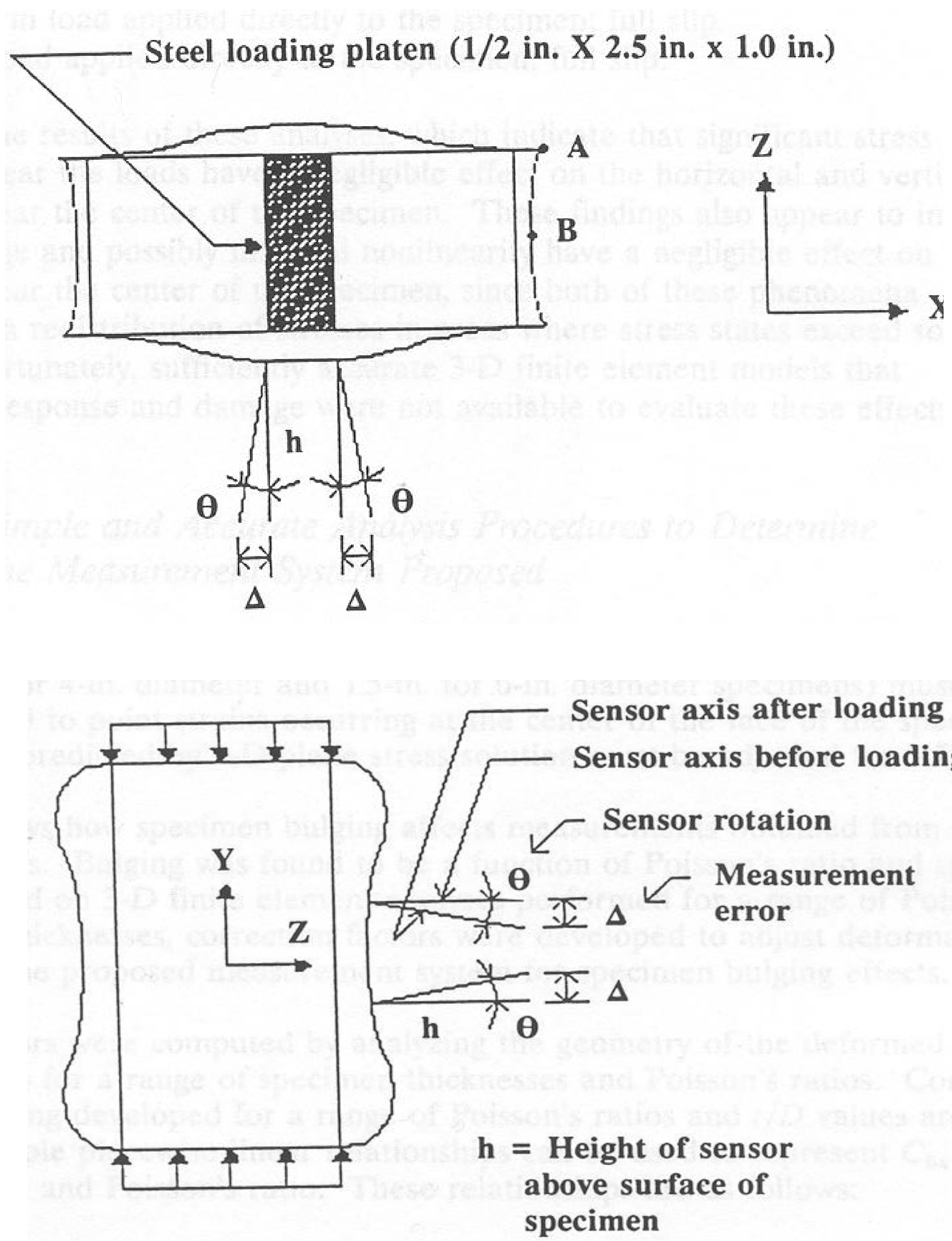

Figure 7.22 Illustration of Bulging Effects (after Roque et al., 1992)

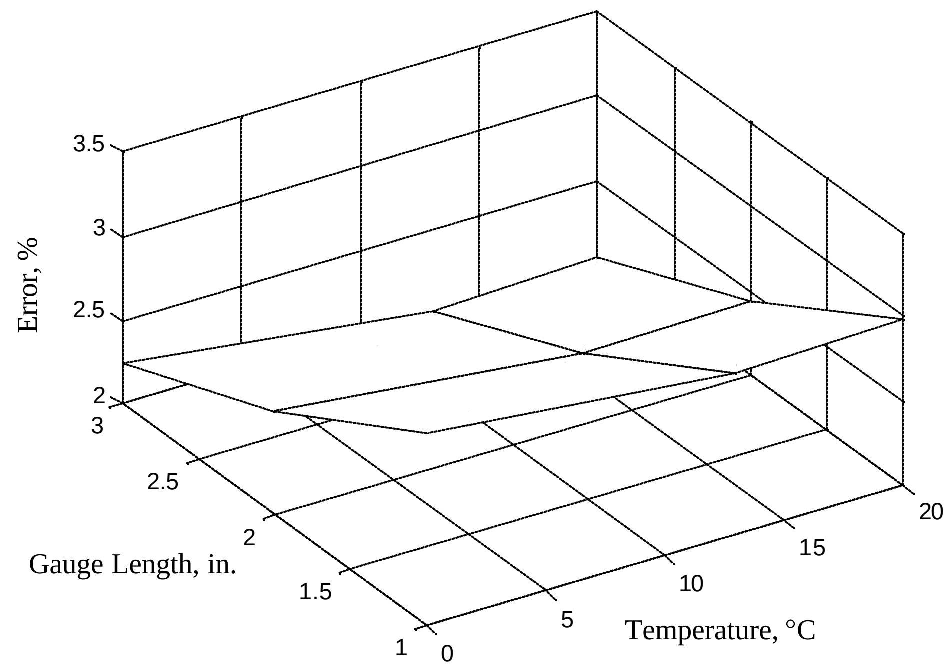

Figure 7.23 Effect of Bulging on Horizontal Measurement

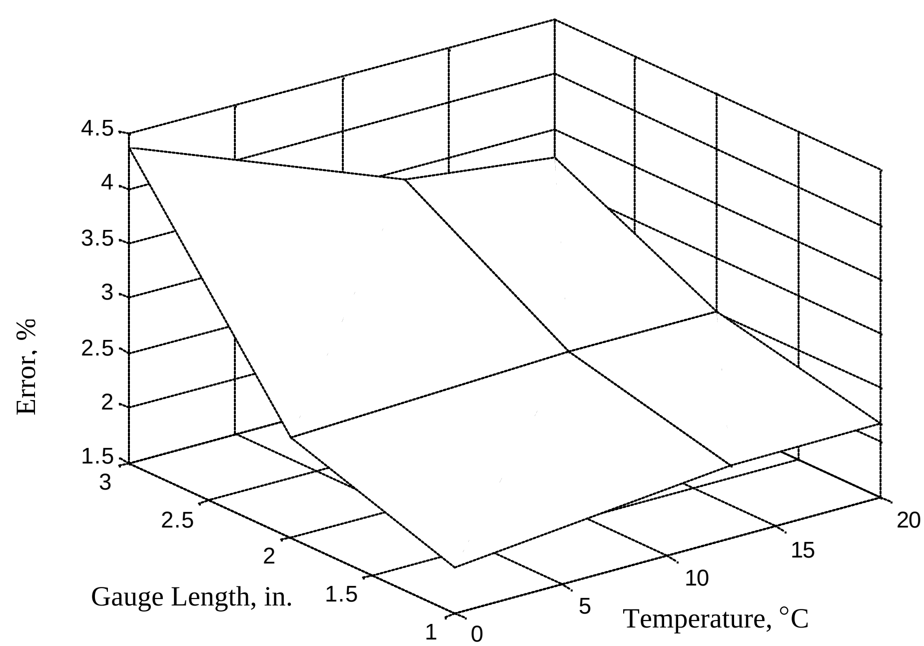

Figure 7.24 Effect of Bulging on Vertical Measurement

8. DEVELOPMENT OF A SIMPLE PERFORMANCE TEST AND VALIDATION

Experimental results from the uniaxial direct tension and indirect tension tests on WesTrack mixtures were analyzed in this section. Various engineering parameters were determined and compared with the field performance of WesTrack pavement sections to develop the simple performance test protocol. A stepwise approach was adopted. A simple performance test was expected to provide reliable information on the performance of asphalt concrete during the volumetric mixture design process using SGC. Therefore, laboratory mixed-laboratory compacted (LMLC) specimens were used to identify promising parameters. However, it is imperative that field cores of pavement be used in order to verify the simple performance test in the laboratory because the laboratory mixing and compacting processes are only intended to simulate field mixing and field compaction. Although the field cores were 150 mm tall, direct tension testing is not recommended because of the weak interface between the top and bottom lifts. Therefore, field cores sampled from several sections of WesTrack were evaluated using the indirect tension test only. The comparative analysis between laboratory test results on the cores and the field performance was performed to finalize the simple performance test protocol for fatigue cracking.

8.1 WesTrack Field Performance

The fatigue performance in the field for the WesTrack sections was measured by the percentage of cracking in the left and right wheelpaths and was obtained from the WesTrack database (2000). The fatigue cracking in the WesTrack project was bottom-up fatigue cracking, confirmed by multiple cores taken from the pavement sections (1998). Table 8.1 shows the field performance for those sections of interest in this study (i.e., the sections from which laboratory-mixed-laboratory-compacted (LMLC) specimens or field cores were available). The three traffic levels shown in Table 8.1 has the following significance: 5 million ESALs were the total traffic volume during the entire WesTrack project period, 2.8 million ESALs were the traffic level at which most of the coarse sections were removed, and 2.2 million ESALs represent the traffic volume the replacement sections were subjected to for the remaining project period.

All the mixtures with 12% air void content (“H” in the middle of the three-letter acronym) were not realistic to fabricate in the laboratory using the Superpave Gyratory Compactor and, therefore, were not available for testing. The coarse mixtures were replaced/reconstructed after the application of about 2.8 million ESALs, and the replacement sections were noted with “r” after the mixture identification.

The comparison of the fatigue performance data shown in Table 8.1, especially the fine mixtures, demonstrates the beneficial effects of a higher asphalt content and lower air void content on the fatigue performance. FHL has a low asphalt content and high air void level and, hence, has the largest amount of fatigue cracking. Since FML has a lower air void level compared to FHL, it has less fatigue cracking and higher fracture energy. FHO, with a higher air void level and asphalt content, shows less cracking compared to FML, indicating that the beneficial effect of increasing the asphalt content from low to optimum on resistance to cracking is predominant, compared to the deleterious effects of increasing the air void level from medium to high.

Table 8.1 Field Fatigue Performance of WesTrack Mixtures

			Traffic (million ESALs)		
			5	2.8	2.2
Mixture	**LMLC[a]**	**Cores**	**Fatigue Cracking (%)**		
FLO	x	x	0.1	0	0
FML	x	x	37.5	7.7	0
FMO1	x	x	0.85	0	0
FMH	x	x	1	0	0
FHL1		x	57.6	N/U[d]	0.9
FHO		x	8.9	N/U	1.1
CLO	x	x	N/A[e]	0	0
CML	x		N/A	96.7	N/U
CMO	x		N/A	49.7, 0[b]	N/U
CMO2r[c]		x	N/A	N/U	0
CMH	x		N/A	0	N/U
CHLr[c]		x	100	N/U	90
CHOr[c]		x	100	N/U	45.05

Notes:
[a]Laboratory-Mixed-Laboratory-Compacted
[b]Fatigue cracking data were available from two replicate sections.
[c]These sections were reconstructed with different aggregate source.
[d]Performance data from these cells were not used because corresponding laboratory data were not available.
[e]Not available.

8.2 Fatigue Performance Prediction Using IDT on LMLC Specimens

Since the simple performance test was expected to provide reliable information on the performance of asphalt concrete during the volumetric mixture design process, LMLC specimens were first used to identify suitable indicator(s) for fatigue cracking. Eight mixtures were selected to fabricate the specimens in the laboratory, four coarse gradation mixtures and four fine gradation mixtures. The four coarse gradation mixtures are CLO, CML, CMO, and CMH and the four fine gradation mixtures are FLO, FML, FMO, and FMH. Some mixtures cannot be realized in the laboratory, such as high air void with high asphalt content or low air void with low asphalt content.

First, compaction efforts for the mixtures were investigated to fabricate the specimens in the laboratory at the target air void contents. The heights of the samples were adjusted to obtain the target air void levels while the mass of each batch of mixture was constant. Secondly, the samples were cored, using a 100 mm diameter masonry bit, and then were cut into two indirect tension specimens, 100 mm in diameter and 38 mm in thickness. Thirdly, indirect tension creep tests were conducted for 200 seconds. After a rest period of half an hour, a tensile strength test was performed with a rate of crosshead movement at 50 mm per minute until failure of the specimen. Both the creep test and strength test were conducted at a temperature of 20°C.

Poisson’s ratio was calculated using Equation (7.16). In a creep test, the load applied should be small enough so that no damage occurs and so that Poisson’s ratio is constant for a particular mixture. However, in a tensile strength test, the crack induced within the range of the gauge length could result in greater horizontal deformation and, hence, a higher Poisson’s ratio. Fairhurst et al. (1990) found that Poisson’s ratio increases with an increase in temperature and concluded that Poisson’s ratio serves as an indicator of excessive damage to a specimen. Figures 8.1 and 8.2 present Poisson’s ratio in a creep test and a tensile strength test, respectively. In Figure 8.1, the initial value of Poisson’s ratio is highly fluctuating, due to the electrical noise of LVDT and small initial deformation of specimen, and then gradually stabilizes at a certain value, while in Figure 8.2, Poisson’s ratio increases with the increase of time.

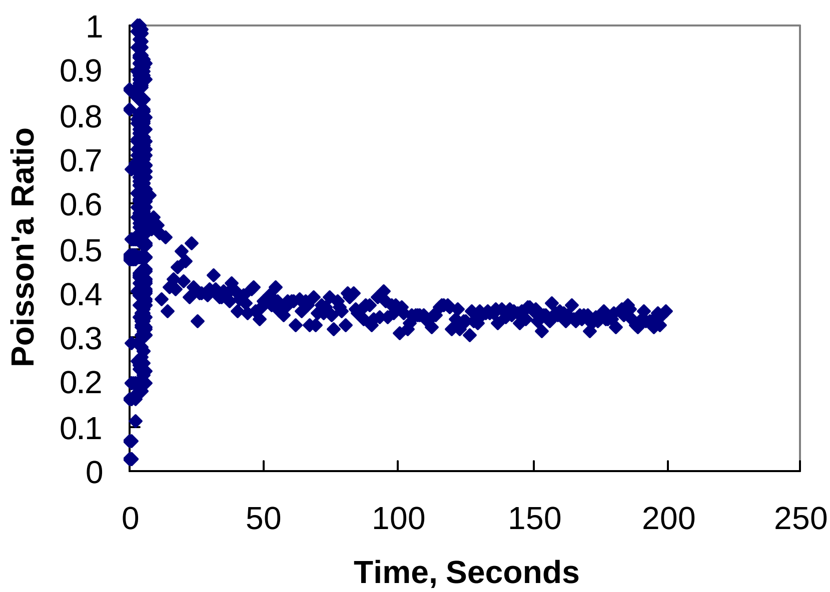

Figure 8.1 Poisson’s Ratio in Creep Test

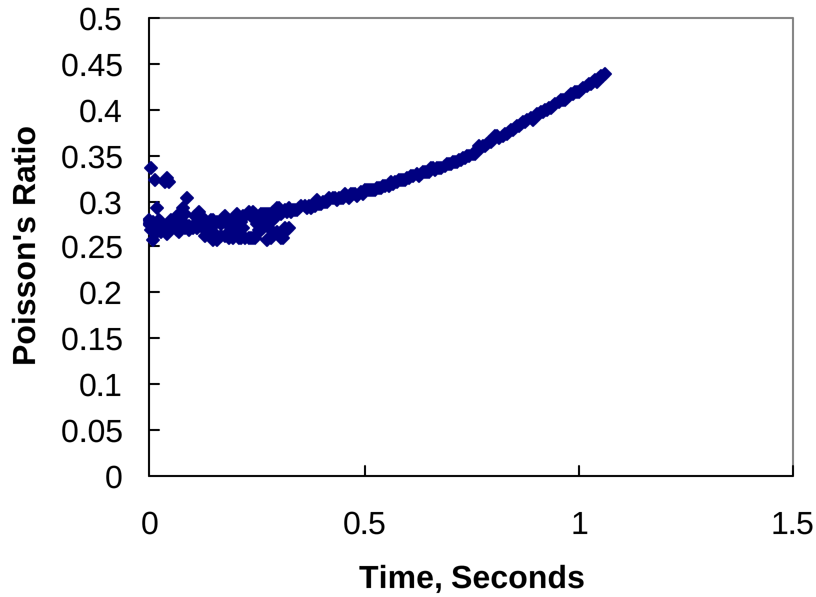

Figure 8.2 Poisson's Ratio in Tensile Strength Test

Figures 8.3 and 8.4 show creep compliances of four coarse and four fine gradation mixtures, respectively, calculated from Equation (7.17). It is seen that at 200 seconds (the end of the creep test), at a constant air void content, the mixture with the higher asphalt content has a higher creep compliance value and that, at a constant asphalt content, the creep compliance value increases with the increase of air void content.

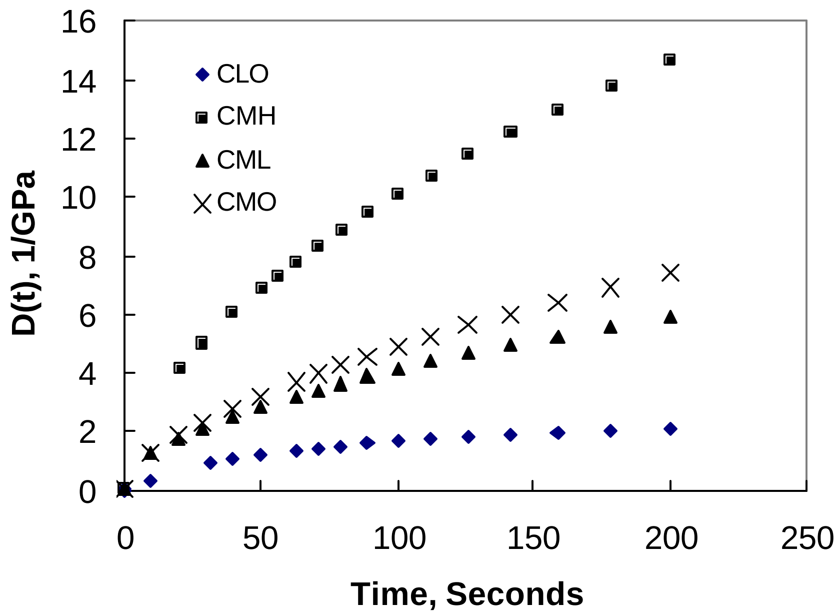

Figure 8.3 Creep Compliance of Four Coarse Gradation Mixtures

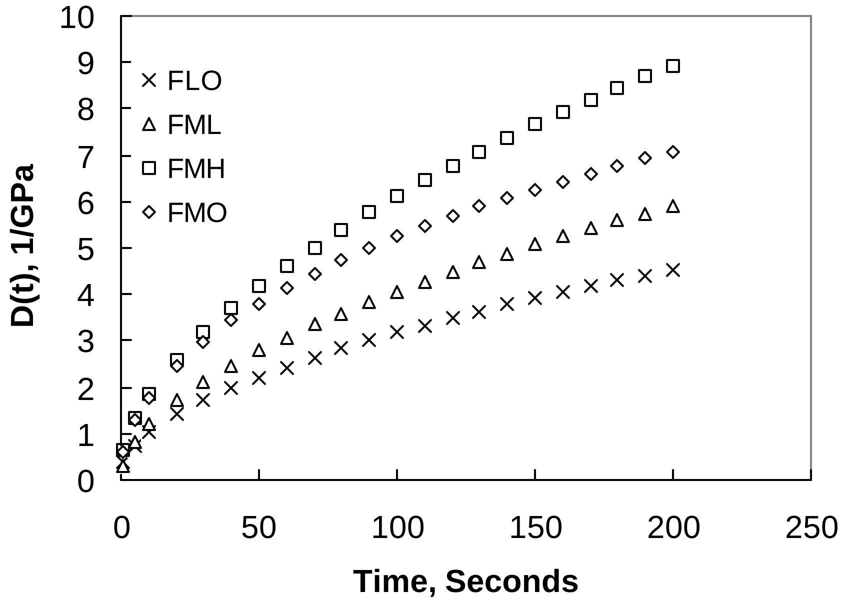

Figure 8.4 Creep Compliance of Four Fine Gradation Mixtures

As shown in Table 8.1, at 5 million ESALs, fatigue performance data are available from only fine mixtures. Therefore, performance data at 2.8 million ESALs were used in identifying the performance indicator(s) from LMLC specimens.

Various engineering parameters were determined from the indirect tensile creep and strength test results. They include: (1) creep compliance at 200 seconds, (2) m-value (the slope of the linear portion of the creep compliance-time curve on a logarithmic scale), (3) indirect tensile strength, (4) horizontal center strain at failure, and (5) fracture energy.

The validity of the first four parameters listed above is checked in Figure 8.5 against the field performance at 2.8 million ESALs. The normalized ratio presented in the ordinate is the value of a specific parameter for a certain mixture, divided by the largest value of that parameter among all the eight mixtures shown. In this figure, the mixtures in the abscissa are listed in the order of increasing resistance to fatigue cracking from left to right. At this level of trafficking, the CML mixture shows the greatest evidence of fatigue cracking, followed by the CMO, and then the FML sections. The remaining mixtures (FLO, FMO, FMH, CLO, CMH) show no or negligible fatigue cracking. The order of these mixtures is determined by engineering judgment as to which mixtures would exhibit more fatigue cracking if loading continued.

Creep compliance is a fundamental property of a viscoelastic material that represents both the stiffness and time-dependence of the material. However, the creep compliance at 200s indicates the stiffness of the material, not the time-dependence. In Figure 8.5, the effect of aggregate gradation on creep compliance is not evident. It appears that the ranking of creep compliance does not match that of field performance. It is inferred that the stiffness of the mixture itself does not contain enough information to predict the resistance of the mix to fatigue cracking.

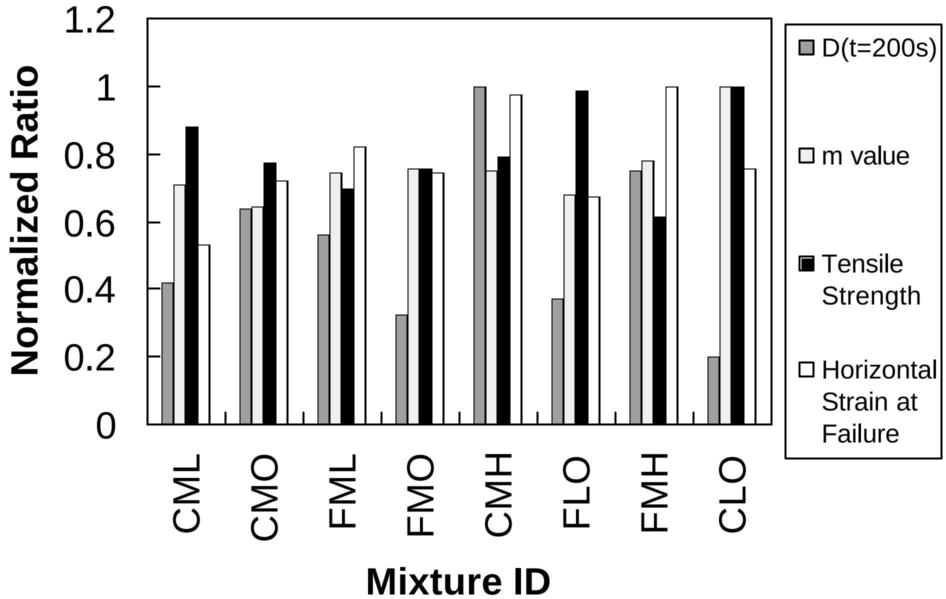

Figure 8.5 Evaluation of Four Engineering Parameters As Performance Indicators Using LMLC Specimens

Theoretical and empirical work by Jacobs et al. (1996) has indicated that the crack propagation is related to the m-value of the creep compliance curve. In Figure 8.5, no clear relationship between the m-value and the amount of fatigue cracking was observed.

Another two typically used parameters in indirect tensile strength testing are the tensile strength and the horizontal strain at failure. Neither the maximum tensile stress nor the horizontal strain at failure can serve as the indicator of resistance to fatigue cracking, according to the trends shown in Figure 8.5.

The fracture energy of a medium, defined by the area under the stress-strain curve in the loading portion, is the sum of the strain energy and the dissipated energy due to structural changes (such as microcracking). It must be pointed out that the resistance of asphalt concrete to fatigue cracking must be quantified by considering both resistance to deformation and resistance to damage. That is, the work applied by a vehicle on a pavement in the field is consumed by deforming the material as well as by creating damage in the material. For example, the resistance to fatigue cracking of a highly elastic material is good because much work is involved in deforming the material before it initiates damage. Therefore, in this type of material, much more work is involved in straining the material before significant damage is initiated. This observation suggests that the fracture energy, the sum of strain energy and damage energy, is the proper indicator for the resistance of asphalt concrete to fatigue cracking.

The fracture energies of the eight LMLC mixtures were determined and plotted against the percentage cracking of these mixtures at 2.8 million ESALs. As shown in Figure 8.6, CML has the lowest fracture energy, followed by CMO and FML, from low to high. It appears that, for CML, CMO, and FML, fracture energies very closely correlate with the amount of fatigue cracking; that is, the mixture with higher fracture energy shows less fatigue cracking. Since other mixtures have no fatigue cracking at 2.8 million ESALs, these mixtures cannot be used to clearly demonstrate the ability of fracture energy for ranking asphalt mixtures with varying factors.

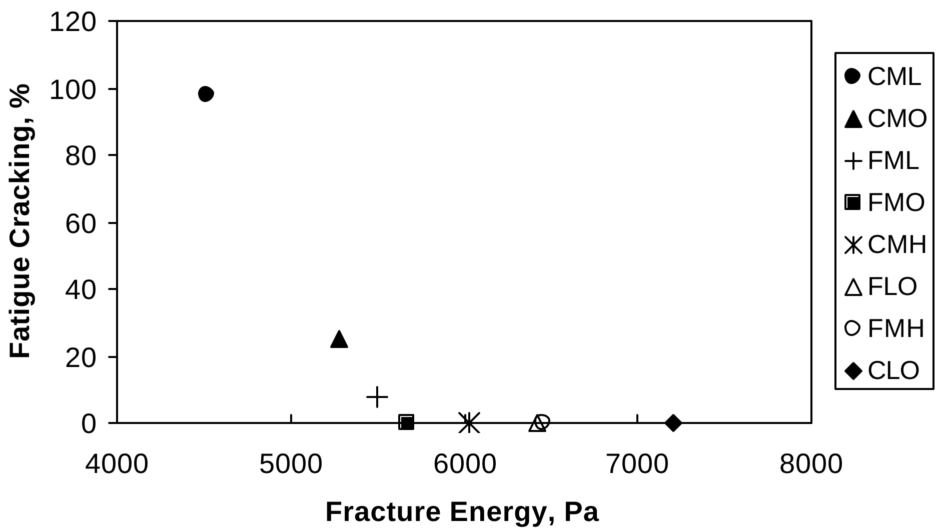

Figure 8.6 Evaluation of Fracture Energy As a Performance Indicator Using LMLC Specimens

However, the well-known effects of asphalt content and air void content on fatigue performance of asphalt mixtures may be used to assess the validity of fracture energy as an indicator for ranking the mixtures. It was reported (Epps 1998) that for both fine and coarse gradation sections at WesTrack, fatigue cracking increases significantly as air void content increases at certain binder content levels, and that an increase in the amount of fatigue cracking is evident as the binder content decreases. It was also pointed out that the coarse gradation section had the most extensive fatigue cracking. It is seen in Figure 8.6 that the fracture energy decreases as air void content increases, while an increase of fracture energy is observed as binder content increases. Based on the above description and the ranking of fracture energies, it was concluded from the LMLC specimens that fracture energy could be a good indicator of the resistance of asphalt concrete to fatigue cracking.

8.3 Fatigue Performance Prediction Using IDT on Field Cores

LMLC samples are both mixed and compacted in the laboratory and are typically used for mixture design purposes. However, it is imperative that field cores of pavement be used in order to verify the simple performance test in the laboratory because the laboratory mixing and compaction processes may not accurately simulate the mixing and compaction processes in the field. Therefore, field cores sampled from the WesTrack pavements were evaluated using the same approach employed for the LMLC specimens, except that the field cores have a 150 mm diameter.

Field cores from ten sections were available for testing. Since they were obtained between two wheelpaths, field cores were not subjected to traffic, but had been aged. CHL, CHO, and CMO2 are from replacement sections and are designated as CHLr, CHOr, and CMO2r, respectively. It is noteworthy that at the end of the WesTrack project, replacement sections experienced only 2.2 million ESALs whereas fine gradation sections experienced approximately 5 million ESALs. Table 8.1 shows the percentage fatigue cracking of these sections where field cores used in this study were obtained. Unlike the LMLC mixtures selected, these mixtures provide a diverse range of fatigue cracking. It is presumed that CMLr and CHOr have 100% fatigue cracking based upon the observation of their performance at 2.2 million EASLs.

Figure 8.7 presents the fracture energy values of the cores against the percentage fatigue cracking at 2.2 million and 5 million ESALs. The fracture energy value shown in these figures is the average of two specimens that were cut from the top and bottom lifts in the field core. Since only three mixtures had cracking at 2.2 million ESALs, the trend line cannot be accurately identified from Figure 8.7(a), although there is a trend that the higher the fracture energy, the more resistant the mix for fatigue cracking. In Figure 8.7(b), for the 5 million ESALs, it is seen that a very good correlation exists between the fracture energy and the percentage fatigue cracking. Since these cores were comprised of varying gradations, asphalt contents, and air void contents, the fracture energy determined from the indirect tensile strength test seems to be a good indicator for the mixtures with these variations.

The relationship between fracture energy and fatigue cracking, shown in Figure 8.7(b), should not be represented by linear or power equations. This effort may lead to an erroneous relationship because linear or power regression may produce an unrealistic (negative or larger than 100%) prediction of fatigue cracking. A modified logit model was proposed in this study to fit the data in Figures 8.7(a) and (b):

$$F = \exp\left(\frac{\ln\dfrac{100-C}{C} - b}{a}\right) \tag{8.1}$$

where F = fracture energy,
C = fatigue cracking percentage, and
a, b = regression coefficients.

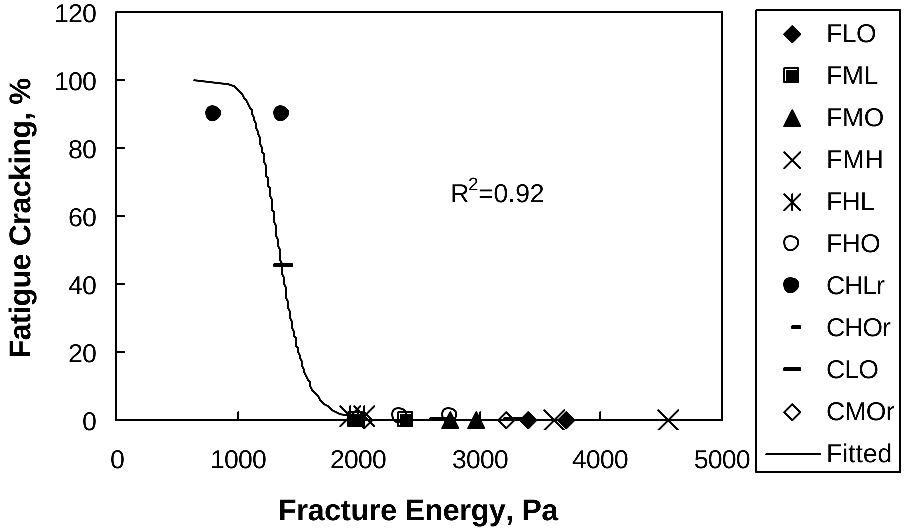

(a) At 2.2 million ESALs

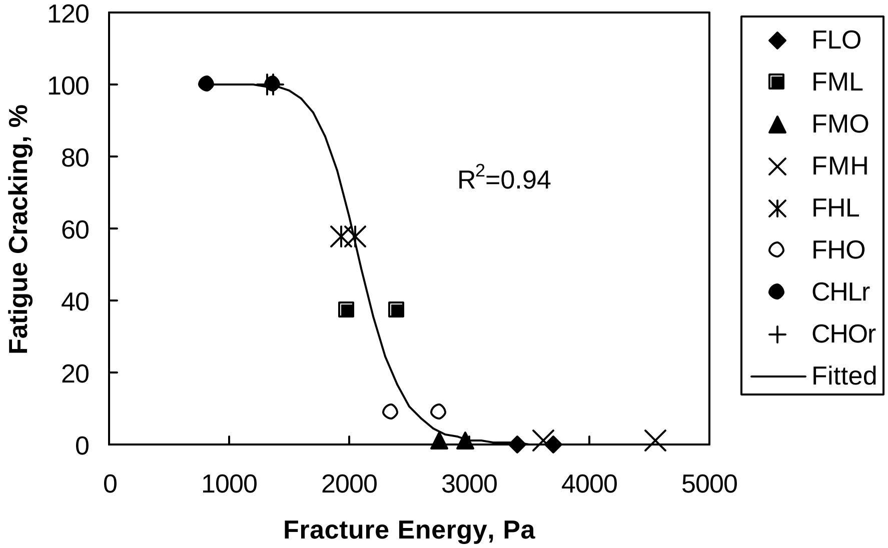

(b) At 5 million ESALs

Figure 8.7 Relationship between Field Fatigue Performance and Fracture Energy (Field Cores)

The advantage of making use of the modified logit model is that it limits the percentage of fatigue cracking to fall within the range of 0-100%, and the "S" shape shows realistic fatigue cracking development. As shown in Figure 4.11, fracture energy consists of strain energy and damage energy. Additional analyses were performed using the strain energy and damage energy, and the results are shown in Figures 8.8 and 8.9. It was found that both strain energy and damage energy are also highly correlated to the amount of fatigue cracking. For 5 million EASLs, the regression coefficients, a and b, in Equation (8.1) are listed in Table 8.2.

Table 8.2 Regression Coefficients in Equation (8.1)

	Fracture Energy	Strain Energy	Damage Energy
a	11.9	12.39	11.29
b	91	88.8	77.3

It is noteworthy that the regression is based on the amount of fatigue cracking at 5 million ESALs and that fracture energy is obtained from indirect tensile strength testing at a rate of ram movement 50 mm per minute at 20°C. Therefore, the coefficients in Equation (8.1) are dependent on traffic volume, test temperature, and rate of ram movement in indirect tensile strength testing.

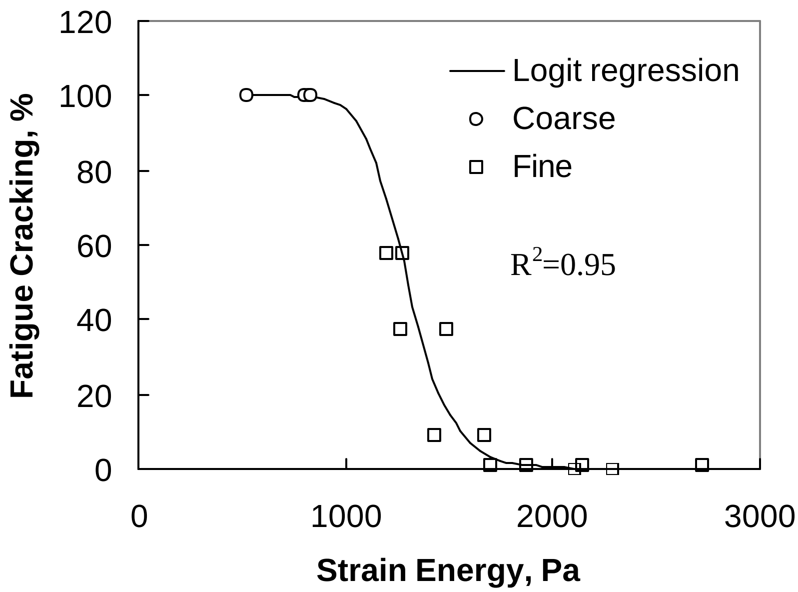

Figure 8.8 Relationship between Strain Energy and Field Performance

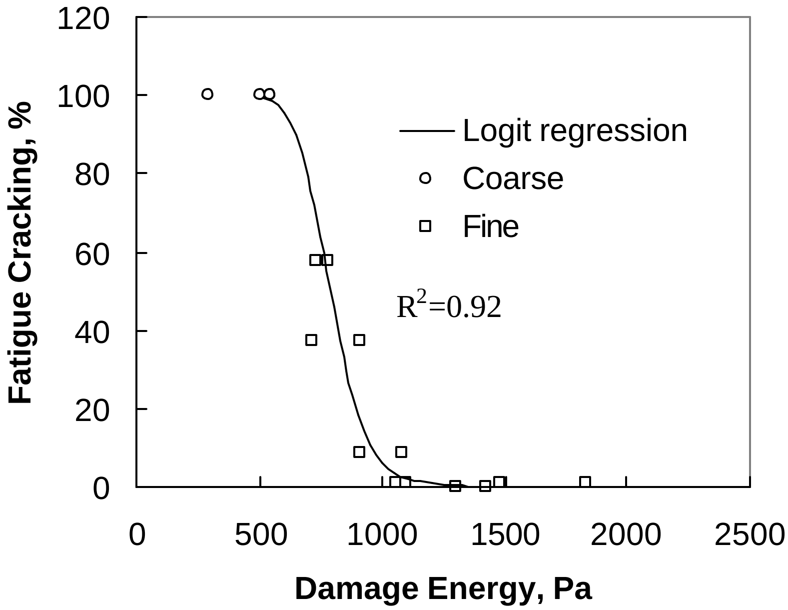

Figure 8.9 Relationship between Damage Energy and Field Performance

8.4 Fatigue Performance Prediction by Uniaxial Testing

Since the field cores could not be used for uniaxial direct tension testing due to their geometry, only LMLC specimens were available for the comparative analysis with field performance. Therefore, the only sections in Table 8.1 that are applicable to the direct tension testing are FLO, FML, FMO, FMH, CLO, CML, CMO, and CMH. Since these mixtures were fabricated using the original materials before the replacement, the fatigue performance among these mixtures must be compared at the 2.8 million ESAL level. At this level of trafficking, the CML mixture has the most fatigue cracking followed by the CMO and then FML sections. The remaining mixtures (FLO, FMO, FMH, CLO, CMH) have no or negligible fatigue cracking. The order of these mixtures is determined by engineering judgment as to which mixtures would exhibit more fatigue cracking if loading continued. This ranking is shown in the abscissa of Figure 8.10 in the increasing order of fatigue cracking potential from left to right. It is interesting to note that the two CMO sections (5 and 24) have very different fatigue performance at the same traffic level. The fatigue cracking in the left wheel path is always greater than the cracking in the right wheel path due to the inclination of the track and shifting payloads (Hand 1998, WesTrack Team 2000b). The in-place air voids reported in the WesTrack database were studied to check if the performance ranking might be affected by the in-place air void content. The target values were not achieved in all cases, but the relative trend with respect to air void values between mixtures is still the same so comparisons can still be made with respect to performance.

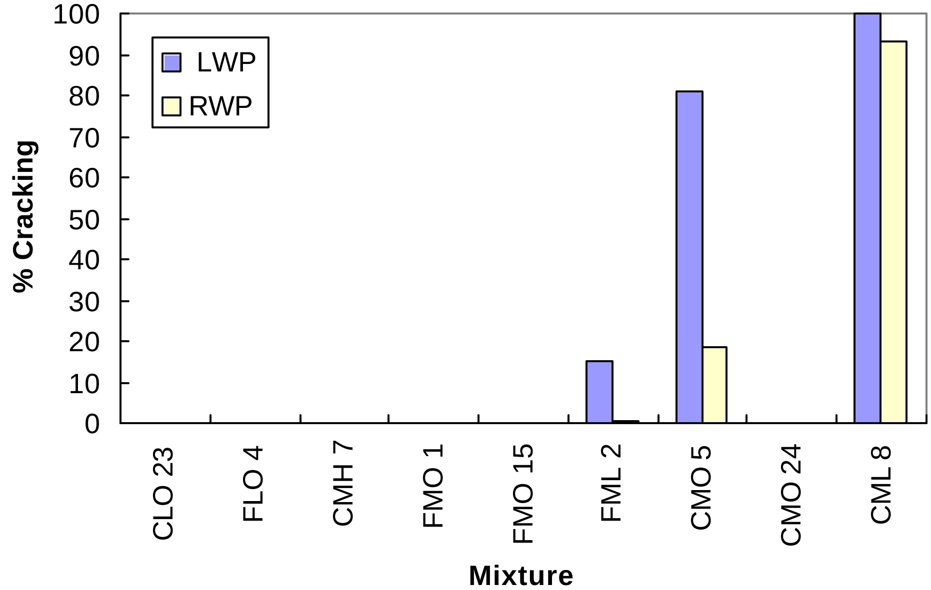

Figure 8.10 Field Performance of WesTrack Mixtures at 2.8 Million ESALs

8.4.1 Using Material Properties and Functions

One method of ranking the WesTrack mixtures is by the material properties or functions such as the dynamic modulus and the characteristic C_1 versus S_1 curve developed in the previous section. Due to the difficulty in achieving the target air void level for the FMH mixture in the laboratory, it is excluded from the ranking analysis. For ranking purposes, each parameter is plotted on the same type of bar chart as the fatigue performance in Figure 8.10 to compare trends; a similar trend indicates that parameter is a good indicator for field performance.

The most efficient way to make a comparison among the mixtures with respect to dynamic modulus is to choose a single frequency. Instead of choosing a random frequency, the frequency corresponding to the actual loading on the track is selected. To determine this frequency, the traffic speed and asphalt layer thickness must be known. According to Kim (1994), at a speed of 64 kph (40 mph) and a depth of 150 mm (6 inches), the load pulse is equivalent to a frequency of 15 Hz. Figure 8.11 shows the dynamic modulus values for the various mixtures at 15 Hz. There is no trend with respect to the field performance; however, the effects of gradation, air void content, and asphalt content on the stiffness of the material in direct tension can be seen. The coarse mixtures show a higher dynamic modulus than the corresponding fine mixtures for all of the air void and asphalt content combinations. Within each mixture, the lower air void content is stiffer, and increasing the asphalt content decreases the stiffness.

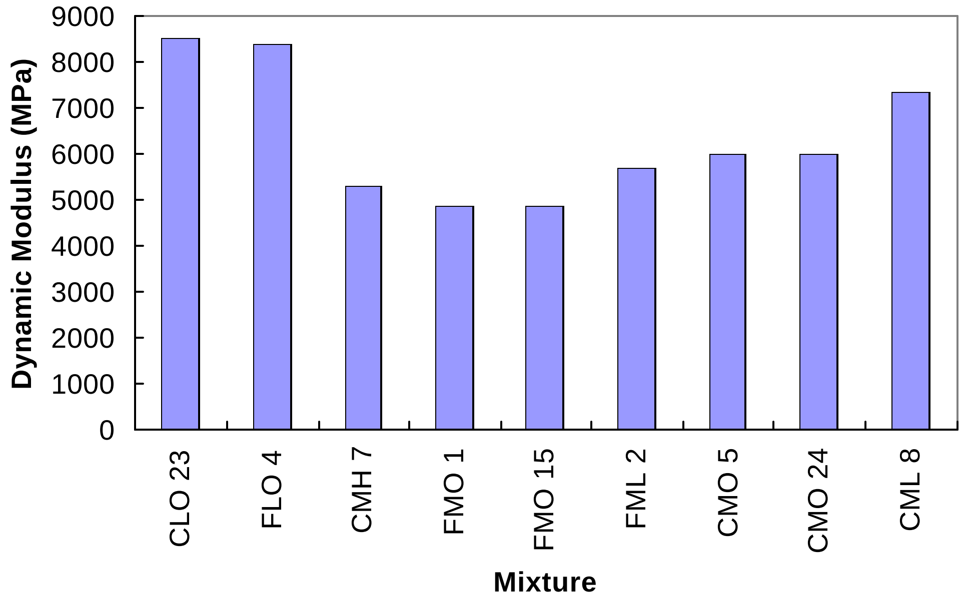

Figure 8.11 Dynamic Modulus Values at 20°C and 15 Hz for WesTrack Mixtures

Several possible indicators from the characteristic curve can be investigated: the coefficients that describe the functional form of the curve (C_{11} and C_{12} in Equation (6.21)) or the value of the damage parameter at failure, S_{1f}. Recall that failure is reached when C_1=0.3. Figures 8.12, 8.13, and 8.14 show the rankings with C_{11}, C_{12}, and S_{1f}, respectively. As can be seen, none of these parameters is a suitable indicator for field performance.

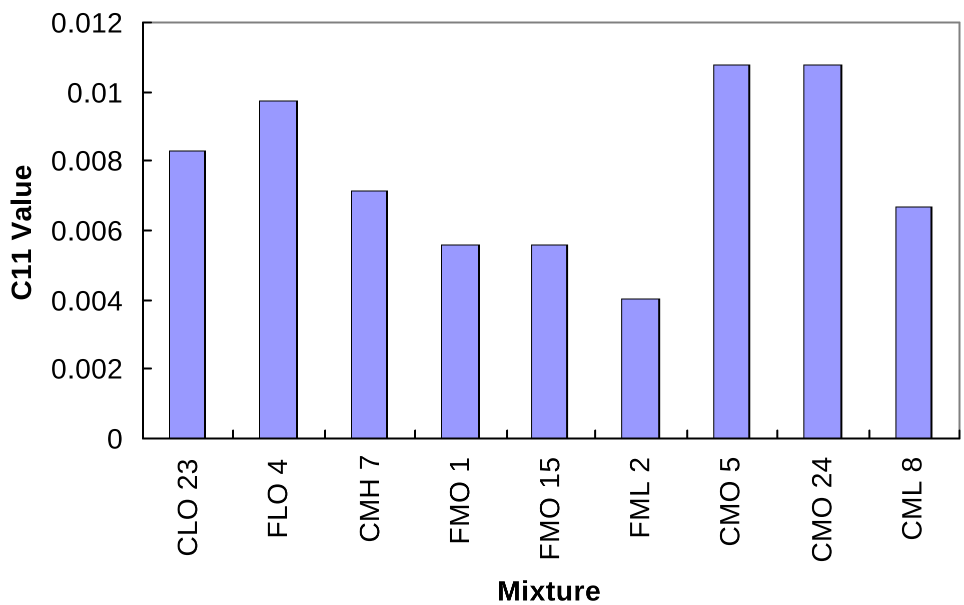

Figure 8.12 Comparison of C_{11} Values among Mixtures

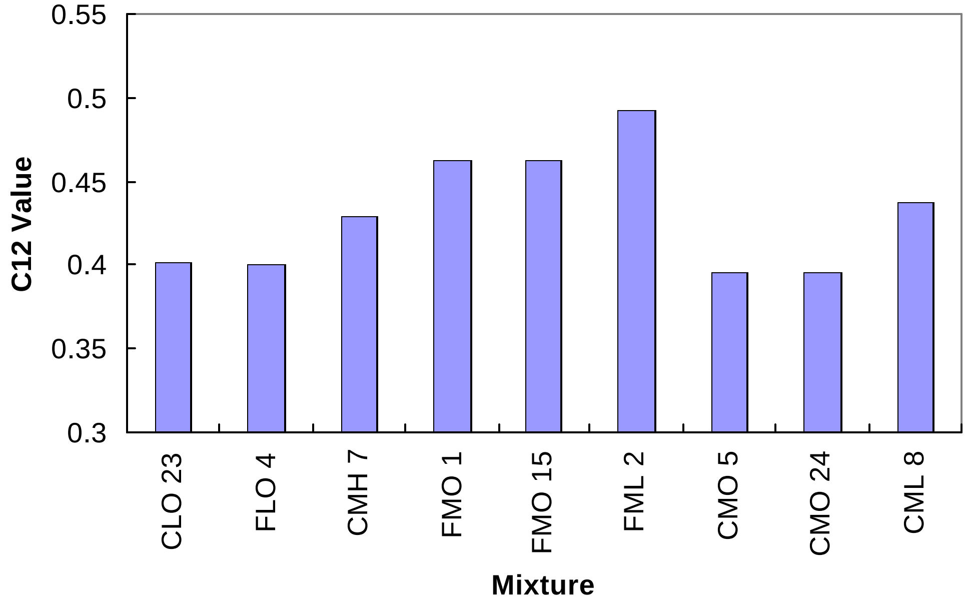

Figure 8.13 Comparison of C_{12} Values among Mixtures

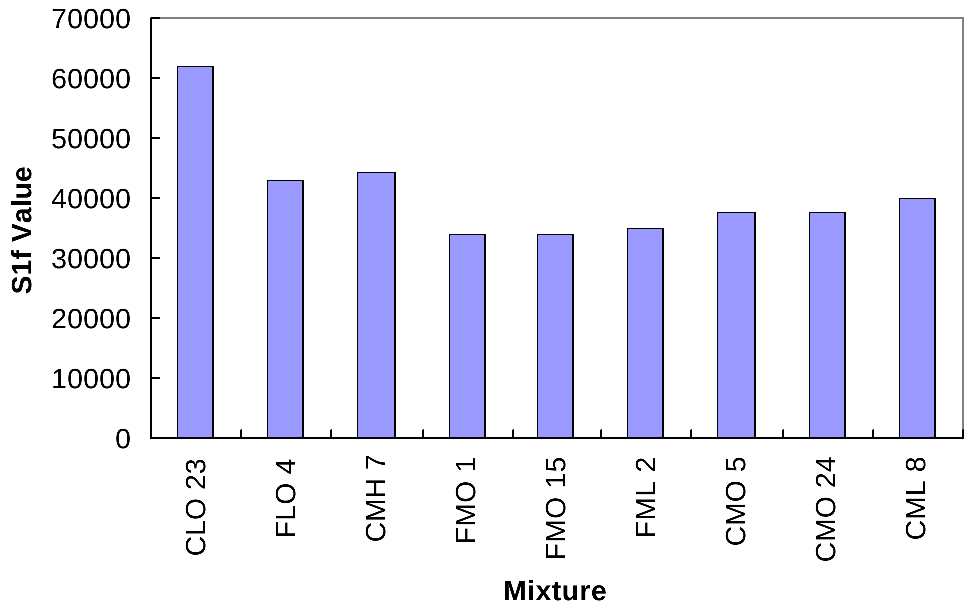

Figure 8.14 Comparison of S_{1f} Values among Mixtures

One final parameter is examined that combines the damage characteristics and stiffness of the material: S_{1f} divided by dynamic modulus. The idea behind this parameter is to account for the different stiffnesses of the asphalt mixtures and the effect of that on the fatigue life when all of the mixtures are placed in the same structural cross-sections. The mixtures that exhibit fatigue cracking in the field will have a lower value than those that show no cracking. This parameter is shown in Figure 8.15 and, with the exception of the FLO mixture, shows a general trend with respect to the fatigue life and shows the correct trend for the coarse mixtures at the high air void content. It is difficult to determine whether the CMH mixture will have a better performance than the CLO mixture due to the increased asphalt content. Examining the ranking potential of this parameter between the two gradations is difficult. The FML mixture has a slightly lower indicator value than the CMO mixture but less fatigue cracking than the CMO5 section and more than the CMO24 section. The very different performance of the two CMO sections makes it impossible to conclude whether this indicator provides an accurate ranking of the field performance between the two different gradations.

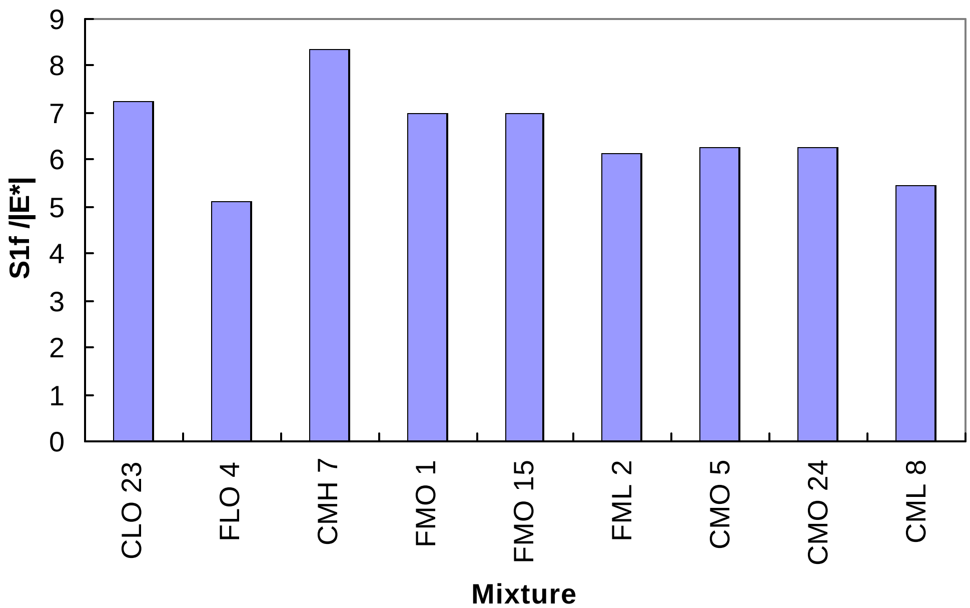

Figure 8.15 Comparison of S_{1f} Divided by Dynamic Modulus Parameter among Mixtures

8.4.2 Using Fracture Energy from Monotonic Predictions

Using the methodology described in Section 6, the stress-strain and stress-pseudo strain curves for constant crosshead rate tests may be predicted for the various mixtures. The stress-strain curves for a constant crosshead strain rate of 0.0045 are shown in Figure 8.16, while the corresponding stress-pseudo strain curves for all of the mixtures are shown in Figure 8.17. From these curves, energies can be calculated and used as possible indicators for fatigue performance.

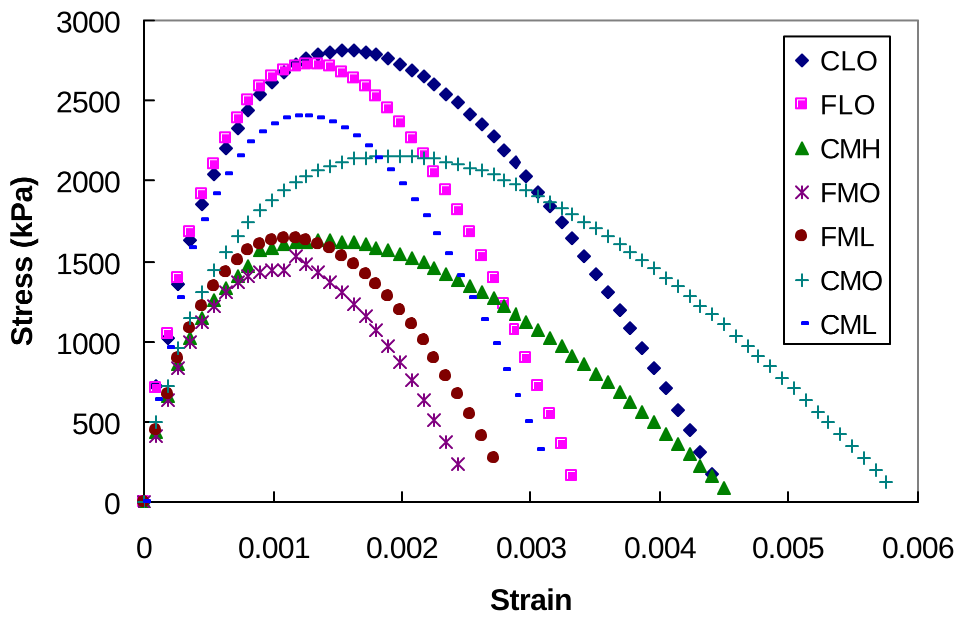

Figure 8.16 Predicted Stress-Strain Curves for Constant Crosshead Rate Test at 0.0045 strain/sec

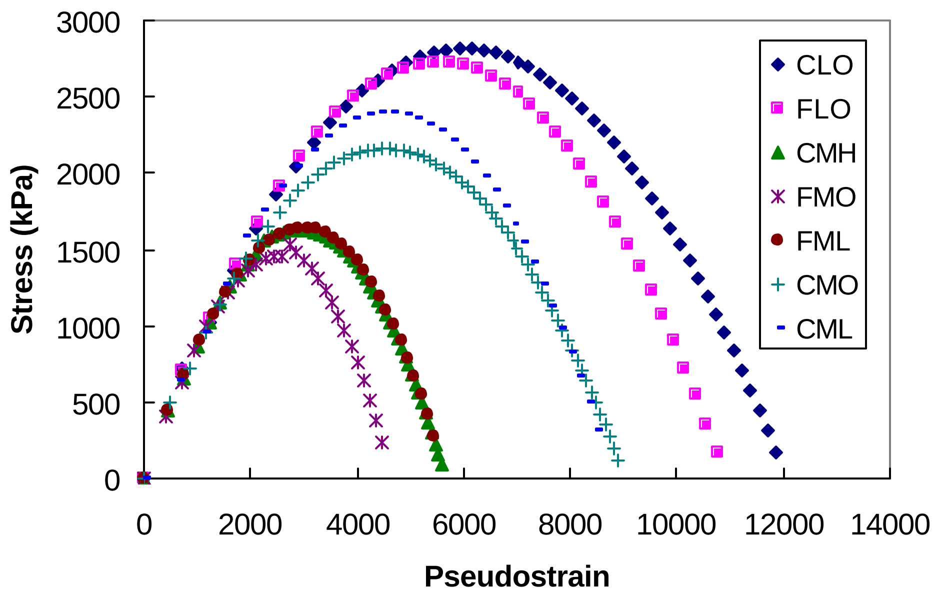

Figure 8.17 Predicted Stress-Pseudo strain Curves for Constant Crosshead Rate Test at 0.0045 strain/sec

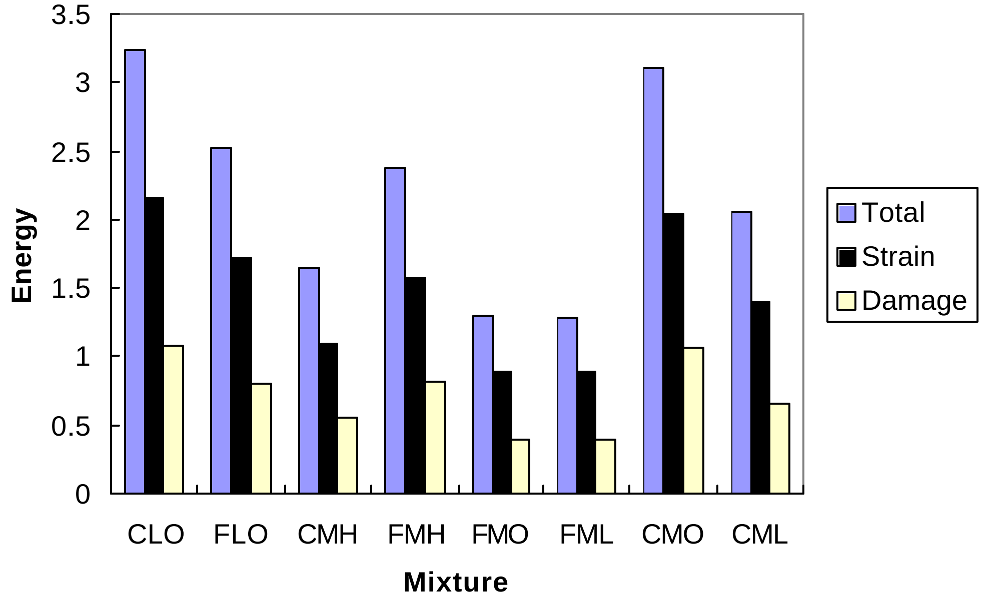

Figure 8.18 Fracture Energies for All Mixtures

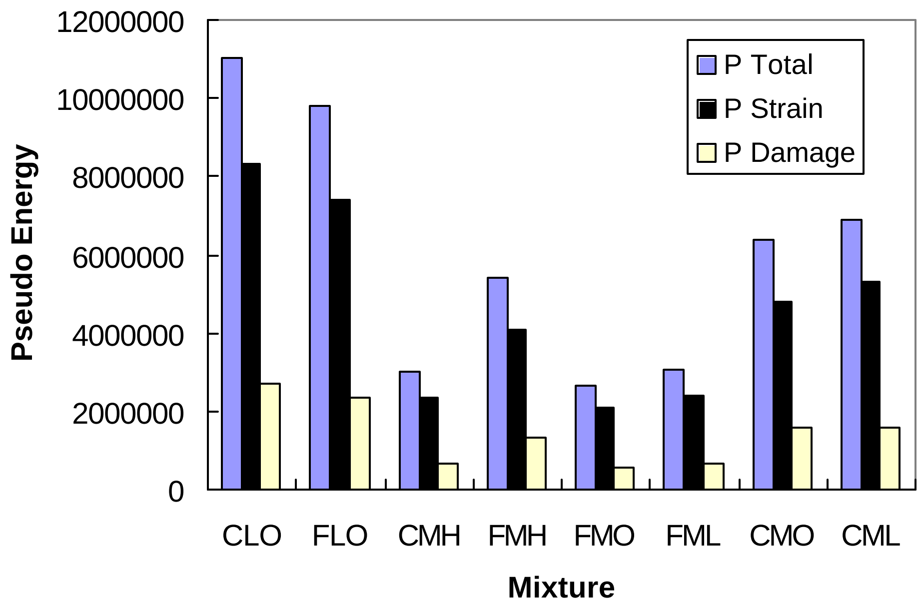

Figure 8.19 Fracture Pseudo Energies for All Mixtures

Figure 4.11 shows a schematic diagram of a stress-strain/pseudo strain curve and the three different energies that are calculated in this analysis. In all cases, the energy is calculated up to the point of peak stress. The total area under the curve is designated as the total energy. The strain energy is the area under a line drawn from the origin to the peak stress. The so-called damage energy is the difference between the total energy and the strain energy. These three energies are calculated for both the stress-strain and stress-pseudo strain curves and are plotted in Figures 8.18 and 8.19, respectively. None of the energy or pseudo energy parameters is a good indicator for the fatigue performance in the field.

8.4.3 Using Fatigue N_f Predictions and Structural Analysis

Since none of the mixture parameters showed promising results in predicting the field performance, fatigue prediction analyses accounting for the variations in sub-surface layers and AC layer were performed in this study. Prediction of the number of cycles to failure under various strain amplitudes is also possible using the methodology that is presented in the next section. In this way, the fatigue life of each mixture can be predicted using the strain amplitude to which the mixture is subject in the field. To do this, a nonlinear elastic analysis is performed on the pavement sections using the Everstress software program.

The pavement cross section for the entire WesTrack test facility consists of 150 mm (6 inches) of asphalt concrete over 300 mm (12 inches) of crushed aggregate base over 450 mm (18 inches) of fine grained engineered fill on top of the existing subgrade (WesTrack Team, 2000a). Both the subgrade modulus and the asphalt concrete modulus values change with the season of the year. A majority of the laboratory testing was performed at 20^{o}C, so it is desirable to perform the structural analysis using seasonal data where the average pavement temperature is close to 20^{o}C. A study of the pavement temperature data available in the WesTrack database (2000) showed that the month of March was a suitable choice. Values reported in the WesTrack project report (2000a) indicate that the subgrade modulus values during the month of March are 110 kPa (16 ksi) and 135 kPa (19.5 ksi) for the south and north tangents, respectively.

The WesTrack database (2000) provides base course and engineered fill resilient modulus information at various confining pressures and axial loads for selected sections on the track. With this information, a stress-dependent analysis can be performed. The aggregate base course is a granular material and the modulus is dependent upon the the value of bulk stress. The engineering fill is a fine-grained material and its resilient modulus is dependent upon the deviatoric stress. The typical stress dependency for coarse and fine-grained materials are reported in various pavement design textbooks (Yoder and Witczak 1975, Huang 1993). The customary relationships for coarse and fine-grained materials are:

$$M_R = K_1 q^{K_2} \quad \text{for coarse-grained materials} \tag{8.7}$$

$$M_R = K_3 s_d^{K_4} \quad \text{for fine-grained materials} \tag{8.8}$$

where M_R = resilent modulus,
θ = bulk stress,
σ_d = deviatoric stress, and
K_x = experimental coefficients.

The K coefficients determined for the available section data are shown in Tables 8.3 and 8.4.

Table 8.3 Resilient Modulus Coefficients for Aggregate Base Course

Section	K_1	K_2
2	4,872.2	0.6386
3	3,389.7	0.6804
4	6,580.4	0.5802
6	3,377.7	0.6675
11	3,661.3	0.6621
15	3,384.1	0.6911
17	5,314.3	0.6274
22	16,400	0.4396

Table 8.4 Resilient Modulus Coefficients for Engineered Fill Material

Section	K_3	K_4
2	157,986	-0.0174
3	155,919	0.018
5	5,600,000	-0.0329
9	121,768	-0.0205
10	125,772	-0.0172
12	164,770	0.0226
13	50,636	0.0462
14	166,002	0.0359
16	150,456	-0.0005
17	128,562	0.0398
18	139,267	0.0304
20	141,037	-0.0133
22	22,005	0.141
24	156,642	-0.0049
25	133,220	0.0459
26	10,298	0.4951

As can be seen, the resilient modulus data are not available for every section. In the cases where data for a particular section are not available, the closest or adjacent section information is used for the structural analysis. Table 8.5 summarizes the analyzed sections and the source of the ABC and fill resilient modulus data along with the appropriate dynamic modulus value for the mixture. Dynamic modulus values at a frequency of 15 Hz were used because that correlates to the truck speed of 64 kph (40 mph) on the track.

Table 8.5 Structural Analysis Information

Mixture	**Track Section**	**ABC M_R Section**	**Fill M_R Section**	**$\|E^*\|$ at 15 Hz & 20^{o}C (MPa)**
FLO	4	4	3	8,377.5
FML	2	2	2	5,697.1
FMO	1	2	2	4,861.8
FMO	15	15	14	4,861.8
FMH	14	15	14	6,213.9
CLO	23	22	22	8,539.7
CML	8	6	9	7,352.0
CMO	5	6	3	6,012.9
CMO	24	22	24	6,012.9
CMH	7	6	9	5,313.4

The triple-trailer combination vehicles used for loading the pavement have an 89 kN (20,000 lb) load applied to each axle. The tire pressure for these vehicles is 700 kPa (100 psi) (WesTrack Team 2000a). Through the analysis of several different locations, the largest strain at the bottom of the asphalt layer was found to occur at the midpoint of two adjacent tires on a single axle. The maximum stress and strain values at the bottom of the asphalt layer for the analyzed sections are shown in Table 8.6.

Table 8.6 Stresses and Strains at the Bottom of HMA

Mixture	**Track Section**	**Stress (kPa)**	**Microstrain**
FLO	4	3,349	300
FML	2	2,800	381
FMO	1	2,553	414
FMO	15	2,404	396
FMH	14	2,773	348
CLO	23	4,314	363
CML	8	3,484	354
CMO	5	2,994	382
CMO	24	2,728	353
CMH	7	2,946	426

Using the strain values determined from the structural analysis, a simulated continuous fatigue test with constant strain amplitude is performed for each section of interest. From this simulation, the number of cycles to failure for each mixture can be predicted. Analysis was also performed using an average strain amplitude of 350 microstrain for all of the mixtures. The resulting number of cycles to failure for these two scenarios are shown in Figure 8.20. Neither approach results in an agreement or even a general trend with respect to the observed performance in the field.

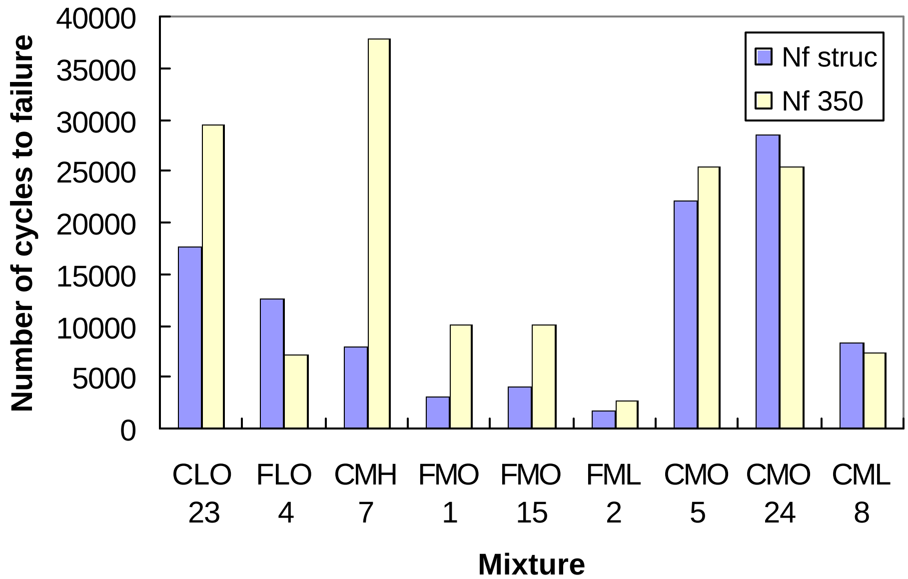

Figure 8.20 Predicted Number of Cycles to Failure Using Structural Analysis Microstrain (Nf struc) and Average 350 Microstrain (Nf 350) Amplitudes

9. CONCLUSIONS AND RECOMMENDATIONS

Based on the full-field displacement measurement using DIC and three-dimensional viscoelastic finite element analysis, a 50 mm gauge length on a 100 mm diameter IDT specimen was recommended for IDT testing. The elastic-viscoelastic correspondence principle was used to develop viscoelastic solutions for Poisson's ratio, creep compliance, and center strain in the indirect tension specimen with varying diameters and gauge lengths. These solutions were verified using three-dimensional viscoelastic finite element analysis using ABAQUS.

Indirect tensile fracture energy at 20°C, obtained from both LMLC samples compacted by Superpave Gyratory Compactor and field cores, is proven to be an excellent indicator of the resistance of mixture to fatigue cracking. The fracture energy is calculated using the strain at the center of the specimen which is determined from displacements with a 50 mm gauge length using the linear viscoelastic solutions. Before indirect tensile strength testing, indirect tensile creep testing needs to be conducted to obtain Poisson's ratio to calculate center strain. Based on the results presented in this paper, the combination of the indirect tensile creep and strength tests is proposed as a simple performance test for fatigue cracking of asphalt concrete. Since samples compacted by the Superpave Gyratory Compactor may be used in indirect tensile testing and the testing time is short, the proposed indirect tensile test protocol may be used to complement the Superpave volumetric mix design.

Damage accumulation under controlled-crosshead uniaxial tensile cyclic and constant rate loading was studied using a viscoelastic, continuum damage model. Testing performed at various cyclic strain amplitudes and frequencies and different monotonic rates produce a single characteristic curve that describes the changing material integrity as damage grows and eventually leads to failure of the mixture. Failure was defined as a 70% reduction in the initial pseudo stiffness through careful examination of both the cyclic and constant crosshead rate test data. The time-temperature superposition principle was successfully employed to describe the characteristic curve at various temperatures. The power of a single characteristic curve and the ability to shift that curve to different temperatures is that the damage evolution under any strain history and temperature can be predicted from a limited testing program. A test and associated analysis procedure for fatigue damage characterization of asphalt mixtures is proposed that takes advantage of the above methodology.

Direct tension testing did not provide a suitable performance indicator for fatigue cracking in the field. The likely reason for the inability of the direct tension testing to provide a reasonable ranking of the mixtures is the anisotropy resulting from the specimen fabrication procedures. To confirm this hypothesis for the WesTrack or any other mixture, a study must be performed on the effects of various compaction levels on the properties measured in both IDT and direct tension. Unfortunately, this is unrealistic for the WesTrack mixtures due to limited materials.

Although the proposed methodology for uniaxial testing was shown to give good predictions for the various WesTrack mixtures, future research is recommended to further expand the applicability to a wide range of situations.

1. Different asphalt-aggregate combinations, including modified binders, need to be evaluated to confirm that the methodology can be universally applied to asphalt mixtures. The WesTrack mixtures included different gradations and air void and asphalt contents, but only a single binder and aggregate source are represented.
2. The methodology needs to be evaluated in the controlled-stress mode-of-loading. The strain response in a controlled-stress case is very similar to the on-specimen response from a controlled crosshead test. Therefore, the current procedure may also apply to the controlled stress case without significant modification.
3. Application to indirect tension and compression testing should be investigated. Indirect tension testing has been shown to provide better ranking with field performance than direct tension testing for the WesTrack mixtures, and the use of this methodology in indirect tension testing could be very beneficial. While the tensile testing evaluates the fatigue cracking behavior, compression testing could be used to evaluate the rutting performance of mixtures.
4. Evaluate the effect of rest periods on the methodology, for example, a 0.1 second loading pulse followed by a 0.9 second rest period. The current methodology was developed using continuous loading which does not accurately represent the loading history a pavement is subject to in service. The piecewise linear approach to pseudo strain calculation will easily allow for the inclusion of rest periods in the analysis.
5. Include the effect of aging on the fatigue behavior of the material. A framework for including the effect of aging in the pseudo strain calculation was developed and needs to be applied to the current methodology. This becomes increasingly important if an accurate prediction of the field performance of a mixture over many years is desired.
6. Finally, more research is required to extend the methodology to multi-axial loading conditions, including the effects of confining pressure.

Additionally, further research is recommended in the indirect tension testing area to validate the developments achieved during this research study.

1. A greater variety of mixtures, besides WesTrack mixtures, should be used to validate the development of a simple performance test. WesTrack mixtures are the combinations of different aggregate gradations, asphalt contents, and air void contents. However, only one binder was used. Different binders, including modified, should be used to expand the range of applicability of the simple performance test developed here.
2. The relationship between fracture energy and field performance was established based on the WesTrack pavement field performance only. Indirect tensile strength testing at different test temperatures and different rates of ram movement is recommended to build a stronger model. In addition, more field performance data from other pavement sections should be used.

10. IMPLEMENTATION AND TECHNOLOGY TRANSFER PLAN

The major obstacle to the implementation of the findings from this project is that NCDOT and many other state highway agencies currently do not have the servo-hydraulic testing machine required to conduct the test procedures proposed in this report. However, recent efforts by the AASHTO and the NCHRP (especially the research work for the development and implementation of the AASHTO 2002 Pavement Design Guide) clearly indicate that this type of equipment will become necessary for future pavement design and asphalt mixture design to be used by state highway agencies.

The research team for the NCHRP 9-29 project is currently developing specifications for simple performance testing machines for asphalt mixtures. By the end of 2002, testing machines capable of performing the static creep test, dynamic modulus test, indirect tension test, and repetitive permanent deformation test will be available. The cost of these machines will be less than $50,000. The authors believe that these machines will play a major role in implementing the findings from this project.

The research findings in this report may not be sufficiently complete to be implemented routinely by state highway agencies yet. However, they clearly demonstrate great potential as a cost-effective performance test/analysis procedure for the fatigue cracking evaluation of asphalt concrete. The findings from this research project have been reported at the 2002 TRB meeting and the 2002 AAPT meeting. At the AAPT meeting, the principal investigator of this project participated in the panel discussion and also was invited to make a presentation on the findings from this project at the Symposium on Physical Tests for Fatigue Cracking Evaluation of Asphalt Mixtures. The responses from these national meetings were very positive in that through this research project a solid theoretical/experimental foundation has now been established in fatigue cracking evaluation of asphalt mixtures. In order to maximize the advantage afforded by these findings, further research is necessary in which the developed procedures are tested with a wider range of mixture types and performance.

11. REFERENCES

Barksdale, R.D., J. Alba, N.P. Khosla, Y.R. Kim, P.C. Lambe, and M.S. Rahman (1997). "*Laboratory Determination of Resilient Modulus for Flexible Pavement Design*" NCHRP 1-28 Final Report.

Chehab,G., E.N. O'Quinn, and Y.R. Kim (2000). "Specimen Geometry Study for Direct Tension Test Based on Mechanical Tests and Air Void Variation in Asphalt Concrete Specimens Compacted by Superpave Gyratory Compactor." *Transportation Research Record*, TRB, No. 1723, pp.125-132

Daniel, J.S. (2001). "Development of a Simplified Fatigue Test and Analysis Procedure Using a Viscoelastic, Continuum Damage Model and its Implementation to WesTrack Mixtures". Ph.D. Dissertation, North Carolina State University, Raleigh, NC.

Daniel, J.S., Y.R. Kim, and H.J. Lee (1998). "Effects of Aging on Viscoelastic Properties of Asphalt-Aggregate Mixtures." *Transportation Research Record*, TRB, No. 1630, pp.21-27.

Epps, J. (1998) Performance of HMA Test Sections at WesTrack. *Proceedings, The Association of Asphalt Paving Technologist*, pp738-782

Epps, J., S. Dewan, A. Hand, and P. Sebaaly (1999). "Resilient Modulus and Tensile Strength Properties of WesTrack Hot-Mix Asphalt Mixtures." WesTrack Technical Report UNR-26.

Hand, A. (1998). "Relationships Between Laboratory-Measured HMA Material and Mixture Properties and Pavement Performance at WesTrack." Ph.D. Dissertation, University of Nevada, Reno, NV.

Hondros, G. (1959). Evaluation of Poisson's Ratio and the Modulus of Materials of a Low Tensile Resistance by the Brazilian (Indirect Tensile) Test with Particular Reference to Concrete. *Austr. J. Appl. Sci.*, Vol. 10, No. 3, 243-268.

Huang, Y.H. (1993). "Pavement Analysis and Design." Prentice Hall, New Jersey.

Jacobs, M. M. J, P. C. Hopman, and A.A.A. Molenaar (1996). Application of Fracture Mechanics Principles to Analyze Cracking in Asphalt Concrete.

Katzke, E. D. (1997). "Non Destructive Evaluation of Asphalt Concrete Surface Layers Using Stress Wave Testing." M.S. Thesis, North Carolina State University, Raleigh, NC.

Kennedy, T. (1977). Characterization of Asphalt Pavement Materials Using the Indirect Tensile Test. *Proceedings, The Association of Asphalt Paving Technologist*, pp. 321-150

Kim, Y. (1997). “In-Situ Evaluation of Microcrack Damage and Healing of Asphalt Concrete Pavements Using Stress Wave Test.” Ph.D. Dissertation, North Carolina State University, Raleigh, NC.

Kim, Y. and Y.R. Kim (1997). "In-Situ Evaluation of Fatigue Damage Growth and Healing of Asphalt Concrete Pavements Using Stress Wave Method." *Transportation Research Record*, No. 1568, Transportation Research Board, National Research Council, Washington, D.C., pp. 106-113.

Kim, N. (1994). “Development of Performance Prediction Models for Asphalt Concrete Layers.” Ph.D. Dissertation, North Carolina State University, Raleigh, NC.

Kim, Y.R. and Y.C. Lee (1995). “Interrelationships Among Stiffnesses of Asphalt-Aggregate Mixtures.” *Journal of the Association of Asphalt Paving Technologists*, Vol. 64, pp.575-606.

Kim, Y.R., Y.C. Lee, and H.J. Lee (1995). “Correspondence Principle for Characterization of Asphalt Concrete.” *Journal of Materials in Civil Engineering*, ASCE, Vol. 7, No.1, pp. 59-68.

Kim, Y.R., H.J. Lee, Y. Kim, J.S. Daniel, and E.D. Katzke (1997). “Healing of Microcracks in Asphalt and Asphalt Concrete.” Final Report submitted to FHWA, Contract No. DTFH61-92-C-00170, Washington, D.C.

Kim, Y.R., H.J.Lee, and D.N. Little (1997). “Fatigue Characterization of Asphalt Concrete Using Viscoelasticity and Continuum Damage Theory.” *Journal of the Association of Asphalt Paving Technologists*, Vol. 66, pp. 520-569.

Kim, Y.R. and D.N. Little (1990). "One-Dimensional Constitutive Modeling of Asphalt Concrete." *ASCE Journal of Engineering Mechanics*, Vol. 116, No. 4, pp. 751-772.

Kim, Y.R. and J.S. Daniel (1997). “Development of a Mechanistic Fatigue Prediction Model for Aging Asphalt-Aggregate Mixtures.” Final Report submitted to Western Research Institute.

Kim, Y.R., G. Chehab, and Y. Seo (2001). “Validation of Time-Temperature Superposition Principle in Asphalt Concrete Mixtures with Damage.” Interim Report, subcontract under NCHRP 9-19.

Lee, H.J. and Y.R. Kim (1998a). “A Uniaxial Viscoelastic Constitutive Model for Asphalt Concrete under Cyclic Loading.” ASCE *Journal of Engineering Mechanics*, Vol. 124, No. 11, pp. 1224-1232.

Lee, H.J. and Y.R. Kim (1998b). "A Viscoelastic Continuum Damage Model of Asphalt Concrete with Healing," *ASCE Journal of Engineering Mechanics*, Vol. 124, No. 11, pp. 1-9.

Lee, H.J., J.S. Daniel, and Y.R. Kim (2000). "Continuum Damage Mechanics-Based Fatigue Model of Asphalt Concrete," *ASCE Journal of Materials in Civil Engineering*, Vol. 12, No. 2, pp. 105-112.

Lee, H.J. (1996). "Uniaxial Constitutive Modeling of Asphalt Concrete Using Viscoelasticity and Continuum Damage Theory." Ph.D. Dissertation, North Carolina State University, Raleigh, NC.

McGraw, E.O. (2000). "Quality Control in Fabricating and Testing Laboratory Asphalt Concrete Specimens." M.S. Thesis, North Carolina State University, Raleigh, NC.

Myers, L.A., R. Roque, and B. Birgisson (2001). "Propagation Mechanisms for Surface-Initiated Longitudinal Wheel Path Cracks." *80th Annual Meeting of the Transportation Research Board*, Paper 01-0433, Preprint CD-ROM.

Park, S.W. Y.R. Kim, and R.A. Schapery (1996). "A Viscoelastic Continuum Damage Model and Its Application to Uniaxial Behavior of Asphalt Concrete." *Mechanics of Materials*, Vol. 24, No. 4, pp. 241-257.

Park, S.W. and R.A. Schapery (1997). A Viscoelastic Constitutive Model for Particulate Composites with Growing Damage, *International Journal of Solids and Structures*, Vol. 34, No. 8, pp. 931-947.

Park, S.W. and Y.R. Kim (1999). "Interconversion between Relaxation Modulus and Creep Compliance for Viscoelastic Solids," *ASCE Journal of Materials in Civil Engineering,* Vol. 11, No. 1, pp. 76-82.

Park, S. W. and Y.R. Kim (2001). "Fitting Prony-Series Viscoelastic Models with Power-Law Pre-Smoothing," *ASCE Journal of Materials in Civil Engineering*. Vol. 13, No. 1, pp. 26-32.

Roque, R. and Buttlar W.G. (1992). The Development of a Measurement and Analysis System to Accurately Determine Asphalt Concrete Properties Using the Indirect Tensile Mode, *Proceedings, The Association of Asphalt Paving Technologist,* pp. 304-333.

Roque, R. and Zhang, Z.W. and Sankar, B. (1999) Determination of Crack Growth Rate Parameters of Asphalt Mixtures Using the Superpave IDT, *Proceedings, The Association of Asphalt Paving Technologist,* pp. 404-434.

Schapery, R.A. (1975). A Theory of Crack Initiation and Growth in Viscoelastic Media, Part I: Theoretical Development, Part II: Approximate Methods of Analysis, Part III: Analysis of Continuous Growth, *Int. J. Fracture*, 11, 141-159, 369-388, pp. 549-562.

Schapery, R.A. (1981). "On Viscoelastic Deformation and Failure Behavior of Composite Materials with Distributed Flaws." *Advances in Aerospace Structures and Materials*, AD-01, ASME, New York, pp. 5-20.

Schapery, R.A. (1982). “ Models for Damage Growth and Fracture in Nonlinear Viscoelastic Particulate Composites.” *Proc. Nineth U.S. National Congress of Applied Mechanics,* Book No. H00228, ASME, New York, pp. 195-223.

Schapery, R.A. (1984). “Correspondence principles and a generalized J-integral for large deformation and fracture analysis of viscoelastic media.” *Int. J. Fract*., Vol. 25, pp.195-223.

Schapery, R.A. (1987a). Deformation and Fracture Characterization of Inelastic Composite Materials Using Potentials, *Polymer Eng. and Sci.*, 27, pp. 63-76.

Schapery, R.A. (1990). “A Theory of Mechanical Behavior of Elastic Media with Growing Damage and Other Changes in Structure.” *J. Mech. Phys. Solids*, 38, pp.215-253.

Schapery, R.A. and S.W. Park (1999). “Methods of interconversion between linear viscoelastic material functions. Part II- an approximate analytical method.” *International Journal of Solids and Structures,* Vol. 36, pp. 1677-1699.

Sias, J.E. (1996). “Rate-Dependent Stiffnesses of Asphalt Concrete Used for Field to Laboratory Prediction and Fatigue and Healing Evaluation.” M.S. Thesis, North Carolina State University, Raleigh, NC.

Wen, H. (2001). Ph.D. Dissertation, North Carolina State University, Raleigh, NC.

WesTrack Team (2000a). “WesTrack Final Report Part III – Project Overview” Draft Report submitted to FHWA.

WesTrack Team (2000b). “WesTrack Final Report Part IV – Observations and Lessons” Draft Report submitted to FHWA.

WesTrack Database (2000). Beta Version - CD.

Wijk, G. (1978). Some New Theoretical Aspects of Indirect Measurements of the Tensile Strength of Rocks. *Int. J. Rock Mech. Min. Sci. & Geomech. Abstr.* Vol 15, pp 149-160

Yoder, E.J. and M.W. Witczak (1975). “Principles of Pavement Design.” John Wiley & Sons, Inc., New York.

Zhang, Z.W. and Roque, R. and Birgisson, B. (2001). Evaluation of Laboratory Measured Crack Growth Rate for Asphalt Mixtures, *Transportation Research Board*, Washington, D.C.

APPENDIX A

RELATIONSHIPS AMONG VISCOELASTIC MATERIAL PROPERTIES

The viscoelastic material properties that are of interest to modeling of asphalt concrete are the creep compliance, relaxation modulus, and complex modulus (from which dynamic modulus and phase angle are determined). The creep compliance and complex modulus can be easily obtained from an appropriate test. The relaxation modulus is more difficult to measure reliably from testing due to the high initial load caused by a step displacement input. However, the relaxation modulus is essential for the calculation of pseudo strain as shown in Equation (3.7) in the main report. Through the theory of linear viscoelasticity, all of these material properties are related and can be predicted from a measured property. Typically, either the creep compliance or frequency sweep test is performed and the remaining properties, particularly the relaxation modulus, are predicted from the measured property. In this research, relaxation modulus is predicted from both complex modulus and creep compliance.

Whether the relaxation modulus is predicted from the complex modulus or creep compliance, the analytical representation of the source property must first be established. Using the time-temperature superposition principle, the time and temperature dependent material properties can be represented using reduced time, ξ. For a constant temperature, the reduced time is defined as:

$$x \equiv \frac{t}{a_T} \tag{A.1}$$

where a_T is the time-temperature shift factor. Complex modulus is described as a function of frequency, so in this case reduced frequency, γ, is used:

$$g = f \; x \; a_T \tag{A.2}$$

The same value of a_T at a particular temperature applies to any of the viscoelastic material properties; be it creep compliance, relaxation modulus, or complex modulus. The individual temperature creep and dynamic modulus curves shown in Figures A.1 and A.2 are shifted horizontally to the 20^{o}C reference curve to construct the master curves shown in Figures A.3 and A.4. The time-temperature shift factors, a_T, at different temperatures are obtained from the shifting process and are shown as a function of temperature in Figure A.5. The shift factors will be the same for any viscoelastic property that is shifted for a particular specimen or mixture. To illustrate this, the shift factors shown in Figure A.5 (obtained from dynamic modulus) are used to create a master phase angle curve for the same specimen in Figure A.6. Once the master curve and the shift factors are known, the material properties at any temperature or rate of loading can be determined by simply shifting the master curve to the desired range. Once the master curves are constructed, an analytical representation of the material property is found. For notational simplicity, reduced time is represented by t and reduced frequency is represented by f. The Prony series representation (or generalized Voight model or Kelvin model) is used for the creep compliance:

$$D(t) = D_0 + \sum_{i=1}^{M} D_i \left(1 - e^{-\frac{t}{t_i}} \right) \qquad \text{(A.3)}$$

where D(t) = creep compliance as a function of time,
D_0, D_i = material constants, and
τ_i = retardation time of i^{th} Voight element.

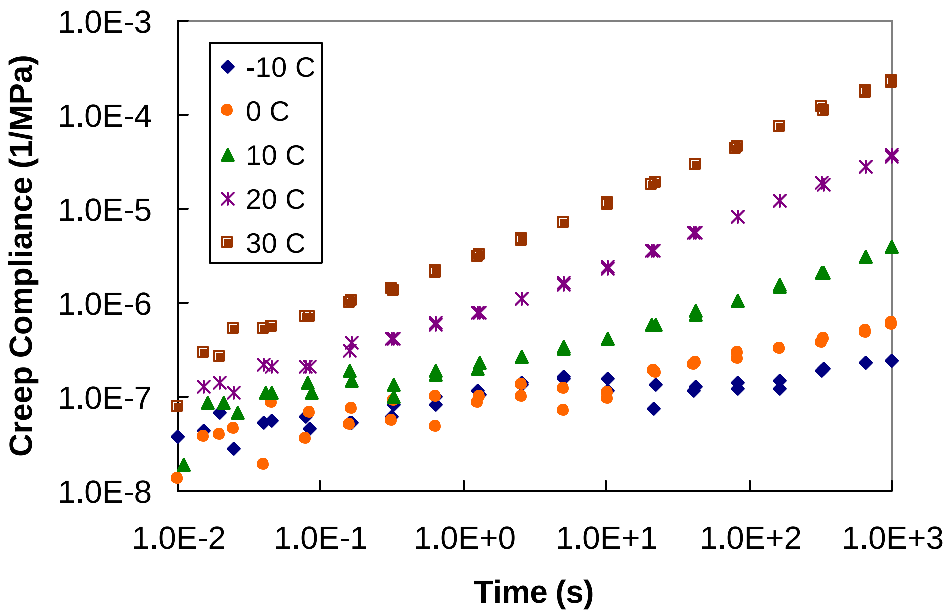

Figure A.1 Individual Creep Compliance Curves at Various Temperatures

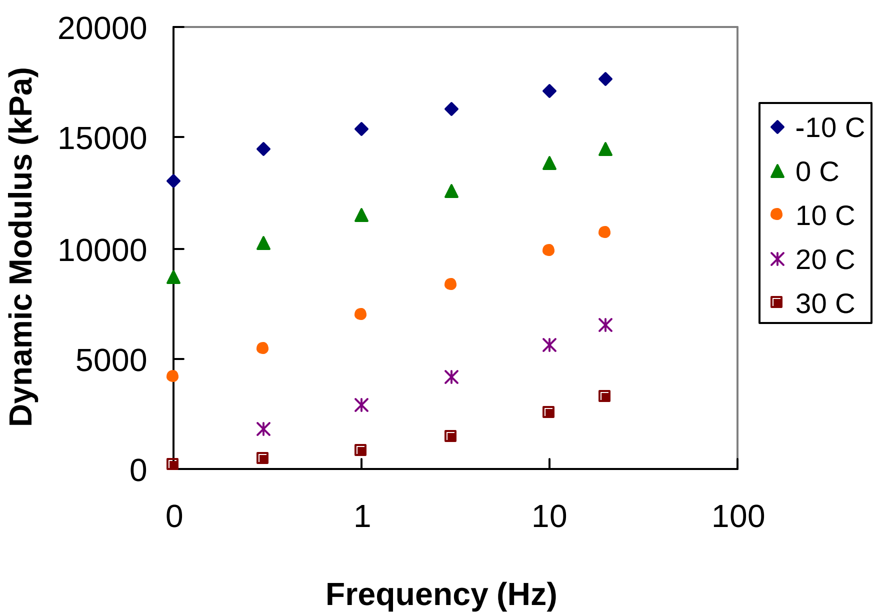

Figure A.2 Individual Dynamic Modulus Curves at Various Temperatures

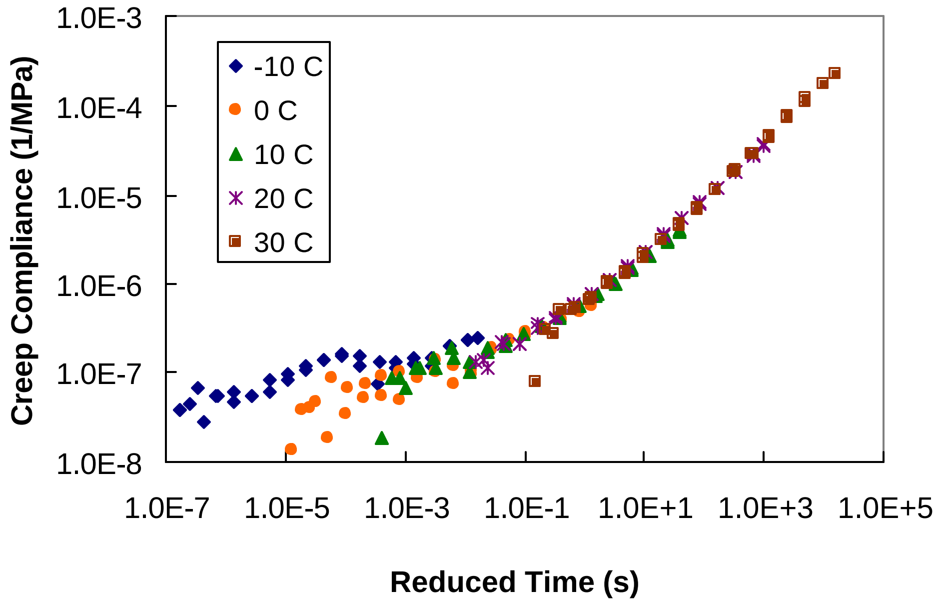

Figure A.3 Master Creep Compliance Curve at Reference Temperature of 20°C

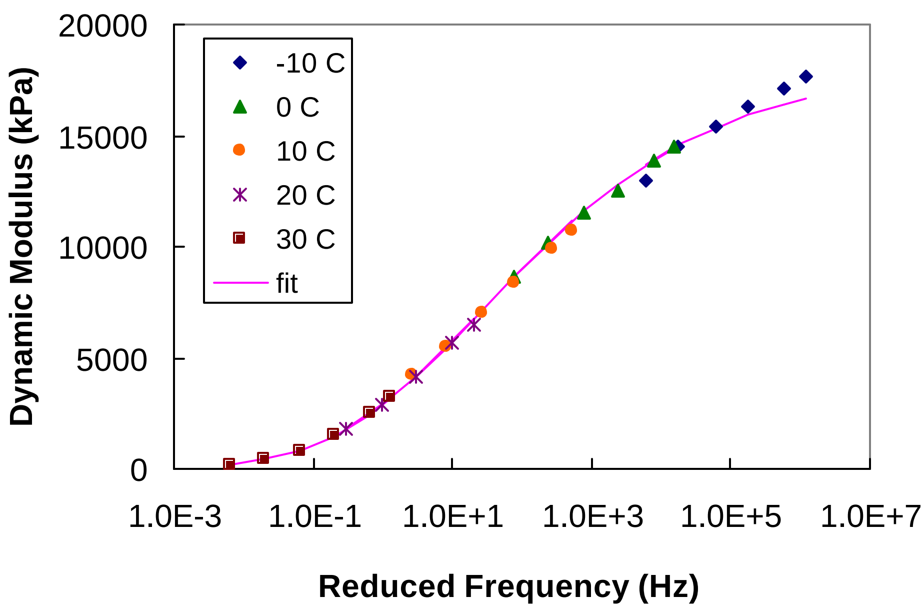

Figure A.4 Master Dynamic Modulus Curve at Reference Temperature of 20°C

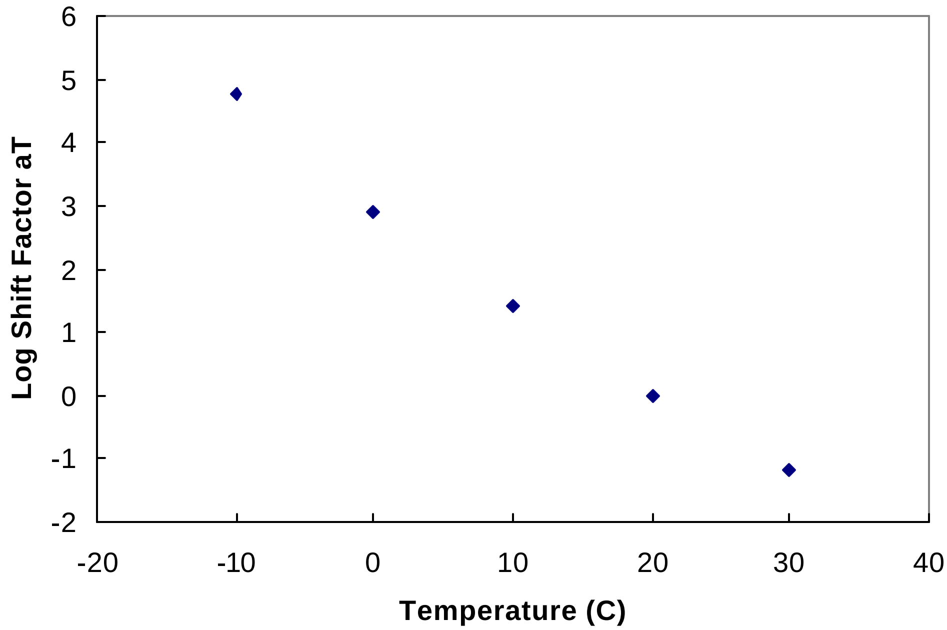

Figure A.5 Time –Temperature Shift Factors Used to Create Creep Compliance and Dynamic Modulus Master Curves

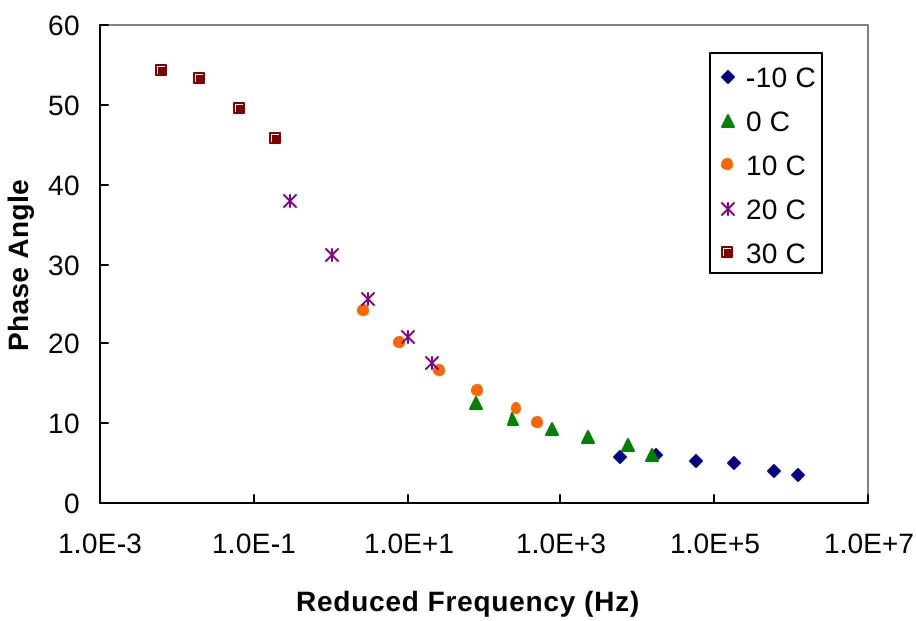

Figure A.6 Master Phase Angle Curve Created Using Shift Factors in Figure A.5

To represent the dynamic modulus and phase angle as a function of time, the following sigmoidal function is used:

$$\log t = a + \frac{b}{\left(1 + \frac{1}{\exp^{d+e(\log f)}}\right)} \tag{A.4}$$

where f is the testing frequency and a, b, d, and e are regression coefficients.

A.1 PREDICTION OF RELAXATION MODULUS FROM CREEP COMPLIANCE

The Prony series representation shown in Equation (A.3) is the preferred model to use for analytical purposes because it is much easier to deal with computationally than a power law representation. However, it is difficult to directly fit the Prony series model to measured data when there is significant variance in the data. This problem is overcome by pre-smoothing the experimental data and then fitting the Prony series model to the smoothed data. In past research, the modified power law (MPL) function in Equation (A.5) has been used to pre-smooth the data.

$$D(t) = D_0 + \frac{D_\infty - D_0}{\left(1 + \frac{t_0}{t}\right)^n} \tag{A.5}$$

where D_∞ = long time compliance, and
τ_0, n = constants.

The MPL does a good job of fitting the upper and lower asymptotes and the constant slope region but has some problems in accurately fitting the transition areas between the constant slope and asymptotes. A power law series (PLS) was proposed by Park and Kim (2001) and is adopted for this research:

$$D(t) = D_0 + \sum_{i=1}^{M} \frac{\hat{D}_i}{\left(1 + \frac{\hat{t}_i}{t}\right)^n} \tag{A.6}$$

where $\hat{D}_i$, $\hat{t}_i$ (i=1,…, M), n, and M are all constants. D_0 represents the glassy compliance as in Equations (A.3) and (A.5). In the PLS, $\hat{t}_i$ values are assigned a priori and D_0 and n (slope of the linear portion of the creep compliance curve) are determined from the measure data. The $\hat{D}_i$ are found by the collocation method which involves solving the resulting system of M equations, and then the Prony series can be fit to the smoothed data. LabView software by National Instruments is used to program this procedure.

Determining D_0 and n from Measured Data

In previous research, the program user would input a value for D_0 and assign a range over which the program would calculate the slope n using linear regression. The user can estimate a reasonable value for D_0 graphically. The regressed n however, depends greatly on the range over which it is calculated and the scatter of the data and may be unreasonable in view of the complete time range of data.

To minimize errors and variability from user in choosing applicable data ranges, a non-linear regression is performed on the measured data to find MPL coefficients, from which the D_0 and n can be taken for use in the PLS. The non-linear regression function in LabView requires a set of initial guessed coefficients and the resulting solution is extremely sensitive to the input values. In the final version of the program, the user assigns a value for D_0 and estimates D_∞ based on the measured data to customize the initial guesses for that data set. The assigned D_0 is used throughout the program for MPL, PLS, and Prony series fitting. The estimated D_∞ is used as an initial guess for the non-linear regression, which returns a value of n to be used in the PLS fitting. This method was found to be the best for returning reasonable n values and producing a satisfactory PLS fit of the measured data. If the user is not satisfied with the fitting of the data, the option of adjusting the D_0 value and re-running the program to adjust the fit is avaliable.

FITTING POWER LAW SERIES

In Equation (A.6), the only unknowns now are $\hat{D}_i$ and $\hat{t}_i$. Once the number of terms (M) is decided, the values for the time constants $\hat{t}_i$ can be specified. Park and Kim (2001) found that M=5 produced a satisfactory fit of the measured data and that more terms did not further enhance the fit. The $\hat{t}_i$ values are selected such that they are evenly distributed over the time range of data on a logarithmic scale. Rearranging Equation (A.6):

$$\sum_{i=1}^{5} \frac{1}{\left(1+\frac{\hat{t}_i}{t}\right)^n} \hat{D}_i = D(t) - D_0 \tag{A.7}$$

puts it into the matrix form of Ax = D. Using the method of least squares $A^T Ax = A^T D$, the column matrix x can be solved for, which contains the $\hat{D}_i$ values. The resulting five-term PLS fit for a particular asphalt concrete mixture is shown in Figure A.7 and as can be seen, the fit is not very good. As a result, the number of terms was increased to 11, which corresponds to $\hat{t}_i$ values about every decade for this data. This fit is also presented in Figure A.7, and although it is better than the 5 term fit, it is not smooth and does not represent a reasonable material response.

To produce a more satisfactory PLS fit, the weighted least squares method was used to solve for the $\hat{D}_i$ values:

$$A^T W A x = A^T W D \tag{A.8}$$

where:

$$W = \begin{bmatrix} \frac{1}{D(t_1)} & 0 & 0 \\ 0 & \text{O} & 0 \\ 0 & 0 & \frac{1}{D(t_n)} \end{bmatrix} \tag{A.9}$$

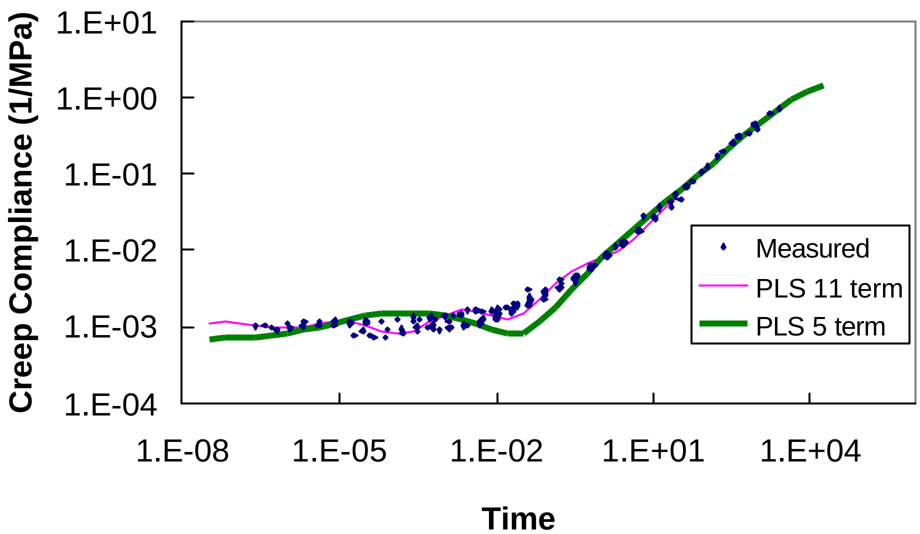

Figure A.7 Least Squares Method for Power Law Series Fit

Figure A.8 shows the resulting PLS fits for 13 term (one $\hat{t}_i$ per decade) and 5 term PLS representations. Use of the weighted least squares method definitely improves the fit, but there is still some waviness to the fit using the 13 terms, likely due to the rather large scatter in the measured data. The extrapolated data beyond the upper region is also unrealistic for the 13 term series. The five-term PLS representation provides an excellent fit over the whole range of data and shows realistic extrapolation at both short and long times. PLS representations with 3, 7, 9, and 11 terms were also investigated, but the 5 term series produced the most satisfactory results. PLS representations with terms M>5 were found to be too sensitive to local fluctuations (scatter) in the measured data. Figure A.9 shows the comparison between 5 and 11 term series for a different set of measured data. The decision was made to use M=5 based upon the findings of Park and Kim (2001) and those presented here.

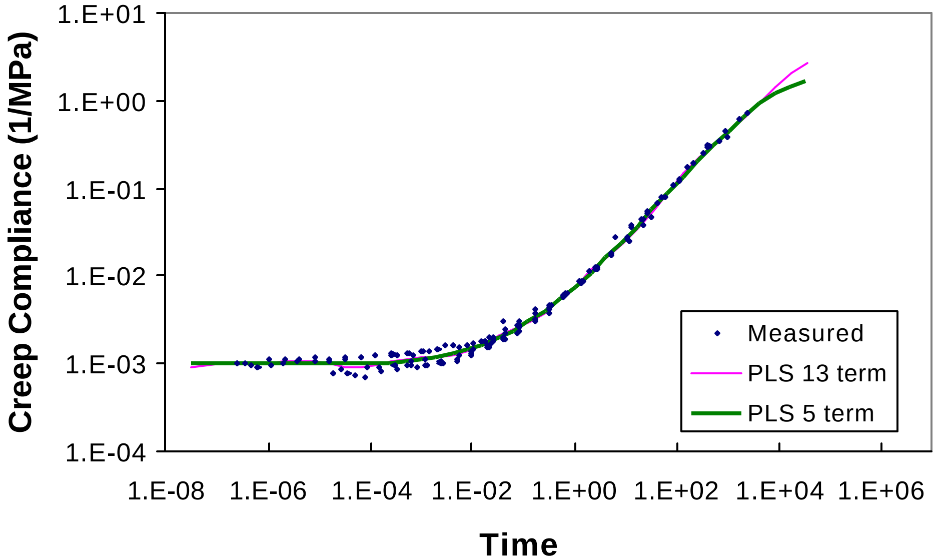

Figure A.8 Weighted Least Squares Method for Power Law Series Fit

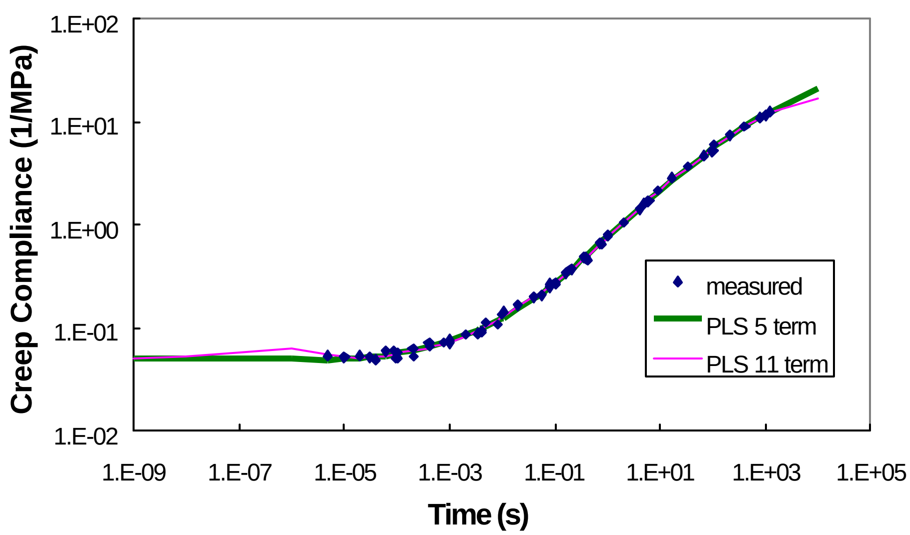

Figure A.9 Power Law Series Fit of Second Data Set

CONVERTING D(T) TO RELAXATION MODULUS, E(T)

Once the pre-smoothing of the measured creep data is satisfactory, the smoothed curve can be used to predict the relaxation modulus using an approximate method proposed by Park and Kim (1999). The approximate interconversion is based on the power law interrelationship between D(t) and E(t). Both the creep compliance and relaxation modulus are represented in a pure power law form:

$$E(t) = E_1 t^{-n} \tag{A.10}$$

$$D(t) = D_1 t^{n} \tag{A.11}$$

where E_1, D_1, and n are postitive constants. Through linear viscoelastic theory, the relationship between Equations (A.10) and (A.11) becomes:

$$E(t)D(t) = \frac{\sin np}{np} \tag{A.12}$$

Since the power law cannot accurately represent either the creep compliance or the relaxation modulus over the entire range of behavior (the power law can not represent short or long time asymptotes), a local power law fit is used. In this way, the creep compliance over the entire time range of interest is represented by a series of local power law representations and the relaxation modulus in each of those ranges is calculated using Equation (A.12). From the converted data, a functional form of the relaxation modulus is needed for use in the pseudo strain analysis. The Prony series shown in Equation (A.13) is used for computational efficiency.

$$E(t) = E_\infty + \sum_{i=1}^{N} E_i \exp^{-\frac{t}{r_i}} \tag{A.13}$$

where E_∞= long-time equilibrium modulus,
E_i = regression coefficients, and
ρ_i = relaxation times.

The Prony series coefficients for the relaxation modulus are determined using the collocation method. One Prony series term is used for each half-decade of the time range to be fit.

A.2 Prediction of Relaxation Modulus from Complex Modulus

The relaxation modulus for each mixture is predicted from the dynamic modulus and phase angle master curves using the following approximate analytical method proposed by Schapery and Park (1999):

$$E(t) \cong \frac{1}{l'} E'(w)\Big|_{w=(1/t)} \tag{A.14}$$

$$l' = \Gamma(1-n)\cos\left(\frac{np}{2}\right) \tag{A.15}$$

$$n \equiv \frac{d \log E'(w)}{d \log w} \tag{A.16}$$

where E(t) = relaxation modulus,
E'(ω) = storage modulus,
ω = angular frequency = $2\pi f$, and
Γ = gamma function.

The storage modulus can be calculated by multiplying the dynamic modulus with cosine of phase angle as in Equation (4.3). A local value of n is used for calculating each relaxation modulus point. Once relaxation modulus values are predicted along the desired time range, the data is fit to a Prony series function (Equation (A.13)) for analysis purposes.

A.3 Prediction of Dynamic Modulus from Creep Compliance

Using linear viscoelastic theory, Kim and Lee (1995) describe a method by which dynamic modulus can be predicted from creep compliance. This method is summarized below. Through linear viscoelastic theory, it can be found that:

$$E^* \, x \, D^* = 1 \tag{A.17}$$

where the complex compliance is defined as:

$$D^* = D' - iD'' \tag{A.18}$$

The storage and loss compliance are D' and D", respectively. Substituting the definitions of complex modulus in Equation (4.1) and complex compliance in Equation (A.18) into Equation (A.17) yields:

$$E' = \frac{D'}{|D^*|^2} \tag{A.19}$$

$$E'' = \frac{D''}{|D^*|^2} \tag{A.20}$$

where

$$|D^*| = \sqrt{(D')^2 + (D'')^2} \tag{A.21}$$

Therefore, to predict the dynamic modulus, |E*|, only the storage and loss compliances need to be calculated. It can be shown that:

$$D^* = s \, \mathcal{L} \{D(t)\}|_{s=iw} \tag{A.22}$$

where $\mathcal{L} \{D(t)\}$ is the Laplace transform of D(t) and ω is the angular velocity.

Assume that the creep compliance is expressed in the generalized power law (GPL) form:

$$D(t) = D_0 + D_1 t^m \tag{A.23}$$

where D_0, D_1, and m are regression constants. Taking the Laplace transform of the creep compliance in Equation (A.23) and substituting into Equation (A.22) yields the complex compliance as a function of the angular frequency ω:

$$D^* = D_0 + D_1 \Gamma(m+1)\left[\cos\left(\frac{mp}{2}\right) - i\sin\left(\frac{mp}{2}\right)\right] w^{-m} \tag{A.24}$$

Hence,

$$D' = D_0 + D_1 \Gamma(m+1)(2pf)^{-m} \cos\left(\frac{mp}{2}\right) \tag{A.25}$$

$$D'' = D_1 \Gamma(m+1)(2pf)^{-m} \sin\left(\frac{mp}{2}\right) \tag{A.26}$$

The gamma (Γ) function is defined as:

$$\Gamma(n) = \int_0^\infty e^{-x} x^{n-1} dx \tag{A.27}$$

The dynamic modulus can then be calculated using Equations (4.2), (A.19), (A.20), (A.21), (A.26) and (A.27) from the GPL representation of creep compliance.

APPENDIX B

MACHINE COMPLIANCE AND INSTRUMENTATION ISSUES

Research and design of asphalt concrete typically requires some amount of experimentation in the laboratory. Currently, the asphalt industry is moving in the direction of mechanistic design, as evidenced by the development of the Simple Performance Test (SPT) for mix design (Witczak 2000) and the upcoming AASHTO 2002 structural design guide. Fundamental material properties required for the mechanistic design are to be measured in the laboratory under various loading and environmental conditions. Application and measurement of stresses and strains to obtain the material properties involves both a mechanism by which load is applied and a system to measure the response of the material to the input loading. Loading is applied through a loading frame with either a mechanical system or hydraulic/pneumatic actuator. Loads can be measured using a load cell and displacements can be measured using some type of transformer or gauge. Current technology uses electronically powered devices from which voltages are read and converted to the appropriate units of load or displacement. The electronic signal passes through various filters and conditioners en route to the data acquisition system. The level of accuracy for both the control and measurement sides of the testing must be adequate to achieve meaningful or appropriate results to extract the desired information from the test.

A FHWA publication (Alavi et al. 1997) describes procedures to be used in laboratory testing and quality control for resilient modulus testing of unbound materials. Appropriate performance verification of electronic systems should be performed on any laboratory machine at the time of initial setup, as described in the report procedures. The performance verification includes characterizing the frequency response of the system and calibrating the load cell and LVDTs. However, once this performance verification is completed, there are additional issues in testing that arise. This appendix addresses some potential problems with machine compliance and instrumentation that can have a significant effect on experimentally measured material properties and, as a result, the research and design in which they are used. The focus is on the measurement of dynamic modulus and phase angle that are measured in the SPT and are needed in AASHTO 2002; however, issues with other types of testing such as creep compliance are addressed as well.

B.1 Testing Equipment and Materials

The research described herein focuses on the testing of asphalt concrete materials using servo-hydraulic closed-loop testing machines and LVDTs for deformation measurements. However, the concepts of machine compliance and various instrumentation issues are applicable to testing with all types of machines on any kind of material. The question is whether these issues are significant enough for a particular application to affect the test results and research.

Testing Machines

The two testing machines evaluated in this study are closed-loop servo hydraulic machines. One is a Materials Testing System (MTS) with 100 kN capacity and the second is a Universal Testing Machine (UTM), made by Industrial Process Controls, Inc. (IPC), with a 25 kN capacity. The MTS system uses a 458 microconsole control system with microprofiler for function generation. LabView software is used with a National Instrument’s 16-bit data acquisition board to collect multiple channels of data. The load cell and actuator LVDT signals are conditioned through the microconsole. The UTM system has both computer control and data acquisition systems using UTM software, in addition to Labview data acquisition. The load cell and actuator LVDT signals for the UTM are conditioned through the UTM control and data acquisition system (CDAS).

Deformation Measurements

Deformation measurements were made on both the MTS and UTM systems using various types of LVDTs. All types were used in testing on both the MTS and UTM systems. All of the LVDTs were obtained from IPC and have signal conditioners compatible with the UTM load cell and ram LVDT and are powered by the CDAS. For testing on the MTS system, the LVDTs were powered by an IPC power supply. Table B.1 summarizes the different LVDT types studied.

TABLE B.1 Summary of LVDT Types

LVDT name	**Type**	**Signal Cond. Model**	**Designation**
GTX 5000	3/8” Spring-loaded	1020	GTX
099XS-B	3/16” Loose core	661	XSB
CD-100	3/8” Loose core	661 and 1020	CDA and CDB

Materials

The asphalt concrete mixtures are standard North Carolina and Maryland mixtures with 19 mm Superpave gradations and PG 70-22 and PG 64-22 asphalt binders, respectively. The actual mixture properties are not as important as the fact that the material is viscoelastic in nature and that certain trends in the measured properties are expected from viscoelastic materials tested under various types of loading. Testing was also performed on an aluminum specimen. Both the asphalt and aluminum specimens were 75 mm diameter and 150 mm tall, based on recommendations by Chehab et al. (2000). Specimens were glued to steel end plates with Devcon Plastic Steel Putty using a gluing jig to ensure proper alignment. Testing was performed in uniaxial direct tension.

Test Methods

Both monotonic (constant crosshead rate) and complex modulus (frequency sweep) tests were performed in this research. Monotonic testing involves pulling the specimen apart at a constant crosshead strain rate until the specimen fails (breaks into two pieces). Frequency sweep testing was performed in the linear viscoelastic range of the material (no damage induced) and involved applying various frequencies of sinusoidal loading to the specimen and then measuring the strain response to obtain the dynamic modulus and phase angle values. Frequency sweep testing can be performed at various temperatures to allow for the construction of a master curve describing the linear viscoelastic material behavior.

B.2 Machine Compliance

Monotonic constant crosshead rate tests and cyclic tests (haversine and sawtooth) conducted on both the UTM and MTS showed that the magnitude of movement of the specimen plates (deformation of specimen itself) is less than that of the actuator. Only when there was no load on the system (i.e., failed specimen or no specimen in the machine) did the plates move the same amount as the actuator. This response suggests that some component or components of the loading system yield under the applied loads. The issue of machine compliance is of concern because it indicates that the specimen does not deform as expected in actuator displacement control tests and that the true material response is not measured by the actuator LVDT during load control tests.

Figure 1 shows the on-specimen, plate-to-plate, and actuator LVDT strains measured from a monotonic test. In this test, a specimen is pulled apart using a constant crosshead strain rate. Due to the machine compliance, the on-specimen and plate-to-plate LVDT measurements follow a power curve until failure. During this time, the specimen does not experience a true controlled-strain or controlled-stress mode of loading, but rather a mixed mode of loading.

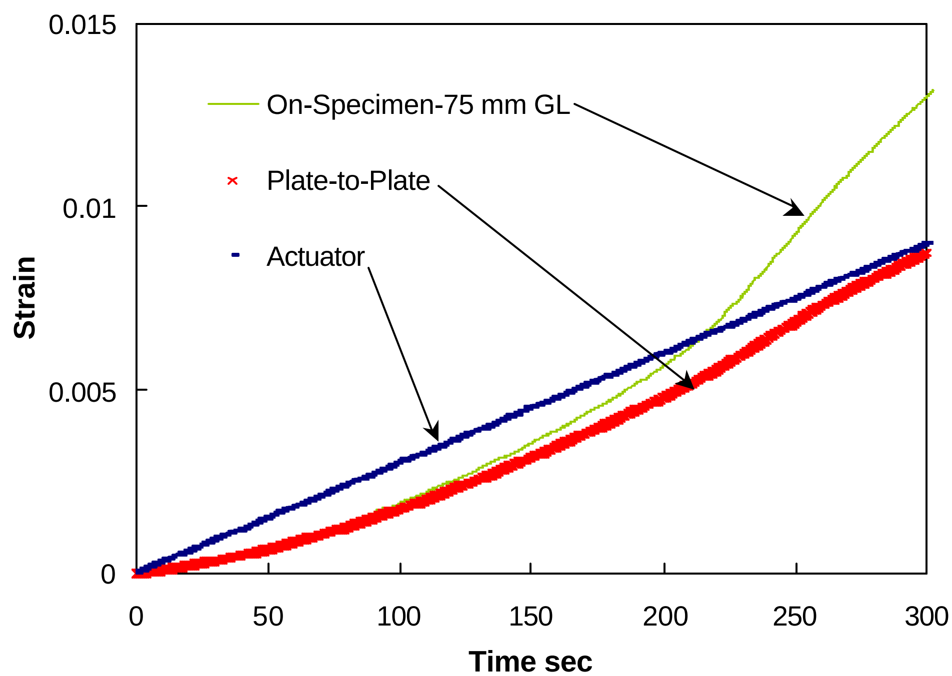

FIGURE B.1 Stress and Strain Measurements for Constant Crosshead Rate Test

After failure, the plate-to-plate measurements become linear with a rate close to that of the crosshead; the increase of on-specimen strain becomes linear as well, but with a higher rate, due to the difference in gauge length from which strains are calculated. The crosshead and plate-to-plate deformations are divided by the same gauge length (length of the specimen), whereas the on-specimen deformations are divided by a smaller gauge length. For the same deformation measurement, which is the case after failure due to the development of a single macrocrack, the strain calculated from the on-specimen LVDTs is larger.

Deformations measured from the actuator LVDT and on-specimen LVDTs differ in frequency sweep testing as well. The calculated strains from the actuator LVDT are greater than those calculated from the on-specimen LVDTs due to the machine compliance. This difference transfers to the calculated dynamic modulus values as the same stress amplitude is divided by different strain amplitudes, resulting in a lower dynamic modulus measured from the actuator LVDT. Figure B.2 shows the difference in dynamic modulus and phase angle measurements calculated from the actuator and on-specimen LVDTs for a Maryland mixture specimen tested at 25^{o}C on the UTM. There is an average difference in the phase angle of 20^{o} between the actuator and on-specimen LVDT measurements. The dynamic modulus measured from the specimen is 4.5 times that measured from the actuator at 20 Hz and 1.4 times that measured from the actuator at 0.1 Hz.

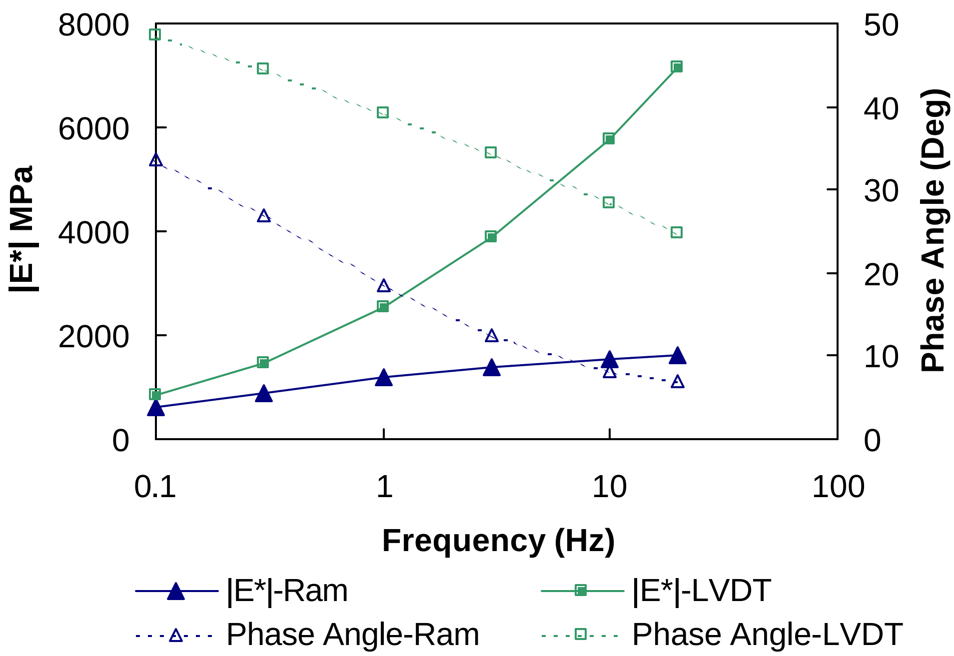

FIGURE B.2 Comparison of Ram and LVDT Dynamic Modulus and Phase Angle Measurements

Testing performed on an aluminum specimen and asphalt specimens at different temperatures and loading rates showed that the magnitude of the machine compliance depends upon the stiffness of the material being tested. As the stiffness of the material increased, the percentage difference between the end plate movement and the actuator movement increased; i.e., there was a greater contribution from the load train to the overall displacement. Additionally, it was noted that the UTM, a 25 kN machine, exhibited higher compliance than the MTS, a 100 kN machine; this difference could be attributed to a difference in the stiffness of the loading system components.

In frequency sweep tests, the difference between the actuator and specimen end plate movement becomes larger as the testing frequency increases, as shown by the dynamic modulus values in Figure B.2. Moreover, for monotonic tests, it was observed that the faster the crosshead strain rate, the greater the effect of the machine compliance. These differences are due to the viscoelastic nature of the material; the faster the loading is applied, the stiffer the material becomes, and hence, the increased effect of machine compliance. This result is also true with testing at different temperatures; there is a greater contribution from machine compliance at lower testing temperatures.

LVDTs were mounted across various joints on the MTS loading system to determine which components were contributing to the machine compliance by deforming under load. A series of haversine and sawtooth cyclic tests in both controlled-strain and controlled-stress modes were performed to measure joint displacements. Several of the threaded connections between adaptors and the ram and load cell were found to exhibit appreciable deformation upon loading. It is worthy to note that although all joints are expected to exhibit some deformation during loading, those deformations should be reduced as much as possible when they are close in magnitude to the specimen deformation. This reduction can be accomplished through regular maintenance and cleaning of all connections. Pre-tensioning of the joints can also reduce deflections, but is not practical in testing where the joints need to be locked and unlocked frequently for different test setups.

While the aforementioned suggestions can help reduce the machine compliance, they will never eliminate it. Since there are various sources of deflection along the load path, some of which are inevitable, it is more practical and less time-consuming to measure the displacements from LVDTs mounted on the specimens rather than from the actuator. When actuator displacement control is required, it is possible to determine a correction factor that, when applied to the crosshead rate, achieves the desired specimen displacement rate.

If deformation attributed to the machine compliance is elastic, then that deformation divided by the load under which the deformation occurs should be a constant for all testing conditions. This constant may be regarded as the stiffness of a spring that characterizes the machine compliance. This phenomenon was investigated for several monotonic test conditions, as shown in Figure B.3. Plate-to-plate strain was subtracted from the crosshead-based strain and the result was divided by the stress. The result is a constant for several different rates of crosshead-based strain up to the value of peak stress. After peak stress occurred, macrocracks in the specimen started to develop and plate-to-plate strains could not be used anymore. At the higher test temperature of 40ºC, the spring constant increased slightly with crosshead strain. This suggests that, in general, the machine compliance deformations are generally elastic.

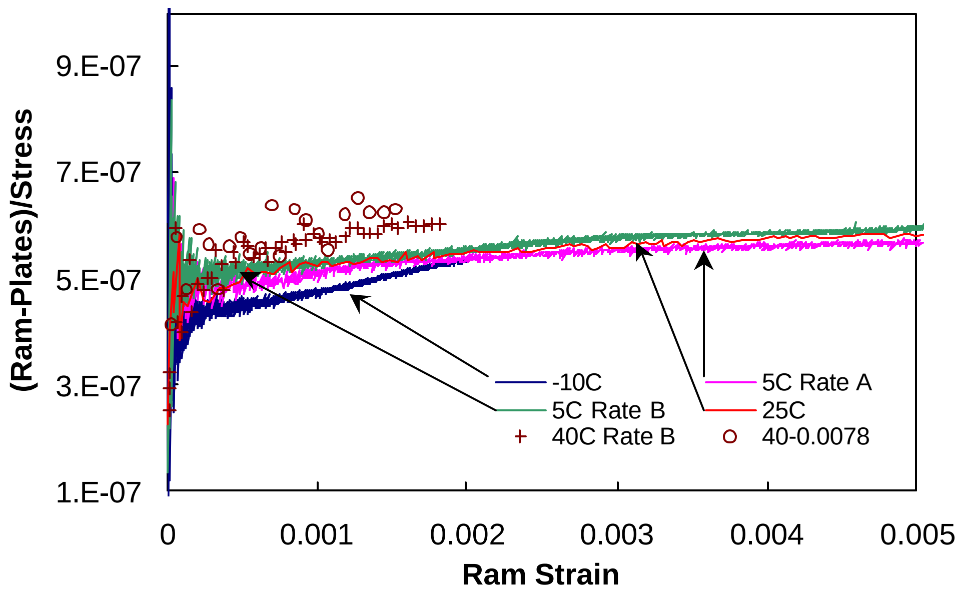

FIGURE B.3 Machine Compliance Evaluated at Different Temperatures and Crosshead Strain Rates for UTM Machine

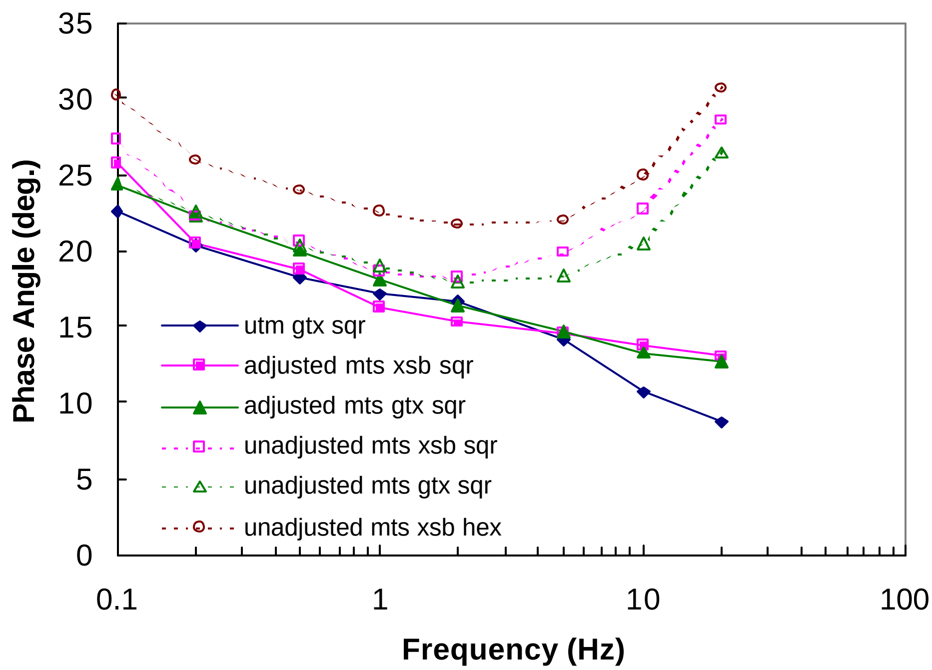

FIGURE B.4 Adjusted and Unadjusted Phase Angle Measurements for Various Machine, LVDT, and Mount Type Combinations

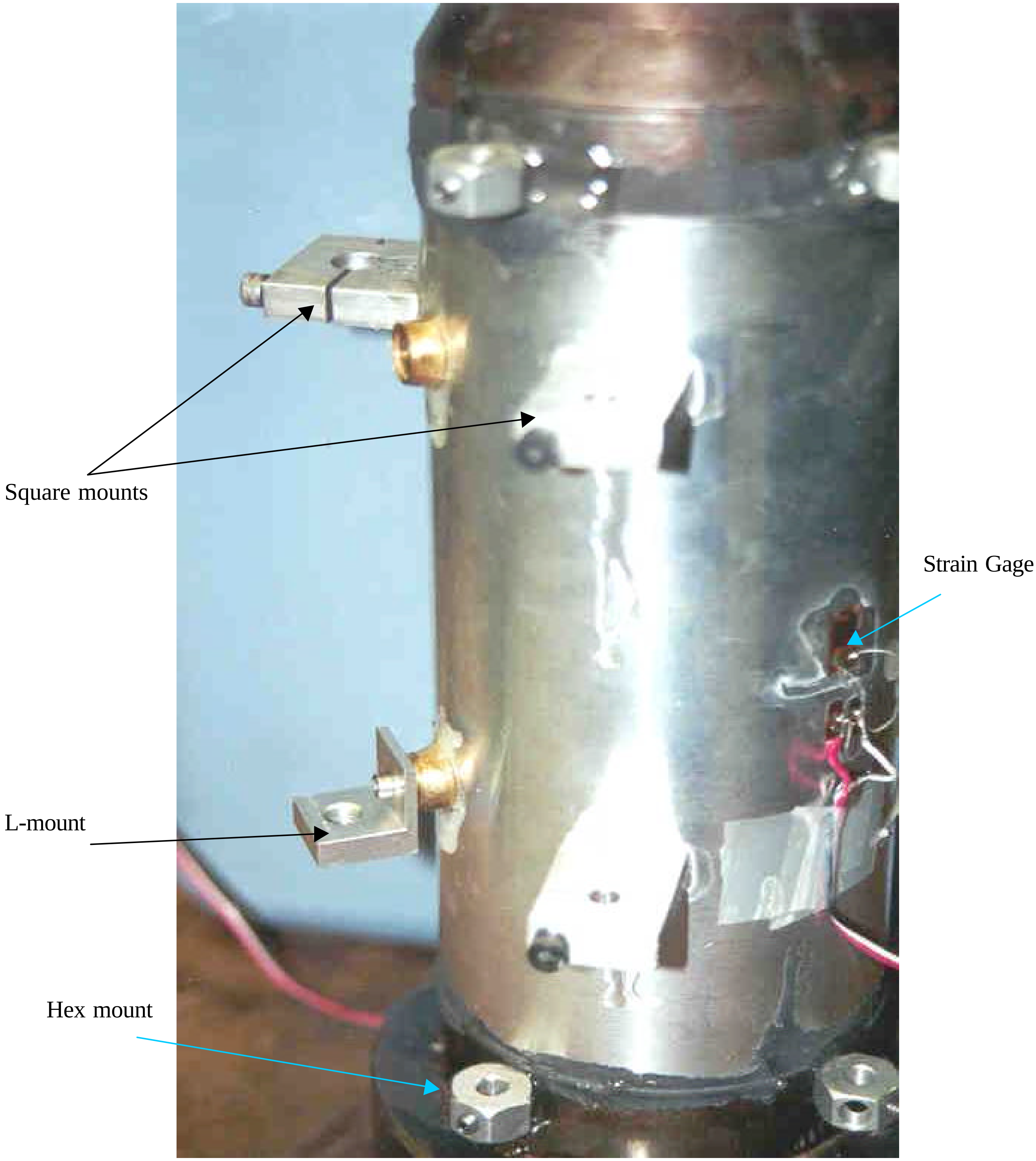

FIGURE B.5 Different LVDT Mount Types on Aluminum Specimen

B.3 Measurement Instrumentation

Complex modulus tests on asphalt specimens performed using the MTS machine resulted in an unreasonable trend for the phase angles calculated using on-specimen LVDT measurements. The typical trend is shown by the dashed lines in Figure B.4; the unadjusted phase angle decreases and then increases with faster frequencies, whereas it should have continued to decrease due to the viscoelastic nature of asphalt concrete. This unexpected pattern for the variation of phase angle with frequency is likely due to a combination of dynamic and electronic effects related to measurement instrumentation. Some of these effects are also identified and discussed with respect to resilient modulus testing of unbound materials (Alavi et al. 1997).

A series of tests were performed on both the MTS and UTM machines using the XSB and GTX LVDTs with various mounting assemblies (L-mount, square mount, hex mount). Testing was performed on an aluminum specimen (elastic response) and on an asphalt specimen. Figure B.5 shows the different mounting assemblies on the aluminum specimen.

Dynamic effects

The dynamic effects include the damping of the whole loading system, especially the mass acceleration and hysteresis of the load cell, in addition to the dynamics of the LVDT and its mounting assembly. These effects depend on the type and weight of the LVDT, mounting assembly, and the measurement mechanism (loose core versus spring loaded).

System Damping: One source of phase shift is loading path dynamics (damping). The mass-acceleration of the actuator, load cell, and other components on the load path causes a phase when a change of actuator movement direction happens. Load cell hysteresis could also introduce a phase shift. Hysteresis is defined as the difference in load measurement when a load value is approached from the ascending versus the descending direction. Force measurement lead/lag could be hysteresis up to the specification value (0.05% for MTS).

LVDT Type: It was concluded that the type of the LVDT does not affect the phase angle. Phase angles measured using GTX LVDTs are similar to those measured from XSB LVDTs using the same mounting mechanism, as seen in Figures B.4 and B.6. It seems that the effect of weight (GTX is heavier than XSB) and measurement mechanism (XSB being a loose core LVDT versus GTX being a spring loaded type LVDT) either cancel each other out or do not significantly affect the phase angle.

Mounting mechanism: The mounting mechanism significantly affects the measured phase angle. This finding was especially true for the XSB LVDTs. The LVDTs attached to the hex mounts always recorded phase angles that were higher than those measured using the LVDTs with the L-mount or square mount assemblies, as shown in Figures B.4 and B.6. This could be attributed to the smaller surface area on the hex mount that provides the contact to the specimen and/or to the different mechanism for securing the LVDT in the mount. (The hex mount uses a single locking screw while the other two use a clamping mechanism; see Figure B.5.)

Electronic Effects

The signal conditioning and filtering could lead to a phase angle that is measured but is physically non-existent. If the circuitry in the signal conditioner of the load cell is different than that of the LVDTs, an electronic phase angle can result and would be measured by the data acquisition system. The load cell on the UTM machine has a signal conditioner that is compatible with both types of LVDT signal conditioners. The difference between machines became apparent when the GTX LVDTs measured different phase angles when used with the MTS versus the UTM. Using the same LVDT type (CD) with the two different conditioners also resulted in different phase angle values and variations in frequency.

The electronic filtering of signals can also cause a phase angle that is physically non-existent. According to the UTM manufacturer, the control module has a first order low pass filter that gives the controlling transducer (load cell in stress control tests) a phase shift of 1.2º at 10 Hz and 2.4º at 20 Hz. With respect to resilient modulus testing of unbound materials (LTPP Protocol P46), an electronics tolerance of 1.8º is allowed (Alavi et al. 1997). The electronic effects on phase angle are expected to be greater with the MTS machine because the LVDTs and the load cell are from two different companies, and are not calibrated together.

Phase Angle Adjustment

Although the dynamic and electronic effects have been identified as probable sources of the phase angle problem, they are very difficult and impractical, if not impossible, to eliminate. Therefore, a method must be developed to adjust the measured phase angle to remove these effects. This was accomplished by performing tests on an aluminum specimen that has no material phase angle (purely elastic). Any phase angle measured from the aluminum specimen must be attributed to the dynamic and electronic effects. To accurately simulate the dynamic effects that occur with an asphalt specimen, an appropriate load level was applied to the aluminum specimen to generate the same strain magnitude (~50 microstrain) as experienced by the asphalt specimen.

Figure B.6 shows the phase angles measured from different LVDTs and mount types on an aluminum specimen tested on the MTS. Immediately noticeable is the fact that a phase angle is measured from the LVDTs and that it increases with increasing frequency. The LVDTs attached to the hex mounts measured a higher phase angle than those attached to the square mounts. There is little difference in the measurements from the GTX and XSB LVDTs. Also shown on this figure are the phase angles measured from the actuator LVDT and from a strain gauge mounted directly on the specimen surface. The actuator phase angle increases slightly at the higher frequencies, which may be attributed to filtering, as mentioned above. The strain gauge, which should exhibit no dynamic effects, shows no phase angle, which is expected since the aluminum is an elastic material.

A comparison between the two signal conditioners on the MTS and UTM machines shows that both signal conditioners measure higher phase angles on the aluminum specimen when used with the MTS machine. The GTX LVDTs show a negligible phase angle when used with the UTM machine. Therefore, use of the GTX LVDTs with L-mounts (or square mounts) on the UTM system will measure the true material response of an asphalt specimen. There is not a mount-LVDT-signal conditioner combination that eliminates the dynamic and/or electronic effects with the MTS machine and, therefore, an adjustment must be made to obtain the true material response.

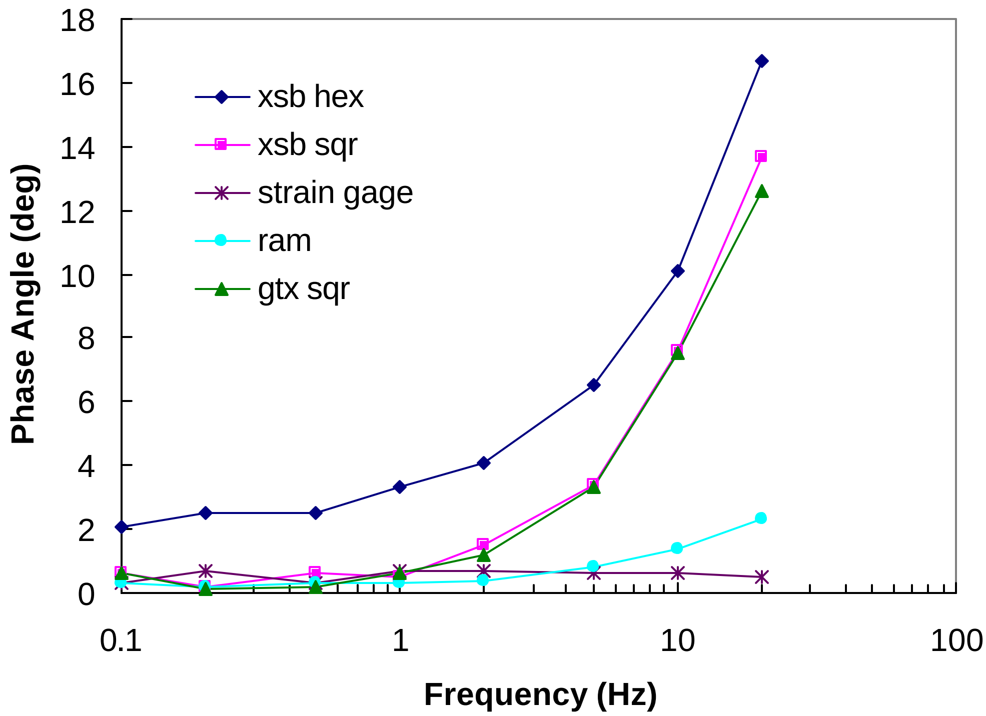

FIGURE B.6 Phase Angle Measurements from Aluminum Specimen Tested with MTS

Figure B.4 shows the phase angles measured from an asphalt specimen tested in both the UTM and MTS machines using various LVDT and mount combinations. The phase angle is calculated by averaging the responses from two LVDTs. The phase angles from the UTM test show an expected decreasing trend with frequency, while those from the MTS test decrease and then increase. The adjusted MTS phase angles, shown with solid lines, were calculated by subtracting the phase angle of the aluminum specimen from that measured from the asphalt specimen, thereby removing any dynamic and electronic effects. The agreement between the adjusted MTS phase angles and the UTM phase angles (measured from the same asphalt specimen) proves that this approach is valid.

The recommended test protocol for use in any test where phase angles will be measured is to first test an aluminum (or other suitable elastic material) specimen using the same geometry, instrumentation (LVDT, mount, etc), and strain levels to be used in the actual testing to develop a fingerprint of any dynamic and/or electronic effects. These effects can then simply be subtracted from the measurements of the actual test specimen to obtain the true material response.

B.4 Electronic Noise

The LVDT signal conditioners have low pass filters installed to eliminate noise that consists of all unwanted frequencies above a certain threshold cutoff frequency. The farther the cutoff frequency is from the operating frequency, the greater the noise. To reduce the amount of noise, the threshold frequency should be decreased. However, this filtering process causes a phase shift; the closer the operating frequency to the threshold cutoff frequency, the greater the shift, as evidenced by the phase angles in Figure B.6. If the operating frequency and the cutoff frequency are the same value, the phase shift will be 45 degrees. To reduce the phase shift, the threshold frequency should be increased. Therefore, there must be a compromise between the acceptable levels of noise and phase shift.

TABLE B.2 Noise Amplitude for Different LVDT Types

LVDT Type	CDA	CDB	GTX	XSB
Mean strain	70 $\mu\varepsilon$	70 $\mu\varepsilon$	70 $\mu\varepsilon$	65 $\mu\varepsilon$
Noise Amplitude	20 $\mu\varepsilon$	7 $\mu\varepsilon$	8 $\mu\varepsilon$	5 $\mu\varepsilon$
% of Mean	28.6	10.0	11.4	7.7

TABLE B.3 Frequency Sweep Results from Aluminum and Asphalt Specimens

	Aluminum Specimen								Asphalt Specimen	
	CDA		CDB		GTX		XSB		|E*| MPa	
Freq (Hz)	|E*| MPa	Phase	|E*| MPa	Phase	|E*| MPa	Phase	|E*| MPa	Phase	GTX	CDA
20.0	76947	0.9	70919	0.9	70067	0.1	72198	12.3	10651	11392
10.0	76317	0.2	71413	0.3	69925	0.4	71891	11.4	9098	9876
3.0	75693	1.1	71239	0.6	70111	0.9	71899	8.0	6605	7261
1.0	76461	0.9	71370	0.7	69258	0.8	72759	7.8	4694	5288
0.3	77073	0.4	70030	1.0	70024	0.6	73901	7.5	3122	3541

This phenomenon is illustrated in Table B.2 with the three LVDTs used in testing the aluminum specimen at a frequency of 20 Hz. The XSB conditioner uses a 200 Hz cutoff frequency, the GTX conditioner uses a 400 Hz cutoff frequency, and the CDA conditioner uses a cutoff frequency greater than 400 Hz. The CDA LVDT exhibits the largest amount of noise (30% of mean signal amplitude) because of the high cutoff frequency and, conversely, the XSB LVDT exhibits the least amount of noise (8 % of mean signal amplitude). The phase angles measured from the aluminum specimen by each of the LVDTs are shown in Table B.3. As expected, the

XSB LVDT exhibits the highest phase shift and the GTX and CDA LVDTs exhibit lower phase shift. Also noticeable is that the XSB phase shift increases as the frequency increases and becomes closer to the cutoff frequency.

In determining the dynamic modulus and phase angle values, the deformation (or strain) measurements are fit to a sinusoidal function to account for the noise effect in determining the correct amplitude and phase. Typically, an error minimization technique is utilized such that the fit follows the mean strain value. This works well with the phase angle measurements; however, this may not work to extract the correct strain amplitude when noise levels are high. This finding is illustrated by the difference in dynamic modulus values measured from the aluminum and asphalt specimens using the CDA, CDB, and GTX LVDTs, shown in Table B.3. There is a 10% error in the modulus value of the aluminum specimen measured with the two different signal conditioners (CDA and CDB LVDTs), whereas the difference between the two LVDTs with the same conditioner (CDB and GTX) is only 3%. Differences of up to 13% in dynamic modulus values from the same asphalt specimen are measured using the different signal conditioners (CDA and GTX LVDTs).

B.5 Drifting Problem

LVDT measurements were found to drift during static loading and rest periods. Spring loaded GTX LVDTs, used with L-mount assemblies that were glued to the specimen using 5-minute Devcon epoxy, measured increasing axial displacements although no load was applied to the specimen. This displacement corresponds to 40 microstrains after 1000 seconds (100 mm gauge length); such a magnitude is significant relative to strains obtained from linear viscoelastic testing. The specimen was disconnected from the actuator and, thus, had no load applied on it. The positive strain indicates tension; thus, the specimen's self-weight and the weight of the end plate, which would cause compressive strains, are not the causes of this drift.

Several possible sources of LVDT drifting during testing could be:

- Faulty LVDTs,
- Error in programming (load was actually applied to specimen during rest),
- Deformation due to thermal stresses,
- Electronic interference,
- Mechanical causes related to LVDT functionality and setup.

The first three possible sources were eliminated through testing with different LVDTs, testing a specimen not connected to the actuator, and testing at constant temperature. No electronic interference from the CDAS or the National Instruments data acquisition board was detected; however, IPC recommends that the in-line signal conditioners on the LVDTs be allowed to warm up for approximately 30 minutes prior to testing to avoid errors in strain measurement due to warming components. After appropriate warm-up time, drifting of the LVDT measurements was still detected, indicating that the drifts are mechanical in nature.

Deformation at the mounts that hold the LVDTs and the connection to the specimen could lead to drift in strains and may be caused by one or a combination of the following:

- Slippage of the LVDT from the mount,
- Deformation (rotation) of the mounts due to force exerted by the LVDT spring on the target mount,
- Movement of the mount due to the self-weight of the LVDT and its cable.

Ensuring that the LVDT was very tight in place eliminated the possibility of any slippage from the mount. To determine whether the two other possible causes were contributing to the drift, a set of mounts were bolted (not glued) to a horizontal aluminum plate. After measuring strains overnight, no drift was detected, indicating that the LVDT type and mounting assembly connection were, in fact, contributing to the drift. The mechanical action(s) affecting the drift may be dependent on the type of LVDT, type of mount assembly (its contact area with the specimen), and type of epoxy used to secure the mounts to the specimen. The findings of an experimental study with these variables are shown in Table B.4. The type of mount assembly shows little effect on drifting.

TABLE B.4 Extent of Drift in Strains for the Different Combinations Tested

LVDT Type	**Mounting assembly**	**Horizontal**		**Vertical**	
		Devcon 5-minute epoxy	Devcon 2-Ton Plastic steel Putty	Devcon 5-minute epoxy	Devcon 2-Ton Plastic steel Putty
GTX	L-mounts	v. significant[a]	significant	v. significant	significant
	Guided rod assembly	significant[b]	-	significant	significant
	Rectangular mounts	-	-	v. significant	significant
XSB	L-mounts	-	No drift	significant	minimal

[a] indicates more than 10 microns of drift in 3 hours for 100 mm gage length.
[b] indicates 5-10 microns of drift in 3 hours for 100 mm gage length.
Dash indicates that combination was not tested.

It can be concluded that the major problem lies in the type of LVDT and the type of glue used. It is the spring force and not the weight of the GTX LVDTs that caused the mounts to deform. This is because the same drift is measured regardless of the orientation of the LVDTs (horizontal or vertical). Moreover, when the specimen and LVDT setup is flipped vertically, the drift remains in the same direction (mounts are being pushed away from each other). The XSB LVDTs do not exhibit drift while in the horizontal direction (no spring force applied to mounts). When the XSBs are in the vertical direction, the drift is sometimes positive and in other times negative, suggesting that both the LVDT and its cable weight (lower mount), in addition to the core and its extension rod (upper mount), cause the deformation of the mounts. It is also clear that the Devcon Plastic Steel Putty should be used instead of 5-minute epoxy to glue the mounts to the specimen. It is important, however, that proper curing time be given (preferably overnight); otherwise the mounts might still deform.

Based on the aforementioned findings, loose core LVDTs with Devcon Plastic Steel Putty is recommended as a deformation measurement system for asphalt mixture testing.

B.6 Summary and Conclusions

There are many potential problems that can affect the values of material properties measured from various tests. The machine compliance and instrumentation issues addressed in this appendix are of particular importance in frequency sweep testing used in the SPT and required for the AASHTO 2002 design guide.

- Machine compliance affects the magnitude and functional form of strains actually felt by the specimen. Machine compliance can be minimized by proper maintenance and installation techniques; however, it cannot be completely eliminated. Up to a 4.5 magnitude difference in dynamic modulus values and 20^{o} difference in phase angle values were found between measurements from the actuator LVDT and on-specimen LVDTs for the machine and mixture studied.
- The particular signal conditioner setup for a certain LVDT affects the phase shift and noise that is measured. There is a trade-off between the noise level and phase shift that must be idealized, depending upon the testing to be performed. Noise in the measured signal affected the dynamic modulus values by about 10%, and the phase shift can result in unreasonable trends in the phase angle versus frequency relationship.
- The type of mounting device and measurement gauge length can also affect the amount of measured phase shift from dynamic effects. The combined dynamic and electronic phase shift can be determined from testing on an elastic material (such as aluminum). This result can then be subtracted from the response measured from the material being tested to achieve the true material response.
- The LVDT and epoxy type can influence drifting of the LVDT measurements during testing. Additionally, the signal conditioners must be warmed up prior to use to eliminate electronic drifting due to the warming of the components.

The significance of each of these problems depends upon the type of testing that is being performed and the application of the resulting measured properties. For illustration, consider two tests to measure the linear viscoelastic properties of a material. In a creep and recovery test, the drift of the LVDT measurements would be a serious problem in measuring the strain under a static load over a period of time and then the recovery with time when the load is released. A drift in the LVDT measurements would either underestimate or overestimate both the strain under the load and during recovery, depending upon the testing and drift directions. However, any phase shift in the signal conditioners would not affect the test results. In a frequency sweep test, any phase shift poses a serious problem in the calculation of phase angles, but drifting of the LVDT measurements does not because only the amplitudes, and not the mean values of stresses and strains, are needed.

REFERENCES

1. Witczak, M. Simple Performance Test: Test Results and Recommendations. Interim Task C Report, NCHRP 9-19, 2000.

2. Alavi, S., T. Merport, T.Wilson, J.Groeger, A. Lopez. *LTPP Materials Characterization Program: Resilient Modulus of Unbound Materials (LTPP Protocol P46) Laboratory Startup and Quality Control Procedure.* Report FHWA-RD-96-176. FHWA, U.S. Department of Transportation, 1997.

3. Chehab,G., E.N. O'Quinn, and Y.R. Kim. Specimen Geometry Study for Direct Tension Test Based on Mechanical Tests and Air Void Variation in Asphalt Concrete Specimens Compacted by Superpave Gyratory Compactor. *Transportation Research Record 1723*, TRB, National Research Council, Washington, D.C., 2000, pp.125-132.

4. Daniel, J.S. *Development of a Simplified Fatigue Test and Analysis Procedure Using a Viscoelastic, Continuum Damage Model and its Implementation to WesTrack Mixtures*. Ph.D. Dissertation, North Carolina State University, Raleigh, NC, 2001.

5. Chehab G., Kim Y.R., Schapey R.A., Witczack M., Bonaquist R., Time-Temperature Superposition for Asphalt Specimens in the Tensile Damaged state. Submitted to *Journal of Asphalt Paving Technologists*, 2001.

6. Daniel, J.S. and Y.R. Kim. Development of a Simplified Fatigue Test and Analysis Procedure Using a Viscoelastic, Continuum Damage Model. Submitted to *Journal of Asphalt Paving Technologists*, 2001.

APPENDIX C

EVALUATION OF DESIGN AND AS-CONSTRUCTED GRADATIONS

The asphalt industry is moving towards performance-based criteria for both design and QC/QA activities. This move has resulted in a more mechanistic approach to design, as evidenced by the development of the simple performance test and the AASHTO 2002 structural design guide. Accordingly, mechanistic modeling to predict the behavior of asphalt concrete has become an important issue in asphalt concrete research for the development of performance-based test and design methods. It is necessary to improve the effectiveness of these models by calibrating the prediction model with field and laboratory data. In laboratory testing and verification, tight control over mixture variables is relatively easy to implement because of the small amounts of materials concerned. However, this same level of control is impossible to achieve in the field.

Years of experience by agencies have demonstrated the qualitative effects of mixture properties on the overall mixture performance. The recently completed WesTrack project, for example, has provided a wealth of information that translates to the quantitative measurement of the effects of aggregate gradation, asphalt content, and air void content on mixture performance. This appendix evaluates issues related to the development and implementation of performance-based testing with respect to mixture variables. Of particular importance are the differences between design and construction gradations and the effect of mixture variables on the variability in fabrication of, and material properties measured from, laboratory specimens to be used in field performance comparisons.

C.1 Materials

The aggregates used in this study are from two sources. The WesTrack aggregates are a crushed andesite from Dayton, Nevada and a natural (Wadsworth) sand (WesTrack Team 2000 a, b). The binder is a PG 64-22 obtained from a west coast refinery and is a blend of US crudes. Several different aggregate gradation, air void content, and asphalt content combinations of the WesTrack materials are evaluated. The WesTrack materials used in this study were obtained from the WesTrack Material Reference Library (MRL).

The North Carolina aggregate is granite obtained from the Martin Marietta Lemon Springs Quarry in Sanford, NC. The North Carolina gradation also included some natural sand and baghouse fines material from Lee Paving Company, also located in Sanford, NC. The North Carolina aggregate is mixed with 5.1% of a PG 70-22 binder obtained from Citgo. This mixture was placed in section 1 (SHRP No. 370965) of the SPS-9 test sections located on US 1 southbound in Lee and Chatham Counties.

C.2 Evaluation of Gradations

This section evaluates the differences between the design and construction gradations. The WesTrack materials were sampled during the mixing process and are assumed to be representative of the material placed on the test track. The North Carolina aggregates were sampled from the stockpiles at the time of construction and are assumed to be representative of the material placed in the field.

WesTrack Gradations

The 19 mm Superpave “coarse” and “fine” WesTrack gradations are evaluated in this study. The coarse gradation falls below the restricted zone and the fine gradation falls above the restricted zone. The coarse gradation is a combination of three stockpiles of the Dayton aggregate whereas the fine gradation is a combination of four Dayton stockpiles and the Wadsworth sand. Both gradations have hydrated lime added. The percentages of each stockpile used in the two gradations are shown in Table C.1.

TABLE C.1 Percentages of Stockpiles in WesTrack Gradations

Gradation	Percent of Stockpile in Gradation				
	19 mm Stockpile	**12.5 mm Stockpile**	**9.5 mm Stockpile**	**Rock Dust Stockpile**	**Wadsworth Sand**
Coarse	47.0	19.0	-	32.5	-
Fine	31.0	19.0	10.0	13.5	25.0

Dash indicates there is no material from that stockpile in the gradation.

A sieve analysis was performed on the five stockpiles in accordance with ASTM C 136-84a. Table C.2 shows the comparison of the design and laboratory-determined gradations for the four stockpiles. The laboratory gradations are an average of three replicates. As with the North Carolina aggregate, the WesTrack laboratory gradations are coarser than the design gradations. A washed sieve analysis was performed on the WesTrack aggregates. A significant amount of fine material (passing 0.075 mm sieve) was found to be adhering to larger aggregate particles in the stockpiles; however, that material did not completely account for the differences between the laboratory and design gradations.

TABLE C.2 Design and Dry Laboratory Gradations for WesTrack Aggregates

Sieve Size (mm)	**19 mm Stockpile % Passing Design (Lab)**	**12.5 mm Stockpile % Passing Design (Lab)**	**9.5 mm Stockpile % Passing Design (Lab)**	**Rock Dust Stockpile % Passing Design (Lab)**	**Wadsworth Sand Stockpile % Passing Design (Lab)**
25.0	100.0 (100.0)	100.0 (100.0)	100.0 (100.0)	100.0 (100.0)	100.0 (100.0)
19.0	99.8 (100.0)	100.0 (100.0)	100.0 (100.0)	100.0 (100.0)	100.0 (100.0)
12.5	63.5 (54.2)	99.9 (99.3)	100.0 (100.0)	100.0 (100.0)	100.0 (100.0)
9.5	33.7 (25.6)	82.6 (79.8)	97.7 (98.9)	100.0 (100.0)	100.0 (100.0)
4.75	10.8 (4.8)	19.5 (19.1)	29.8 (32.2)	99.9 (99.7)	99.7 (100.0)
2.36	5.0 (1.0)	4.3 (2.4)	6.4 (3.2)	76.6 (74.4)	99.0 (98.6)
1.18	4.3 (0.9)	3.2 (1.5)	5.0 (1.2)	54.1 (49.7)	96.0 (95.2)
0.600	4.0 (0.9)	2.9 (1.3)	4.4 (1.0)	39.2 (34.3)	79.9 (76.1)
0.300	3.7 (0.8)	2.6 (1.2)	3.9 (1.0)	28.7 (19.0)	40.1 (22.0)
0.150	3.4 (0.7)	2.4 (1.0)	3.4 (0.9)	20.3 (7.1)	11.0 (4.7)
0.075	1.9 (0.4)	1.3 (0.7)	1.8 (0.7)	8.8 (2.5)	2.1 (0.9)

The as-constructed gradations for the WesTrack mixtures are shown with the laboratory dry and washed sieve analyses and design gradations in Table C.3. The as-constructed gradations were determined from 45 tests conducted during the course of construction. Whereas all of the gradations fall within the Superpave control points, the as-constructed gradations are coarser than the design gradations, and the laboratory washed sieve gradations are coarser than the as-constructed gradations with the exception of the 0.075 mm sieve.

TABLE C.3 Design, Dry Lab, Washed Lab, and Construction Gradations for WesTrack

Sieve Size (mm)	Coarse Gradation % Passing				Fine Gradation % Passing			
	Design	Dry Lab	Washed Lab	Constr.	Design	Dry Lab	Washed Lab	Constr.
25.0	100.0	100.0	100.0	100.0	100.0	100.0	100.0	100.0
19.0	99.9	100.0	100.0	100.0	99.9	100.0	100.0	100.0
12.5	82.8	78.3	78.4	81.8	88.7	85.7	85.7	88.3
9.5	65.5	61.2	61.3	66.3	75.9	73.0	73.1	75.9
4.75	42.7	39.8	40.0	42.1	49.9	48.3	48.5	48.3
2.36	29.6	26.6	26.9	27.2	39.6	37.3	37.5	36.7
1.18	21.7	18.4	18.7	19.9	35.2	32.7	33.0	32.3
0.600	16.6	13.3	13.8	14.9	29.0	25.7	26.1	26.4
0.300	13.0	8.2	9.1	11.0	17.4	10.1	10.7	15.1
0.150	10.0	4.2	6.2	7.9	8.7	4.0	5.1	7.4
0.075	4.8	1.9	4.1	5.5	3.5	1.7	2.9	4.4

WesTrack performance data show a significant difference in the fatigue and rutting performance of the coarse and fine gradations (WesTrack Team 2000 a, b; WesTrack Database 2000). However, the difference in performance between the design, as-constructed, and washed laboratory gradations is unknown. Although there are tolerances for construction gradations, the effect of those tolerances on the actual pavement performance is unclear.

North Carolina Gradation

The 12.5 mm North Carolina gradation is a combination of four stockpiles and baghouse fines. The #67, #78, and screenings stockpiles are the Lemon Springs aggregates and the fourth stockpile is natural sand. These four stockpiles comprise 15.0 %, 55.0 %, 19.0 %, and 10.0 %, respectively, of the design gradation. The percentage of baghouse fines in the design gradation is 1.0 %.

A sieve analysis was performed on the four stockpiles in accordance with ASTM C136-84a. Three replicates of the Lemon Springs stockpiles and five replicates of the sand stockpile were performed and averaged to obtain the laboratory-determined gradation. Table C.4 shows the design and laboratory gradations for the four stockpiles. All four stockpiles show that the laboratory gradation is coarser than the design gradation, indicating that the as-constructed gradation is coarser than that used in the mixture design, as was the case for the WesTrack gradations. A washed sieve analysis was performed on the four stockpiles in accordance with ASTM C 117-90. Three replicates found that there was no significant difference between the washed sieve analysis and dry sieve analysis for the North Carolina aggregates. Table C.5 shows the overall design gradation and the overall gradation determined using the results of the laboratory sieve analysis and stockpile percentages reported above.

TABLE C.4 Design and Laboratory Gradations for North Carolina Aggregates

Sieve Size (mm)	#67 Stockpile % Passing Design (Lab)	#78 Stockpile % Passing Design (Lab)	Screenings Stockpile % Passing Design (Lab)	Natural Sand Stockpile % Passing Design (Lab)
19.0	100.0 (100.0)	100.0 (100.0)	100.0 (100.0)	100.0 (100.0)
12.5	62.0 (46.7)	99.0 (99.8)	100.0 (100.0)	100.0 (100.0)
9.5	30.0 (23.0)	90.0 (90.4)	100.0 (100.0)	100.0 (100.0)
4.75	5.2 (4.6)	23.0 (15.9)	99.0 (100.0)	99.9 (100.0)
2.36	2.1 (1.0)	4.0 (0.5)	83.0 (74.5)	99.7 (100.0)
1.18	1.5 (0.8)	3.0 (0.4)	57.0 (47.4)	94.0 (94.7)
0.600	1.0 (0.7)	2.0 (0.3)	40.0 (31.4)	70.0 (53.1)
0.300	1.0 (0.7)	1.0 (0.3)	27.0 (19.6)	22.0 (12.1)
0.150	0.8 (0.6)	1.0 (0.3)	19.0 (9.1)	12.0 (2.9)
0.075	0.6 (0.4)	0.5 (0.2)	13.0 (3.3)	6.6 (0.6)

TABLE C.5 North Carolina Design and Laboratory Gradations

Sieve Size (mm)	12.5 mm Superpave Control Points		Design Gradation % Passing	Laboratory Gradation % Passing
	Minimum	Maximum		
19.0		100.0	100.0	100.0
12.5	90.0	100.0	93.8	91.9
9.5		90.0	84.0	83.2
4.75			43.2	39.4
2.36	28.0	58.0	29.3	25.6
1.18			23.1	19.8
0.600			16.9	12.5
0.300			9.0	6.2
0.150			6.5	3.3
0.075	2.0	10.0	4.5	1.9

This finding shows that the laboratory gradation violates the Superpave specifications for a 12.5 mm mix. The percentage passing on the 2.36 mm and 0.075 mm sieves falls below the minimum control point values for the Superpave gradation. The as-constructed gradation was not measured; however, assuming the same pattern between the WesTrack gradations exists with the North Carolina gradation, the North Carolina as-constructed gradation would fall between the design and lab gradations.

Design Tolerances

For quality control purposes, agencies institute design tolerances on aggregate gradations. While there are established tolerances for stockpiles, agency-established quality control measures are used during the construction process for any particular design gradation.

The North Carolina Department of Transportation (NCDOT) quality control for aggregate gradation involves sampling of the plant mix and recovering the aggregate by the ignition method, or sampling aggregates from the cold feed belts before mixing (NCDOT 2001). Several control sieves (2.36 mm, 0.075 mm, and one sieve below the NMSA) are checked, and a moving average of four tests must be within a certain tolerance for the quality control criteria to be met. Additionally, individual test limits are applied, and in the case of the laboratory gradation, the percentage passing the 0.075 mm sieve would have resulted in stoppage of production as it is outside the individual test limits (± 2.5) and the specification design limits for a 12.5 mm Superpave gradation.

The quality control and quality assurance checks for the construction of the WesTrack pavement sections were more stringent than in typical pavement construction due to the research-oriented nature of the project. The details of the WesTrack QC/QA procedures and construction specifications and tolerances may be found in the series of WesTrack technical reports (Epps et al. a, b 2000).

Sources of Discrepancy

There are several possible sources for the discrepancy between the design gradation and the as-constructed and laboratory-determined gradations. From the time a mix design is performed to the time of construction, the stockpile gradations can change within allowable tolerances which will, in turn, affect the combined gradation. This phenomenon in and of itself does not account for the fact that the three gradations evaluated in this study were coarser than the design gradation, as stockpile gradations can fluctuate in both directions. A loss of fine material during the mixing procedure would explain the coarser as-constructed gradations. The sampling, storage, and measurement processes that take place for the laboratory materials can also contribute to the loss of fine material and may explain why the laboratory-determined gradations are coarser than the as-constructed gradations.

Consequences of Variations in Gradation

The effects of variation in aggregate gradation may be discussed with regard to the actual pavement construction and performance as well as the laboratory evaluation and research of these mixtures. The effect on the actual field performance is of obvious importance to agencies, contractors, and the general public. The effect on the laboratory evaluation is becoming increasingly important as the asphalt industry moves towards more mechanistic design with the associated requirement for field validation and verification of the design methods.

The performance of the WesTrack pavement sections clearly shows that the aggregate gradation has a significant effect on the pavement performance. The coarse mixtures performed poorly compared to the fine mixtures with respect to both rutting and fatigue. This result is the opposite to conventional theory on the influence of aggregate gradation on asphalt mixture performance. Epps et al. (2002) report that the coarse mixture exhibited much higher variability in gradation and was much more sensitive to mixture variables. This finding, coupled with the fact that the three gradations evaluated in this study were coarser than design gradations, indicates that the effects of this phenomenon merit further investigation.

Due to the sensitivity of the mixture performance to different variables and to the interaction of these variables, the industry has indicated that a truly performance-related mixture design and test is needed. The mixture design procedure must be able to account for the effect of construction tolerances if those are found to have a significant effect on the field performance. Additionally, this study shows that it is important to have accurate information on the as-constructed gradations as research into possible design and test procedures and field validation becomes more widespread. The coarser laboratory gradations will make it necessary to obtain more material to replicate the finer construction gradations in laboratory-fabricated specimens.

C.3 Specimen Fabrication

Asphalt concrete specimens fabricated in the laboratory are compacted using the standard Superpave gyratory compactor. A specimen geometry study by Chehab et al. (2000) shows that actual test specimens must be cut and cored from compacted gyratory plugs to obtain a representative volume element required for determining fundamental material properties. The resulting test specimens have the most consistent air void distribution in both the vertical and radial directions. The specimens fabricated in this study were to be used in direct tension testing with a final test specimen size of 75 mm in diameter and 150 mm tall.

TABLE C.6 WesTrack Compaction Information and Air Void Measurements

Mixture	Compaction Height (mm)	Avg # Gyrations to Compaction	Target Air Void (%)	Average Air Void (%)	Air Void Standard Deviation
FLO	187.4	10.9	4.0	3.9	0.42
FML	197.8	2.8	8.0	8.2	0.51
FMO	197.8	2.6	8.0	7.8	0.71
FMH	197.8	1.7	8.0	5.3	0.36
CLO	185.7	33.7	4.0	4.1	0.56
CML	197.0	19.5	8.0	7.8	0.29
CMO	197.0	11.4	8.0	8.2	0.42
CMH	197.0	10.5	8.0	7.9	0.50

Eight WesTrack mixtures were evaluated in this portion of the study. The coarse (C) and fine (F) gradations at the 8% (M) air void content were evaluated at the low (L), optimum (O), and high (H) asphalt contents, as well as the two gradations at 4% (L) air void content and optimum asphalt content. The as-constructed aggregate gradation was used and mixed with the asphalt cement at 150°C, then aged for four hours at 135°C (short-term oven aging) before being compacted at 140°C. The appropriate air void content was achieved by compacting a standard amount of mixture (7200g) to predetermined heights. The compaction heights and average number of gyrations are shown in Table C.6. The low air void mixtures required more gyrations and, as the asphalt content decreased with the 8% air void mixtures, more gyrations were needed because of the stiffer mixture. The fine gradation mixtures were more easily compacted, with the 8% air void specimens only requiring a couple of gyrations to reach the desired height. The gyratory compactor does not apply partial gyrations, so in many cases the specimens were over-compacted with the application of a whole number of gyrations. This process resulted in a larger variability in measured air voids, as shown in Table C.6. Moreover, a higher percentage of those specimens could not be used for testing because they were outside the ±0.5% air void content tolerance. In the case of FMH (fine gradation, 8% air, high AC) mixture, 8% air voids could not be achieved. The low number of gyrations also causes concern about the aggregate orientation within the specimens and the possible specimen-to-specimen variability. A fewer number of gyrations would result in less consistent aggregate orientation and perhaps greater anisotropy with respect to air void distribution in the specimen.

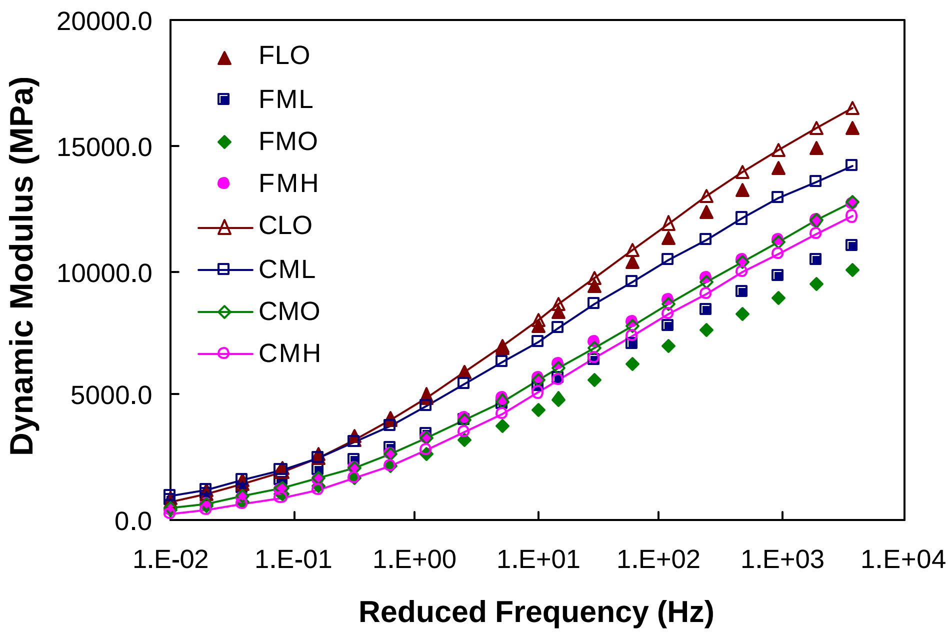

FIGURE C.1 AVERAGE DYNAMIC MODULUS CURVES FOR COARSE AND FINE WESTRACK MIXTURES

The fundamental viscoelastic material properties for the eight WesTrack mixtures were measured from the frequency sweep test. All eight mixtures were tested at 20^{o}C. Eight frequencies (20, 10, 5, 2, 1, 0.5, 0.2, and 0.1 Hz) were used for these mixtures, with a data acquisition rate of 100 points per cycle. Frequency sweep tests at 0^{o}C or 5^{o}C using six frequencies (20, 10, 3, 1, 0.3, and 0.1 Hz) were performed on some of the mixtures. Master curves were then generated using the time-temperature superposition principle. Figure C.1 shows the response of each of the mixtures and allows for comparison of the coarse and fine gradations. The modulus values for the coarse mixture show the expected trends with respect to air voids and asphalt content. The 4% air void mixture (CLO) has a higher modulus than the 8% air void mixture (CMO). Within the 8% air void content mixtures, increasing asphalt content resulted in lower dynamic modulus values. The resilient modulus values reported by Epps, et al. (1999) show the same trend with respect to air void and asphalt content. The fine mixtures follow the same trends with the exception of FMH, which has a higher dynamic modulus than both FML and FMO mixtures. This difference is due to the lower air void content in the FMH mixtures. The FMH mixtures could only be fabricated with 5.5% air voids while both the FML and FMO mixtures contained 8% air voids. In three cases, the coarse mixture was stiffer than the corresponding fine mixture (i.e., CMO versus FMO). The CMH and FMH mixtures could not be compared due to the air void differences. However, one can observe that the FMH mixture would also have a lower dynamic modulus than the CMH mixture if it fell below the FMO mixture, as would be expected at 8% air voids.

The individual (points) and average (solid line) master curves at 20^{o}C for the FML and CLO mixtures are shown in Figures C.2 and C.3, respectively. The individual and average master curves for the other mixtures may be found in Appendix D. The effect of the number of gyrations for compaction on the variability of the dynamic modulus values is evident as the CLO mixture which required the greatest number of gyrations to compaction shows much less sample-to-sample variability than the FML mixture. The mean square error (mse) is calculated for each mixture using the following equation as a measure of specimen-to-specimen variability.

$$mse = \sqrt{\frac{1}{n-1}\sum\left(y-\hat{y}\right)^2}$$

where n = number of observations
y = measured value
$\hat{y}$ = predicted value

Table C.7 summarizes the dynamic modulus and phase angle mse values for each mixture. In general, the fine mixtures show greater variablilty in the dynamic modulus measurements than the coarse mixtures, with the exception of CML. This difference likely stems from the specimen fabrication process and the difference in compatibility of the two gradations. As shown in Table C.6, the fine gradation required fewer gyrations to reach compaction height, and there is likely a less consistent aggregate orientation and air void distribution, which results in a higher sample-to-sample variability in testing, as shown by the dynamic modulus measurements. The mse for the phase angle measurements shows no trend with respect to the gradation.

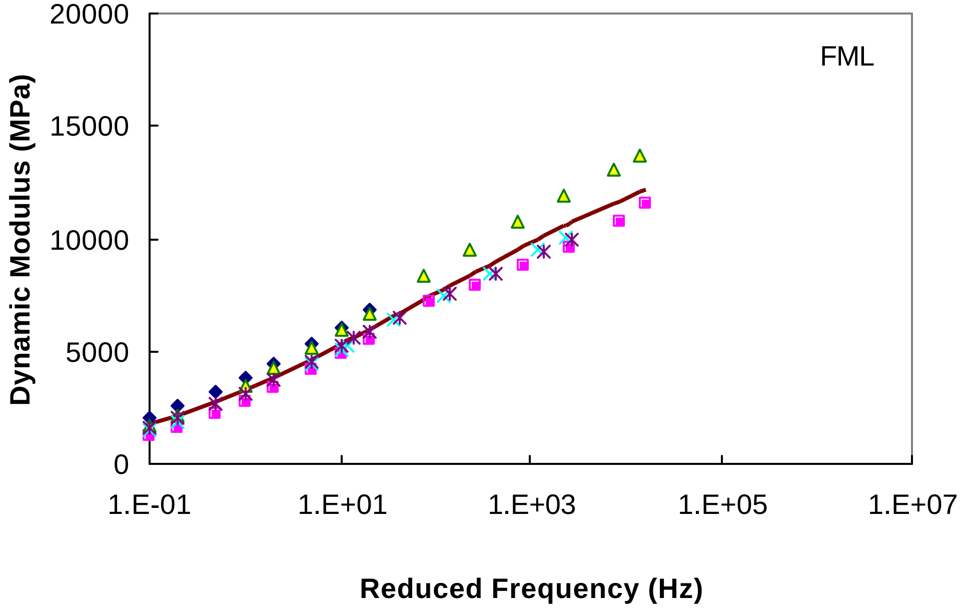

FIGURE C.2 Individual and Average Dynamic Modulus Curves for FML Mixture

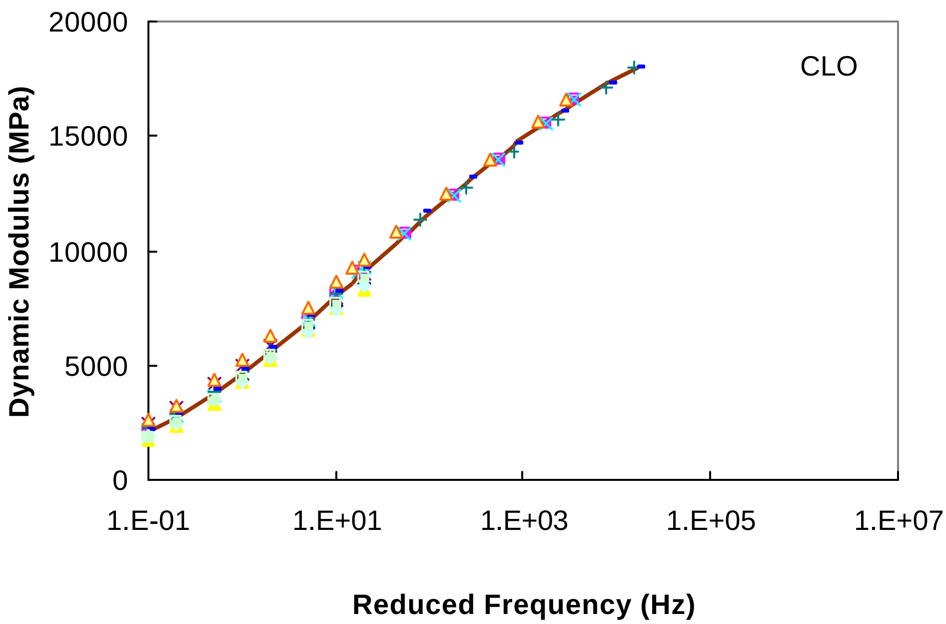

FIGURE C.3 Individual and Average Dynamic Modulus Curves for CLO Mixture

TABLE C.7 Mean Square Error Values for Dynamic Modulus and Phase Angle

Mixture	Dynamic Modulus (MPa)	Phase Angle (degrees)
FLO	593	2.02
FML	624	1.24
FMO	275	1.44
FMH	805	2.51
CLO	305	1.71
CML	661	2.11
CMO	396	2.15
CMH	352	2.77

Higher sample-to-sample variability affects both model development and the practical implementation of laboratory mixture testing. The larger the variability, the greater the need for more replicate testing to obtain the average mixture properties, thus resulting in a greater time and materials requirement. The measurement of dynamic modulus is a part of the proposed simple performance test and is required in the AASHTO 2002 design guide. The mixture properties such as gradation, asphalt content, and air void content clearly have an effect on the variability of the dynamic modulus measurement as measured in the laboratory. The variability must be accounted for when field validation is done on laboratory-developed models and in the eventual implementation of performance-based laboratory testing.

C.4 Summary and Conclusions

This study evaluated the differences between design and construction gradations as well as the effects of mixture variables on the fabrication of laboratory specimens and the measurement of fundamental material properties. Laboratory sieve analysis of three different aggregate gradations showed that the materials sampled from the construction process were coarser than those used for the original mix design. In the case of the two WesTrack gradations, the as-constructed gradations were available and found to be coarser than the design gradations, but not as coarse as the gradations determined from the laboratory analysis. These findings emphasize the need for the use of as-constructed gradations in performance-based laboratory testing. It also raises the question of the effect of these differences in gradation on the performance of the pavement. The results of the WesTrack project show that there is clearly an effect of gradation on the mixture performance, but the difference in performance within current construction tolerances is unknown. Therefore, more research is required in this area. Further investigation is also needed to determine if the trend of coarser construction gradations is typical or not. This question is of particular concern as WesTrack researchers found that the coarse mixture exhibited much higher variability in gradation and was more sensitive to changes in mix properties.

A study of eight WesTrack mixtures shows that mixture variables (gradation, asphalt content, air void content) can have a significant effect on the fabrication of laboratory specimens and their material properties. Mixtures that compacted in a relatively small number of gyrations were found to have higher sample-to-sample variability. This variability can affect both the development and implementation of material models based on the measurement of fundamental material properties such as dynamic modulus.

REFERENCES

1. WesTrack Team. *WesTrack Final Report Part III – Project Overview.* Draft Report submitted to FHWA, 2000.

2. WesTrack Team. *WesTrack Final Report Part IV – Observations and Lessons.* Draft Report submitted to FHWA, 2000.

3. WesTrack Database.(CD-ROM) Beta Version, 2000.

4. North Carolina DOT Document. Quality Management System for Asphalt Pavements – Superpave Version, 2001.

5. Epps, J., A. Hand, P. Sebaaly. *QC Aggregate Gradation – Original Construction. WesTrack.* UNR-22 Technical Report, 1999.

6. Epps, J., A. Hand, P. Sebaaly. *WesTrack Construction Specifications.*. WesTrack UNR-31 Technical Report, 1999.

7. Epps, A. L., A. J. Hand, J. A. Epps, and P. E. Sebaaly. Aggregate Contributions to the Performance of Hot Mix Asphalt at WesTrack. *Aggregate Contribution to Hot Mix Asphalt (HMA) Performance, ASTM STP 1412,* T. D. White, S. R. Johnson, and J. J. Yzenas, Eds., American Society for Testing and Materials, West Conshohocken, PA, 2002.

8. Chehab,G., E.N. O'Quinn, and Y.R. Kim. Specimen Geometry Study for Direct Tension Test Based on Mechanical Tests and Air Void Variation in Asphalt Concrete Specimens Compacted by Superpave Gyratory Compactor. In *Transportation Research Record 1723*, TRB, National Research Council, Washington, D.C., 2000, pp.125-132.

9. Epps, J., S. Dewan, A. Hand, and P. Sebaaly. *Resilient Modulus and Tensile Strength Properties of WesTrack Hot-Mix Asphalt Mixtures.* WesTrack Technical Report UNR-26, (1999).

APPENDIX D

MATERIAL PROPERTIES AND PERFORMANCE INFORMATION ON WESTRACK MIXTURES

D.1 Dynamic Modulus Curves for All WesTrack Mixtures

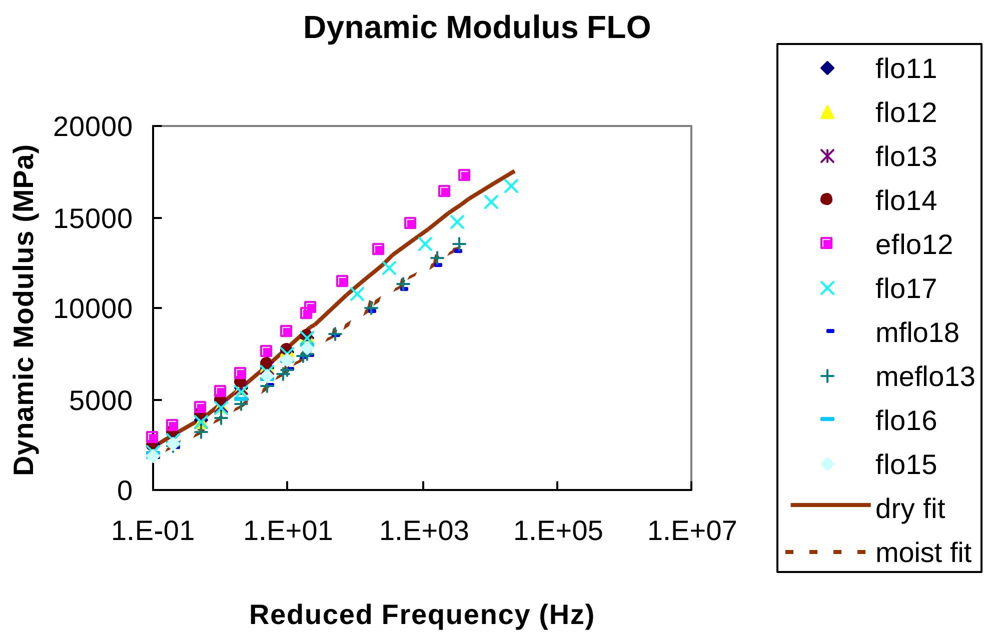

Figure D.1 Dynamic Modulus Master Curves for FLO Mixture

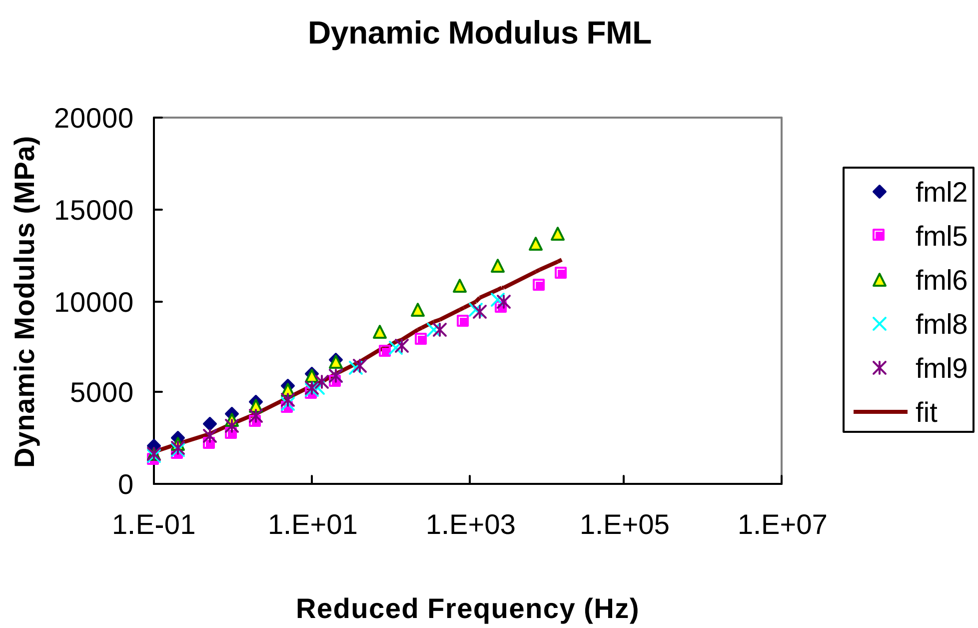

Figure D.2 Dynamic Modulus Master Curves for FML Mixture

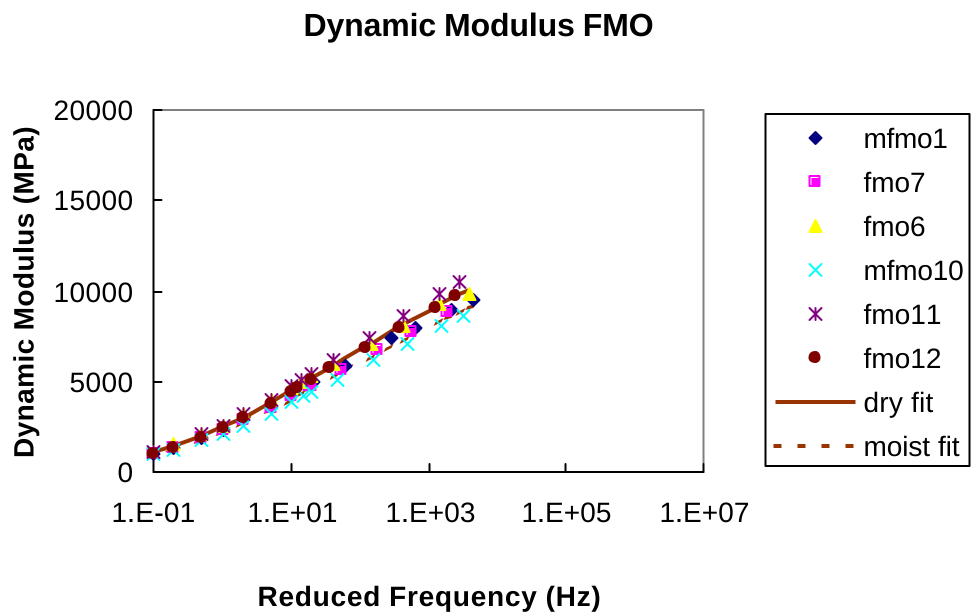

Figure D.3 Dynamic Modulus Master Curves for FMO Mixture

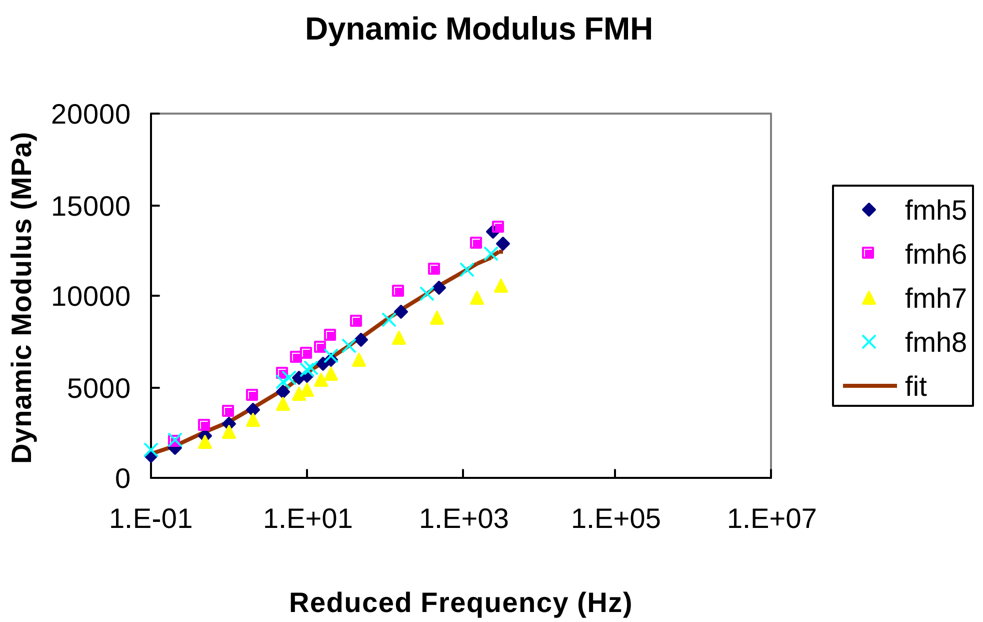

Figure D.4 Dynamic Modulus Master Curves for FMH Mixture

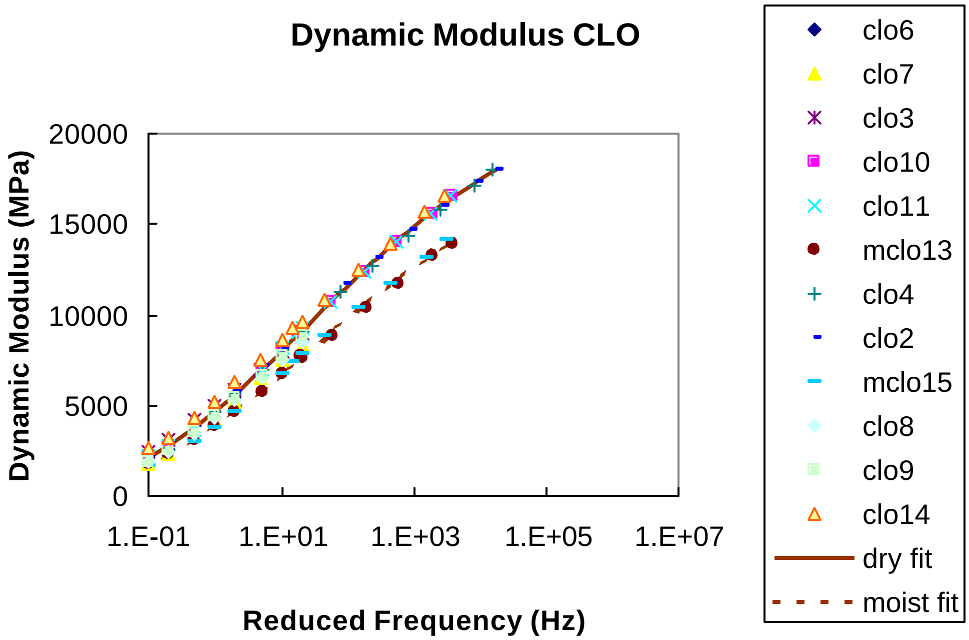

Figure D.5 Dynamic Modulus Master Curves for CLO Mixture

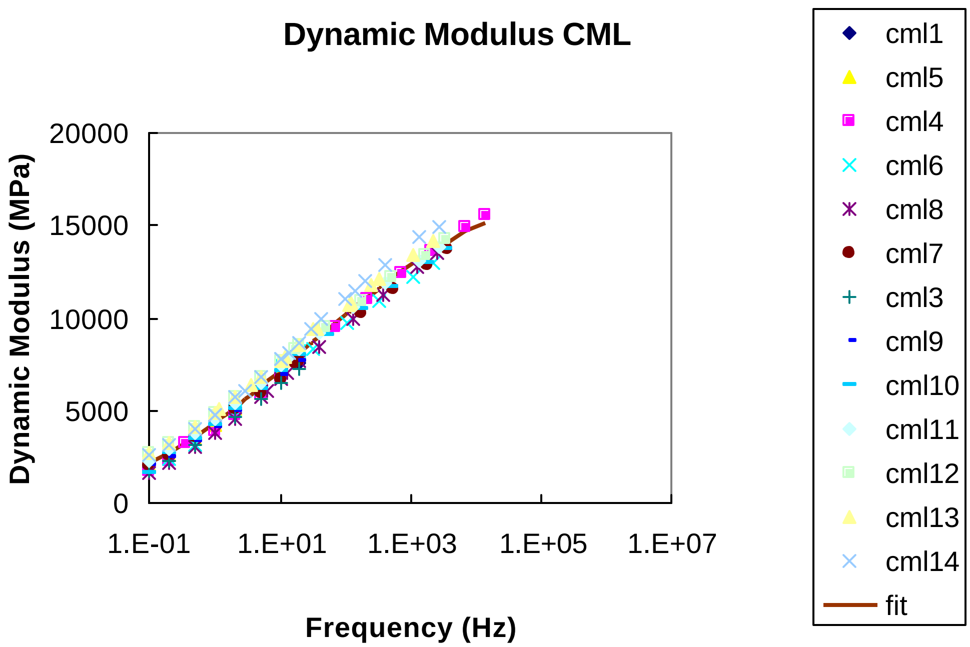

Figure D.6 Dynamic Modulus Master Curves for CML Mixture

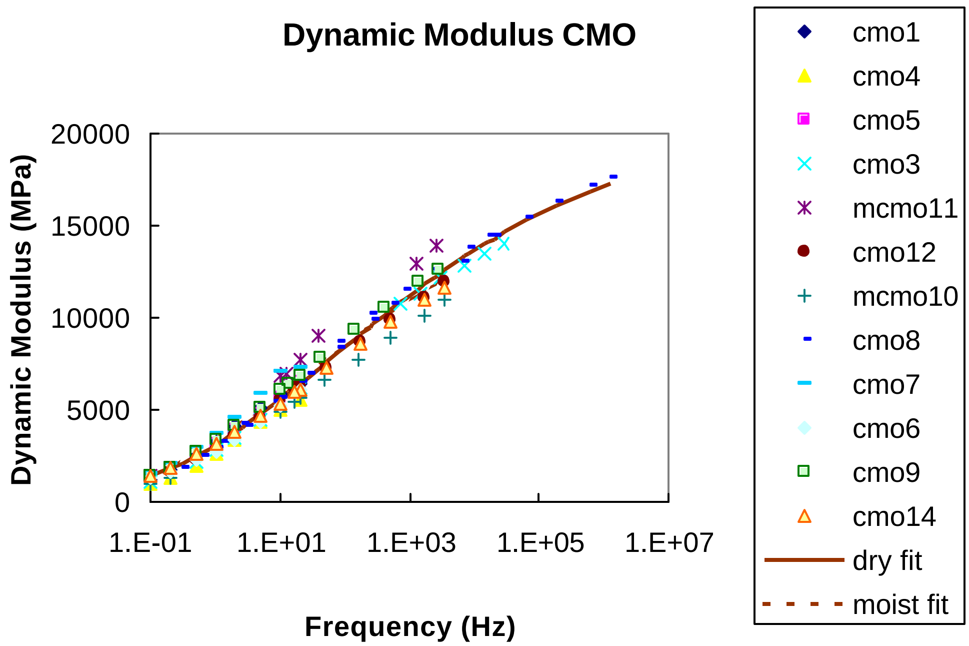

Figure D.7 Dynamic Modulus Master Curves for CMO Mixture

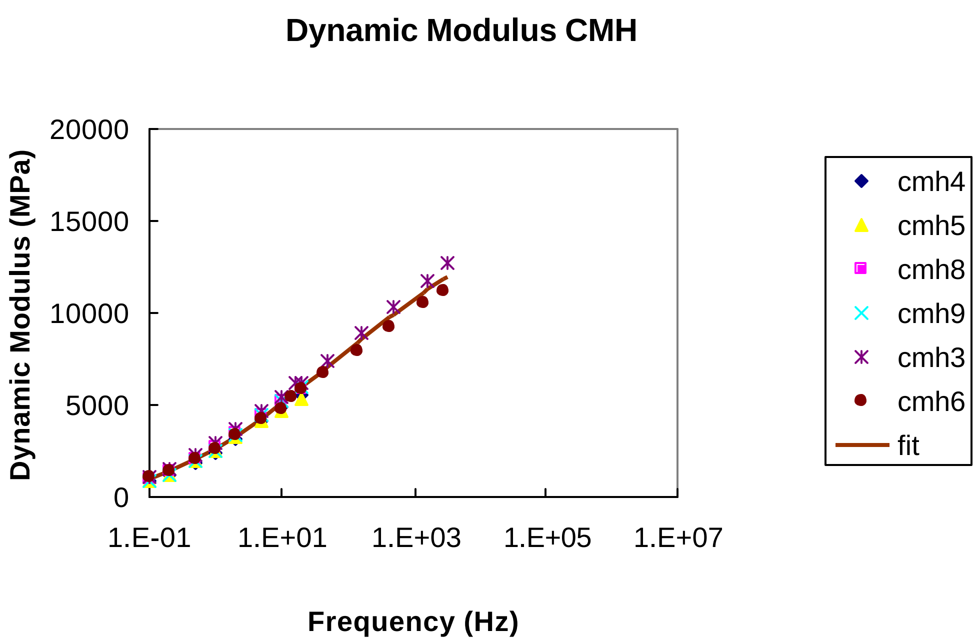

Figure D.8 Dynamic Modulus Master Curves for CMH Mixture

D.2 Characteristic Curves for All WesTrack Mixtures

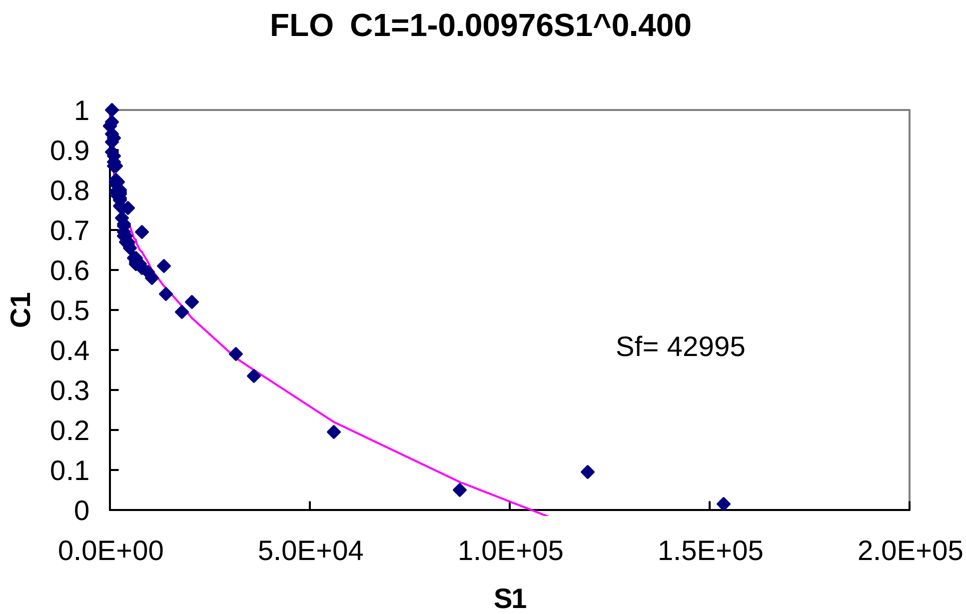

Figure D.9 Characteristic Curve for Cyclic FLO Data

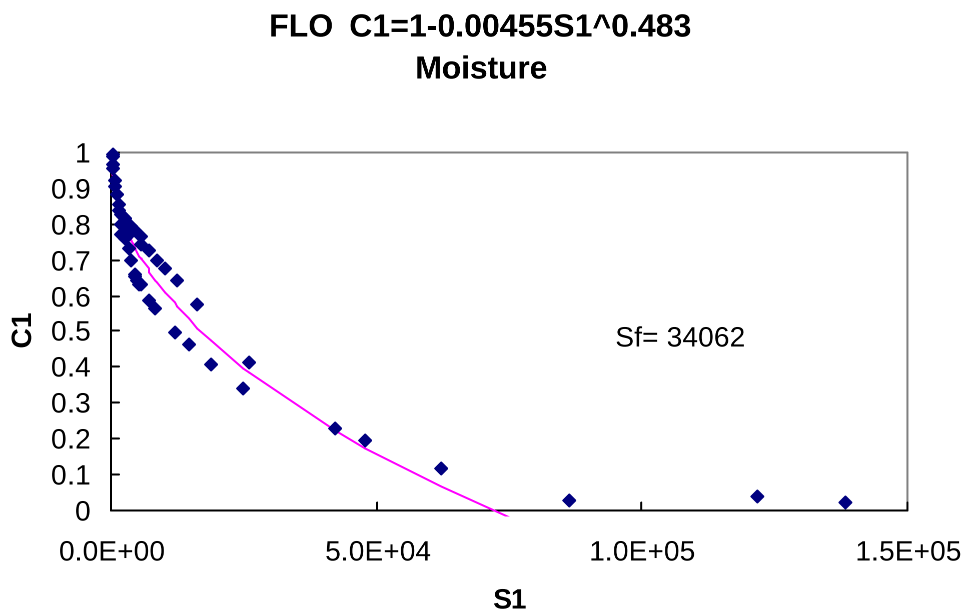

Figure D.10 Characteristic Curve for Moisture Cyclic FLO Data

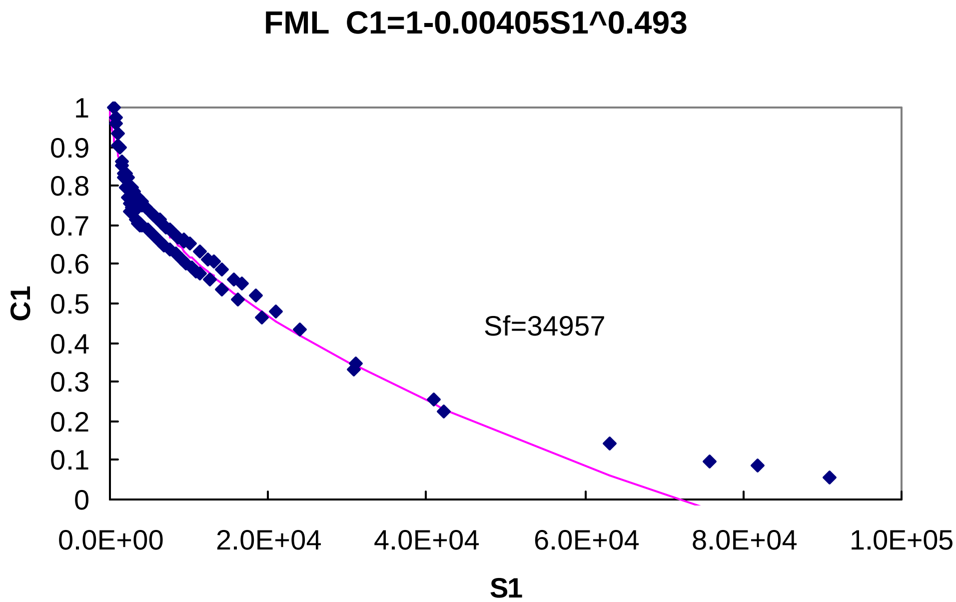

Figure D.11 Characteristic Curve for Cyclic FML Data

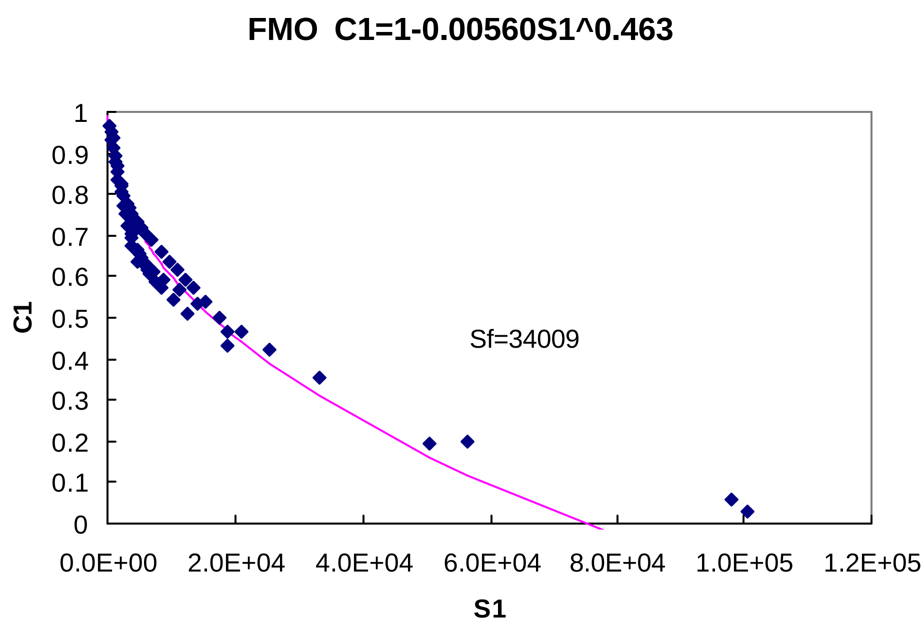

Figure D.12 Characteristic Curve for Cyclic FMO Data

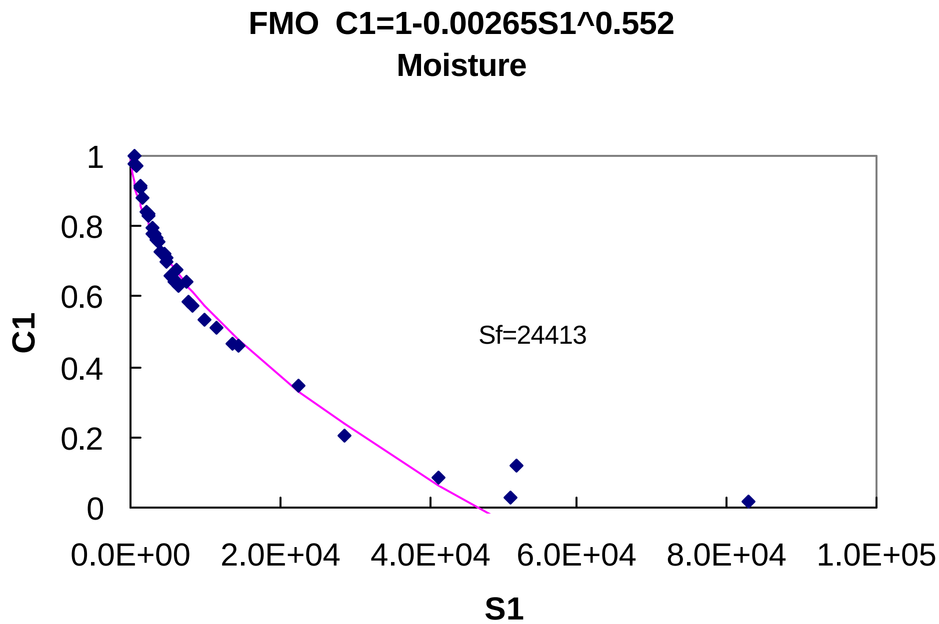

Figure D.13 Characteristic Curve for Moisture Cyclic FMO Data

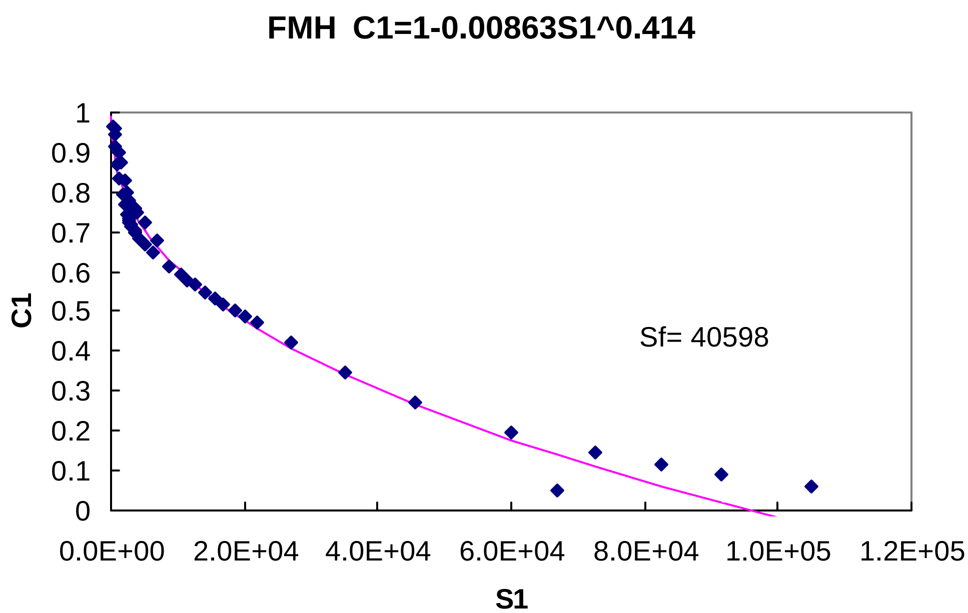

Figure D.14 Characteristic Curve for Cyclic FMH Data

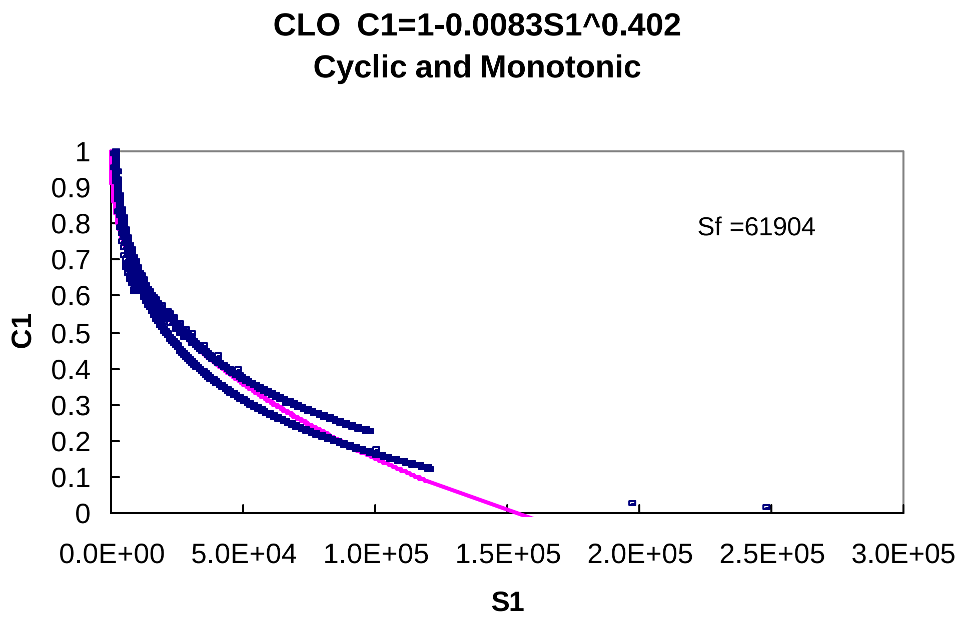

Figure D.15 Characteristic Curve for Cyclic and Monotonic CLO Data

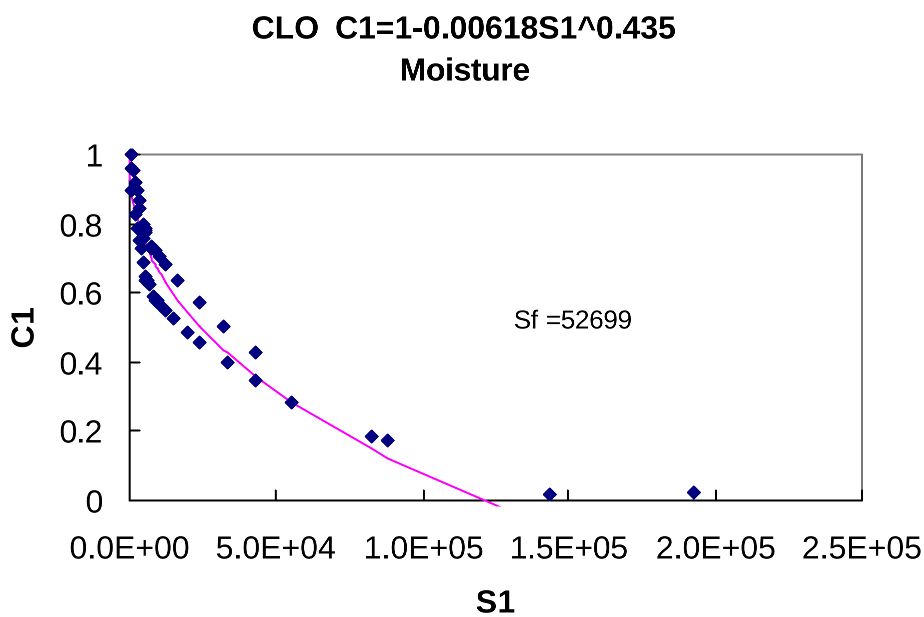

Figure D.16 Characteristic Curve for Moisture Cyclic CLO Data

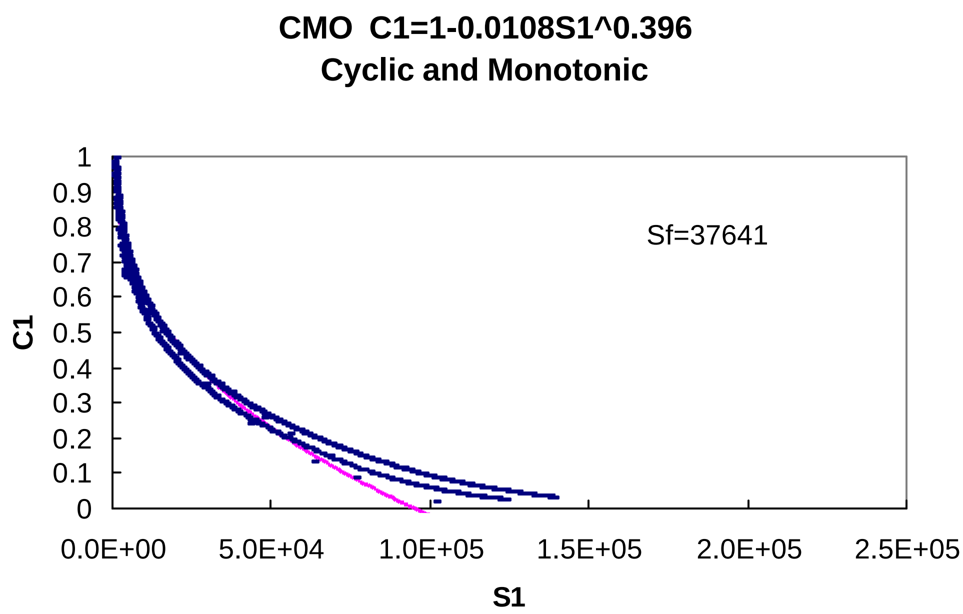

Figure D.17 Characteristic Curve for Cyclic and Monotonic CMO Data

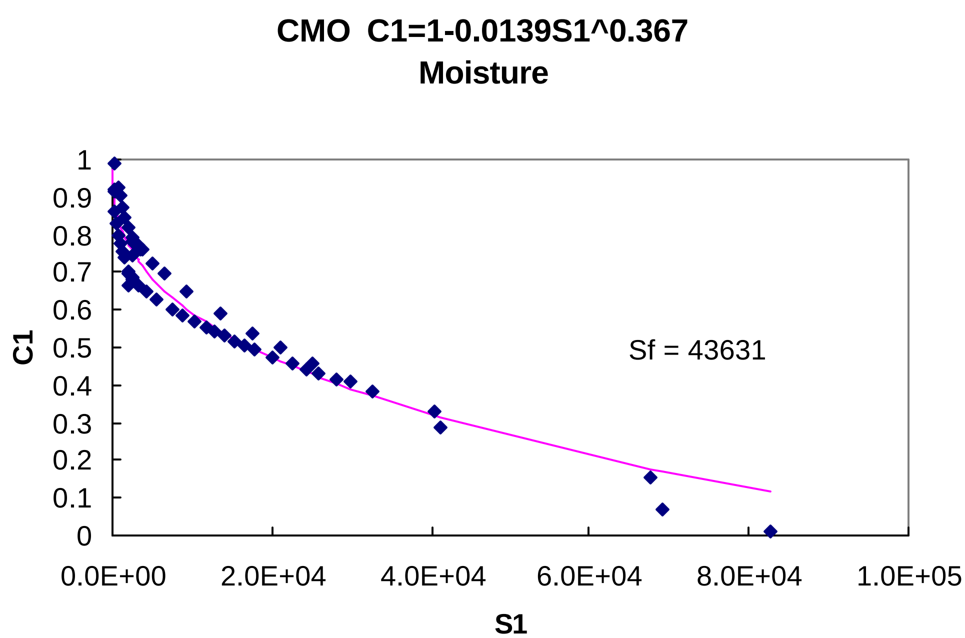

Figure D.18 Characteristic Curve for Moisture Cyclic CMO Data

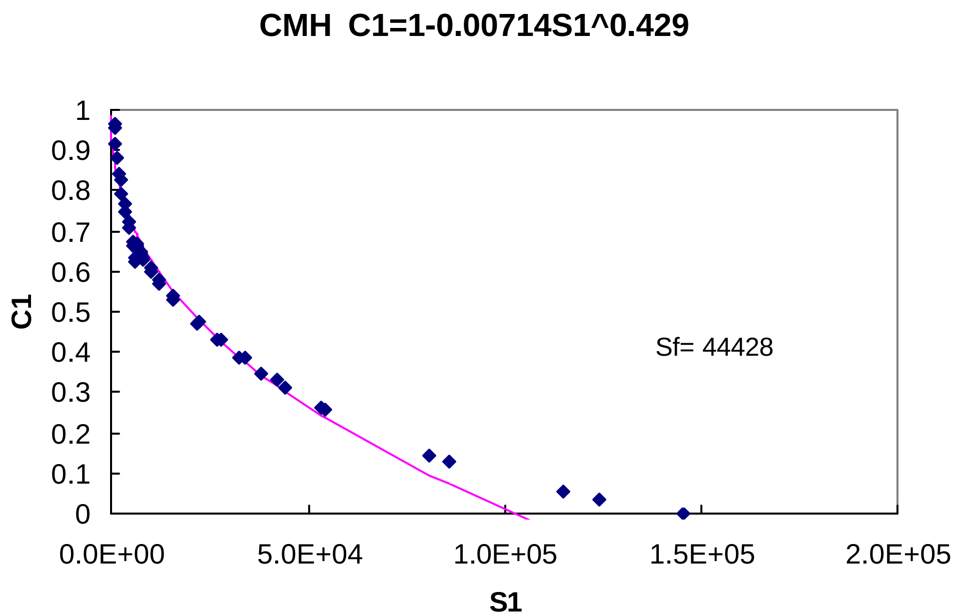

Figure D.19 Characteristic Curve for Cyclic CMH Data

D.3 Resilient Modulus Data for WesTrack ABC and Engineered Fill

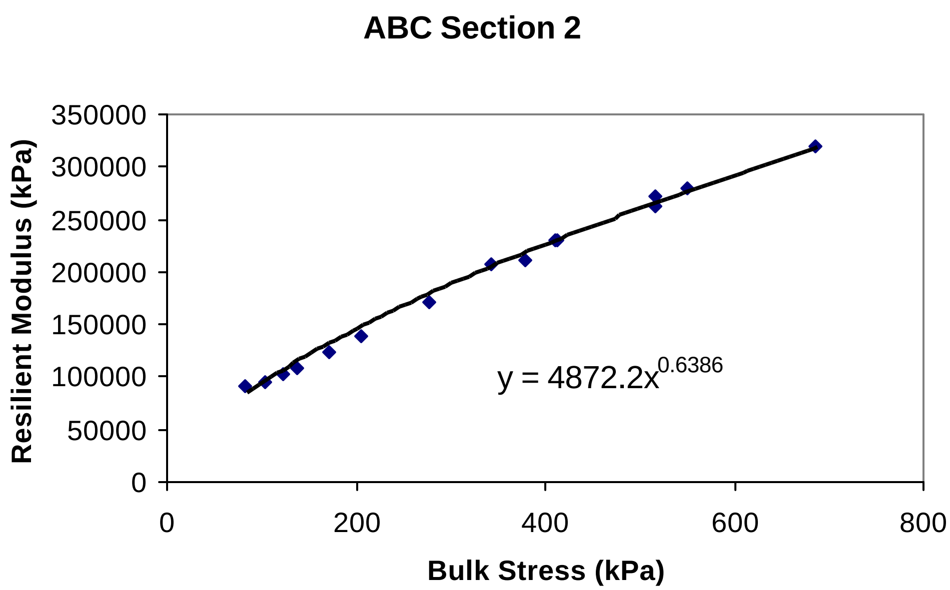

Figure D.20 ABC Resilient Modulus Data for WesTrack Section 2

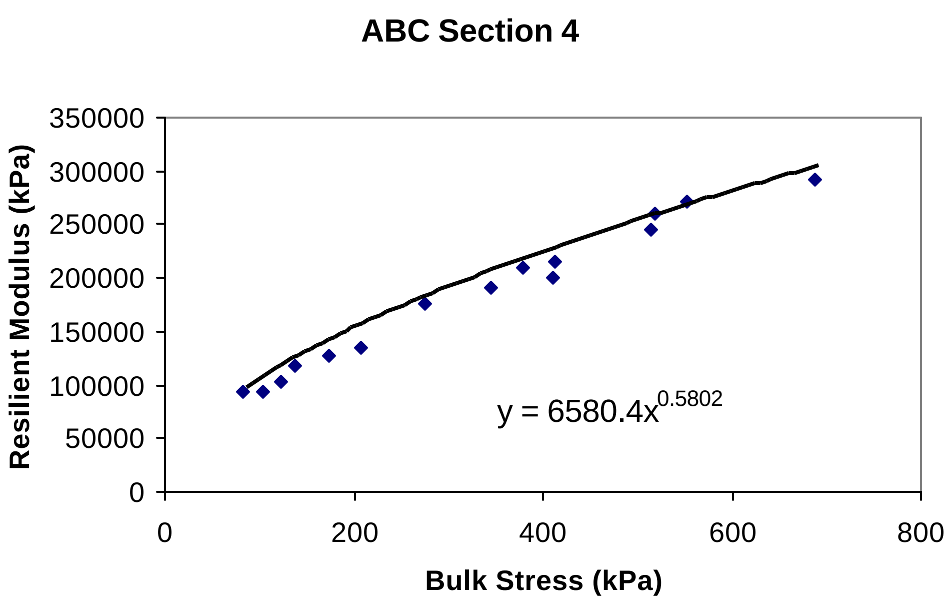

Figure D.21 ABC Resilient Modulus Data for WesTrack Section 4

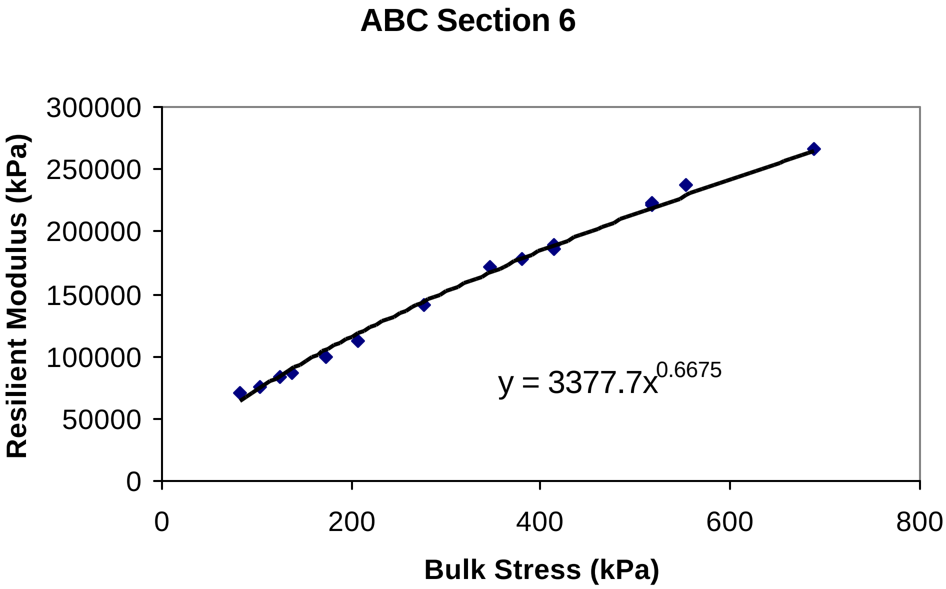

Figure D.22 ABC Resilient Modulus Data for WesTrack Section 6

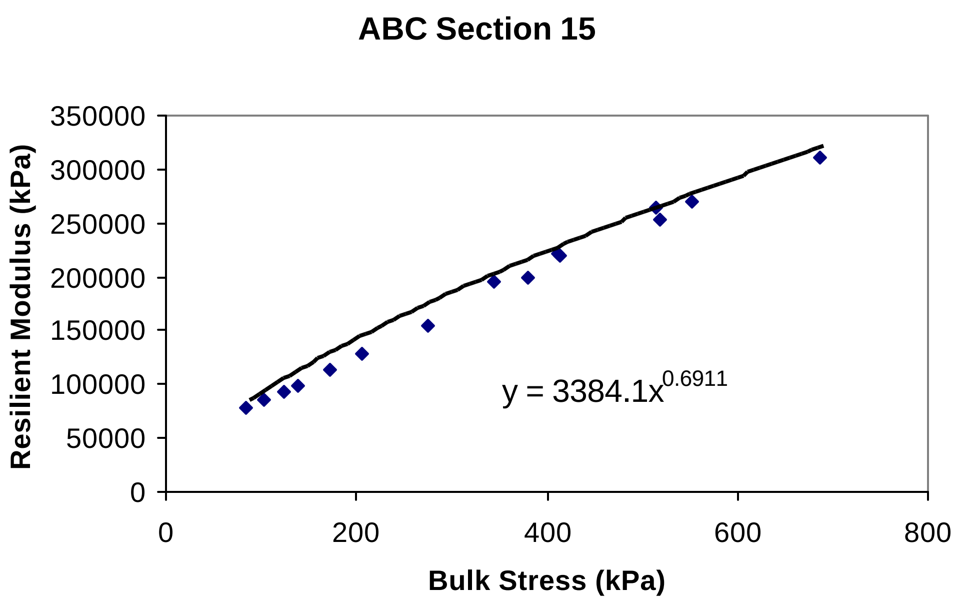

Figure D.23 ABC Resilient Modulus Data for WesTrack Section 15

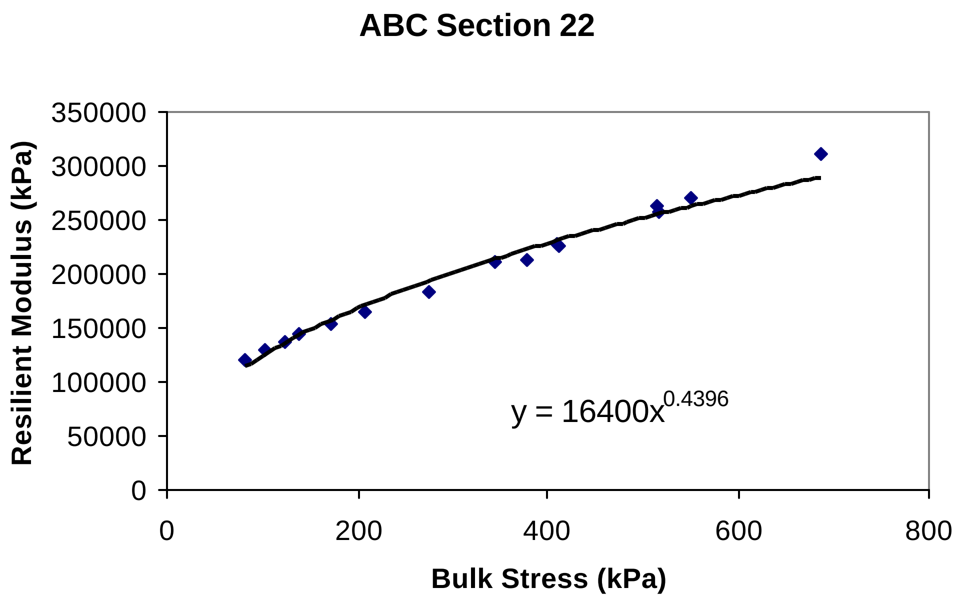

Figure D.24 ABC Resilient Modulus Data for WesTrack Section 22

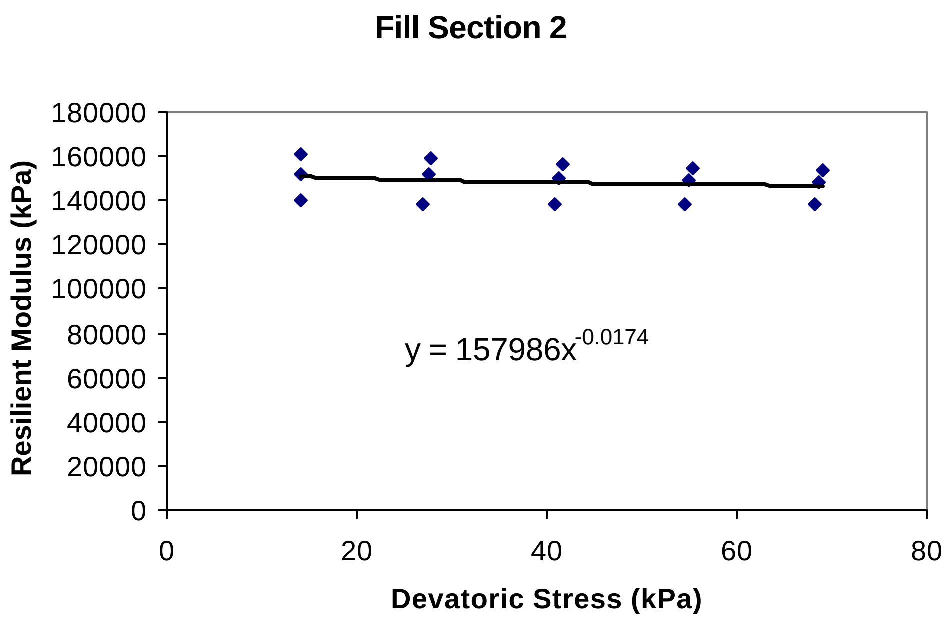

Figure D.25 Fill Resilient Modulus Data for WesTrack Section 2

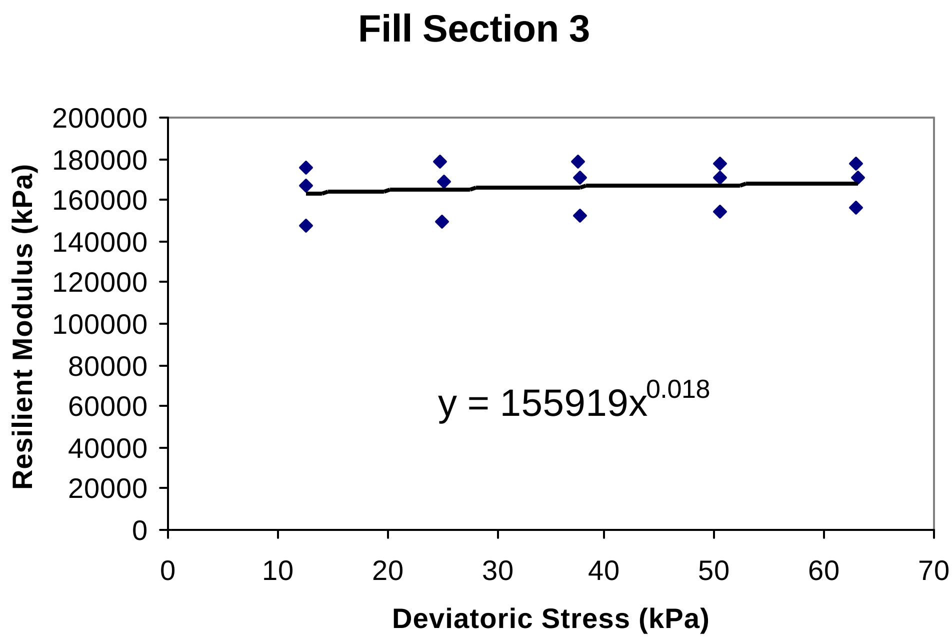

Figure D.26 Fill Resilient Modulus Data for WesTrack Section 3

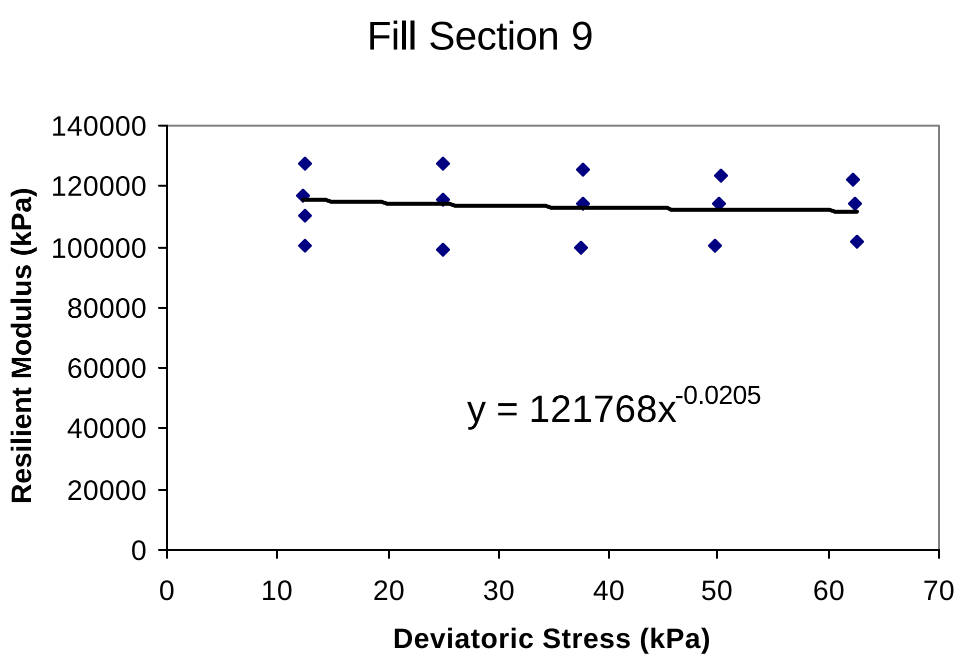

Figure D.27 Fill Resilient Modulus Data for WesTrack Section 9

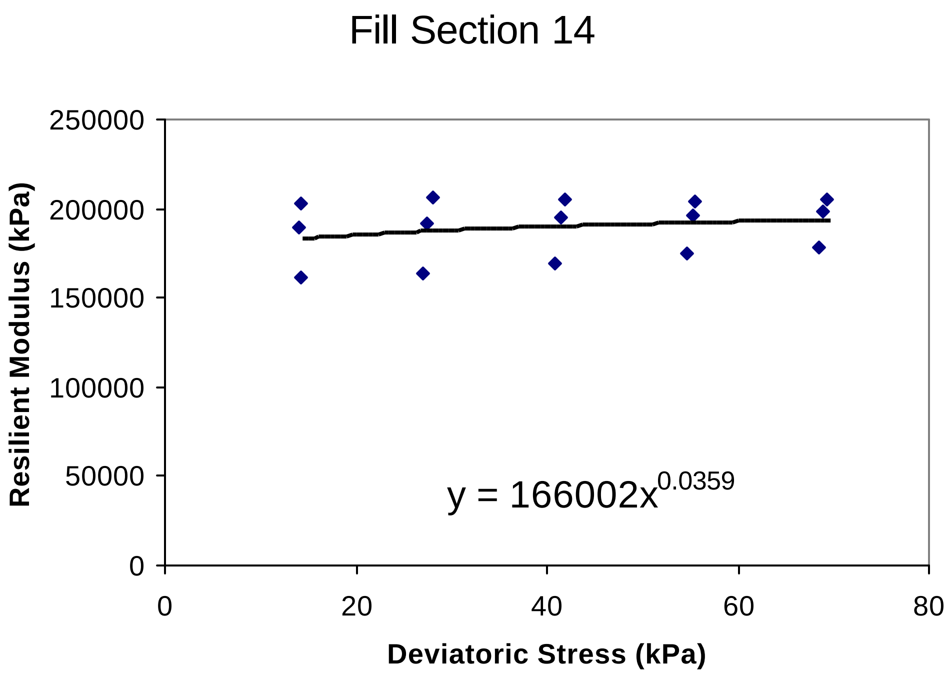

Figure D.28 Fill Resilient Modulus Data for WesTrack Section 14

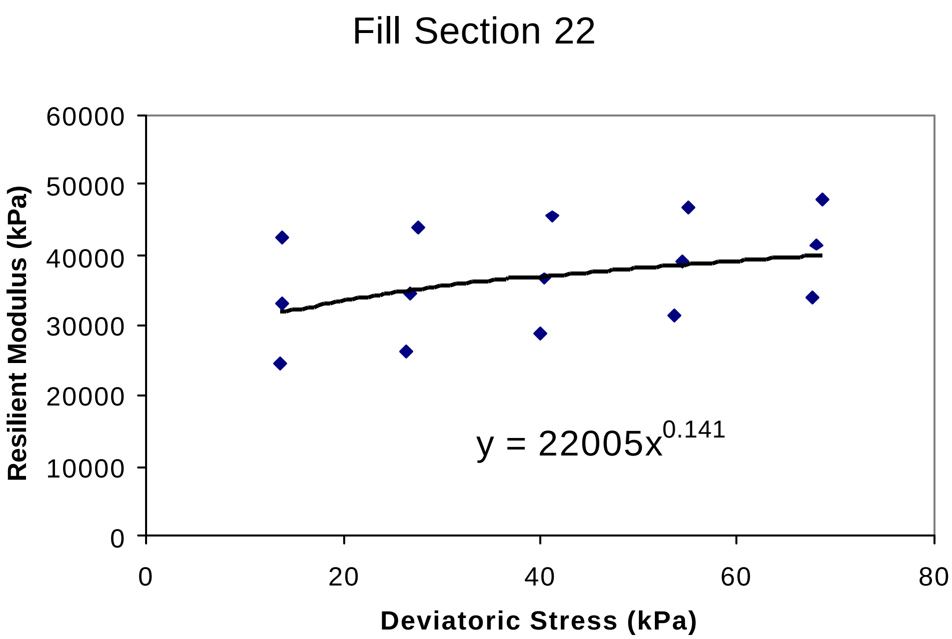

Figure D.29 Fill Resilient Modulus Data for WesTrack Section 22

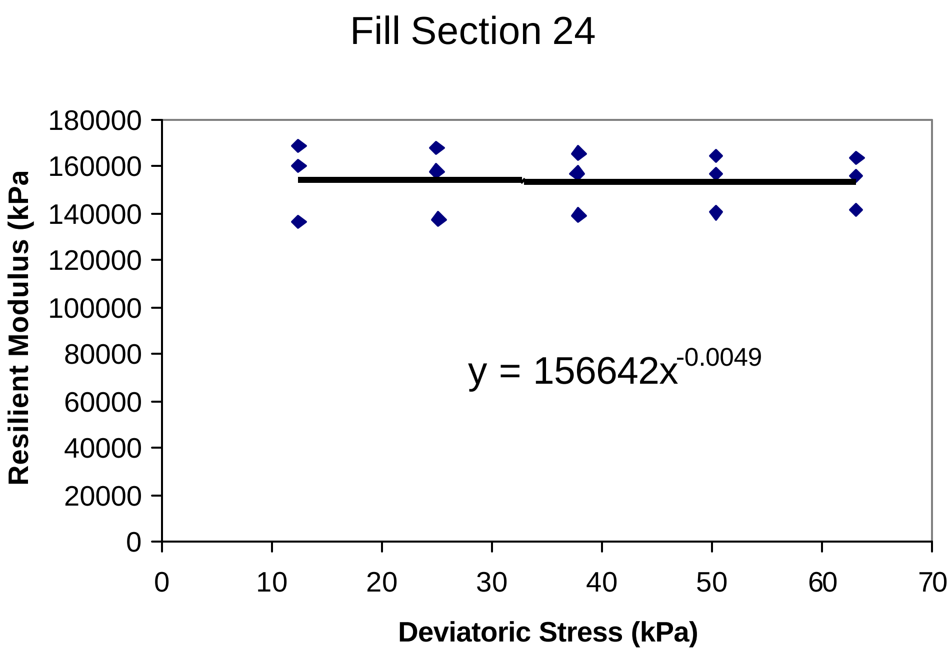

Figure D.30 Fill Resilient Modulus Data for WesTrack Section 24

D.4 **Predicted and Measured Peak Stresses for Monotonic Tests**

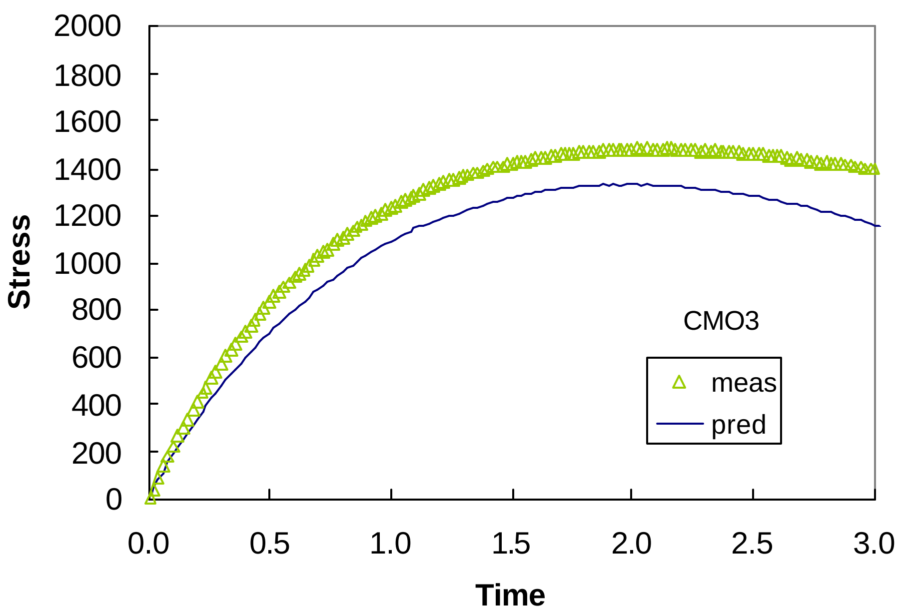

Figure D.31 Measured and Predicted Values for CMO3

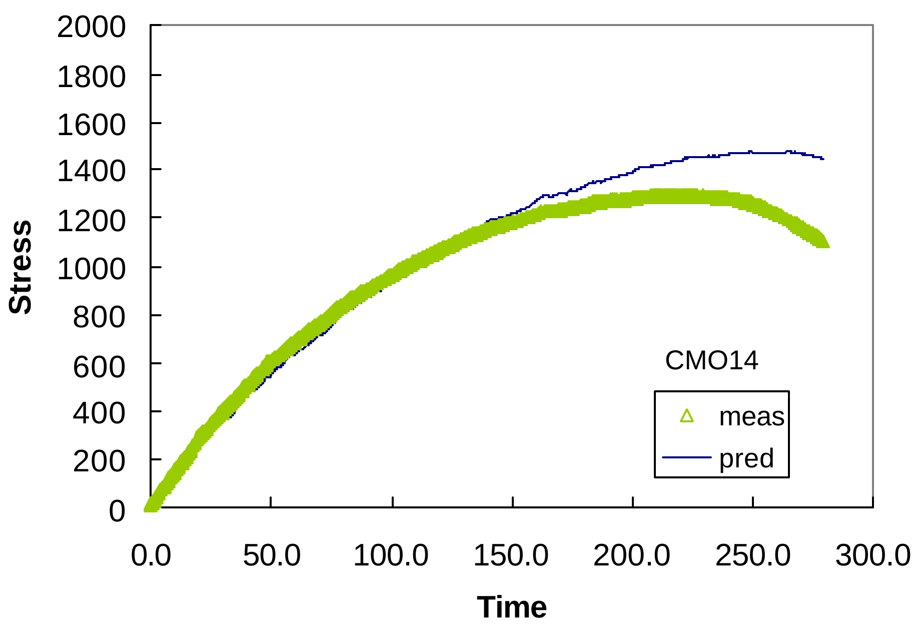

Figure D.32 Measured and Predicted Values for CMO14

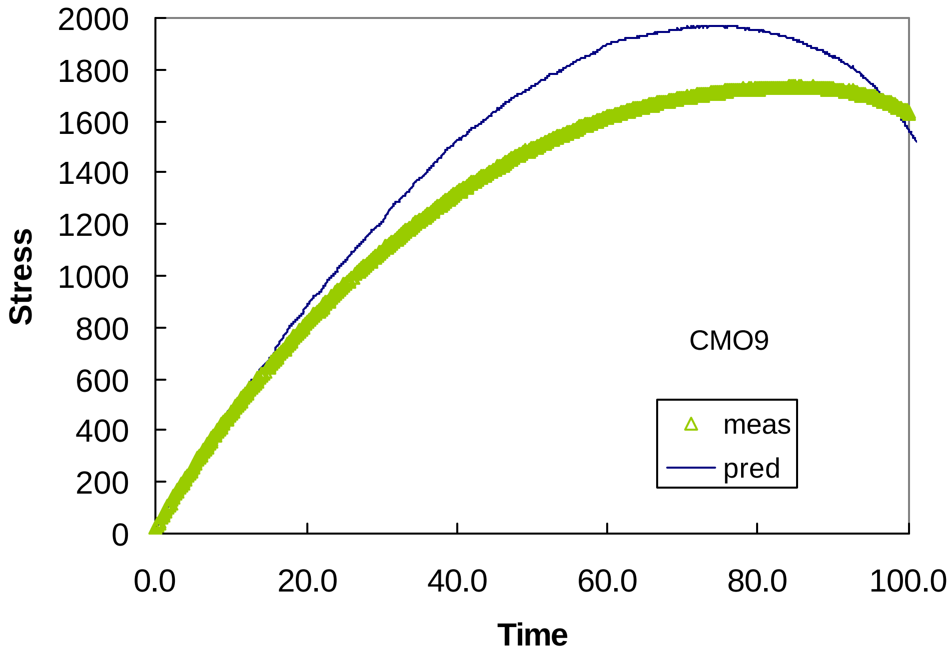

Figure D.33 Measured and Predicted Values for CMO9

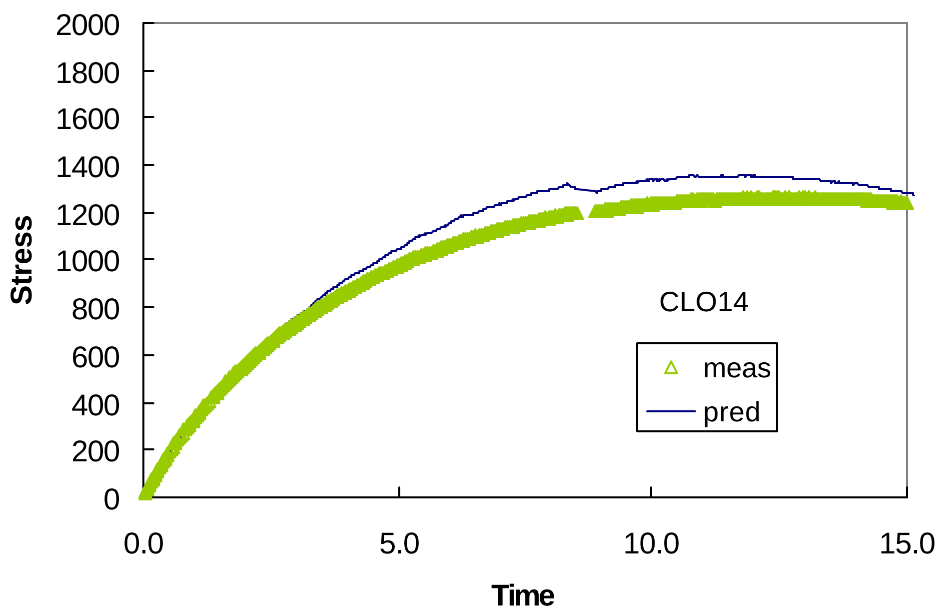

Figure D.34 Measured and Predicted Values for CLO14

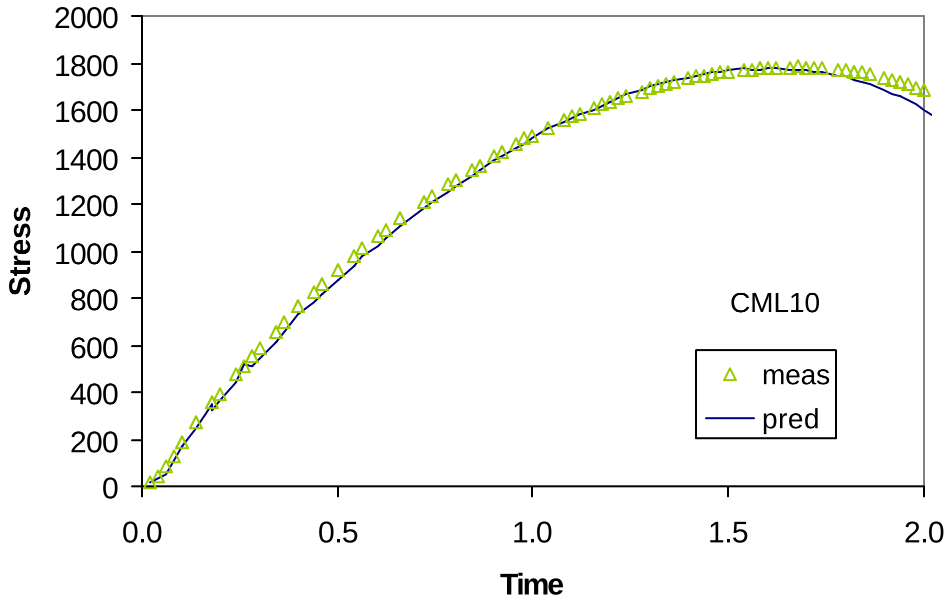

Figure D.35 Measured and Predicted Values for CML10

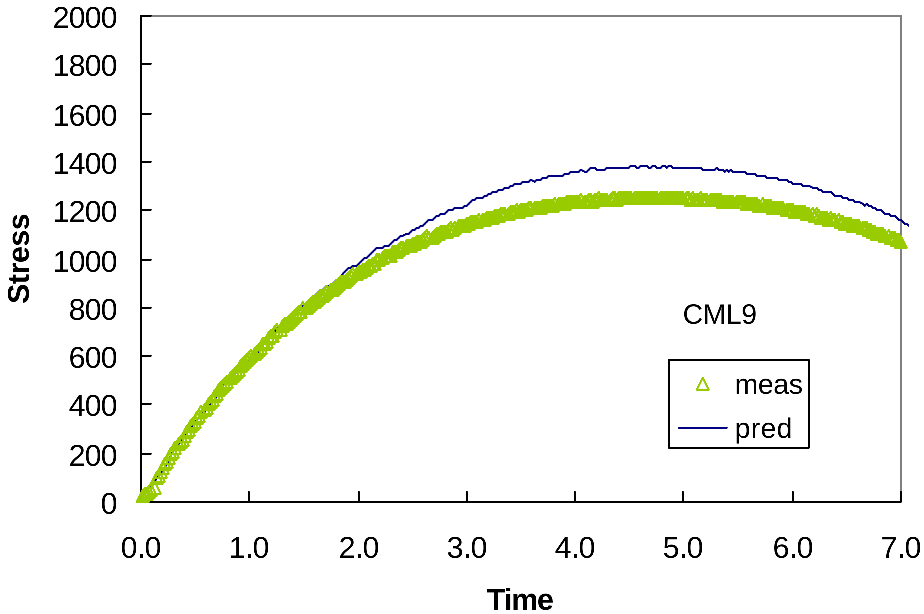

Figure D.36 Measured and Predicted Values for CML9

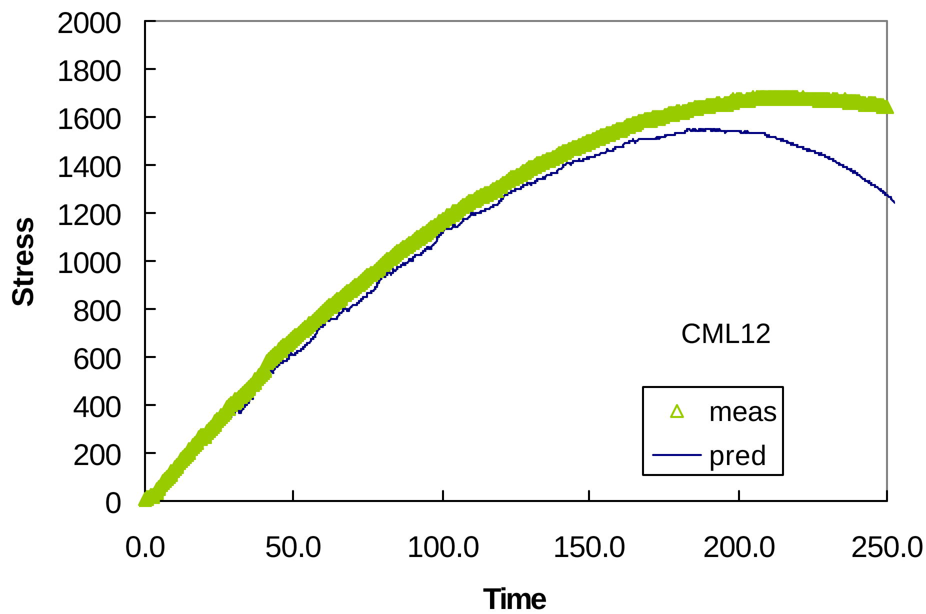

Figure D.37 Measured and Predicted Values for CML12

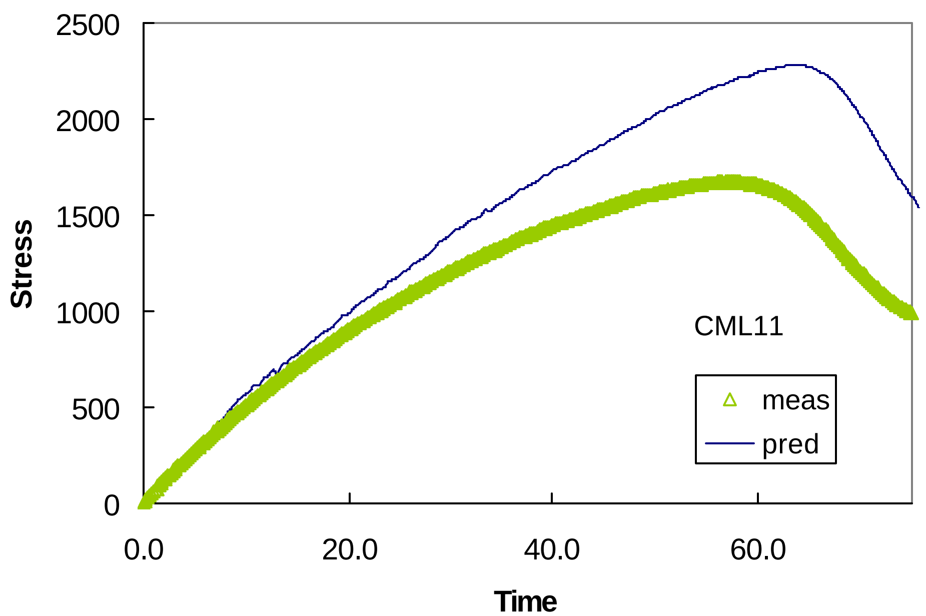

Figure D.38 Measured and Predicted Values for CML11

D.5 **Predicted and Measured Peak Stresses for Cyclic Tests**

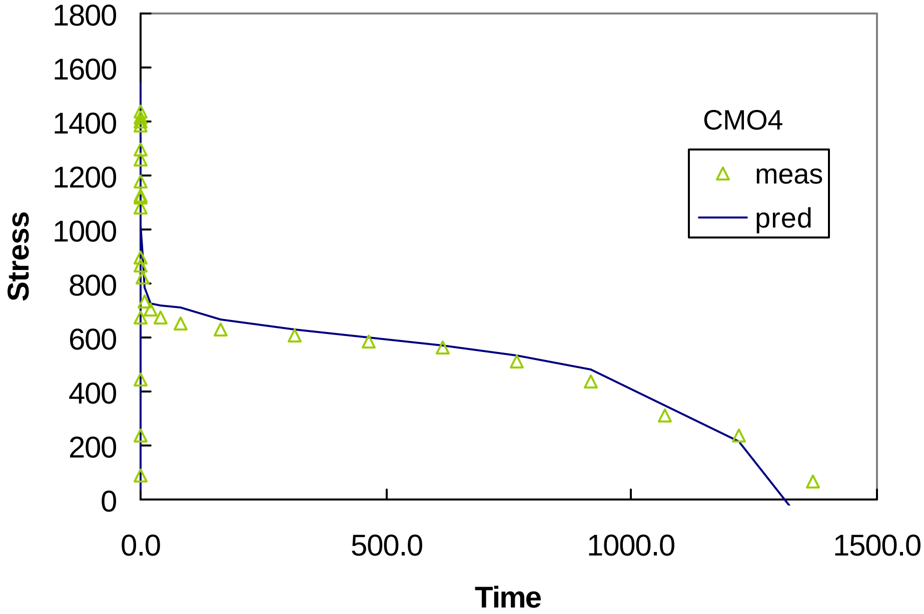

Figure D.39 Measured and Predicted Values for CMO4

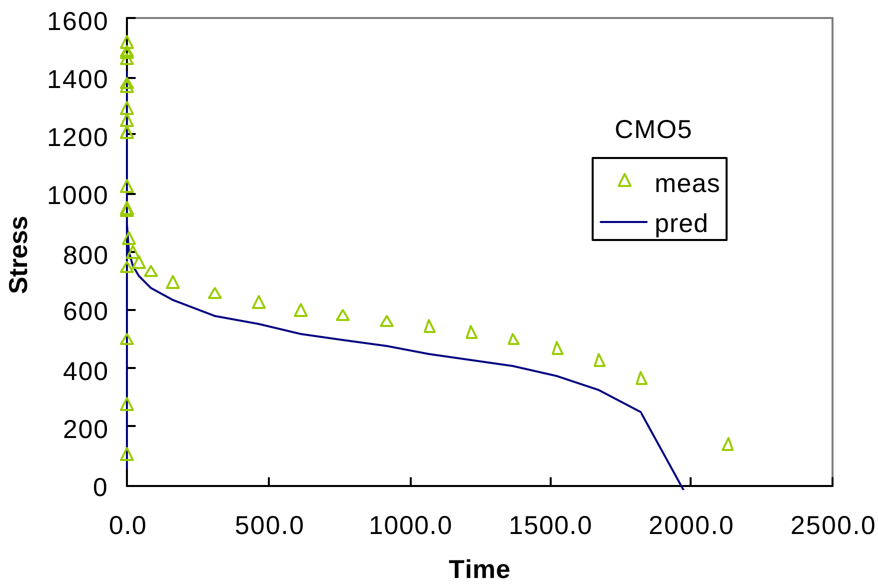

Figure D.40 Measured and Predicted Values for CMO5

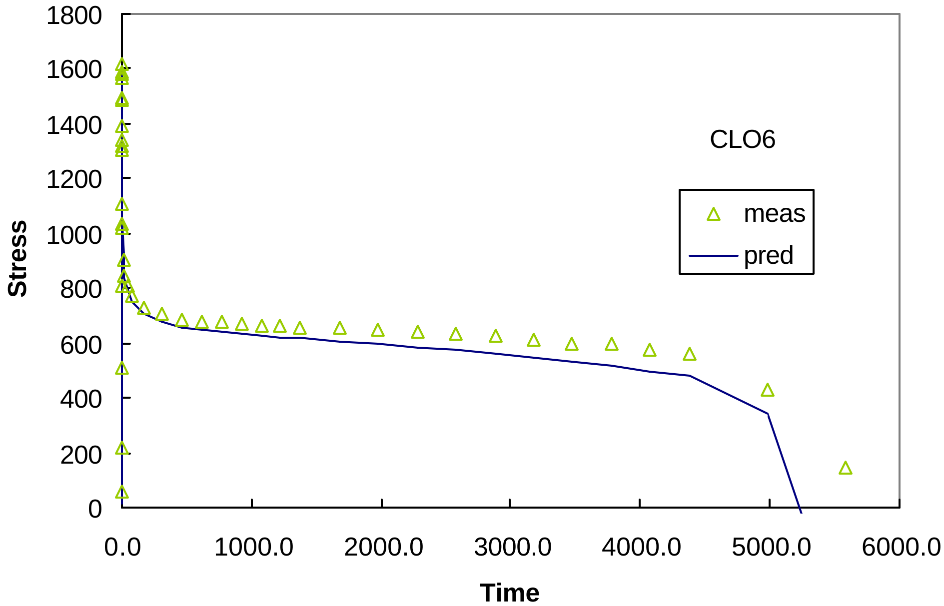

Figure D.41 Measured and Predicted Values for CLO6

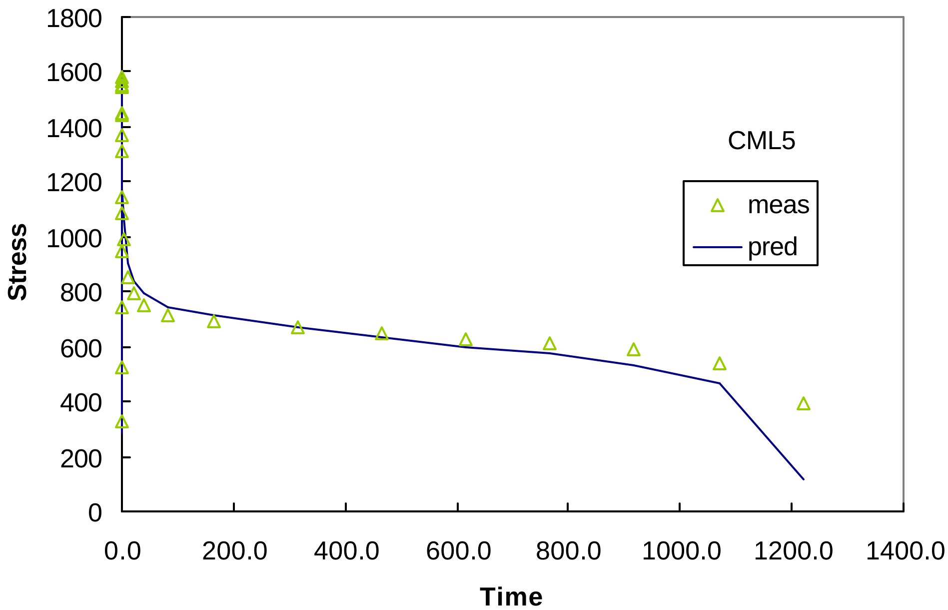

Figure D.42 Measured and Predicted Values for CML5

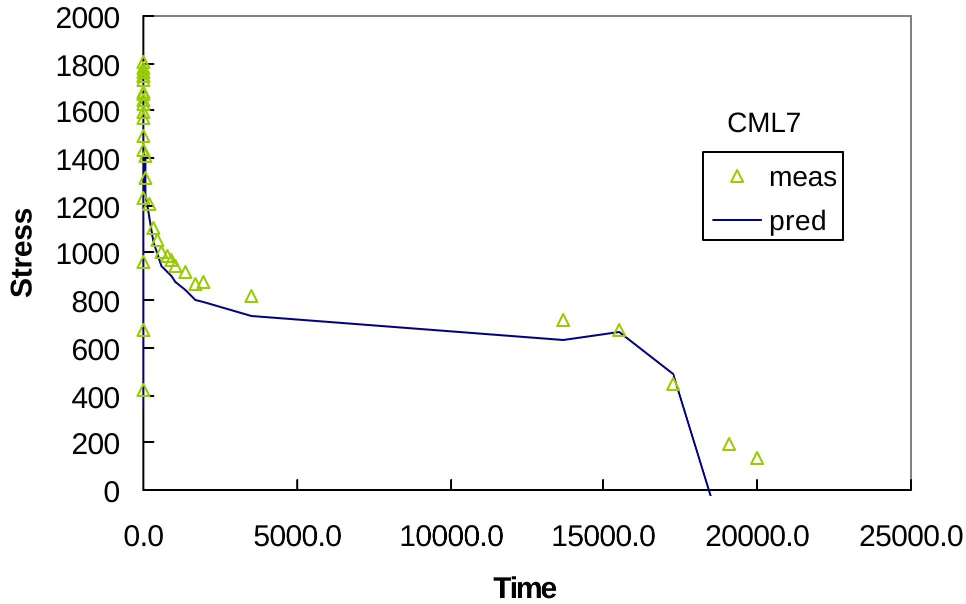

Figure D.43 Measured and Predicted Values for CML7

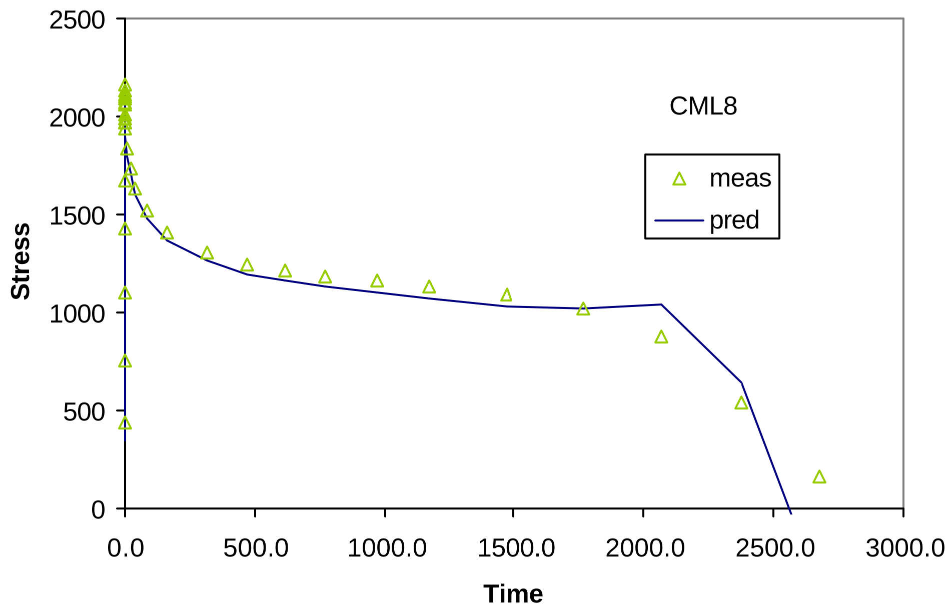

Figure D.44 Measured and Predicted Values for CML8

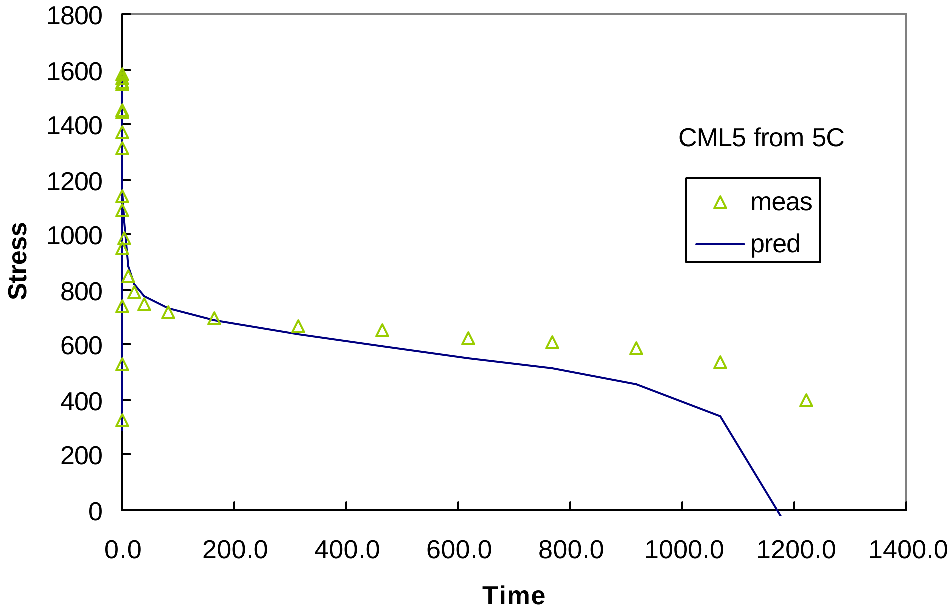

Figure D.45 Measured and Predicted Values for CML5 from 5C Curve

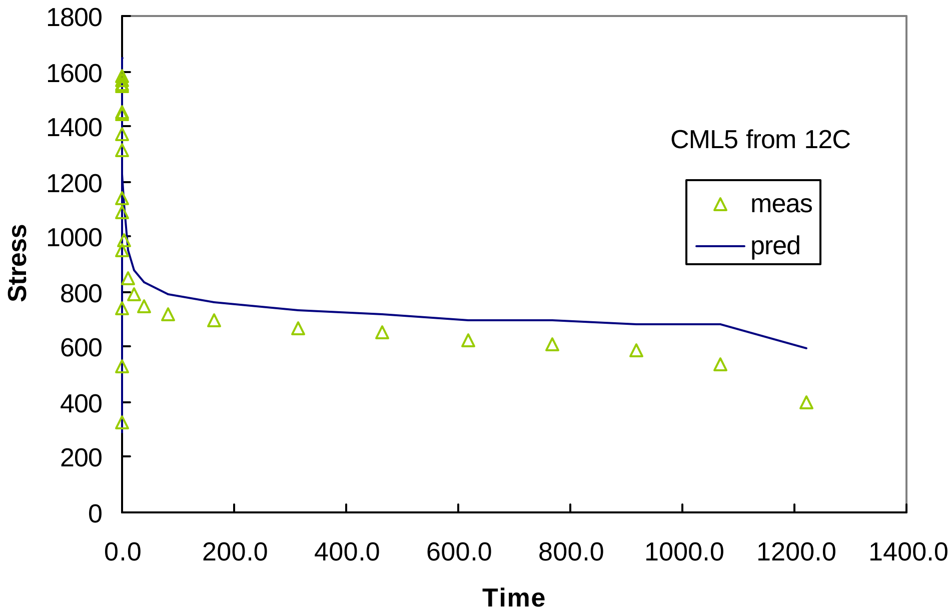

Figure D.46 Measured and Predicted Values for CML5 from 12C Curve

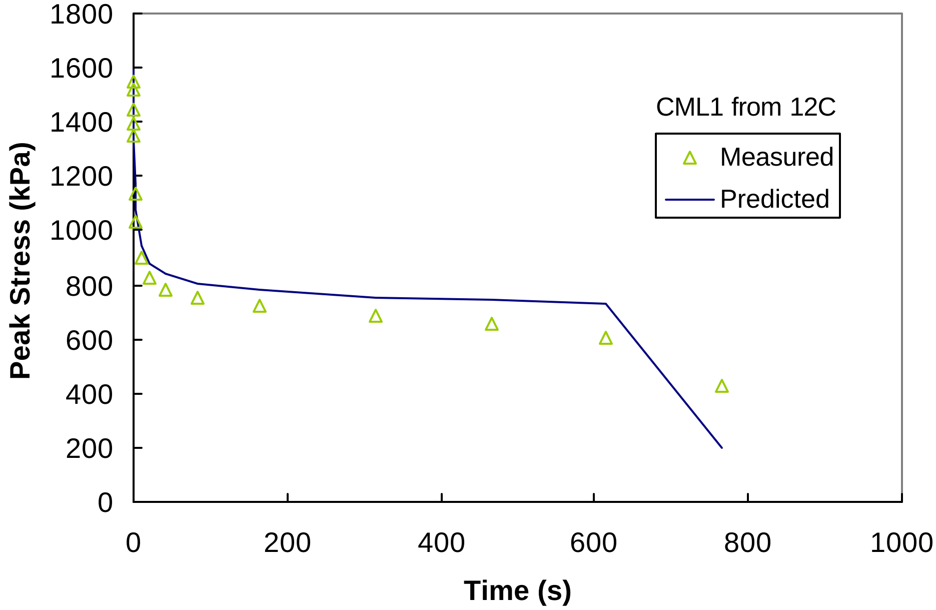

Figure D.47 Measured and Predicted Values for CML1 from 12C Curve

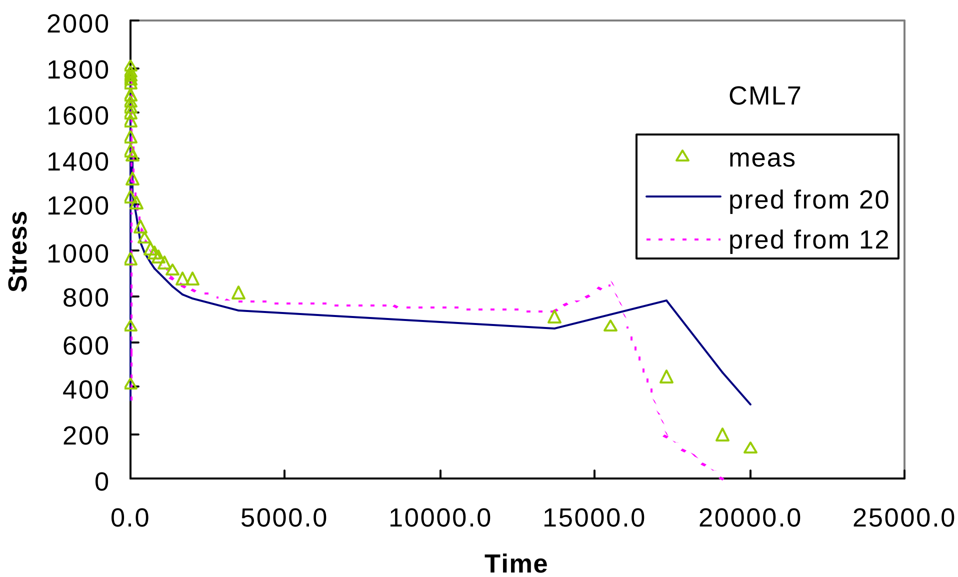

Figure D.48 Measured and Predicted Values for CML7 from 20C and 12C Curves

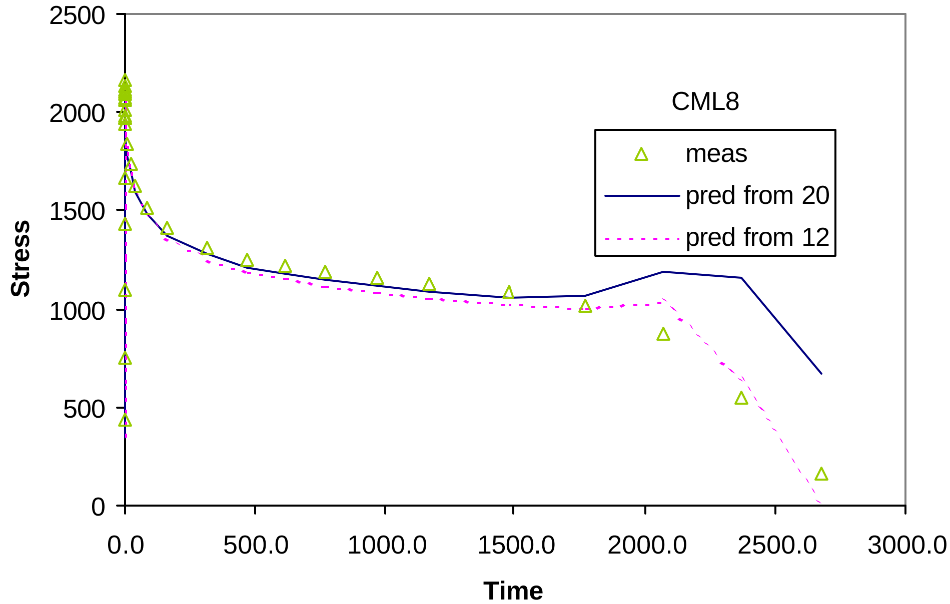

Figure D.49 Measured and Predicted Values for CML8 from 20C and 12C Curves

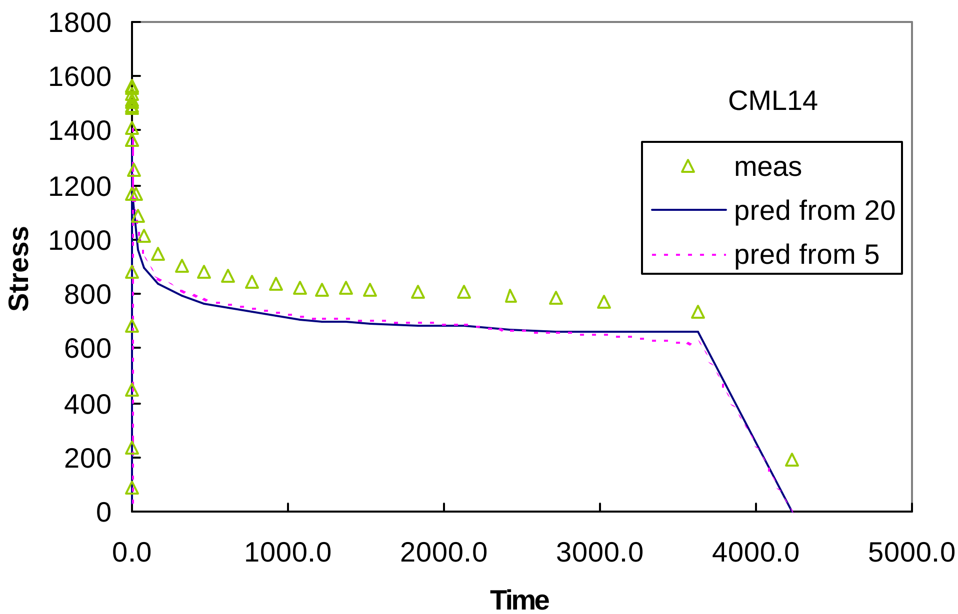

Figure D.50 Measured and Predicted Values for CML14 from 20C and 5C Curves

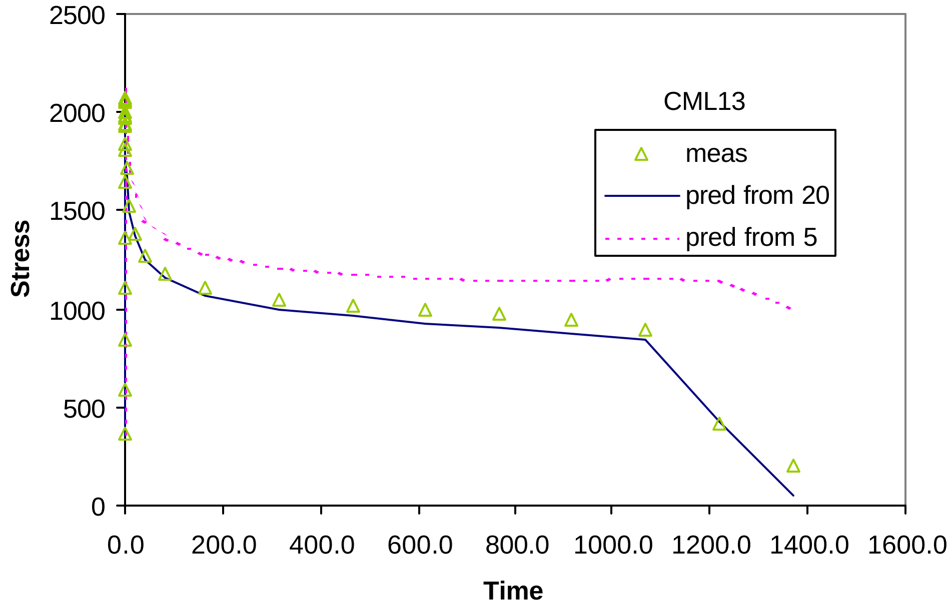

Figure D.51 Measured and Predicted Values for CML13 from 20C and 5C Curves